

Single-molecule microscopy in zebrafish embryos Góra, R.J.

Citation

Góra, R. J. (2022, November 23). Single-molecule microscopy in zebrafish embryos. Retrieved from https://hdl.handle.net/1887/3487015

Version: Publisher's Version

Licence agreement concerning inclusion of doctoral thesis License:

in the Institutional Repository of the University of Leiden

Downloaded from: https://hdl.handle.net/1887/3487015

Note: To cite this publication please use the final published version (if applicable).

SINGLE-MOLECULE MICROSCOPY IN ZEBRAFISH EMBRYOS

RADOSŁAW JAKUB GÓRA

Single-Molecule Microscopy in Zebrafish EmbryosCover and layout by **Radosław Jakub Góra**

ISBN: 978-94-6423-906-5

This publication was funded by the Marie Sklodowska-Curie Interactive Training Network (ITN) *ImageInLife* (Grant Agreement 721537)

Figures on pages 22, 25, 27 and 168 created with BioRender.com

Cover image: an artistic representation of trajectories of single molecules diffusing inside a multicellular organism

Copyright © 2022 by Radosław Jakub Góra. All rights reserved. No parts of this book may be reproduced, stored in retrieval system, or transmitted in any form or by any means without prior permission of the author

SINGLE-MOLECULE MICROSCOPY IN ZEBRAFISH EMBRYOS

Proefschrift

ter verkrijging van
de graad van doctor aan de Universiteit Leiden,
op gezag van rector magnificus prof. dr. ir. H. Bijl,
volgens besluit van het college voor promoties
te verdedigen op woensdag 23 november 2022
klokke 15.00 uur

door

RADOSŁAW JAKUB GÓRA

geboren te Wrocław, Polen in 1991

Promotores:

Dr. M.J.M. Schaaf

Prof. dr. A.H. Meijer

Promotiecommissie:

Prof. dr. G. van Wezel

Prof. dr. A. Briegel

Prof. Dr. A. Cambi (Radboud University Medical Center, Nijmegen)

Dr. P. Loza-Alvarez (The Institute of Photonic Sciences, Castelldefels)

Dr. J.J. Willemse

Keep the ship outside the spray and surge Homer, the Odyssey To everyone who joined me on the ship

TABLE OF CONTENTS

1.	INTE	RODUCTION	13
	1.1.	THE ORIGINS OF SINGLE-MOLECULE STUDIES	13
	1.2.	FLUORESCENCE AND FLUOROPHORES USED IN SMM	14
	1.3.	THE DEVELOPMENT OF SINGLE-MOLECULE MICROSCOPY (SMM)	16
	1.4.	MICROSCOPY SETUPS USED FOR SMM	19
	1.5.	SMM TO STUDY PROTEIN DYNAMICS IN VIVO	.20
	1.6.	ANALYSIS OF THE DATA OBTAINED THROUGH SMM IMAGING	22
	1.7.	H-RAS AND THE GLUCOCORTICOID RECEPTOR (GR): MODEL PROTEINS	
	FOR SI	NGLE-MOLECULE STUDIES IN THE MEMBRANE AND THE NUCLEUS	.24
	1.8.	OUTLINE OF THE DOCTORAL THESIS	.26
	REFER	ENCES	.30
2.	ANA	LYSIS OF THE H-RAS MOBILITY PATTERN IN VIVO SHOWS CELLULAR	
Н	ETEROC	GENEITY INSIDE EPIDERMAL TISSUE	.37
	ABSTR	ACT	. 37
	2.1.	INTRODUCTION	.38
	2.2.	RESULTS	41
	The r	mobility pattern of YFP-C10H-Ras and YFP-H-Ras in HEK293T cells.	
		41	
		mobility pattern of YFP-C10H-Ras and YFP-H-Ras in epidermal cells of zebrafish	
		ryos	
		mobility pattern of YFP-C10H-Ras in zebrafish embryos at different developmental	
	9	mobility pattern of YFP-H-Ras ^{VI2} and YFP-H-Ras ^{NI7} in epidermal cells of zebrafish	
		ryos	
	The r	nobility pattern of YFP-H-Ras and YFP-H-Ras ^{v12} in epidermal cells of zebrafish	
	emb	ryos after treatment with Latrunculin B and Methyl-β-cyclodextrin	
		49	
	Thes	sources of variability of the results52	
	2.3.	DISCUSSION	
	2.4.	MATERIALS AND METHODS	.60
		afish60	
		cultures, transfection, and fixation60	
	Micro	pinjection of DNA in zebrafish embryos61	

(MBCD)	Tre	eatment of zebrafish embryos with Latrunculin B (LatB) and	Methyl-β-cyclodextrin	
Confocal laser-scanning microscopy	(M	1BCD)	61	
Total internal reflection fluorescence microscopy (TIRFM)	Flo	uorescence stereomicroscopy	62	
Analysis of protein diffusion patterns	Сс	onfocal laser-scanning microscopy	62	
Experimental design	To	etal internal reflection fluorescence microscopy (TIRFM)	62	
Statistical Analysis	Ar	nalysis of protein diffusion patterns	63	
REFERENCES	Ex	perimental design	65	
33. MULTIFOCAL TWO-PHOTON EXCITATION FLUORESCENCE MICROSCOPY REVEALS HOP DIFFUSION OF H-RAS MEMBRANE ANCHORS IN EPIDERMAL CELLS OF ZEBRAFISH EMBRYOS	St	atistical Analysis	65	
3. MULTIFOCAL TWO-PHOTON EXCITATION FLUORESCENCE MICROSCOPY REVEALS HOP DIFFUSION OF H-RAS MEMBRANE ANCHORS IN EPIDERMAL CELLS OF ZEBRAFISH EMBRYOS	REF	ERENCES		67
REVEALS HOP DIFFUSION OF H-RAS MEMBRANE ANCHORS IN EPIDERMAL CELLS OF ZEBRAFISH EMBRYOS	SUPI	PLEMENTARY FIGURE		73
REVEALS HOP DIFFUSION OF H-RAS MEMBRANE ANCHORS IN EPIDERMAL CELLS OF ZEBRAFISH EMBRYOS				
ABSTRACT	3. M	ULTIFOCAL TWO-PHOTON EXCITATION FLUORESCE	NCE MICROSCOPY	
ABSTRACT	REVEA	LS HOP DIFFUSION OF H-RAS MEMBRANE ANCHOR	S IN EPIDERMAL CEL	LS
3.1. INTRODUCTION	OF ZEE	BRAFISH EMBRYOS	•••••	75
3.2. RESULTS	ABS	TRACT		75
Imaging of GFP-C10H-Ras molecules in epidermal cells of zebrafish embryos using 2PEFM	3.1.	INTRODUCTION		76
Analysis of the mobility pattern of GFP-C10H-Ras molecules in epidermal cells of zebrafish embryos using 2PEFM	3.2.	RESULTS		79
Analysis of the mobility pattern of GFP-C10H-Ras molecules in epidermal cells of zebrafish embryos using 2PEFM	Im	naging of GFP-C10H-Ras molecules in epidermal cells of zebr	afish embryos using 2PE	FM
embryos using 2PEFM			_	
Comparison of the GFP-C10H-Ras dynamics between 2PEFM and TIRFM with different temporal resolutions	Ar	nalysis of the mobility pattern of GFP-C10H-Ras molecules in	epidermal cells of zebrai	fish
temporal resolutions	en	nbryos using 2PEFM	84	
Analysis of the excitation laser power impact on the GFP-C10H-Ras mobility pattern	Сс	omparison of the GFP-C10H-Ras dynamics between 2PEFM c	and TIRFM with different	
	te	mporal resolutions	86	
The mobility pattern of GFP-C10H-Ras in epidermal cells of zebrafish embryos after treatment with Latrunculin B and Methyl-β-cyclodextrin	Ar	nalysis of the excitation laser power impact on the GFP-C10H	l-Ras mobility pattern	
treatment with Latrunculin B and Methyl-β-cyclodextrin			90	
Analysis of the single GFP-C10H-Ras trajectories based on the 2PEFM imaging	Th	ne mobility pattern of GFP-C10H-Ras in epidermal cells of zeb	orafish embryos after	
3.3. DISCUSSION	tre	eatment with Latrunculin B and Methyl-β-cyclodextrin	92	
3.3. DISCUSSION	Ar	nalysis of the single GFP-C10H-Ras trajectories based on the .	2PEFM imaging	
3.4. MATERIALS AND METHODS			95	
Zebrafish	3.3.	DISCUSSION		99
Treatment of zebrafish embryos with Latrunculin B (LatB) and Methyl-β-cyclodextrin (MBCD)104 Sample preparation and mounting105 Two-Photon Excitation Fluorescence Microscopy (2PEFM)105	3.4.	MATERIALS AND METHODS		.104
(MBCD)104 Sample preparation and mounting105 Two-Photon Excitation Fluorescence Microscopy (2PEFM)105	Ze	ebrafish		
Sample preparation and mounting105 Two-Photon Excitation Fluorescence Microscopy (2PEFM)105	Tre	eatment of zebrafish embryos with Latrunculin B (LatB) and	Methyl-β-cyclodextrin	
Two-Photon Excitation Fluorescence Microscopy (2PEFM)105				
, , ,	Sa	ample preparation and mounting	105	
Total internal reflection fluorescence microscopy (TIRFM)106	Tv	vo-Photon Excitation Fluorescence Microscopy (2PEFM)	105	
	То	otal internal reflection fluorescence microscopy (TIRFM)	106	

An	alysis of protein diffusion patterns	106	
An	alysis of photobleaching	108	
An	alysis of GFP-C10H-Ras trajectories	109	
Exp	perimental design	109	
Sto	itistical Analysis	110	
REFE	RENCES		112
SUPF	PLEMENTARY FIGURES		118
4. AN	IALYSIS OF INTRACELLULAR PROTEIN DYNAMICS II	N LIVING ZEBRAFISH	1
EMBRY	OS USING LIGHT-SHEET FLUORESCENCE SINGLE-MO	OLECULE MICROSCO)PY
* D.C.T.	DA CT		
	RACT		
4.1.	INTRODUCTION		122
4.2.	RESULTS		126
An	LSFM platform for in vivo SMM imaging (LSFSMM)	126	
Ch	aracterization of detected fluorescence signals from individ	ual YFP-GR molecules	
		131	
Exp	periments on live fish and data analysis	133	
4.3.	DISCUSSION		139
LSF	-SMM setup	139	
The	e glucocorticoid receptor mobility patterns in zebrafish emb	ryos 140	
The	e effect of dexamethasone treatment on the mobility patter	rns of the glucocorticoid	d
rec	eptor subpopulations	142	
Va	riability of the glucocorticoid receptor mobility patterns	144	
4.4.	MATERIALS AND METHODS		144
Zel	brafish	144	
Mic	croinjection and treatment of embryos	144	
LSF	-SMM setup details	145	
De	termination of imaging parameters	146	
Cu	ltured cells fixation, mounting, and LSFSMM imaging	147	
De	termination of the fluorescence signals characteristics deriv	ed from individual YFP	
mo	olecules	147	
Live	e zebrafish embryo mounting and LSFSMM imaging	147	
Live	e imaging using the muviSPIM setup	148	
Da	ta Analysis	149	
Exp	perimental Design	150	
REFE	RENCES		153

	SUPPL	EMENTARY FIGURES	. 158
5.	SUM	IMARY AND DISCUSSION	161
	5.1.	SUMMARY OF THE THESIS	161
	5.2.	THE MOBILITY PATTERNS OF H-RAS AND C10H-RAS IN EPIDERMAL CELL	S
	OF LIVI	NG ZEBRAFISH EMBRYOS (CHAPTERS 2 AND 3)	.163
	5.3.	THE MOBILITY PATTERN OF THE GLUCOCORTICOID RECEPTOR IN LIVING	G
	ZEBRA	FISH EMBRYOS (CHAPTER 4)	169
	5.4.	THE SOURCES OF VARIABILITY OF THE SMM MEASUREMENTS IN THE	
	ZEBRA	FISH EMBRYO MODEL (Chapters 2 and 4)	171
	REFER	ENCES	.174
		NDSE SAMENVATTING	
CI	JRRICU	LUM VITAE	183
LI	ST OF P	PUBLICATIONS	.185

1. INTRODUCTION

In this thesis, research is described aimed at developing tools of single-molecule microscopy (SMM) to image individual proteins and analyze their dynamic behavior inside cells of living zebrafish (*Danio rerio*) embryos. In this study, the zebrafish model is imaged using SMM in order to investigate mobility patterns of proteins that are anchored in the plasma membrane as well as proteins traversing the cell nuclei. This thesis provides novel applications of SMM for studying mobility patterns of individual molecules in an intact vertebrate biological system, and offers insights into the *in vivo* dynamics of the single molecules under investigation.

1.1 THE ORIGINS OF SINGLE-MOLECULE STUDIES

Because of the emphasis placed on molecules as the minimal functional units of biological systems, research at the single-molecule level plays an important role in a range of fields of biological investigations. Over the years, a myriad of scientific experiments in biology has been conducted with a focus laid on the population level. The outcomes of such experiments are established based on the information retrieved from ensemble analyses, which take into consideration the generalized behavior of the studied population (Shashkova and Leake, 2017). For instance, in ensemble studies performed on cell cultures, it is often expected that members of the populations – comprising thousands of cells – will all exhibit a similar type of action in response to a certain treatment or other biochemical stimuli. While producing the mean of all the observations can eliminate potential outliers present in the data, such as cells exhibiting anomalous behavior, the same approach risks losing valuable information rooted in the biological heterogeneity of all cell populations (Leake, 2013; Rubin, 1990).

The ensemble analyses of biochemical properties lead to a loss of information regarding any deviations in measured parameters, and can ultimately result in misinterpretations of the underlying physiological relevance of existing molecular subpopulations. Therefore, studies at the single-molecule level are especially important in the scientific fields where biological diversity is rife, such as biophysics, systems and synthetic biology (Lenn and Leake, 2012). Ultimately, single-molecule examinations are critical to any research

area where enhancement of both the effective spatial and temporal resolution might shed new light on the processes taking place at the molecular level. Modern techniques enable researchers to directly investigate biochemical interactions of the signal transductions dynamics, which facilitates a more detailed understanding of crucial biological processes, such as protein trafficking, localization, and clustering (Kusumi et al., 2012; Lommerse et al., 2004; Shashkova and Leake, 2017; Shashkova et al., 2017)

One of the most important techniques that is employed to examine biological processes at the single-molecule resolution and that is currently undergoing rapid technical development is the SMM in which fluorescence microscopy is utilized (Miller et al., 2018). This form of SMM has transformed into a valuable method used in many biophysical, biochemical and cell biological studies. Fluorescence SMM allows for observations of the real-time behavior of individual biomolecules, allowing researchers to observe their dynamics and other, detailed features. Proteins, having multiple biological functions, have constituted the primary focus for the majority of SMM studies, and previous research on protein activities performed by SMM helped us better understand a variety of biochemical processes, including protein-DNA interactions or kinetics of protein transport (Yokota, 2020). Single-molecule fluorescence microscopy has uncovered many fundamental biological processes that were not studied previously due to the limitations imposed by ensemble averaging, including studies of the bacterial flagellar motor rotation (Sowa et al., 2005), protein folding and translocation (Bryan et al., 2014), signal transduction (Wollman and Leake, 2016), DNA replication and remodeling (Reyes-Lamothe et al., 2010), oxidative phosphorylation (Lenn and Leake, 2016), cell division mechanisms (Biteen et al., 2008), mitochondrial protein dynamics (Kuzmenko et al., 2011), and many others.

1.2 FLUORESCENCE AND FLUOROPHORES USED IN SMM

The phenomenon of fluorescence occurs when a fluorophore, in a form of an atom or an entire molecule, absorbs a photon and subsequently reemits a photon. Upon absorption of a photon, electrons in the fluorophore transit from a ground state to a higher energy state, in a process that takes less than one femtosecond. After the switch to this excited state, the electron returns to the ground state. This return is accompanied by the emission of a photon, which has a smaller level of associated energy, and therefore

the wavelength of the emission light is longer than the wavelength of the excitation light (Shashkova and Leake, 2017). The loss of energy occurs due to vibrations that result from the oscillations of the atomic orbitals based on the difference in charge distributions between the electrons and the nuclei. The shift in wavelength between the excitation and emission light is named after Sir George Stokes, who was the first person to properly describe the physical foundations of fluorescence (Zimmer, 2009).

A class of fluorophores that is widely used in SMM comprises autofluorescent proteins, such as green and yellow fluorescent proteins (GFP and YFP, respectively). GFP was isolated from the jellyfish Aequorea victoria and was first described in 1962 (Shimomura et al., 1962). Around 30 years later, the gene encoding GFP was cloned and in 1992 the first studies were performed in which GFP was expressed in living cells (Chalfie et al., 1994; Prasher et al., 1992). Nowadays, GFP cDNA is often fused to a cDNA encoding a protein of interest and the resulting fluorescent fusion protein is expressed in biological models such as cell cultures, microorganisms or transgenic plants or animals, enabling the detection of this protein in these models by fluorescence microscopy. A variety of GFP mutants are available with modified biophysical characteristics, including the S65T mutant with increased GFP photostability and fluorescence output, the F64L mutant with increased folding efficiency at 37°C, and the A206K mutant without self-oligomerization properties (Zacharias et al., 2002). Moreover, numerous GFP color mutants have been designed, such as T203Y for a yellow fluorescent protein (YFP), or Y66W for a cyan (CFP) one (Lippincott-Schwartz and Patterson, 2003). Other autofluorescent proteins, which are differently colored have been isolated, such as a red fluorescent protein (RFP), which was originally found in Discosoma sp., and served afterwards as the template for several derivatives, of which DsRed and mCherry are most commonly used (Miyawaki et al., 2012; Shaner et al., 2004). In addition, many photoconvertible fluorescent proteins, e.g., mEos, mMaple or Dendra, are currently available and can convert between different excitation-emission spectra of emitted light after illumination with lower (mostly UV) wavelengths. Photoconversion can be used for specific applications such as lineage tracing and protein turnover studies (Baker et al., 2010). Nonetheless, despite all the benefits offered by the use of these autofluorescent proteins, these fluorophores are highly unstable and undergo irreversible photobleaching after a certain time spent exposed to excitation light. Photobleaching is caused by the accumulation of free radicals present in the surrounding aqueous solutions that cause chemical damage to the structure

of the fluorescent proteins. Repetitive fluorophore excitation also contributes to the photobleaching events, as the excited fluorophores might not necessarily emit photon energy in the form of fluorescent light, but enter the dark (triplet) state instead. Being trapped in this state, fluorophores are increasingly vulnerable to undergoing a multitude of photochemical reactions, ultimately resulting in an irreversible loss of their fluorescence, a phenomenon known as photobleaching (Donnert et al., 2009).

As an alternative for labeling proteins with autofluorescent proteins, a multitude of approaches has been designed (Filonov et al., 2011; Los et al., 2008; Stagge et al., 2013; Lippincott-Schwartz and Patterson, 2003). Organic fluorescent dyes with superior characteristics can be attached to proteins of interest through linkers, including HALO- and SNAP-tags. In such cases, the DNA encoding the protein of interest is first genetically fused to the protein tag, i.e., HALO- or SNAP-tag, which consists of a DNA repair protein (in the case of SNAP), or a haloalkane dehalogenase enzyme (in the case of HALO). Following that, the biological sample expressing this fusion protein is incubated with a secondary probe, which is able to covalently bind to the protein tag. The secondary probes are fluorescently labelled with organic dyes, such as coumarin, tetramethylrhodamine, Alexa Fluor dyes, and others. Thus, this methodology enables the use of brighter and more photostable fluorophores when compared to the use of traditional fluorescent proteins. Multiple other labelling strategies are currently being developed or are already available. These include quantum dots, which are nanoparticles that are extremely bright and photostable, spontaneously blinking dyes (Bentolila et al., 2005), such as hydroxymethyl Si-rhodamine, HMSiR, which exploit reversible, pH-dependent chemical reactions and enable performing SMM at defined pH values in aqueous solutions (Uno et al., 2014), and temporally blinking dyes, such as PAINT, which do not require fluorophore switching and instead employ dyes that freely diffuse until their interactions with target molecules via permanent or transient binding (Giannone et al., 2010).

1.3 THE DEVELOPMENT OF SINGLE-MOLECULE MICROSCOPY (SMM)

SMM represents a family of powerful imaging techniques with a high spatial resolution that are used to visualize biological structures at the molecular scale. Due to diffraction, an image of a point source of light, visualized using a lens-based microscope, is not a single point but a point spread function (PSF). The PSF is usually an Airy disc pattern

with a central Gaussian peak, being the diffraction maximum, that is surrounded by less intense concentric rings. This PSF results in the blurring of any structures with a size that is smaller than the size of this central peak. This diffraction limit determines the resolution of an optical system and as a result, the capacity of an optical microscope to resolve the subcellular localization of single molecules and complexes thereof. In a practical sense, the resolution of a microscope is defined as the smallest separation distance between two point-like objects at which they can still be distinguished as individual objects. Therefore, the majority of resolution criteria, including the Sparrow limit and the Rayleigh criterion, refer to the properties and the geometry of the PSF (Sheppard, 2017). The Rayleigh criterion, for instance, states that two point sources of light are only resolved when the center of the Gaussian peak of one Airy disc overlaps with the middle of the first dark ring that surrounds the other one, or is further removed from the center of the other disc. Otherwise, the two PSFs merge and the two sources cannot be distinguished. The Rayleigh criterion enables the calculation of the resolution of a given microscopy setup and is described by equation 1:

Rayleigh Resolution_{x,y} =
$$\frac{0.61\lambda}{NA}$$
 (1)

where λ denotes the light wavelength, and NA is the numerical aperture of the objective used in the system. Hence, for an optical system using an objective with an NA of 1.49, often employed in SMM studies, the resolution in the visible light spectrum (λ from 380 to 680 nm) ranges between 155 and 278 nm (Chen et al., 2016; Lelek et al., 2021).

In general, SMM techniques are based on the premise that the spatial coordinates of single fluorescent molecules can be identified with high precision by determining the location of the center of their PSFs, if these PSFs never overlap. Using this approach, the localization precision is bound by the signal to noise ratio (SNR), but not by the wavelength of light or the pixel size (Lelek et al., 2021). Microscopy techniques that make use of this localization method most often keep the concentration of active fluorescent molecules low to avoid the overlap between the PSFs of the individual fluorescent molecules. Examples of this approach include super-resolution techniques, such as photoactivated localization microscopy (PALM) and stochastic optical reconstruction microscopy (STORM), which are based on low concentrations of fluorescent molecules, resulting from photoactivation or photoswitching of only a subpopulation of fluorophores.

Both PALM and STORM have been extensively used in cancer biology research, including the visualization of exosomes in human breast and cervical cancer cells (Chen et al., 2016; Lelek et al., 2021).

Thus far, many different technical approaches have been applied to perform fluorescence SMM. Imaging at the single-molecule level requires detection of signals from individual fluorophores and hence low background fluorescence levels. This can be achieved through limitations imposed on the illumination volumes, thereby reducing the number of excited fluorophores present in the illuminated sample. The first developed microscopy technique designed to reduce the illumination volume was confocal microscopy, established by Minsky in 1961 (Minsky, 1988). In this technique, a pinhole that is conjugate to the sample plane is placed in front of a detector. The incident light that is focused on the pinholes reaches the detector, whereas the out-of-focus light does not pass through the pinhole and thus does not reach the detector. Consequently, the use of confocal microscopes significantly improves the SNR in the recorded images since it removes out-of-focus fluorescence

The earliest reports of SMM, which focused on imaging myosin and its ATPase in an aqueous solution, utilized total internal fluorescence (TIRF) microscopy, which dramatically decreases the background signal by reducing the illumination volume (Funatsu et al., 1995). TIRF microscopy is founded on the optical principle of evanescent waves, which are generated when an incident light beam is totally reflected at the interface between two media with a different refractive index. This phenomenon occurs when the first medium has a larger refractive index than the second medium, and when the light rays reach the interface at an angle of incidence larger than the critical angle, which is achieved when the angle of refraction is 90° or larger. In fluorescence microscopy, TIRF occurs when a laser beam arrives at the interface between a coverglass and the aqueous environment of a sample. The critical angle for water and glass media equals approximately 62°, above which, at the interface, a total internal reflection of the laser beam into the coverglass occurs instead of it being transmitted through the water. As a result, an evanescent wave is created just above the coverglass that can be used to excite fluorophores located within 100 to 150 nm above the coverglass. Hence, TIRF is suitable for the detection of single molecules that are associated with the plasma membranes of cells or molecules that are immobilized on glass coverslips (Shashkova and Leake, 2017; Yokota, 2020). TIRF microscopy has been used as an SMM tool to study, among other biodynamic processes, cytoskeleton assembly mechanisms, microtubule interactions, presynaptic filament dynamics, single lipopolysaccharide transfer onto the toll-like 4 receptors, and capping of individual actin filaments in vertebrate organisms (Kim, 2018; Ross and Dixit, 2010; Stoppin-Mellet et al., 2020, Fujiwara et al., 2016; Kuhn and Pollard, 2007; Umemura et al., 2008)

In other early SMM studies, conformational dynamics of single proteins and other molecules were studied by single-molecule Förster resonance energy transfer (smFRET). This technique employs the principle of energy transfer between fluorescent donor and acceptor molecules. If these molecules are close to each other, i.e., within less than 10 nm from each other, the donor in an excited state relays its energy to an acceptor, which then gets excited and subsequently emits light. FRET is commonly utilized in research focusing on molecular interactions, such as protein-protein and protein-nucleic acid associations, as well as on conformational changes of enzymes and nucleosomes, protein folding, and dynamics of intrinsically disordered proteins (Buning and van Noort, 2010; Koopmans et al., 2007; König et al., 2015; Metskas and Rhoades, 2020; Ha et al., 1999)

1.4 MICROSCOPY SETUPS USED FOR SMM

SMM techniques require a wide-field microscope equipped with standard, continuous-wave lasers for fluorophore excitation together with a camera sensitive enough to detect single molecules. A plethora of both commercial and custom, open-source hardware implementations have been developed. Most of SMM setups utilize scientific or industry grade, powerful lasers with a power of at least 100 mW (Holm et al., 2014; Kwakwa et al., 2016). A dichroic filter with multiple passbands might be selected to reflect excitation laser lines onto the sample and transmit emission wavelengths to the detector. In the case of multicolor microscopy, multiple laser lines can be combined and co-aligned using dichroic mirrors. The fluorescence emission of the specimen is imaged through an objective lens. Typically, 60X to 100X oil immersion objectives with a NA of 1.4 or higher are used to ensure efficient photon collection (Fig. 1A). Most commercial microscopes for SMM contain in-built automated control systems to keep specimens in focus. When imaging molecules located close to the interface of the sample and the coverslip, such as cellular membranes, TIRF microscopy along with its derivative, highly

inclined and laminated optical sheet illumination (HILO), can be used to reduce the out-of-focus background and improve SNR (Fig. 1B). Several methods exist that facilitate SMM imaging in three dimensions, for example by inserting a cylindrical lens into the optical path (Lelek et al., 2021; Mashanov et al., 2003).

For high sensitivity detection of the emitted light, an electron-multiplying charge-coupled device (EM-CCD) or a scientific complementary metal-oxide-semiconductor (sCMOS) camera is generally used. The EM-CCDs enable the detection of single photons with reduced noise levels and are particularly suited for structures with low photon counts. On the other hand, sCMOS cameras are less sensitive to signals with low photon counts, but have higher frame rates that allow imaging larger Field of Views (FoVs), and achieve SNRs similar to EM-CCDs for bright fluorescent dyes. At the detector, the pixel size should be approximately equal to the PSF standard deviation, typically in the range of 100 to 150 nm. The optimal magnification should be determined individually, taking into account specific background and photon numbers, both inherent to the microscopy setup chosen (Thompson et al., 2002; Tokunaga et al., 2008).

1.5 SMM TO STUDY PROTEIN DYNAMICS IN VIVO

The applications of SMM have also been extended to study the dynamic behavior of the proteins inside living zebrafish (Schaaf et al., 2009). Zebrafish embryos, due to their optical clarity, are excellent model organisms for visual analyses of biodynamic processes and for research using fluorescently labeled molecules (Canedo and Rocha, 2021; Detrich et al., 2011; Garcia et al., 2016; Gore et al., 2018; Lieschke and Currie, 2007). Furthermore, the high fecundity and short generation time of the model facilitate genetic screens and the identification of mutant phenotypes (Haffter et al., 1996; Reisser et al., 2018). Using TIRF to reduce out-of-focus excitation, the mobility pattern of YFP fused to the membrane anchor of the human H-Ras protein was determined in the apical membranes of cells in the outer epidermal layer of two-day-old zebrafish embryos. This study showed the differences between cultured cells and proper *in vivo* models at the single-molecule level, thereby underlining the importance of applying SMM in intact living organisms.

In the research described in this thesis, we aimed to further extend the possibilities of SMM in zebrafish embryos beyond imaging of proteins in the epidermal cell membranes. Therefore, to enable visualization of proteins in the cytoplasm or nuclei of cells anywhere in the zebrafish embryos, two microscopy approaches have been used that until recently had not been employed as SMM tools before: Light-Sheet Fluorescence Microscopy (LSFM) and Two-Photon Excitation Fluorescence Microscopy (2PEFM). In LSFM, two objectives, illumination and a detection objective, are positioned orthogonally to each other. A plane of excitation light, called a light sheet, is sent from the illumination objective through the specimen, exciting only the fluorophores present at the detection focal plane. Photons emitted by the fluorophores in the illuminated sample section are collected by the detection objective. This microscopy technique enables fast imaging with a low background signal as well as optical sectioning of specimens. However, the use of LSFM in SMM applications has been limited due to spatial constraints imposed by the geometry of the objectives, meaning that the size of the objectives with high NAs, necessary for the SMM imaging, has not always been compatible with the designs of many LSFM setups. This problem can be circumvented by the use of longworking-distance air objectives for the illumination, or by using LSFM configurations that employ a modified light path, such as prism-based LSFM (PCLSM) and reflected LSFM (RLSFM) (Bernardello et al., 2021). LSFM has been used to visualize fluorescently labelled molecules in aqueous solutions, cell nuclei of salivary glands extracted from C. tentans, and nuclei of cultured cells (Gebhardt et al., 2013; Ritter et al., 2010).

In 2PEFM, a fluorophore is simultaneously excited with two photons. The use of two photons means that approximately half the energy per photon is required to excite a molecule, extending the wavelength of the excitation light to the near-infrared (NIR) spectrum. Two-photon excitation (2PE) is achieved by using pulsed laser sources in combination with focusing the laser beam (Benninger and Piston, 2013). The pulsed laser sources generate high peak intensities that are necessary for 2PE, whereas the average laser power remains relatively low, reducing linear absorption, heating, and phototoxic damage to the sample (Soeller and Cannell, 1999). Focusing the laser beam with the objective lens ensures the selective excitation of fluorescent molecules in the confocal volume, which means that the background fluorescence is eliminated without the use of a pinhole. A major benefit of the 2PEFM technique is that biological tissues are exposed to less light scattering and absorption at NIR than at visible wavelengths,

allowing for imaging fluorescent signals located deeper in the tissues of a biological model. The 2PEFM technique has, for instance, been used to perform live imaging of transient neuronal Ca²⁺ fluxes in rodent brains (Schwille et al., 1999; Stosiek et al., 2003).

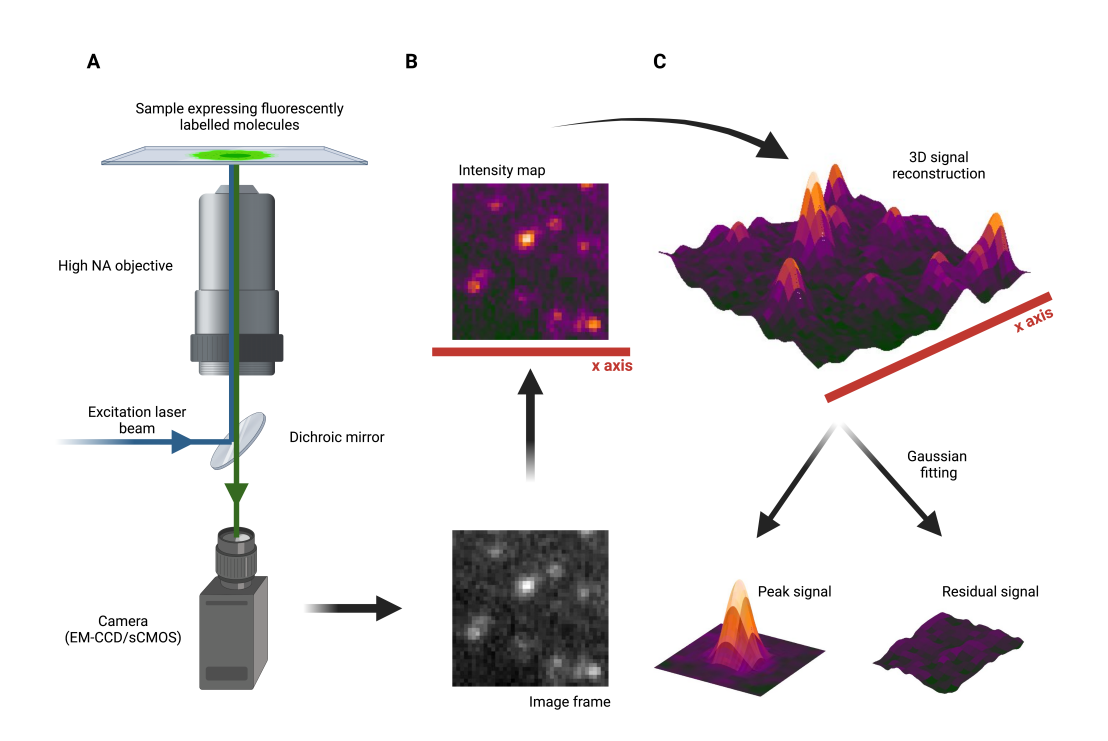


FIGURE 1: Representative image of the SMM setup used to visualize and analyze single fluorescent

peaks. (A) A schematic of an SMM setup used to visualize single molecules. Fluorescently labelled molecules present in a sample are excited by an incident laser beam and images are acquired using an objective with a high NA. The collected fluorescence signals pass through the dichroic mirror and are then recorded by a camera. (B) An example of an image obtained through SMM (below) and its color-coded version (above), presented to visualize differing intensity levels. (C) A 3D signal reconstruction of a frame presented in (B). Based on this 3D fluorescence intensity map, a 3D Gaussian fitting can be performed, and by determining the center of the Gaussian peak the location of the fluorescent molecules in the sample can be determined with high precision.

1.6 ANALYSIS OF THE DATA OBTAINED THROUGH SMM IMAGING

An extensive analysis of the mobility patterns of single molecules requires detailed quantification of the localization and displacements of molecules throughout the imaging process (Fig. 1B). In this doctoral thesis, we employ various methods that have

been designed to describe the dynamic behavior of the investigated populations of molecules. This analysis begins with the localization of the molecules with high positional accuracy, by fitting the detected fluorescence intensity signals to a three-dimensional Gaussian function (Fig. 1C). The peak of the Gaussian function denotes the location of a molecule, whereas the height of this function, which provides information on the intensity, and its full width at half maximum (FWHM) are both used as selection tools to differentiate between single fluorescent molecules and their aggregates. The band-pass filters, in turn, are the tools used to reject signals having unwanted parameters and background noise (Fig. 1C) In order to distinguish different subpopulations of molecules and to establish values of diffusion coefficients and the potential existence of confinement areas, custom-designed, Particle Image Correlation Spectroscopy (PICS) software is used (Semrau and Schmidt, 2007). This software does not track individual particles but determines correlations between the location of molecules in consecutive frames. In this way, cumulative probability distributions of all correlations are plotted, and by subtracting all random correlations, distribution plots of all squared displacements between consecutive frames are generated. By fitting these plots to populationbased models, the number of molecular fractions present in the studied populations and their mean squared displacements are determined. Subsequently, this procedure is repeated for different time lags. To evaluate whether any of the populations confine to specific areas, the mean squared displacement values of the populations are plotted against the time lag. These plots are then fitted either to a free Brownian diffusion model, represented by a linear function, in which the molecules move freely and are unconstrained, or a confined diffusion model, represented by an exponential function that reaches a plateau, in which the molecules also move freely, but their movement is confined to a specific area surrounded by impermeable barriers.

It is well established that many proteins fulfil their biological functions not as a monomer but in the form of polymers. It has been suggested that more than 35% of protein molecules in cells are polymeric (Goodsell and Olson, 2000). Single-molecule imaging can be used to quantify the number of biomolecules in a polymer or a cluster, which facilitates understanding the stoichiometry of these complexes (Marianayagam et al., 2004). Single-step photobleaching (SSP) analysis is a straightforward and powerful method that allows for the counting of molecules within a protein complex. The stoichiometry is determined by observing the number of discrete descending steps as an

effect of photobleaching of individual fluorophores comprising the complex. In this doctoral thesis, the SSP analysis is performed using the ImageJ plug-in TrackMate (Tinevez et al., 2017). The detection of individual particles is performed by determining a maximum intensity value in a circular selection with a predetermined diameter, which denotes an individual molecular complex. The TrackMate software also enables trajectory reconstruction of the localized particles and determines, therefore, whether they show the same type of dynamic behavior throughout this trajectory, or rather switch between different molecular subpopulations with different mobility patterns.

1.7 H-RAS AND THE GLUCOCORTICOID RECEPTOR (GR): MODEL PROTEINS FOR SINGLE-MOLECULE STUDIES IN THE MEMBRANE AND THE NUCLEUS

Two model proteins have been used in this doctorate project. For investigations of the protein mobility patterns in the plasma membranes of epidermal cells in the living zebrafish embryos, the human H-Ras proteins have been used (Chapters 2 and 3). For studies focusing on the mobility patterns of nuclear proteins in cells of zebrafish embryo yolk syncytial layer (YSL), the glucocorticoid receptors (GR) have been utilized (Chapter 4).

H-Ras is an important signaling protein that is mainly localized at the plasma membrane in numerous cell types of vertebrate organisms, though some fractions have also been reported to exist in membranes of endosomes, the endoplasmic reticulum and the Golgi apparatus. It is a member of the Ras protein family that activate intracellular signaling cascades and regulate crucial biological processes taking place in various cells, such as growth, proliferation, and differentiation (Malumbres and Barbacid, 2003). Ras proteins are small GTPases that switch between an inactive, GDP-bound state, and an active, GTP-bound state that delivers signals from the tyrosine kinase receptors activated by growth factors at the cell surface, to promote proliferation and survival programs. Upon growth factor binding, the receptors transmit the extracellular signal through its transmembrane domain, resulting in the growth factor activation and phosphorylation of the tyrosine kinase receptor. The phosphorylated receptor recruits the son of sevenless (SOS) protein via several adaptor proteins, such as GRB2. The SOS protein, being a guanine nucleotide exchange factor, leads to the Ras activation by exchanging GDP by GTP. Subsequently, the active, GTP-bound form of Ras binds to the

RAF kinase, promoting its dimerization and activation. Activated RAF phosphorylates and activates MEK, which, in turn, phosphorylates and activates ERK. Finally, activated ERK phosphorylates a number of substrates, including the transcription factors Elk-1, and serum response factors (SRFs), which then trigger transcriptional programs related to cell cycle progression, protein translation, angiogenesis, metastasis, and cell death evasion (Fig. 2A) (Downward, 2003; Samatar and Poulikakos, 2014). Various isoforms of Ras proteins exist, such as H-Ras, K-Ras and N-Ras, which largely differ in their carboxylterminal hypervariable region (HVR), formed by 25 amino acids. The most carboxylterminal part of the HVR is an anchor that is responsible for attaching Ras proteins to the cytoplasmic leaflet of the cell membranes upon posttranslational lipidations. In H-Ras, the anchoring domain consists of the CAAX motif, which is responsible for signaling the posttranslational, prenyltransferase-mediated addition of farnesyl or geranylgeranyl lipid groups that anchor the H-Ras protein in the cytoplasmic leaflet of the plasma membrane (Brunsveld et al., 2009; Willumsen et al., 1984).

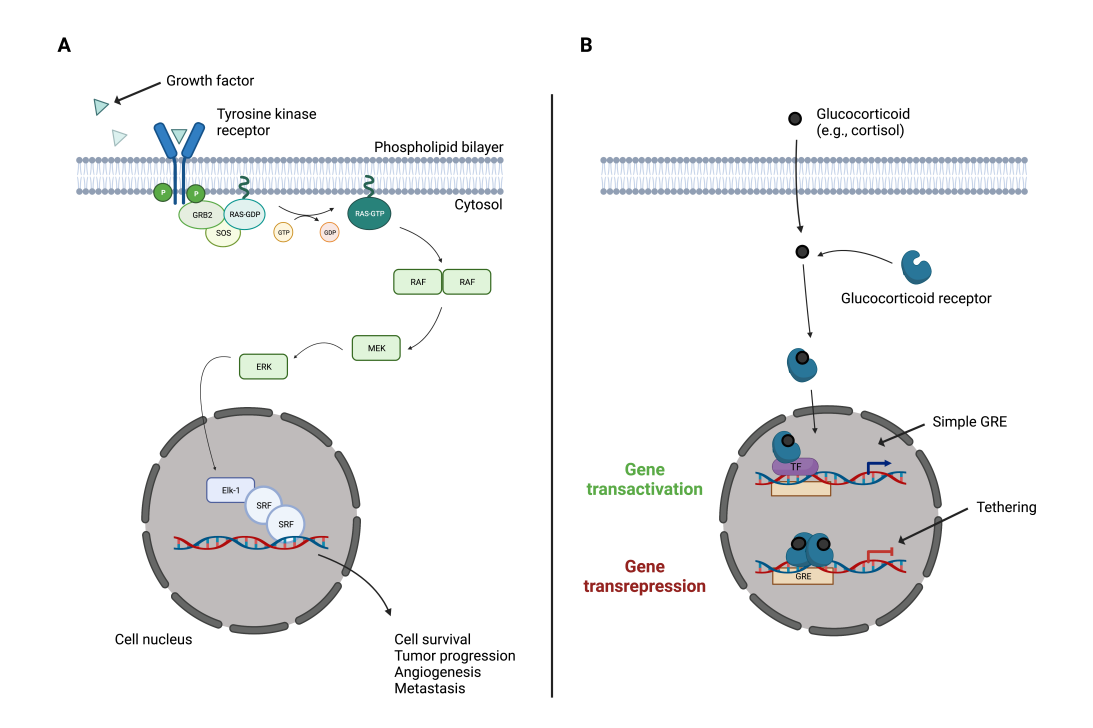


FIGURE 2: Biochemical signaling pathways of the model molecules employed in the research described in this thesis. (A) The H-Ras protein is an early-stage player in the signaling pathway leading to cell cycle control and apoptosis evasion. After activation by a growth factor, a receptor tyrosine kinase

recruits several proteins, which results in Ras activation by exchanging GDP with GTP. Subsequently, in its active, GTP-bound form, Ras activates RAF kinase, what starts the activation cascade leading to the ERK activation. Ultimately, ERK phosphorylates a number of substrates in the cell nucleus, which execute transcriptional programs related to cell cycle progression, protein translation, angiogenesis, metastasis, and cell death evasion **(B)** The GR protein is an important factor that controls many processes ranging from cell metabolism to blood pressure. Upon activation by a glucocorticoid ligand (i.e., cortisol), the GR translocates to the nucleus. In the nucleus, the GR acts as a transcription factor (TF) and regulates the expression of many genes by binding to specific DNA sequences, called glucocorticoid response elements (GREs), and by interacting with other TFs participating in RNA transcription. Legend: GRB2 – growth factor receptor-bound protein 2, SOS – son of sevenless, Elk-1.- transcription activator, SRF – serum response factor.

The GR is a well-studied steroid receptor, which mediates the effects of glucocorticoids, such as the endogenous stress hormone cortisol. Upon activation by cortisol, the biological function of the GR is to maintain metabolism and energy homeostasis. The receptor is also involved in controlling blood pressure through the inhibition of vasodilators, and has been implicated in memory formation as well as the proper functioning of the cells involved in the immune system response. Because of their suppressive effects on the immune system, synthetic glucocorticoids, such as prednisone or dexamethasone, are widely used clinically as anti-inflammatory drugs. Upon activation by a glucocorticoid ligand (i.e., cortisol), the GR translocates to the nucleus, where it acts as a transcription factor (TF). The GR regulates the expression of a large number of genes by binding to specific DNA sequences, called glucocorticoid response elements (GREs), and the stimulation of the expression of GRE-dependent genes, what is generally known as transactivation. Alternatively, the activated GR may also interfere with the activity of other TFs, including nuclear factor kappa B (NF- \square B), a mechanism that is commonly referred to as transrepression (Fig. 2B) (Groeneweg et al., 2014; Keizer et al., 2019). Both the human and the zebrafish genomes contain only one gene encoding a GR protein, and it has been shown that the zebrafish GR displays a high level of similarity to its human counterpart at the structural and functional levels (Schaaf et al., 2008; Kadmiel and Cidlowski, 2013; Liu et al., 2019).

1.8 OUTLINE OF THE DOCTORAL THESIS

The aim of the project described in this doctoral thesis is to extend the applications of SMM techniques to study the dynamics of single proteins *in vivo*. The outcomes of the

thesis show that it is possible, using TIRF, LSFM and 2PEFM techniques, to study the mobility patterns of single and fully functional proteins in living zebrafish embryos, both at the plasma membranes as well as in the nuclei of embryonic cells. Furthermore, the results shed new light on the single-molecule dynamics of the model proteins used and offer new perspectives on single-molecule data interpretation. This thesis consists of three experimental chapters:

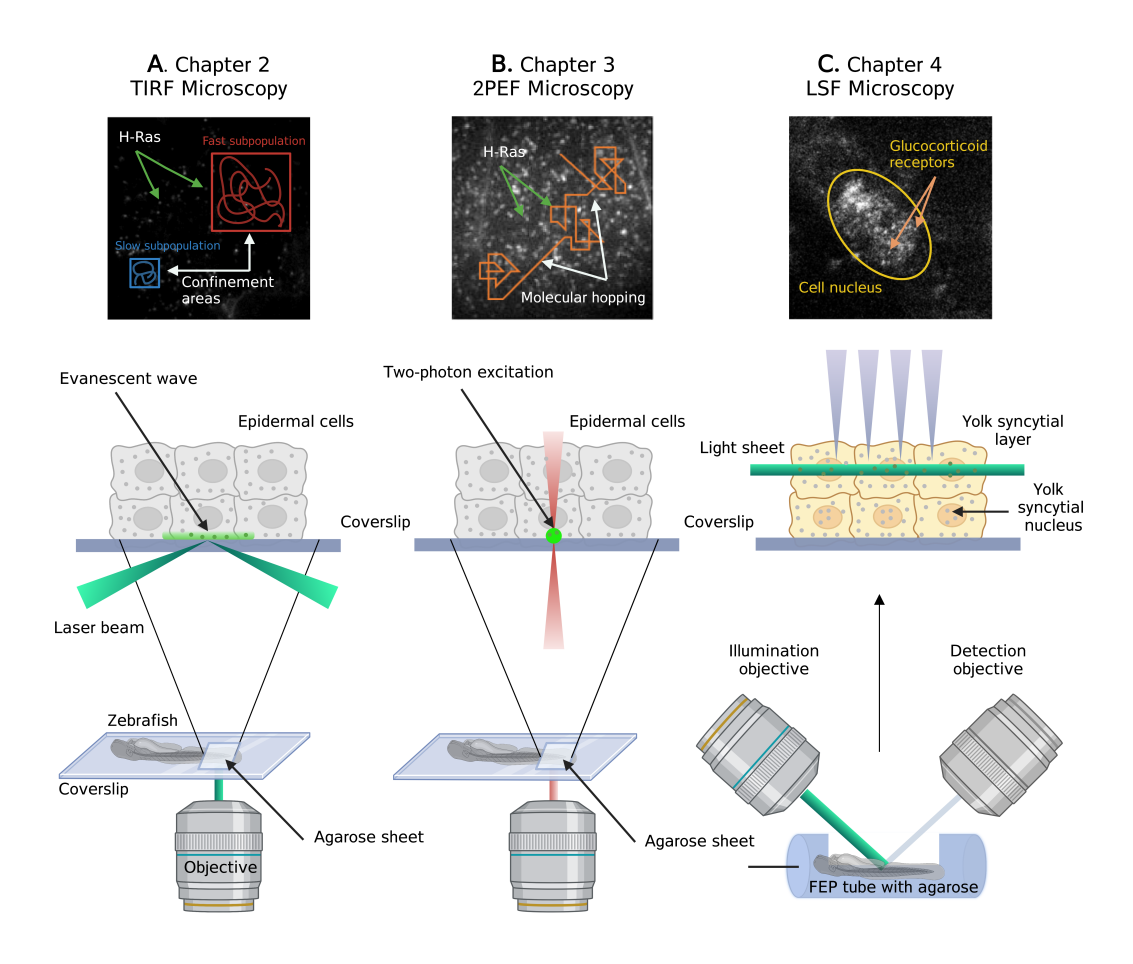


FIGURE 3: Single-Molecule Microscopy (SMM) techniques employed in the research described in this thesis. (A) TIRF microscopy has been used to determine mobility patterns of the full-length H-Ras proteins, its membrane anchors and genetic mutants. In the TIRF microscopy technique, an incident laser beam is positioned against the coverglass-sample interface at the angle larger than the critical angle, creating an evanescent wave that excites fluorophores in the epidermal cell membranes of the zebrafish embryo. Analysis of the TIRF microscopy data allows for differentiation between different protein

subpopulations and determination of their initial diffusion coefficients and the size of their confinement areas. **(B)** 2PEF microscopy dramatically reduces photobleaching and has been used to image H-Ras membrane anchors over a prolonged period of time as well as to reconstruct their molecular trajectories. Fluorophore excitation with two photons takes place only in the focal plane of an image, due to the highest photon density in that area. In the two-photon excitation mode, out-of-focus fluorescence signal is eliminated. This technique enables determination of different dynamic states exhibited by a single H-Ras anchor particle, and visualization of anomalous diffusion patterns, such as 'hop' diffusion. **(C)** LSF microscopy has been used to determine mobility patterns of GR proteins in the yolk syncytial nuclei of zebrafish embryos. In this technique, illumination and detection objectives are separated and positioned orthogonally to each other. The light sheet created by the illumination objective enables excitation of the fluorophores located deeper in the zebrafish embryo tissues and, for instance, studies on the dynamics of transcription factors in the cell nucleus.

In **chapter 2**, SMM is applied *in vivo*, using the zebrafish embryo model. The dynamics of the membrane protein H-Ras is studied using a TIRFM setup and compared with those of its membrane-anchoring domain, C10H-Ras, and several H-Ras mutants (Fig. 3A). The results confirm the presence of a fast- and a slow-diffusing subpopulation of molecules, which both confine to microdomains within the plasma membrane. The constitutively active mutant H-Ras^{V12} exhibits higher diffusion rates and is confined to larger domains than the wild-type H-Ras and its inactive mutant H-Ras^{N17}. Subsequently, it is demonstrated that the structure and composition of the plasma membrane have an imperative role in modulating specific aspects of H-Ras mobility patterns and that differences between individual cells within the epidermis of the embryo largely contribute to the overall data variability

In **chapter 3**, the dynamics of GFP fused to the H-Ras membrane-anchoring domain, C10H-Ras, is studied using a 2PEFM setup. With the two-photon excitation mode, which substantially increases the stability of the fluorescent proteins, it is possible to follow single C10H-Ras particles over a long time and reconstruct their molecular trajectories (Fig. 3B). The trajectories exhibit that the slow-diffusing population of GFP-C10H-Ras fusion proteins show a dynamic behavior that is referred to as 'hop diffusion', and is characterized by long periods of slow diffusion in a confined area that are intermitted by brief periods of relatively fast diffusion, i.e., hops, over longer distances.

In **chapter 4**, an LSFM setup is utilized for imaging individual GRs inside nuclei of YSL cells in living zebrafish embryos over a prolonged time. The optical configuration of the

setup can readily make this SMM approach available in many laboratories, whereas a dedicated sample-mounting system ensures sample viability and mounting flexibility (Fig. 3C). To validate the robustness of the LSFM setup, the GR mobility patterns are analyzed with and without the administration of dexamethasone. As anticipated, dexamethasone administration significantly alters the dynamics of GR. By further characterization of the sources of variation in the *in vivo* results, it is found that most of the variability in the results comes from imaging different areas within an individual zebrafish embryo.

In **chapter 5**, the outcomes of this thesis are summarized and discussed. Future perspectives of the SMM techniques for *in vivo* applications are provided.

REFERENCES

- **Baker, S. M., Buckheit, R. W. and Falk, M. M.** (2010). Green-to-red photoconvertible fluorescent proteins: tracking cell and protein dynamics on standard wide-field mercury arc-based microscopes. *BMC Cell Biol.* **11**, 15.
- Benninger, R. K. P. and Piston, D. W. (2013). Two-photon excitation microscopy for the study of living cells and tissues. *Curr. Protoc. Cell Biol.* Chapter 4, Unit 4.11.1-24.
- Bentolila, L. A., Michalet, X., Pinaud, F. F., Tsay, J. M., Doose, S., Li, J. J., Sundaresan, G., Wu, A. M., Gambhir, S. S. and Weiss, S. (2005). Quantum dots for molecular imaging and cancer medicine. *Discov. Med.* **5**, 213–218.
- Bernardello, M., Gora, R. J., Van Hage, P., Castro-Olvera, G., Gualda, E. J., Schaaf, M. J. M. and Loza-Alvarez, P. (2021). Analysis of intracellular protein dynamics in living zebrafish embryos using light-sheet fluorescence single-molecule microscopy. *Biomed. Opt. Express* 12, 6205–6227.
- Biteen, J. S., Thompson, M. A., Tselentis, N. K., Bowman, G. R., Shapiro, L. and Moerner, W. E. (2008).

 Super-resolution imaging in live Caulobacter crescentus cells using photoswitchable EYFP. *Nat. Methods* **5**, 947–949.
- **Brunsveld, L., Waldmann, H. and Huster, D.** (2009). Membrane binding of lipidated Ras peptides and proteins The structural point of view. *Biochim. Biophys. Acta BBA Biomembr.* **1788**, 273–288.
- **Buning, R. and van Noort, J.** (2010). Single-pair FRET experiments on nucleosome conformational dynamics. *Biochimie* **92**, 1729–1740.
- Bryan, S. J., Burroughs, N. J., Shevela, D., Yu, J., Rupprecht, E., Liu, L.-N., Mastroianni, G., Xue, Q., Llorente-Garcia, I., Leake, M. C., et al. (2014). Localisation and interactions of the Vipp1 protein in cyanobacteria. *Mol. Microbiol*.
- Chalfie, M., Tu, Y., Euskirchen, G., Ward, W. W. and Prasher, D. C. (1994). Green fluorescent protein as a marker for gene expression. *Science* **263**, 802–805.
- Canedo, A. and Rocha, T. L. (2021). Zebrafish (Danio rerio) using as model for genotoxicity and DNA repair assessments: Historical review, current status and trends. *Sci. Total Environ.* **762**, 144084.
- Chen, C., Zong, S., Wang, Z., Lu, J., Zhu, D., Zhang, Y. and Cui, Y. (2016). Imaging and Intracellular Tracking of Cancer-Derived Exosomes Using Single-Molecule Localization-Based Super-Resolution Microscope. ACS Appl. Mater. Interfaces 8, 25825–25833.

- **Detrich, H. W., III, H. W. D., Westerfield, M. and Zon, L. I.** (2011). The Zebrafish: Genetics, Genomics and Informatics. Academic Press.
- **Donnert, G., Eggeling, C. and Hell, S. W.** (2009). Triplet-relaxation microscopy with bunched pulsed excitation. *Photochem. Photobiol. Sci. Off. J. Eur. Photochem. Assoc. Eur. Soc. Photobiol.* **8**, 481–485.
- Downward, J. (2003). Targeting RAS signaling pathways in cancer therapy. Nat. Rev. Cancer 3, 11-22.
- Filonov, G. S., Piatkevich, K. D., Ting, L.-M., Zhang, J., Kim, K. and Verkhusha, V. V. (2011). Bright and stable near-infrared fluorescent protein for in vivo imaging. *Nat. Biotechnol.* **29**, 757–761.
- Fujiwara, T. K., Iwasawa, K., Kalay, Z., Tsunoyama, T. A., Watanabe, Y., Umemura, Y. M., Murakoshi, H., Suzuki, K. G. N., Nemoto, Y. L., Morone, N., et al. (2016). Confined diffusion of transmembrane proteins and lipids induced by the same actin meshwork lining the plasma membrane. *Mol. Biol. Cell* 27, 1101–1119.
- **Funatsu, T., Harada, Y., Tokunaga, M., Saito, K. and Yanagida, T.** (1995). Imaging of single fluorescent molecules and individual ATP turnovers by single myosin molecules in aqueous solution. *Nature* **374**, 555–559.
- Garcia, G. R., Noyes, P. D. and Tanguay, R. L. (2016). Advancements in zebrafish applications for 21st century toxicology. *Pharmacol. Ther.* 161, 11–21.
- Gebhardt, J. C. M., Suter, D. M., Roy, R., Zhao, Z. W., Chapman, A. R., Basu, S., Maniatis, T. and Xie, X. S. (2013). Single-molecule imaging of transcription factor binding to DNA in live mammalian cells. Nat. Methods 10, 421–426.
- Giannone, G., Hosy, E., Levet, F., Constals, A., Schulze, K., Sobolevsky, A. I., Rosconi, M. P., Gouaux, E., Tampé, R., Choquet, D., et al. (2010). Dynamic superresolution imaging of endogenous proteins on living cells at ultra-high density. *Biophys. J.* **99**, 1303–1310.
- **Goodsell, D. S. and Olson, A. J.** (2000). Structural symmetry and protein function. *Annu. Rev. Biophys. Biomol. Struct.* **29**, 105–153.
- Gore, A. V., Pillay, L. M., Galanternik, M. V. and Weinstein, B. M. (2018). The zebrafish: A fintastic model for hematopoietic development and disease. *WIREs Dev. Biol.* **7**, e312.
- Groeneweg, F. L., Royen, M. E. van, Fenz, S., Keizer, V. I. P., Geverts, B., Prins, J., Kloet, E. R. de, Houtsmuller, A. B., Schmidt, T. S. and Schaaf, M. J. M. (2014). Quantitation of Glucocorticoid Receptor DNA-Binding Dynamics by Single-Molecule Microscopy and FRAP. *PLOS ONE* **9**, e90532.

- Ha, T., Ting, A. Y., Liang, J., Caldwell, W. B., Deniz, A. A., Chemla, D. S., Schultz, P. G. and Weiss, S. (1999).
 Single-molecule fluorescence spectroscopy of enzyme conformational dynamics and cleavage mechanism. *Proc. Natl. Acad. Sci. U. S. A.* 96, 893–898.
- Haffter, P., Granato, M., Brand, M., Mullins, M. C., Hammerschmidt, M., Kane, D. A., Odenthal, J., van Eeden, F. J., Jiang, Y. J., Heisenberg, C. P., et al. (1996). The identification of genes with unique and essential functions in the development of the zebrafish, Danio rerio. *Development* 123, 1–36.
- Holm, T., Klein, T., Löschberger, A., Klamp, T., Wiebusch, G., van de Linde, S. and Sauer, M. (2014). A Blueprint for Cost-Efficient Localization Microscopy. *ChemPhysChem* **15**, 651–654.
- **Kadmiel, M. and Cidlowski, J. A.** (2013). Glucocorticoid receptor signaling in health and disease. *Trends Pharmacol. Sci.* **34**, 518–530.
- Keizer, V. I. P., Coppola, S., Houtsmuller, A. B., Geverts, B., van Royen, M. E., Schmidt, T. and Schaaf, M.
 J. M. (2019). Repetitive switching between DNA-binding modes enables target finding by the glucocorticoid receptor. *J. Cell Sci.* 132, jcs217455.
- **Kim, S. H.** (2018). TIRF-Based Single-Molecule Detection of the RecA Presynaptic Filament Dynamics. *Methods Enzymol.* **600**, 233–253.
- Koopmans, W. J. A., Brehm, A., Logie, C., Schmidt, T. and van Noort, J. (2007). Single-pair FRET microscopy reveals mononucleosome dynamics. *J. Fluoresc.* 17, 785–795.
- König, I., Zarrine-Afsar, A., Aznauryan, M., Soranno, A., Wunderlich, B., Dingfelder, F., Stüber, J. C., Plückthun, A., Nettels, D. and Schuler, B. (2015). Single-molecule spectroscopy of protein conformational dynamics in live eukaryotic cells. *Nat. Methods* 12, 773–779.
- **Kuhn, J. R. and Pollard, T. D.** (2007). Single molecule kinetic analysis of actin filament capping. Polyphosphoinositides do not dissociate capping proteins. *J. Biol. Chem.* **282**, 28014–28024.
- Kusumi, A., Fujiwara, T. K., Chadda, R., Xie, M., Tsunoyama, T. A., Kalay, Z., Kasai, R. S. and Suzuki, K. G. N. (2012). Dynamic Organizing Principles of the Plasma Membrane that Regulate Signal Transduction: Commemorating the Fortieth Anniversary of Singer and Nicolson's Fluid-Mosaic Model. Annu. Rev. Cell Dev. Biol. 28, 215–250.
- Kuzmenko, A., Tankov, S., English, B. P., Tarassov, I., Tenson, T., Kamenski, P., Elf, J. and Hauryliuk, V. (2011). Single molecule tracking fluorescence microscopy in mitochondria reveals highly dynamic but confined movement of Tom40. Sci. Rep. 1, 195.

- Kwakwa, K., Savell, A., Davies, T., Munro, I., Parrinello, S., Purbhoo, M. A., Dunsby, C., Neil, M. A. A. and French, P. M. W. (2016). easySTORM: a robust, lower-cost approach to localisation and TIRF microscopy. *J. Biophotonics* **9**, 948–957
- Leake, M. C. (2013). The physics of life: one molecule at a time. *Philos. Trans. R. Soc. Lond. B. Biol. Sci.* 368, 20120248.
- Lelek, M., Gyparaki, M. T., Beliu, G., Schueder, F., Griffié, J., Manley, S., Jungmann, R., Sauer, M., Lakadamyali, M. and Zimmer, C. (2021). Single-molecule localization microscopy. *Nat. Rev. Methods Primer* 1, 1–27.
- **Lenn, T. and Leake, M. C.** (2012). Experimental approaches for addressing fundamental biological questions in living, functioning cells with single molecule precision. *Open Biol.* **2**, 120090.
- **Lenn, T. and Leake, M. C.** (2016). Single-molecule studies of the dynamics and interactions of bacterial OXPHOS complexes. *Biochim. Biophys. Acta* **1857**, 224–231.
- **Lieschke, G. J. and Currie, P. D.** (2007). Animal models of human disease: zebrafish swim into view. *Nat. Rev. Genet.* **8**, 353–367.
- **Lippincott-Schwartz, J. and Patterson, G. H.** (2003). Development and use of fluorescent protein markers in living cells. *Science* **300**, 87–91.
- Liu, B., Zhang, T.-N., Knight, J. K. and Goodwin, J. E. (2019). The Glucocorticoid Receptor in Cardiovascular Health and Disease. *Cells* 8, E1227.
- Lommerse, P. H. M., Blab, G. A., Cognet, L., Harms, G. S., Snaar-Jagalska, B. E., Spaink, H. P. and Schmidt, T. (2004). Single-Molecule Imaging of the H-Ras Membrane-Anchor Reveals Domains in the Cytoplasmic Leaflet of the Cell Membrane. *Biophys. J.* **86**, 609–616.
- Los, G. V., Encell, L. P., McDougall, M. G., Hartzell, D. D., Karassina, N., Zimprich, C., Wood, M. G., Learish, R., Ohana, R. F., Urh, M., et al. (2008). HaloTag: a novel protein labeling technology for cell imaging and protein analysis. *ACS Chem. Biol.* **3**, 373–382.
- Malumbres, M. and Barbacid, M. (2003). RAS oncogenes: the first 30 years. Nat. Rev. Cancer 3, 459-465.
- Marianayagam, N. J., Sunde, M. and Matthews, J. M. (2004). The power of two: protein dimerization in biology. *Trends Biochem. Sci.* 29, 618–625.

- Mashanov, G. I., Tacon, D., Knight, A. E., Peckham, M. and Molloy, J. E. (2003). Visualizing single molecules inside living cells using total internal reflection fluorescence microscopy. *Methods San Diego Calif* 29, 142–152.
- Metskas, L. A. and Rhoades, E. (2020). Single-Molecule FRET of Intrinsically Disordered Proteins. *Annu. Rev. Phys. Chem.* **71**, 391–414.
- Miller, H., Zhou, Z., Shepherd, J., Wollman, A. J. M. and Leake, M. C. (2018). Single-molecule techniques in biophysics: a review of the progress in methods and applications. *Rep. Prog. Phys. Phys. Soc. G. B.* 81, 024601.
- Minsky, M. (1988). Memoir on inventing the confocal scanning microscope. Scanning 10, 128-138.
- Miyawaki, A., Shcherbakova, D. M. and Verkhusha, V. V. (2012). Red fluorescent proteins: chromophore formation and cellular applications. *Curr. Opin. Struct. Biol.* 22, 679–688.
- Prasher, D. C., Eckenrode, V. K., Ward, W. W., Prendergast, F. G. and Cormier, M. J. (1992). Primary structure of the Aequorea victoria green-fluorescent protein. *Gene* 111, 229–233.
- Reisser, M., Palmer, A., Popp, A. P., Jahn, C., Weidinger, G. and Gebhardt, J. C. M. (2018). Single-molecule imaging correlates decreasing nuclear volume with increasing TF-chromatin associations during zebrafish development. *Nat. Commun.* **9**, 5218.
- Reyes-Lamothe, R., Sherratt, D. J. and Leake, M. C. (2010). Stoichiometry and architecture of active DNA replication machinery in Escherichia coli. *Science* **328**, 498–501.
- Ritter, J. G., Veith, R., Veenendaal, A., Siebrasse, J. P. and Kubitscheck, U. (2010). Light sheet microscopy for single molecule tracking in living tissue. *PloS One* 5, e11639.
- Ross, J. L. and Dixit, R. (2010). Multiple color single molecule TIRF imaging and tracking of MAPs and motors. *Methods Cell Biol.* **95**, 521–542.
- Rubin, H. (1990). The significance of biological heterogeneity. Cancer Metastasis Rev. 9, 1–20.
- Samatar, A. A. and Poulikakos, P. I. (2014). Targeting RAS-ERK signaling in cancer: promises and challenges. *Nat. Rev. Drug Discov.* 13, 928–942.
- Schaaf, M. J. M., Champagne, D., van Laanen, I. H. C., van Wijk, D. C. W. A., Meijer, A. H., Meijer, O. C., Spaink, H. P. and Richardson, M. K. (2008). Discovery of a functional glucocorticoid receptor beta-isoform in zebrafish. *Endocrinology* **149**, 1591–1599.

- Schaaf, M. J. M., Koopmans, W. J. A., Meckel, T., van Noort, J., Snaar-Jagalska, B. E., Schmidt, T. S. and Spaink, H. P. (2009). Single-Molecule Microscopy Reveals Membrane Microdomain Organization of Cells in a Living Vertebrate. *Biophys. J.* **97**, 1206–1214.
- **Schwille, P., Haupts, U., Maiti, S. and Webb, W. W.** (1999). Molecular dynamics in living cells observed by fluorescence correlation spectroscopy with one- and two-photon excitation. *Biophys. J.* **77**, 2251–2265.
- Semrau, S. and Schmidt, T. (2007). Particle Image Correlation Spectroscopy (PICS): Retrieving Nanometer-Scale Correlations from High-Density Single-Molecule Position Data. *Biophys. J.* **92**, 613–621.
- Shaner, N. C., Campbell, R. E., Steinbach, P. A., Giepmans, B. N. G., Palmer, A. E. and Tsien, R. Y. (2004). Improved monomeric red, orange and yellow fluorescent proteins derived from Discosoma sp. red fluorescent protein. *Nat. Biotechnol.* 22, 1567–1572.
- **Shashkova, S. and Leake, M. C.** (2017). Single-molecule fluorescence microscopy review: shedding new light on old problems. *Biosci. Rep.* **37**, BSR20170031.
- Shashkova, S., Wollman, A. J. M., Leake, M. C. and Hohmann, S. (2017). The yeast Migl transcriptional repressor is dephosphorylated by glucose-dependent and -independent mechanisms. *FEMS Microbiol. Lett.* **364**.
- Sheppard, C. J. R. (2017). Resolution and super-resolution. Microsc. Res. Tech. 80, 590-598.
- **Shimomura, O., Johnson, F. H. and Saiga, Y.** (1962). Extraction, purification and properties of aequorin, a bioluminescent protein from the luminous hydromedusan, Aequorea. *J. Cell. Comp. Physiol.* **59**, 223–239.
- **Soeller, C. and Cannell, M. B.** (1999). Two-photon microscopy: imaging in scattering samples and three-dimensionally resolved flash photolysis. *Microsc. Res. Tech.* **47**, 182–195.
- Sowa, Y., Rowe, A. D., Leake, M. C., Yakushi, T., Homma, M., Ishijima, A. and Berry, R. M. (2005). Direct observation of steps in rotation of the bacterial flagellar motor. *Nature* **437**, 916–919.
- Stagge, F., Mitronova, G. Y., Belov, V. N., Wurm, C. A. and Jakobs, S. (2013). SNAP-, CLIP- and Halo-tag labelling of budding yeast cells. *PloS One* **8**, e78745.
- **Stoppin-Mellet, V., Bagdadi, N., Saoudi, Y. and Arnal, I.** (2020). Studying Tau-Microtubule Interaction Using Single-Molecule TIRF Microscopy. *Methods Mol. Biol. Clifton NJ* **2101,** 77–91.

- Stosiek, C., Garaschuk, O., Holthoff, K. and Konnerth, A. (2003). In vivo two-photon calcium imaging of neuronal networks. *Proc. Natl. Acad. Sci. U. S. A.* 100, 7319–7324.
- **Thompson, R. E., Larson, D. R. and Webb, W. W.** (2002). Precise nanometer localization analysis for individual fluorescent probes. *Biophys. J.* **82**, 2775–2783.
- Tinevez, J.-Y., Perry, N., Schindelin, J., Hoopes, G. M., Reynolds, G. D., Laplantine, E., Bednarek, S. Y., Shorte, S. L. and Eliceiri, K. W. (2017). TrackMate: An open and extensible platform for single-particle tracking. *Methods San Diego Calif* 115, 80–90.
- **Tokunaga, M., Imamoto, N. and Sakata-Sogawa, K.** (2008). Highly inclined thin illumination enables clear single-molecule imaging in cells. *Nat. Methods* **5**, 159–161.
- Umemura, Y. M., Vrljic, M., Nishimura, S. Y., Fujiwara, T. K., Suzuki, K. G. N. and Kusumi, A. (2008). Both MHC class II and its GPI-anchored form undergo hop diffusion as observed by single-molecule tracking. *Biophys. J.* **95**, 435–450.
- Uno, S.-N., Kamiya, M., Yoshihara, T., Sugawara, K., Okabe, K., Tarhan, M. C., Fujita, H., Funatsu, T., Okada, Y., Tobita, S., et al. (2014). A spontaneously blinking fluorophore based on intramolecular spirocyclization for live-cell super-resolution imaging. *Nat. Chem.* **6**, 681–689.
- Willumsen, B. M., Christensen, A., Hubbert, N. L., Papageorge, A. G. and Lowy, D. R. (1984). The p21 ras C-terminus is required for transformation and membrane association. *Nature* **310**, 583–586.
- Wollman, A. J. M. and Leake, M. C. (2016). Single-Molecule Narrow-Field Microscopy of Protein-DNA Binding Dynamics in Glucose Signal Transduction of Live Yeast Cells. *Methods Mol. Biol. Clifton NJ* 1431, 5–15.
- Yokota, H. (2020). Fluorescence microscopy for visualizing single-molecule protein dynamics. *Biochim. Biophys. Acta Gen. Subj.* **1864**, 129362.
- Zacharias, D. A., Violin, J. D., Newton, A. C. and Tsien, R. Y. (2002). Partitioning of lipid-modified monomeric GFPs into membrane microdomains of live cells. *Science* **296**, 913–916.
- Zimmer, M. (2009). GFP: from jellyfish to the Nobel prize and beyond. Chem. Soc. Rev. 38, 2823-2832.

2. ANALYSIS OF THE H-RAS MOBILITY PATTERN IN VIVO SHOWS **CELLULAR HETEROGENEITY INSIDE EPIDERMAL TISSUE**

Radoslaw J. Gora, Babette de Jong, Patrick van Hage, Mary Ann Rhiemus, Fjodor van

Steenis, John van Noort, Thomas Schmidt, Marcel J.M. Schaaf

ABSTRACT

Developments in single-molecule microscopy (SMM) have enabled imaging individual

proteins in biological systems, focusing on the analysis of protein mobility patterns inside cultured cells. In the present study, SMM was applied in vivo, using the zebrafish

embryo model. We studied dynamics of the membrane protein H-Ras, its membrane-

anchoring domain, C10H-Ras, and mutants, using total internal reflection fluorescence

microscopy (TIRFM). Our results consistently confirm the presence of fast- and slow-dif-

fusing subpopulations of molecules, which confine to microdomains within the plasma

membrane. The active mutant H-Ras^{VI2} exhibits higher diffusion rates and is confined

to larger domains than the wild-type H-Ras and its inactive mutant H-Ras^{N17}. Subse-

quently, we demonstrate that the structure and composition of the plasma membrane

have an imperative role in modulating H-Ras mobility patterns. Ultimately, we establish that differences between cells within the same embryo largely contribute to the overall

data variability. Our findings agree with a model where the cell architecture and the

protein activation state determine protein mobility, underlining the importance of SMM

imaging to study factors influencing protein dynamics in an intact living organism.

Keywords: H-Ras, zebrafish, single-molecule microscopy, total internal reflection fluo-

rescence microscopy, membrane microdomains, diffusion

Dis Model Mech. 15(2): dmm049099

37

2.1 INTRODUCTION

Plasma membranes mostly consist of proteins and lipids that move laterally within the fluidic membrane plane and interact with each other in both random and organized manners (Singer and Nicolson, 1972). Until now, it has remained unclear what the origins are of many of such interactions and how the organization and mobility of all membrane constituents are governed (Gheber, 2018). Furthermore, not much is known about the role of structural complexes, such as the subjacent actomyosin cortex, in the dynamics of proteins and lipids in the plasma membrane. Subsequently, definitions of membrane domains and their sizes remain inconsistent. These domains include clathrin-coated pits and lipid rafts, and are believed to compartmentalize the membrane, facilitate the assembly of signaling complexes, and serve as the platforms for response amplification to the extracellular signaling molecules (Kusumi et al., 2012). For instance, it is now estimated that lipid rafts, cholesterol-enriched membrane domains, are predominantly transient complexes of 10-200 nm in size. Such lipid rafts are able to adjust their size and stability in response to ongoing membrane trafficking or signal transduction processes (Eggeling et al., 2009; Jacobson et al., 2019).

An important signaling protein that is present in the plasma membrane of many cell types in vertebrate organisms is H-Ras. The H-Ras protein is a member of the Ras protein family, which consists of small GTPases that activate intracellular signaling cascades, and thereby regulate crucial biological processes taking place in various cells, such as growth, proliferation, and differentiation (Malumbres and Barbacid, 2003). Gainof-function mutations in genes encoding Ras proteins are found in ca. 25% of human cancers, which makes Ras proteins interesting targets of cancer therapies (Hobbs et al., 2016). These proteins are mainly localized at the plasma membrane, though some fractions have also been reported to be present in membranes of endosomes, the endoplasmic reticulum, and Golgi apparatus. Various Ras isoforms exist, which differ predominantly in their so-called hyper variable region (HVR), formed by 25 amino acids present in their carboxyl-terminal end. The most carboxyl-terminal part of the HVR comprises an anchoring domain, which is responsible for anchoring Ras proteins in the cytoplasmic leaflet of the cell membranes upon posttranslational modifications, mostly the addition of lipid groups. In H-Ras, this domain comprises a CAAX motif, which can

be farnesylated, and two cysteine residues that can be (reversibly) palmitoylated (Brunsveld et al., 2009; Willumsen et al., 1984).

Single-molecule microscopy (SMM) has been used in many studies to visualize individual molecules in the plasma membrane to study and characterize their organization and mobility. This technique is mostly performed using advanced fluorescence microscope techniques, such as light sheet fluorescence microscopy (LSFM) or total internal reflection fluorescence microscopy (TIRFM). The used microscopy setups are equipped with a laser for excitation of the fluorescent molecules and with a highly sensitive charged-couple device (CCD) or a complementary metal oxide semiconductor (CMOS) camera for capturing the emitted photons. Molecules subjected to SMM experimentation are often fluorescently labeled. There are several options for selecting a suitable fluorescent label, based on the biological model used or a spectrum of excitation laser light available in the setup (Chudakov et al., 2010; Harms et al., 2001; Seefeldt et al., 2008). Most often, autofluorescent proteins, such as Green or Yellow Fluorescent Proteins (GFP, YFP) fused with an endogenous protein, are used, as they are not toxic to living organisms and their use does not require permeabilization or fixation of the cells.

The mobility of Ras proteins or Ras membrane anchors fused to autofluorescent proteins has been studied and characterized by SMM in cultured cells with a positional accuracy of up to 30 nm and a temporal resolution in the span from 5 to 50 milliseconds (Harms et al., 1999; Lommerse et al., 2004; Lommerse et al., 2005). It was demonstrated that populations of H-Ras molecules in the plasma membrane segregate into a slowand a fast-diffusing fraction. The slow-diffusing fraction of H-Ras proteins, which is also referred to as immobile fraction because its displacements are very close to the positional accuracy, contains 10-40% of molecules depending on the cell type, and increases in size upon activation of H-Ras by administration of insulin or EGF to the cells, or by making a mutation in the protein that induces constitutive activation (e.g. as in H-Ras^{V12}) (Lommerse et al., 2004; Lommerse et al., 2005; Murakoshi et al., 2004). Studies in which the H-Ras anchoring domain was fused with YFP (referred to as YFP-C10H-Ras) showed that the anchor exhibits similar mobility patterns to the non-activated, full-length H-Ras protein and to other anchors of human Ras proteins (e.g., K-Ras) (Lommerse et al., 2006).

Studying cultured cells has the advantage of easier control and manipulation when compared to living organisms. Nevertheless, experiments involving cultured cell models do not take into consideration the influence of cell-cell interactions and extracellular stimuli that are present within a tissue. Furthermore, they do not take into account factors an entire organism might be presented with that alter the context of the cells under investigation, such as changes due to the diurnal cycle or the response to a stressor. Therefore, in order to perform SMM studies with more translational value, we extended the applicability of the single-molecule research to a more physiologically relevant system, using the zebrafish embryo as a model organism for studying protein mobility patterns in vivo. Due to their optical clarity, zebrafish embryos serve as excellent model organisms for visual analyses of physiological processes and for research using fluorescently labeled cells and proteins (Canedo and Rocha, 2021; Detrich et al., 2011; Garcia et al., 2016; Gore et al., 2018; Lieschke and Currie, 2007). The high fecundity and short generation time of the zebrafish facilitate genetic screens and identification of mutant phenotypes (Haffter et al., 1996; Reisser et al., 2018). Apart from that, genetically modified zebrafish embryos can be readily created by use of microinjection techniques.

In several zebrafish models for cancer, oncogenic transformation of specific cell types is induced in embryos by overexpression of human H-Ras, in particular its constitutively active mutant H-Ras^{V12}. For example, transformation of melanocytes and melanoma formation is induced upon H-Ras^{V12} overexpression in these cells (Feng et al., 2010; Michailidou et al., 2009; Santoriello et al., 2010), whereas H-Ras^{V12} overexpression in neural progenitor cells results in the formation of brain tumors (Mayrhofer et al., 2017). A similar, constitutively active mutant form of human K-Ras in myoblasts leads to the initiation of rhabdomyosarcoma (Langenau et al., 2007). Thus, the zebrafish embryo is a highly suitable model for studying the signaling pathways induced by human Ras proteins.

In a previous study, we used a TIRFM-based approach to perform SMM in zebrafish, and we analyzed the dynamics of YFP-C10H-Ras in epidermal cells of two-day-old embryos. The observed mobility patterns in the zebrafish embryos were different from those found in cultured cells, which underlined the importance of performing this type of studies *in vivo*. Therefore, in the present study, we extended this application of the *in vivo* SMM technique to the full-length H-Ras protein. In addition to the wild-type H-Ras, we used a constitutively active and inactive H-Ras mutant (H-Ras^{V12} and H-Ras^{N17},

respectively) to examine how the protein activity influences the patterns of diffusion and confinement of the H-Ras molecules. Furthermore, we studied the alterations in the mobility pattern during embryonic development and after treatment with Latrunculin B (LatB), a chemical inhibitor of actin polymerization, and with Methyl- β -cyclodextrin (MBCD), which disrupts membrane organization by depleting cells of cholesterol. Ultimately, we performed experiments with YFP-C10H-Ras and the full-length H-Ras in human embryonic kidney cells (HEK293T) to compare the results obtained in the zebrafish embryos with results obtained in cultured cells using the same experimental protocol.

Our findings reveal that for YFP-C10H-Ras, YFP-H-Ras, YFP-H-Ras^{V12} and YFP-H-Ras^{N17}, in epidermal cells of the zebrafish embryos and in cultured HEK293T cells, a slow- and a fast-diffusing population of molecules can be distinguished and that both populations show confined diffusion. Differences in the fast-diffusing fraction initial diffusion coefficients and confinement sizes are also detected between the full-length, wild-type H-Ras and its constitutively active, oncogenic mutant, H-Ras^{V12}. In addition, we show that treatment with both LatB and MBCD significantly influences values of initial diffusion coefficients as well as sizes of confinement area, pointing to a dominant role of plasma membrane composition in regulating H-Ras protein dynamics. Interestingly, in zebrafish embryos, the mobility pattern does not change during embryonic development and the variability between individual embryos is smaller than the variability between different areas in the epidermis of one embryo.

2.2 RESULTS

The mobility pattern of YFP-C10H-Ras and YFP-H-Ras in HEK293T cells

As an initial step in our SMM study, the YFP fusion proteins of the H-Ras anchoring domain and full-length H-Ras protein (YFP-C10H-Ras and YFP-H-Ras respectively) were studied in cultured HEK293T cells using our TIRFM setup. These experiments aimed to compare findings obtained using the TIRFM setup with data previously obtained in cell cultures (Bobroff, 1986; Lommerse et al., 2005), and with our previous findings in zebrafish embryos (Schaaf et al., 2009). Prior to the SMM imaging, cells were transiently transfected with YFP-C10H-Ras and YFP-H-Ras expression vectors and screened in

order to analyze the expression levels and subcellular localization of the fluorescent proteins. Images of HEK293T cells expressing YFP-C10H-Ras, obtained through confocal laser scanning microscopy, indicated predominant membrane localization of the signal coming from the YFP fused with the C10H-Ras membrane anchor, which is in line with patterns observed before in mouse fibroblast and human embryonic kidney cells (3T3-A14 and ts201, respectively) (Lommerse et al., 2004; Lommerse et al., 2005).

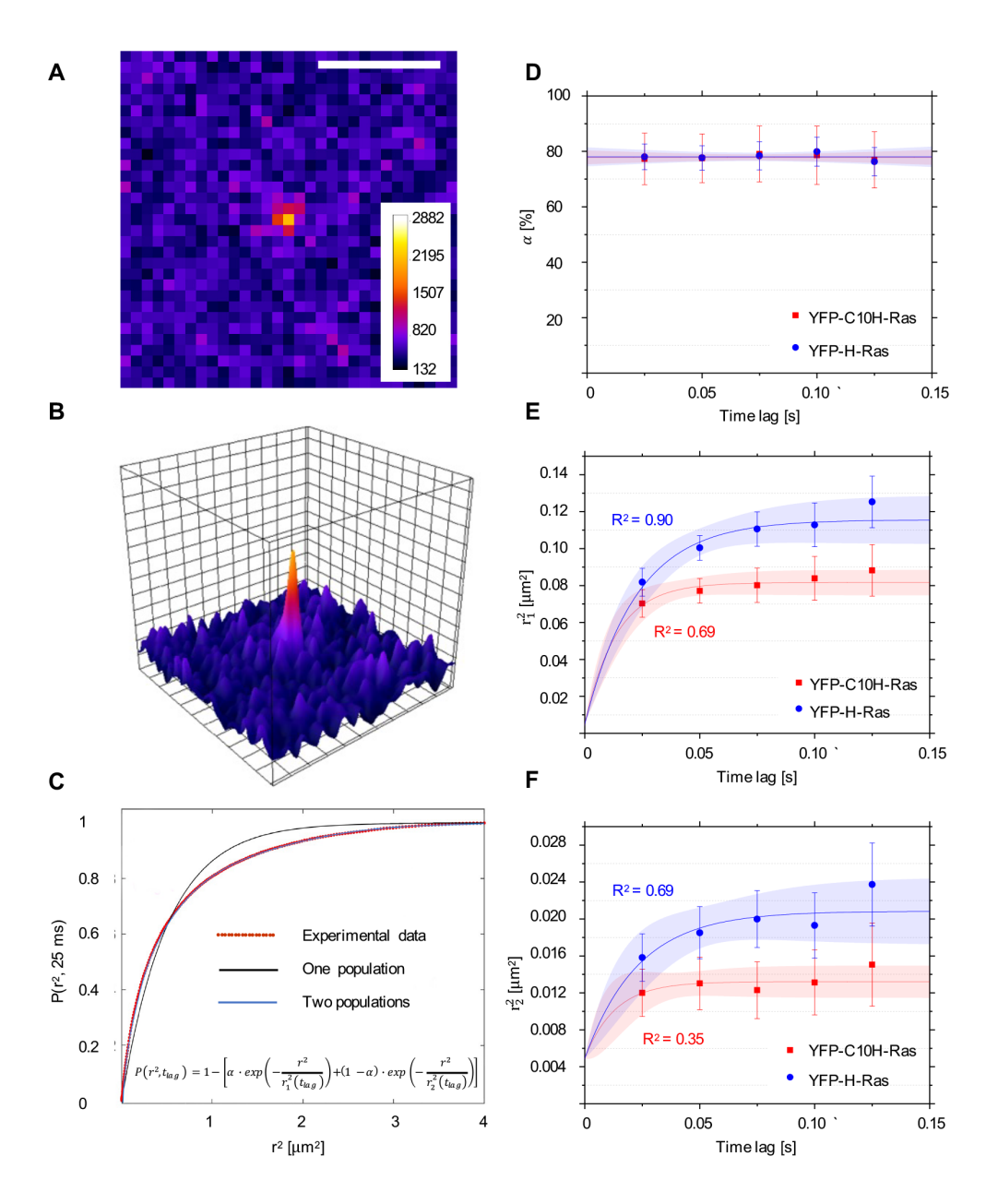


FIGURE 1: Single-Molecule Microscopy (SMM) analysis: protein localization and mobility patterns of YFP-C10H-Ras and YFP-H-Ras in HEK293T cells. (A) SMM intensity map showing signal of a YFP-C10H-Ras molecule located in the basal membrane of a HEK29T cell. A scale bar corresponds to 2 µm. (B) 3D representation of the image shown in (A), depicting fluorescence intensities of each pixel. One visible intensity peak is shown that is attributed to a single YFP-C10H-Ras molecule. Over these peaks, two-dimensional Gaussian surfaces were fitted. (C) Representative cumulative distribution plot of squared displacements determined using Particle Image Correlation Spectroscopy (PICS) analysis. Data points are shown in red, and the two populations biexponential model that best fits the data points in blue (formula shown). Fitting of the data points to the two populations model allows for calculation of a relative size of the subpopulations (α) and their mean squared displacements (r_t^2 and r_r^2). This procedure was repeated for each of the time lags used. (D) Fraction size of the fast-diffusing population (α), plotted against the time lag. (E) Mean squared displacements plotted against the time lag for the fast-diffusing fraction (r_1^2) . (F) Mean squared displacements plotted against the time lag for the slow-diffusing fraction (r_2^2) . Results of the fits are summarized in Table 1. To establish the values of dynamic parameters, at least 3 individual HEK293T cells per each H-Ras construct (YFP-C10H-Ras and YFP-H-Ras) were imaged on each of the 3 different experimental days Each datapoint is presented in the form of a mean ± s.e.m., and the 95% c.i. of the mathematical fit is shown. Shapiro-Wilk statistical test was performed to check for normality of the data set. Statistical analysis was performed using an unpaired t-test with the resulting P-value $P(\alpha, r_1^2, r_2^2)$ > 0.05 at a t_{lag} of 25 ms. Pearson correlation coefficients (R^2) are presented to show fitness of the data to the model of confined diffusion.

Three days after transfection, YFP-C10H-Ras and YFP-H-Ras expression levels in HEK293T cells were significantly decreased. The sparse distribution allowed for identification of single YFP-C10H-Ras molecules in the basal cell membrane, using our TIRFM setup. Diffraction-limited fluorescence intensity peaks were observed and Gaussian curves were fitted over these peaks (Fig. 1AB). FWHM and intensity values of the Gaussian distributions corresponding to signals from single YFP molecules were established in fixed HEK293T cells, taking into consideration only these molecules that displayed single-step photobleaching, indicating that their signal originated from an individual YFP molecule. These values were subsequently used to determine cutoff values for peak selection. The signal-to-noise ratio (SNR), defined as the quotient between the average intensity of a single fluorophore (2215 counts) and the standard deviation of the background signal (74 counts), approximated to 30. The positional accuracy equaled approximately 22 nm in one dimension for the localization of these single molecules. Image sequences were acquired using a time lag of 25 ms, and the mobility pattern of the proteins was determined by Particle Image Correlation Spectroscopy (PICS) software (Semrau and Schmidt, 2007). Using a multistep analysis, information was yielded for five

different time lags: 25, 50, 75, 100, and 125 ms. By means of the PICS software, correlations between the location of molecules in consecutive frames were determined, and cumulative probability distributions of the displacements were generated for each time lag. The data were then fitted to a one- or two-population model (Fig. 1C). The two-population model fitted significantly better, indicating the presence of two fractions of molecules with different mobility patterns. Using these curves, the relative size of the fast-diffusing fraction (α) and the mean squared displacements of the fast and slow diffusing fractions (r_1^2 and r_2^2) were established for each time lag.

Subsequently, for both YFP-C10H-Ras and YFP-H-Ras, the parameters α , r_1^2 , and r_2^2 were plotted against the chosen time lags (Fig. 1DEF). The relative size of the fast-diffusing fraction α was constant over all time lags (Fig. 1D), and equaled 77.8 \pm 0.4% and 78.0 \pm 0.5% for YFP-C10H-Ras and YFP-H-Ras, respectively. The curves presenting the relationship between mean squared displacements $(r_1^2 \text{ and } r_2^2)$ and the time lag for the fast and slow diffusing fractions are non-linear and reach a plateau (Fig. 1EF). We therefore fitted these curves using a confined diffusion model, in which the movement of YFP-C10H-Ras and YFP-H-Ras is confined within an area of size L with an initial diffusion coefficient D_0 (Bobroff, 1986; Lingwood and Simons, 2010; Schaaf et al., 2009). The mobility patterns of the two fusion proteins were remarkably similar. For YFP-C10H-Ras, Do of the fastdiffusing fraction equaled 1.40 \pm 0.20 μm^2 s⁻¹ and the size of the confinement area Lequaled 480 ± 7 nm. For YFP-H-Ras, the fast-diffusing fraction had a D_0 of 1.22 \pm 0.13 μ m² s^{-1} and was confined in an area of which L equaled 576 \pm 11 nm. The slow-diffusing fractions of YFP-C10H-Ras and YFP-H-Ras moved dramatically slower (D_0 of 0.158 \pm 0.056 μ m² s⁻¹ and 0.173 \pm 0.036 μ m² s⁻¹) and were confined in smaller areas (L of 157 \pm 5 nm and 219 ± 8 nm, respectively).

The mobility pattern of YFP-C10H-Ras and YFP-H-Ras in epidermal cells of zebrafish embryos

In order to successfully image membrane proteins in living zebrafish embryos, we focused our observation on the outer epidermal cell layer in the tail fin of 2 days-post-fertilization (dpf) zebrafish embryos (Fig. 2). Embryos were injected at the one-cell stage with DNA constructs encoding YFP-C10H-Ras and YFP-H-Ras in order to stably express the YFP-tagged H-Ras anchor and the full-length H-Ras protein in the zebrafish tail fin.

This outer cell layer of the skin (the superficial stratum) is a homogenous layer of hexagonal cells (Fig. 2, epifluorescence mode) and forms the upper part of the skin (the epidermis) together with an underlying cell layer. The localization of GFP-C10-HRas in the cells in this layer is illustrated by a representative confocal microscopic image of a 1 dpf embryo taken from a transgenic zebrafish line expressing this fusion protein in all cells (Fig. 3A).

The tail fins of 2 dpf zebrafish embryos are morphologically stable enough to resist coverage with a 0.75-mm-thick sheet of agarose, which was used in order to gently press the tail fin towards the surface. This enables the evanescent field to excite the fluorophores present in the outer membrane of cells in the outer epidermal cell layer. For imaging, we focused on the tail fin region of the zebrafish embryo, while the rest of the zebrafish body was immersed in a drop of water. Zebrafish vital functions, such as heartbeat and the blood flow in the cardiovascular system, were checked under a stereofluorescence microscope post-imaging.

As in HEK293T cells, we observed fast- and slow-diffusing protein fractions in zebrafish embryos (Fig. 3B). The fast-diffusing fraction size α equaled 65.0 \pm 0.5% for the YFP-C10H-Ras, and 65.9 \pm 0.6% for YFP-H-Ras. In both of the fractions, molecules followed a confined diffusion pattern (Fig. 3CD), with sizes of the confinement areas L for the fast-diffusing fractions being approximately 3 to 4 times larger than for the slow-diffusing ones (see Table 1, part 1.1 and 1.2). The initial diffusion coefficient D_0 of the fast-diffusing fraction equaled 1.10 \pm 0.15 μ m² s⁻¹ for YFP-C10H-Ras and 0.71 \pm 0.05 μ m² s⁻¹ for YFP-H-Ras. The initial diffusion coefficients for the slow-diffusing fractions were at least 8 times lower than the ones for their fast-diffusing counterparts. When we compared these data to those obtained in the HEK293T cells, we found a significant difference between the mobility patterns of YFP-H-Ras in HEK293T cells and in epidermal cells of zebrafish embryos. The initial diffusion coefficients D_0 of both the fast- and the slow-diffusing fractions were significantly lower in the zebrafish embryonic cells (see Table 2). No significant differences were found between the YFP-C10-H-Ras mobility patterns in HEK293T cells and in zebrafish embryos.

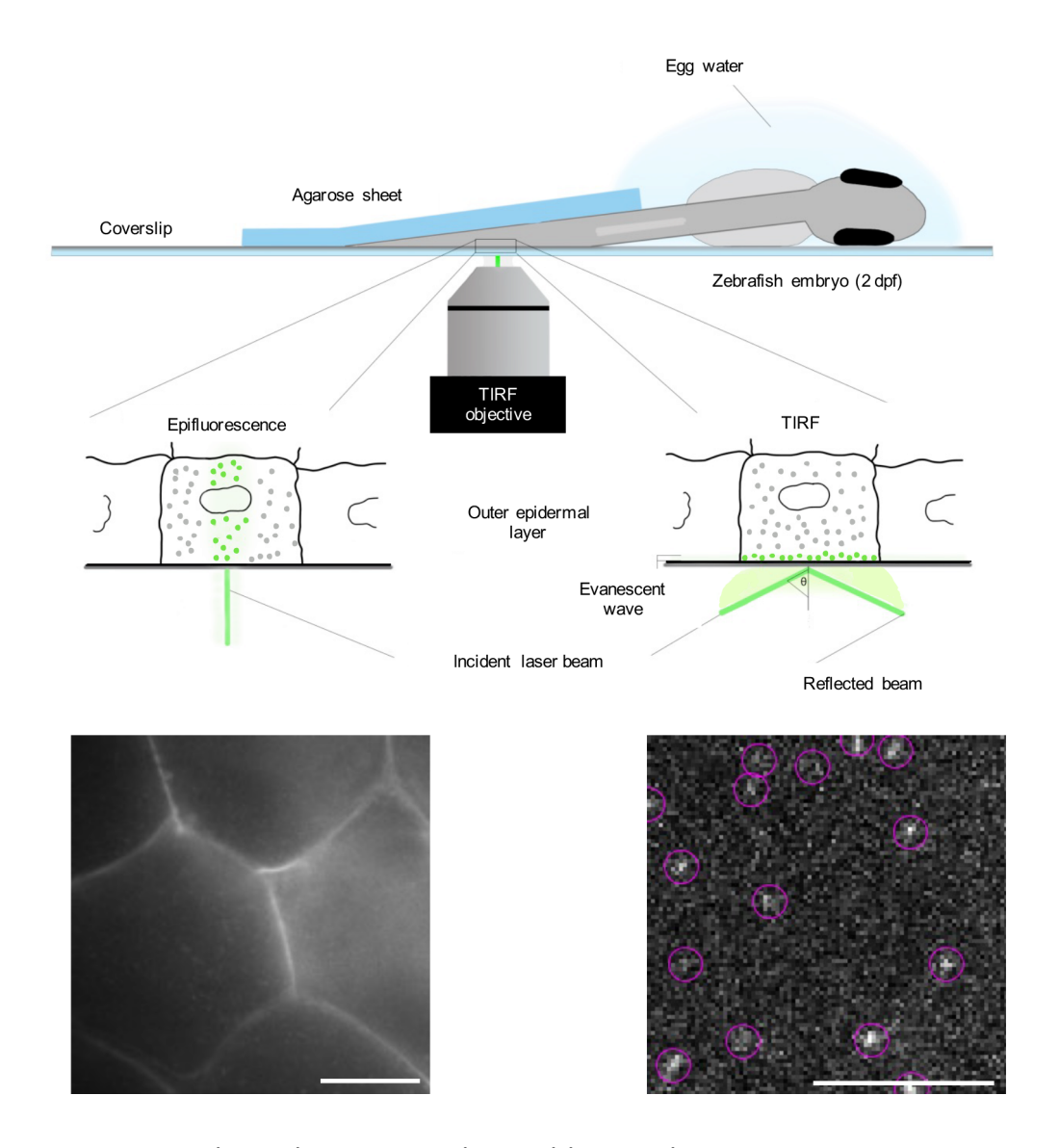


FIGURE 2: Schematic overview of SMM applied to a living zebrafish embryo. A zebrafish embryo was injected with an expression vector for a YFP fusion protein shortly after fertilization. At 2 dpf, it was placed on a coverslip coated with poly-L-lysine in a drop of egg water. The tail region of the embryo was covered with a 0.75-mm-thick agarose (2%) sheet. On the lower left part of the figure, an epifluorescence picture is presented of the outer layer of the epidermis showing the fluorescent signal of YFP-C10-H-Ras in the cell membranes. Morphologically, the cells in this layer are homogenous and are characterized by a hexagonal shape. On the lower right part, a TIRFM image of an area within the FOV of the epifluorescence picture is presented, with examples of individual YFP molecules shown in circles. A scale bar corresponds to 5 μ m.

The mobility pattern of YFP-C10H-Ras in zebrafish embryos at different developmental stages

To study the stability of the data obtained in the zebrafish embryos over different developmental stages, we analyzed the mobility patterns of YFP-C10H-Ras at 48, 56, 72 and 80 hours post-fertilization (hpf). At each stage, the values for the parameters α , r_1^2 , and r_2^2 were determined for each time lag, and D_0 and L were determined for both fast- and slow-diffusing populations (Table 1, part 1.3, Fig. S1). The results showed that a difference in the developmental stage of the zebrafish embryo did not significantly influence any of these parameters (Table 2). This means that the C10H-Ras mobility patterns remain stable within the time frame of our experiments.

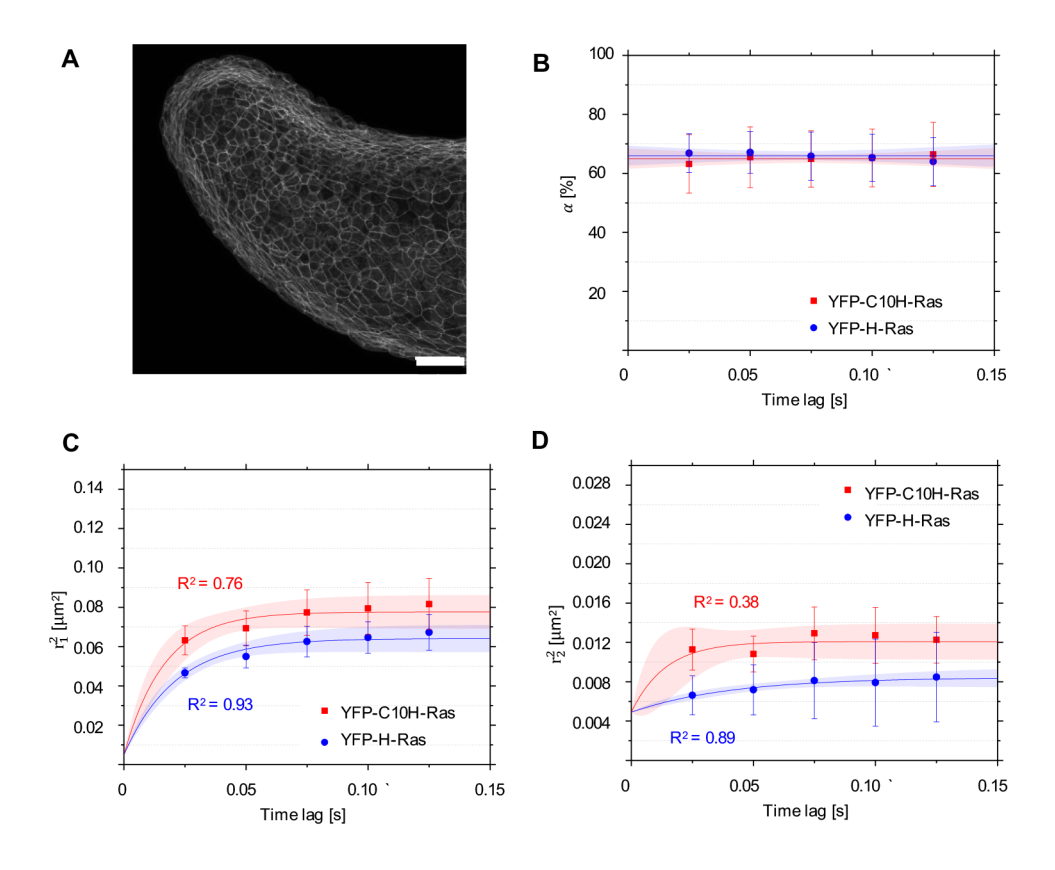


FIGURE 3: Mobility patterns of YFP-C10H-Ras and YFP-H-Ras in epidermal cells of the zebrafish embryos. (A) Confocal microscopy image of the outer epidermal cell layer of a 2 dpf zebrafish embryo from the transgenic line $Tg(bactin:GFP-C10H-Ras)^{vul19}$, showing the fluorescence signal from GFP-C10H-Ras. A scale bar corresponds to 50 µm. (B) Fraction size of the fast-diffusing population (α), plotted against the time lag. (C) Mean squared displacements plotted against the time lag for the fast-diffusing fraction (r_1^2).

(D) Mean squared displacements plotted against the time lag for the slow-diffusing fraction (r_2^2) . Results of the fits are summarized in Table 1. To establish the values of dynamic parameters, 3 different embryos per each H-Ras construct (YFP-C10H-Ras and YFP-H-Ras) were imaged on each of the 3 (6 for YFP-C10H-Ras) different experimental days. Each datapoint is presented in the form of a mean \pm s.e.m., and the 95% c.i. of the mathematical fit is shown. Shapiro-Wilk statistical test was performed to check for normality of the data set. Statistical analysis was performed using an unpaired t-test with a resulting P-value of P(α , r_1^2 , r_2^2) > 0.05 at a t_{lag} of 25 ms. Pearson correlation coefficients (R^2) are presented to show fitness of the data to the model of confined diffusion.

The mobility pattern of YFP-H-Ras^{V12} and YFP-H-Ras^{N17} in epidermal cells of zebrafish embryos

To study the effect of the activation state of the H-Ras protein, the constitutively active H-Ras^{V12} mutant (with a valine replacing a glycine at position 12) and the inactive mutant H-Ras^{N17} (with an asparagine replacing a serine at position 17) were used. The fusion proteins YFP-H-Ras, YFP-H-Ras^{V12} and YFP-H-Ras^{N17} were expressed in 2 dpf zebrafish embryos, and the mobility patterns of the each of these constructs were analyzed. Again, we observed fast- and slow-diffusing fractions of molecules. The size of the fast-diffusing fraction did not differ significantly between the constructs, and equaled $66.0 \pm 0.5\%$ for YFP-H-Ras, 61.7 \pm 0.7% for YFP-H-Ras V12 , and 63.2 \pm 0.2% for YFP-H-Ras N17 (Fig. 4A). All fractions showed confined diffusion. Initial diffusion coefficients D_0 for the fast-diffusing fraction equaled 0.70 \pm 0.05 μ m² s⁻¹ for YFP-H-Ras, 1.05 \pm 0.06 μ m² s⁻¹ for YFP-H-Ras^{VI2}, and 0.72 \pm 0.07 μm^2 s⁻¹ for YFP-H-Ras^{N17}, with the diffusion coefficient for YFP-H-Ras^{V12} being significantly higher than those for the other two constructs (Fig. 4B). Similarly, the size of the confinement area L for YFP-H-Ras^{V12} (572 \pm 7 nm) was significantly higher than those for YFP-H-Ras and YFP-H-Ras $^{\rm N17}$ (421 \pm 8 nm and 444 \pm 9 nm, respectively). The initial diffusion coefficients and the sizes of the confinement areas for the slow diffusing fractions of YFP-H-Ras^{V12} and YFP-H-Ras^{N17} did not show any significant difference from the values determined for the wild-type YFP-H-Ras $(0.022 \pm 0.003 \,\mu\text{m}^2\,\text{s}^{-1})$ and $103 \pm 5 \,\text{nm}$; for detailed results, see Table 1, part 1.4, Table 2, and Fig. 4C).

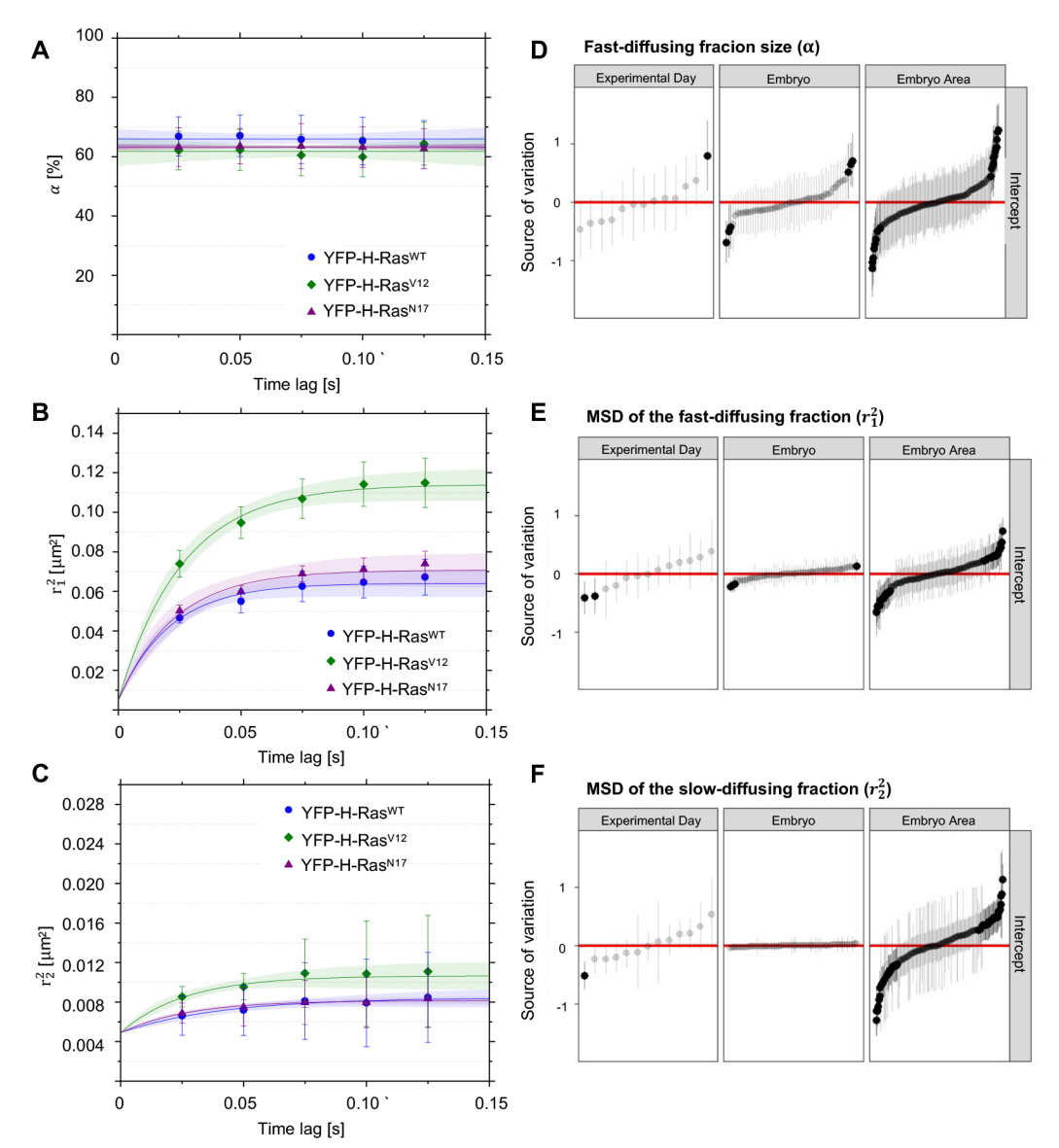


FIGURE 4: Mobility patterns of YFP-H-Ras and its mutants, YFP-H-Ras^{N17}, and YFP-H-Ras^{N17}, in epidermal cells of the zebrafish embryos. (A) Fraction size of the fast-diffusing population (α), plotted against the time lag. (B) Mean squared displacements plotted against the time lag for the fast-diffusing fraction (r_1^2). (C) Mean squared displacements plotted against the time lag for the slow-diffusing fraction (r_2^2). Results of the fits are summarized in Table 1. To establish the values of dynamic parameters, 3 different embryos per each H-Ras genetic mutant (YFP-H-Ras, YFP-H-Ras^{N12}) and YFP-H-Ras^{N17}) were imaged on each of the 3 different experimental days. Each datapoint is presented in the form of a mean \pm s.e.m., and the 95% c.i. of the mathematical fit is shown. Shapiro-Wilk statistical test was performed to check for normality of the data set. Statistical analysis was performed, using a one-way ANOVA (P-value P(α) > 0.05 and

 $P(r_1^2, r_2^2) < 0.05$ at a t_{lag} of 25 ms) with a Tukey's range post-hoc test (for details of the post-hoc test results, see Table 2). **(DEF)** Caterpillar plots presenting the effect range of a different experimental day, different embryos within an experimental day, and different areas within an embryo to an overall variability in **(D)** the fast-diffusing fraction size, **(E)** mean squared displacement of the fast-diffusing fraction, and **(F)** the slow-diffusing fraction. Effect ranges represent the relative deviation of group intercepts from the overall mean with 95% confidence intervals. Red lines indicate the overall mean of the data, while black points denote groups that significantly deviate from the overall mean among experimental days, individual embryos, and areas within an embryo. The data points are sorted based on their deviation from the total average, beginning with the ones most negatively deviating from the overall mean. The values in **(D)** were logit-transformed and the values in **(E)** and **(F)** were logarithm-transformed to meet the statistical hypotheses of the hierarchical linear model.

The mobility pattern of YFP-H-Ras and YFP-H-Ras^{V12} in epidermal cells of zebrafish embryos after treatment with Latrunculin B and Methyl- β -cyclodextrin

In order to understand how actin microfilaments and cholesterol affect H-Ras mobility, 2-day-old zebrafish larvae expressing YFP-H-Ras or its constitutively active mutant, YFP-H-Ras^{V12}, were incubated with Latrunculin B (LatB) or Methyl- β -cyclodextrin (MBCD). After the treatment with LatB or MBCD, SMM was performed and we observed a fast- and a slow-diffusing fraction of molecules in all experimental groups. Interestingly, the size of the fast-diffusing fractions significantly increased after LatB and MBCD treatment for YFP-H-Ras (from 64.4 \pm 0.4% to 76.2 \pm 0.5% and 77.5 \pm 0.3% after LatB and MBCD treatment, respectively) (Fig. 5A) and YFP-H-Ras^{V12} (from 63.7 \pm 0.9% to 79.6 \pm 1.5% and 75.9 \pm 0.4% after LatB and MBCD treatment, respectively) (Fig. 5D). Additionally, treatment with LatB and MBCD significantly increased the initial diffusion coefficients and the sizes of the confinement areas of the fast-diffusing fraction for both YFP-H-Ras and YFP- H-Ras^{V12} (Fig. 5BE).

For YFP-H-Ras, treatment with LatB increased this diffusion coefficient from 0.89 \pm 0.10 $\mu m^2\,s^{-1}$ to 3.92 \pm 0.46 $\mu m^2\,s^{-1}$, while treatment with MBCD changed it to 3.56 \pm 0.41 $\mu m^2\,s^{-1}$. The size of the confinement area of the fast fraction grew from 462 \pm 8 nm to 837 \pm 10 nm after LatB treatment and to 801 \pm 9 nm after MBCD treatment (Table 1, part 1.5, Fig. 5B). For the YFP-H-Ras^{V12} mutant, treatment with LatB increased the diffusion coefficient of the fast-diffusing fraction from 1.35 \pm 0.12 $\mu m^2\,s^{-1}$ to 2.86 \pm 0.45 $\mu m^2\,s^{-1}$, while treatment with MBCD altered it to 2.67 \pm 0.31 $\mu m^2\,s^{-1}$. The size of the YFP-H-Ras^V12 fast fraction's confinement area increased from 589 \pm 6 nm to 723 \pm 14 nm after LatB

treatment and to 800 \pm 11 nm after MBCD treatment (Table 1, part 1.5, Fig. 5E). Taken together, these data show that treatment with LatB and MBCD abolished differences between H-Ras and H-Ras^{V12} dynamics by increasing the diffusion coefficient and confinement area of the fast-diffusing fractions.

TABLE 1: Summary of the mobility patterns' analysis for YFP-C10H-Ras, YFP-H-Ras, YFP-H-Ras^{V12}, and YFP-H-Ras^{N17}.

Experiment	D_{0FD}	D_{0SD}	L_{FD}	L_{SD}	α [%]				
	[µm² s-1]	[µm² s⁻¹]	[nm]	[nm]					
1.1. YFP-C10H-Ras: comparison between HEK293T cells and zebrafish embryos									
HEK293T	1.40 ± 0.20	0.158 ± 0.056	480 ± 7	157 ± 5	77.8 ± 0.4				
Zebrafish	1.10 ± 0.15	0.128 ± 0.057	467 ± 9	147 ± 6	65.0 ± 0.5				
1.2. YFP-H-Ras ^{WT} : comparison between HEK293T cells and zebrafish embryos									
HEK293T	1.22 ± 0.13	0.173 ± 0.036	576 ± 11	219 ± 8	78.0 ± 0.5				
Zebrafish ¹	0.71 ± 0.05	0.022 ± 0.003	421 ± 8	103 ± 5	65.9 ± 0.6				
1.3. YFP-C10H-Ras in zebrafish embryos: developmental study									
48 hpf	1.84 ± 0.44	0.114 ± 0.036	507 ± 10	170 ± 7	68.2 ± 1.3				
56 hpf	1.54 ± 0.07	0.199 ± 0.047	610 ± 5	197 ± 6	60.6 ± 0.5				
72 hpf	1.27 ± 0.04	0.128 ± 0.032	616 ± 3	124 ± 2	62.9 ± 0.4				
80 hpf	1.10 ± 0.20	0.107 ± 0.026	572 ± 19	153 ± 3	52.4 ± 0.4				
1.4. YFP-H-Ras(WT, N17, V12) in zebrafish embryos: comparison of the mutants									
YFP-H-Ras ^{WT, 2}	0.71 ± 0.05	0.022 ± 0.003	421 ± 8	103 ± 5	65.9 ± 0.6				
YFP-H-Ras ^{N17}	0.72 ± 0.07	0.030 ± 0.002	444 ± 9	100 ± 2	63.2 ± 0.1				
YFP-H-Ras ^{V12}	1.05 ± 0.06	0.055 ± 0.006	572 ± 7	132 ± 5	61.8 ± 0.8				
1.5. YFP-H-Ras(WT, V12) in zebrafish embryos: effect of Latrunculin B (LatB) and Methyl-β-cyclodex-									
trin (MBCD) treatment									
YFP-H-Ras ^{WT} in vehicle	0.89 ± 0.10	0.330 ± 0.060	462 ± 8	250 ± 4	64.4 ± 0.4				
YFP-H-Ras ^{WT} + LatB	3.92 ± 0.46	0.399 ± 0.087	837 ± 10	221 ± 3	76.2 ± 0.5				
YFP-H-Ras ^{WT} + MBCD	3.56 ± 0.41	0.304 ± 0.019	801 ± 9	290 ± 2	77.5 ± 0.3				
YFP-H-Ras ^{VI2} in vehicle	1.35 ± 0.12	0.257 ± 0.029	589 ± 6	266 ± 6	63.7 ± 0.9				
YFP-H-Ras ^{VI2} + LatB	2.86 ± 0.45	0.647 ± 0.098	723 ± 14	260 ± 3	79.6 ± 1.5				
YFP-H-Ras ^{VI2} + MBCD	2.67 ± 0.31	0.434 ± 0.084	800 ± 11	242 ± 4	75.9 ± 0.4				

Results of YFP-H-Ras used for comparison between the models are extracted from the experiment in which YFP-H-Ras, YFP-H-Ras^{V12} and YFP-H-Ras^{N17} are compared (part 1.4).

²Results used to compare the YFP-H-Ras mobility between the HEK293T cells and zebrafish embryos in part 1.2.

 D_{0FD} , D_{0SD} – Initial diffusion coefficients for fast- and slow-diffusing fractions, respectively; L_{FD} , L_{SD} – Sizes of the confinement area of fast- and slow-diffusing fractions, respectively; α – Fast-diffusing fraction size.

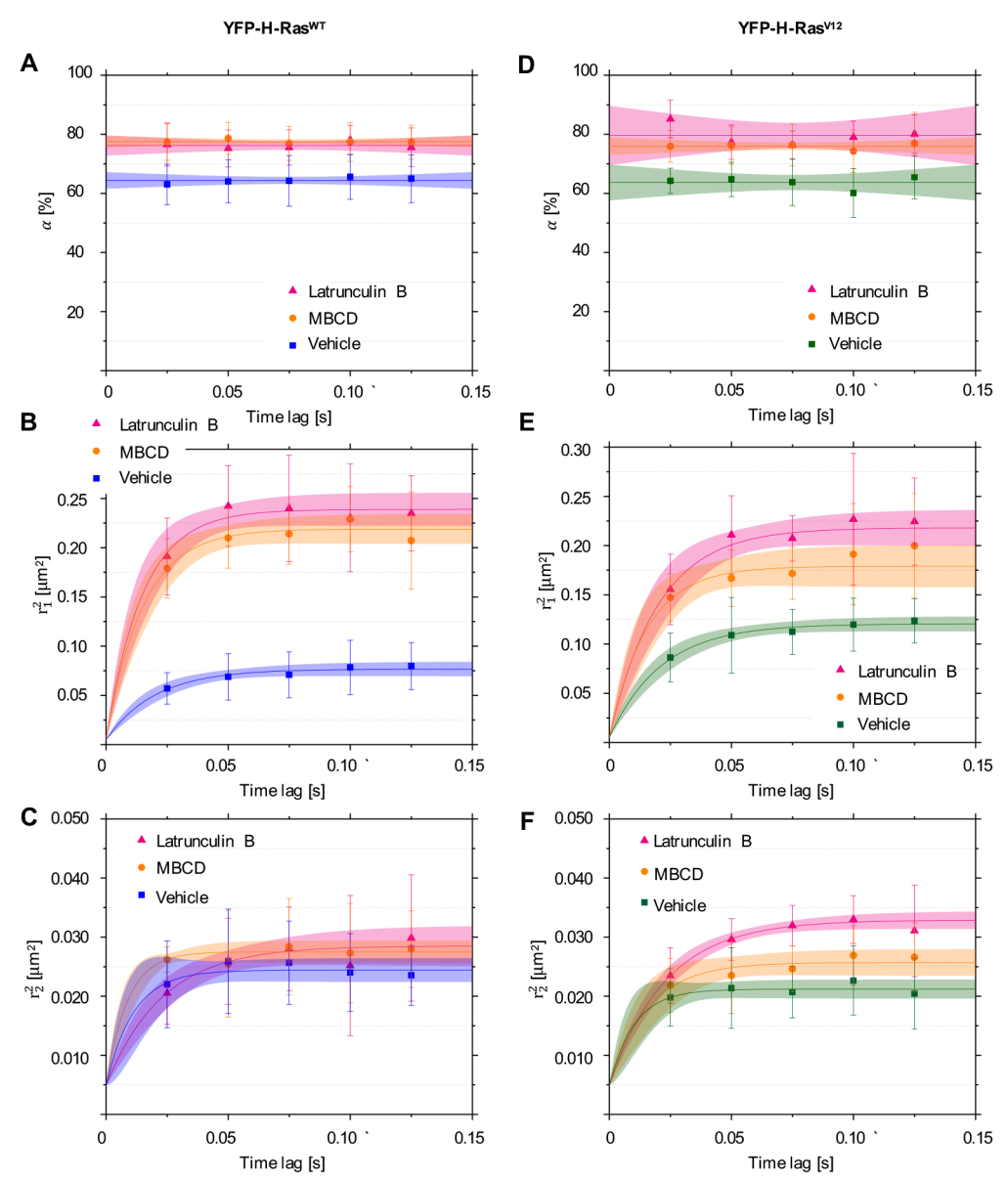


FIGURE 5: Mobility patterns of YFP-H-Ras and the constitutively active mutant YFP-H-Ras^{V12}, in epidermal cells of the zebrafish embryos after treatment with Latrunculin B (LatB) and Methyl-β-cyclodextrin (MBCD). (A, B, C) Plots representing mobility patterns of the wild-type YFP-H-Ras. (A) Fraction size of the fast-diffusing population (α), plotted against the time lag. (B) Mean squared displacements plotted against the time lag for the fast-diffusing fraction (r_2^2). (DEF) Plots representing mobility patterns of the constitutively active YFP-H-Ras^{V12}. (D) Fraction size of the fast-diffusing population (α), plotted against the time lag. (E) Mean squared displacements plotted against the time lag for the fast-diffusing fraction (r_1^2).

(F) Mean squared displacements plotted against the time lag for the slow-diffusing fraction (r_2^2) . Parameters obtained upon curve fitting are presented in Table 1. To establish the values of dynamic parameters, 3 different embryos per each treatment group (vehicle, LatB and MBCD) and construct (YFP-H-Ras^{VI2}, YFP-H-Ras) were imaged on each of the 3 different experimental days. Each datapoint is presented in the form of a mean \pm s.e.m., and the 95% c.i. of the mathematical fit is shown. Shapiro-Wilk statistical test was performed to check for normality of the data set. Statistical analysis was performed using a one-way ANOVA (for both H-Ras^{WT} and H-Ras^{VI2} P-value P(r_2^2) > 0.05 and P(α , r_1^2) < 0.05 at a t_{lag} of 25 ms) with a Tukey's range post-hoc test (for details of the post-hoc test results, see Table 2).

TABLE 2: Statistical analysis performed for the values of mean squared displacements and fast-diffusing fraction sizes obtained experimentally for the time lag of 25 ms.

Statistical significance	Mean squared displacement: fast-diffusing fraction (r_1^2)	Mean squared displacement: slow-diffusing fraction (r_2^2)	Fraction size: fast-diffusing fraction ($lpha$)	
YFP-C10H-Ras: HEK293T cells vs zebrafish em- bryos ¹	P > 0.05	P > 0.05	P > 0.05	
YFP-H-Ras ^{wT} : HEK293T cells vs zebrafish em- bryos ¹	P < 0.001	P < 0,001	P > 0.05	
YFP-C10H-Ras in zebrafish embryos: de- velopmental stage ²	P > 0.05	P > 0.05	P > 0.05	
YFP-H-Ras ^{WT} , YFP-H- Ras ^{V12} , and YFP-H-Ras ^{N17} in zebrafish embryos ²	P(WT, N17) > 0.05 P(WT, V12) < 0.001 P(N17, V12) < 0.001	P(WT, N17) > 0.05 P(WT, V12) = 0.016 P(N17, V12) = 0.011	P > 0.05	
YFP-H-Ras ^{WT} in zebrafish embryos treated with LatB and MBCD ²	P(Vehicle, LatB) < 0.001 P(Vehicle, MBCD) < 0.001 P(LatB, MBCD) > 0.05	P > 0.05	P Vehicle, LatB) = 0.042 P(Vehicle, MBCD) = 0.032 P(LatB, MBCD) > 0.05	
YFP-H-Ras ^{VI2} in zebrafish embryos treated with LatB and MBCD ²	P(Vehicle, LatB) = 0.029 P(Vehicle, MBCD) = 0.043 P(LatB, MBCD) > 0.05	P > 0.05	P(Vehicle, LatB) = 0.026 P(Vehicle, MBCD) < 0.00 P(LatB, MBCD) > 0.05	

For comparisons between two biological models, HEK293T cells and zebrafish embryos, an unpaired t-test was used.

NS – non-significant (P > 0.05); * - P < 0.05; **** - P < 0.001.

²For comparisons of protein mobility patterns in zebrafish embryos between different developmental stage, genetic mutants of YFP-H-Ras, and different chemical treatments, a one-way ANOVA was used. In case the differences between groups were significant in the one-way ANOVA, results of multiple groups comparison are shown, performed by a Tukey's range post-hoc test.

The sources of variability of the results

Finally, we analyzed the sources of variability of the results obtained in zebrafish embryos for YFP-H-Ras and the two mutants, YFP-H-Ras^{V12} and YFP-H-Ras^{N17}. For this purpose, we first studied the correlation between the number of individual molecules within images and the parameters α , r_1^2 , and r_2^2 . Correlation coefficients between the number of molecules and the corresponding parameters were low (0.22, 0.19 and 0.28, respectively), indicating that the correlation between the number of molecules in an image and the parameters describing protein mobility is very weak. Thus, we report that the number of molecules has a negligible impact on the H-Ras mobility analysis.

TABLE 3: Summary of the variance values (σ^2) per source parameter and their percentage contribution (%) towards the total variance for the given parameter.

Source of variation	α		r_1^2		r_2^2	
	σ^2	%	σ^2	%	σ^2	%
Experimental Day	0.188	33.1	0.097	49.2	0.111	35.6
Embryo	0.122	21.5	0.018	9.0	0.004	1.4
Imaging Area	0.173	30.4	0.066	33.7	0.157	50.5
Residual ¹	0.085	14.9	0.016	8.1	0.039	12.5

Residuals account for variance that cannot be explained by the experimental design.

Secondly, the contribution of three factors to the overall variability in the results was analyzed. These factors were: different experimental days, different individual embryos, and different areas imaged within a single embryo. By use of hierarchical linear mixed models, we generated caterpillar plots for α , r_1^2 , and r_2^2 , which present random effects distribution, being the deviation of the group intercept from an overall mean, and the contribution of each of the three factors to the overall mean of a given parameter (Fig. 4DEF). Subsequently, we quantified the percentage contribution of each of the selected sources of variation towards the overall data variability (Table 3). These caterpillar plots and the quantitative source of variation analysis both show that, for every parameter, most of the random effects come from imaging embryos on different experimental days (contribution to the total variability of 33.1% for the fraction size, 49.2% for the fast-diffusing fraction diffusion coefficient) and imaging different areas within the epidermis of the same zebrafish embryo (contribution of 50.1% for the slow-diffusing subpopulation diffusion coefficient). Interestingly, imaging different embryos from the same zebrafish batch was the smallest source of variability for all parameters, and did not

introduce nearly as much variability as imaging different areas within the same individual embryo (Table 3).

2.3 DISCUSSION

In the present study, we have applied single-molecule microscopy to an in vivo model system, using living zebrafish embryos. As our model molecule we have used a YFPfusion of H-Ras, a signaling protein that is anchored in the cytoplasmic leaflet of the plasma membrane. Based on the observed mobility patterns in epidermal cells of the embryos, two fractions of H-Ras molecules were distinguished: a fast- and a slow-diffusing one, which both show confined diffusion. The fast fraction contained the majority of molecules and showed an initial diffusion coefficient that is approximately 10 to 15 times higher than that of the slow-diffusing fraction. This fraction showed similar mobility for wild-type H-Ras, the constitutively inactive H-Ras mutant H-Ras^{N17}, and the C10-H-Ras membrane anchor fused to YFP. However, the fast fraction of a constitutively active H-Ras mutant (H-Ras^{V12}) exhibited a higher diffusion coefficient and a larger confinement area. Treatment of the zebrafish embryos with LatB and MBCD significantly increased initial diffusion coefficients of the fast-diffusing fractions for both wild-type H-Ras and its constitutively active, oncogenic mutant, H-Ras^{V12}, together with their fraction sizes. Interestingly, the largest variation in these experiments was not found between individual embryos, but between different experimental days and the areas within a single embryo.

In this study, the observation of a fast- and a slow-diffusing fraction of H-Ras molecules that were both confined was highly consistent between experimental models used, i.e., between cultured human embryonic kidney (HEK293T) cells and epidermal cells of zebrafish embryos, between different stages of the zebrafish embryonic development, and between the full-length H-Ras protein, its constitutively active and inactive mutants, and its membrane anchor (C10H-Ras). These fast- and slow-diffusing fractions have been found before in several single-molecule microscopy studies on H-Ras or C10H-Ras (the latter also in zebrafish embryos), with diffusion coefficients comparable to those found in the present study (Lommerse et al., 2004; Lommerse et al., 2005; Lommerse et al., 2006; Schaaf et al., 2009). However, confinement of these fractions was not

always observed, which in most cases may have been due to the shorter time ranges used in these studies, combined with larger variation or smaller sample sizes.

Although the observed mobility patterns were remarkably stable in our experiments, we did observe some important differences. First, the full-length H-Ras protein displayed lower diffusion coefficients in the epidermal cells of the embryos compared to the diffusion coefficients found in the HEK293T cells. This difference was observed for both fractions of this protein, but was not found for any of the fractions of the C10H-Ras protein. Apparently, the cell type plays a role in determining the mobility of full-length H-Ras, but is less important for the dynamics of the membrane anchor, which suggests that interactions between H-Ras and cytoplasmic components are involved.

Second, the constitutively active mutant protein H-Ras^{V12} showed increased mobility of its fast-diffusing fraction when compared to the wild-type H-Ras protein, the inactive mutant H-Ras^{N17} and the anchoring domain C10H-Ras, which was reflected in an increased initial diffusion coefficient and a larger confinement area for the active mutant. In a previous study on the mobility of this mutant in cultured mouse embryonic fibroblasts (3T3 cells), this increased mobility was not observed (Lommerse et al., 2006). In addition to the shorter time range, larger variation, and smaller sample sizes mentioned earlier as an explanation for such discrepancies, the cell type used may also be a possible factor underlying the absence of this effect in the earlier study. Since wild type H-Ras, the constitutively inactive mutant H-Ras^{N17}, and the anchoring domain C10H-Ras display a similar mobility pattern which is distinct from the pattern observed for the constitutively active mutant H-Ras^{V12}, we suggest that the vast majority of H-Ras proteins is in an inactive state in epidermal cells of zebrafish embryos at this stage of development, and that endogenous H-Ras signaling, activated by growth factors such as EGF, is apparently not significantly affecting the dynamics of the H-Ras protein.

This different mobility of the H-Ras^{VI2} compared to the inactive forms of H-Ras is in line with the ability of the active mutant to induce oncogenic transformation in a variety of cell types in zebrafish upon overexpression, although phenotypic effects of H-Ras^{VI2} were not observed in our study since the formation of tumors does not start before 4 weeks of age (Feng et al., 2010; Michailidou et al., 2009; Santoriello et al., 2010). The alteration in the mobility pattern most likely results from an altered affinity of H-Ras proteins

for specific plasma membrane microdomains upon activation, which has already been studied in great detail (Hancock and Parton, 2005; Plowman et al., 2005; Prior et al., 2001; Prior et al., 2003; Zhou et al., 2018). Studies using electron microscopy and other techniques, such as fluorescence recovery after photobleaching (FRAP), Förster resonance energy transfer (FRET) and fluorescence correlation spectroscopy (FCS) have revealed that the inactive, GDP-loaded H-Ras (as well as its minimal membrane anchor) can form nanoclusters that are located in small (< 15 nm) lipid rafts (Plowman et al., 2005; Prior et al., 2001; Prior et al., 2003). These rafts are domains that are smaller than 10-100 nm in size and are dependent on the presence of cholesterol (Garcia-Parajo et al., 2014; Lingwood and Simons, 2010; Nickels et al., 2015; Zhou and Hancock, 2015). Interestingly, a similar dependence on cholesterol was observed for nanoclusters of activated (GTPloaded) N-Ras, but not for K-Ras nanoclusters or active forms of H-Ras, indicating the formation of alternative nanoclusters in distinct membrane domains that are slightly smaller and cholesterol-independent for these Ras proteins (Plowman et al., 2005; Prior et al., 2001; Prior et al., 2003). Such a preferential dependence on lipids suggests that each type of Ras nanoclusters has a unique lipid composition and might, therefore, reflect varying lipid-binding properties between different Ras proteins and between their active and inactive forms (Zhou et al., 2018). It has been demonstrated that the cholesterol-dependent nanoclusters of GDP-bound H-Ras are rich with anionic lipids, such as phosphatidylinositol 4,5-biphosphate (PIP2), which enables H-Ras to activate PI3K that binds to PIP2 via the P110 subunit (Ghosh et al., 1996; van Rheenen et al., 2005). In addition, phosphatidylserine (PtdSer) and phosphatidylinositol 4-phosphate (PI₄P) are found in clusters of both GDP- and GTP-bound H-Ras, but only K-Ras localization and clustering on the plasma membrane are sensitive to varying PtdSer concentrations, enabling PtdSer content-sensitive sorting of H- and K-Ras into spatially distinctive lipid assemblies (Zhou et al., 2014). These results show that Ras nanoclusters assemble a distinctive set of plasma membrane phospholipids, which corresponds to their specific effector activation profiles (Zhou and Hancock, 2015; Zhou et al., 2018).

The increased diffusion coefficient and confinement zone of the fast-diffusing fraction observed for H-Ras^{V12} in our study most likely reflect the different diffusion properties of the domains in which the activated protein is preferentially localized. Apparently, the lower affinity for lipid rafts results in an increase in diffusion rate and confinement zone size. These confinement zones in the plasma membrane have been suggested to reflect

membrane compartmentalization resulting from the structure of the membrane cyto-skeleton, a filamentous actin meshwork associated with the cytoplasmic surface of the plasma membrane, and to various transmembrane proteins anchored to and aligned along the actin filaments (Fujiwara et al., 2002; Kusumi et al., 2010). It could be argued that the diffusion of non-active H-Ras clusters in lipid rafts is even more hindered by these cytoskeleton-based boundaries than the clusters of activated H-Ras molecules, due to their larger size. In line with this proposition, the disruption of the cytoskeleton by LatB treatment increased the fast-diffusing fraction's confinement zone size for both the wild-type H-Ras and its constitutively active mutant, H-Ras^{VI2}.

Furthermore, we demonstrate that MBCD administration also increases the initial diffusion coefficients and size of confinement areas for wild-type H-Ras and H-Ras^{V12}. In the presence of this compound, the differences between the mobility patterns of the non-activated and activated form of H-Ras were no longer observed. MBCD depletes cells of cholesterol, thereby disrupting the formation of lipid rafts, which is in line with the largest effect of this compound on the non-active H-Ras form with its larger affinity for lipid rafts. It has previously been shown that LatB disrupts clustering of the non-active H-Ras forms, and it has therefore been suggested that an intact cytoskeleton is required for lipid raft formation (Plowman et al., 2005). Since it has also been shown that cholesterol depletion disrupts the actin cytoskeleton, the interaction between lipid rafts and the cytoskeleton may be bidirectional (Kwik et al., 2003). This interaction is in line with our findings that LatB and MBCD have a similar effect on H-Ras mobility.

In addition, it has been shown that GTP-loading increases the probability of H-Ras clusters to be transiently (< 1 s) immobilized (Murakoshi et al., 2004), and that interactions with cytoplasmic proteins, such as Galectin-1 and Sur-8, are involved in the formation of these immobile H-Ras clusters, which are cholesterol-independent and are considered to be the sites where active signaling occurs (Belanis et al., 2008; Hancock and Parton, 2005; Herrero et al., 2016; Li et al., 2000; Shalom-Feuerstein et al., 2008; Zhou et al., 2018). The slow-diffusing fraction observed in our study has a diffusion rate similar to this previously identified immobile population (Murakoshi et al., 2004), hence we suggest that the slow-diffusing population contains the actively signaling H-Ras molecules. In contrast to the previous experiments performed in cultured cells, the size of this fraction in the current study was not increased for the active form of H-Ras (Lommerse et al., 2005;

Murakoshi et al., 2004). Furthermore, the size of the slow-diffusing H-Ras fraction decreased significantly for both wild-type H-Ras and H-Ras^{V12} upon treatment with LatB and MBCD, which underlines the indispensable role of the structure and composition of the plasma membrane in the process of H-Ras clusters' immobilization.

Using the mobility data obtained in zebrafish embryos, we studied the factors that contributed to the variation in these data. Interestingly, differences between individual embryos had only a modest effect on the overall variation in the results. However, different experimental days and different areas of the embryonic epidermis that we imaged both appeared to be factors that showed a large contribution to the overall variation in the data. The area that we imaged had a size of 16.6x16.6 µm, which is approximately the area of a single cell. Thus, we assume that cell-to-cell variation within the epidermal tissue was a main source of the observed variation. This also indicates that the cellular context largely determines H-Ras mobility, and that differences between cells within the epidermal tissue of one individual embryo are larger than the differences in average cellular context in the tissue between embryos. The observation that the membrane anchor C10H-Ras fused to YFP shows a mobility pattern similar to the full-length YFP-H-Ras fusion protein indicates that the structure of the inactive, GDP-loaded protein does not define the mobility patterns and that, therefore, interactions with structural elements of the cell, such as specific membrane domains and the cytoskeleton, are determining the dynamics of H-Ras in the absence of an activating stimulus. A role of the endogenous zebrafish H-Ras signaling pathway in this cell-to-cell variability cannot be excluded.

In addition to the cell-to-cell variation, day-to-day variation also contributed to the total variability. As there was not much variability originating from the use of different zebrafish embryos, we suggest that these differences may stem from minimal changes in mounting and imaging procedures, even though the experiments were performed by the same researcher. This source of variation may in future studies be minimized by imaging an identical, well-defined region of the larval tail fin. Furthermore, small differences in treatment conditions might affect embryonic development, alter complex metabolic pathways and induce stress responses, which may cause the observed differences in the values of the measured dynamic parameters on different experimental days. Finally, The AB/TL zebrafish wild type strain that was used is not an inbred strain,

and its genetic heterogeneity might underlie batch-to-batch variation. This source of variation can in future studies be minimized by utilizing embryos from an isolated and identical couple of adult zebrafish.

In conclusion, in the present study we have used a previously developed TIRFM-based approach to perform SMM in an intact vertebrate organism. Our study confirms that this technology is highly useful for studying the molecular behavior of individual receptors and signaling molecules, and enables further *in vivo* studies to unravel exact molecular mechanisms governing molecular interactions and their role in physiological and pathological processes, such as skin cancer, wound healing, or tissue regeneration (Kaufman et al., 2016; Kawakami et al., 2004). We have studied the mobility pattern of H-Ras in the epidermis of living zebrafish embryos, and our data show the consistent presence of a fast- and a slow-diffusing fraction of H-Ras molecules, which both show confinement. Activation of H-Ras changes the mobility and confinement of the fast-diffusing fraction, which is dependent the presence of specific membrane microdomains. Interestingly, our data demonstrate that epidermal tissue shows a large degree of heterogeneity between individual cells.

2.4 MATERIALS AND METHODS

Zebrafish. Wild-type ABTL zebrafish (*Danio rerio*) and zebrafish from the transgenic line $Tg(bactin:GFP-C10H-Ras)^{vu119}$ were grown and maintained according to standard protocols (http://ZFIN.org), exposed to a 14h light and 10h dark diurnal cycle at 28°C. Fertilization was performed by natural spawning at the beginning of the light period. Eggs were collected and raised in egg water (60 µg/ml Instant Ocean Sea salts, Cincinnati, OH, USA) at 28°C. All experiments performed on living zebrafish embryos were done in compliance with the directives of the local animal welfare committee of the Leiden University.

Cell cultures, transfection, and fixation. In all cell culture experiments, authenticated human embryonic kidney cells (HEK293T) were used (ATCC, VA, USA). Cells were screened for mycoplasma contamination on a monthly basis. Cells were cultured in DMEM (Dulbecco's Modified Eagle Medium, Invitrogen, Waltham, MA, USA) supplemented with penicillin and streptomycin (10 µg ml⁻¹, Invitrogen), Glutamax (10 µg ml⁻¹, Invitrogen) and 10% fetal calf serum (Invitrogen) at 37°C in a humidified atmosphere

containing 5% of CO₂. Cells were passaged every 3 to 4 days and kept in use for a maximum of 12 passages. Before transfection, cells were transferred onto a sterile, glass coverslip (diameter 25 mm, Marienfeld, Lauda-Königshofen, Germany) placed in a well of a 6-well plate. At a confluency level of 20-30%, cells were transfected with 1 µg of DNA per well, using FuGENE 6, according to the manufacturer's protocol (Roche Molecular Biochemicals, Indianapolis, USA). The transfection efficiency, determined by fluorescence microscopy screening at 48h after transfection (EVOS M7000 Cell Imaging Systems, ThermoScientific, Waltham, MA, USA), was approximately 30%. Cells were imaged at least 4 days post-transfection to lower the expression level of the YFP-fused proteins and to be able to efficiently observe single molecules. Prior to the single-molecule microscopy experiments, DMEM was replaced by PBS (phosphate-buffered saline; 150 mM NaCl, 10 mM Na₂HPO₄/NaH₂PO₄, pH 7.4) kept at room temperature. Finally, the coverslips with cells were mounted on a microscope holder, and 500 µl of room-temperature PBS was pipetted onto the cells. For single-step photobleaching experiments, transfected cells were fixed using 4% paraformaldehyde (PFA) in PBS overnight, at 4°C. Immediately before the experiments, the cells were washed three times, 5 minutes each time, with PBS. Finally, the cells were rinsed twice with PBST (PBS with TweenTM-20, 0.1%), for 5 minutes each time.

Microinjection of DNA in zebrafish embryos. The cDNAs encoding YFP-C10H-Ras, YFP-H-Ras, YFP-H-Ras^{V12}, and YFP-H-Ras^{N17} were cloned from pcDNA3.1(+) mammalian expression plasmids into pCS2(+) plasmids, which then served as vectors for expression of the fluorescent proteins of interest. DNA plasmid microinjections were performed at concentration dose of 30 pg per embryo at the 1-2 cell stage, resulting in a mosaic expression of the fluorescent protein in the zebrafish embryos at later stages. Microinjections were done using a Femtojet microinjector (Eppendorf, Hamburg, Germany) and a micromanipulator with pulled microcapillary pipettes. The procedure of microinjections was controlled under a stereomicroscope (M165C, Leica Microsystems, Wetzlar, Germany). Injected eggs were then left to develop in an incubator at 28°C. Viability and development of the eggs after microinjections was checked on a daily basis using fluorescence stereo- or confocal microscopy.

Treatment of zebrafish embryos with Latrunculin B (LatB) and Methyl- β -cyclodextrin (MBCD). Inhibition of actin polymerization was induced using a protocol described

previously (Kugler et al., 2019). LatB (Sigma-Aldrich, USA) was dissolved in 96% ethanol to a 500 μ M stock concentration. At 48 hpf, zebrafish embryos were dechorionated and treated with 100 nM LatB, dissolved in egg water, for 1 hour. A control group was treated with diluted vehicle (0.02% ethanol) only. After LatB treatment, zebrafish were immediately transferred and imaged under the SMM setup. Treatment with MBCD was based on protocols described before (Bello-Perez et al., 2020; Silva et al., 2019). MBCD (Sigma-Aldrich, USA) was dissolved in PBS (pH 7.4) to a stock concentration of 400 nM. Analogously to the LatB treatment, dechorionated zebrafish embryos were treated with MBCD, in a final concentration of 40 nM, at 48 hpf. A control group was treated with diluted vehicle (10x diluted PBS in egg water) only. After MBCD treatment, zebrafish were immediately transferred and imaged under the SMM setup.

Fluorescence stereomicroscopy. For screening zebrafish embryos expressing YFP-fused proteins, a Leica M205FA fluorescence stereomicroscope (Leica Microsystems) was used. Images of the zebrafish embryos were taken using a Leica DFC 345FX camera.

Confocal laser-scanning microscopy. A Leica SPE confocal laser-scanning microscope (Leica Microsystems) was used to investigate the fluorescent signal in the zebrafish embryo. Excitation was done using an argon laser at 514 nm. Images were obtained using a 20x and 40x non-immersion objectives (NA 0.70, NA 0.80, respectively), and a 63x water immersion objective (NA 1.20).

Total internal reflection fluorescence microscopy (TIRFM). Glass coverslips were washed with 99% ethanol (twice), HPLC-grade water (twice), KOH (1M, twice), and acetone (99%, thrice). Each wash was followed by a 30-minute-long sonication period at 50°C. If not used immediately, the coverslips were stored in acetone. Prior to the mounting of the zebrafish embryos, the glass coverslips were coated with 50 μg ml⁻¹ of poly-L-lysine (Sigma-Aldrich, St. Louis, MO, USA) for 5 minutes, followed by a double wash with deionized water and drying with nitrogen gas. Two-day-old zebrafish embryos were equilibrated at room temperature for an hour, anaesthetized with 0.02% aminobenzoic acid ethyl ester (tricaine, Sigma-Aldrich) and dechorionated using tweezers. Subsequently, a single zebrafish embryo was placed on a coverslip with a lateral side against the coverslip, while excess water was aspirated. The tail of the embryo was pressed against the surface of the coverslip by a thin agarose sheet (2%, thickness 0.75 mm). A drop of egg

water was added to cover the rest of the embryo's body. All the TIRFM measurements were performed at room temperature. The coverslip with the embryo was placed on a microscope holder and mounted on the TIRFM setup. This setup was a custom-made microscope with a 100x oil-immersion objective (NA 1.45, Nikon, Tokyo, Japan). Excitation was performed using a 515 nm laser (iChrome MLE, Toptica Photonics, Germany), the field of view was set to a 100x100 pixels region with a pixel size of 166 nm, and the laser power equaled to 20% of the maximal laser power (40 mW). The incident laser beam was set at the critical angle against the coverslip-water interface, thus being totally reflected and creating the evanescent wave for excitation of fluorophores close to the coverslip-sample interface. Emission light was filtered using a long pass filter (ET5701p, Chroma Technology, VT, USA), and image sequences were collected using an on-chip multiplication gain CCD camera (model 512B, Cascade, Roper Scientific, Tucson, AZ, USA). Each image sequence contained 1200 frames separated by a 25 ms time lag, resulting in the total acquisition time of 30 seconds.

Analysis of protein diffusion patterns. The analysis of the position of individual molecules was done as described previously. Fluorescence intensity signals corresponding to YFP molecules were fitted to a two-dimensional Gaussian surface, using previously custom-developed software. (Groeneweg et al., 2014; Lommerse et al., 2004; Lommerse et al., 2005). The software, in the form of a code written in MATLAB programming environment (The MathWorks, Natick, MA), can be obtained by directly contacting Thomas Schmidt (Leiden Institute of Physics, Leiden University). Subsequently, the corresponding signals were filtered based on their full width at half maximum (FWHM) value and their intensity count, based on the microscopy setup. The FWHM and intensity threshold values were obtained in the single-step photobleaching experiments (performed using fixed HEK293T cells), by averaging the Gaussian distributions of 20 different YFP molecules in the last step prior to the photobleaching-induced final intensity drop (using TrackMate plug-in, ImageJ). The location of a molecule was defined by the center of the Gaussian curve. Positional accuracy dx of the peak localization equaled approximately 22 nm (Groeneweg et al., 2014; Schütz et al., 1997).

To study the mobility pattern of the proteins, Particle Image Correlation Spectroscopy (PICS) software was used, which has been previously described (Semrau and Schmidt, 2007). The PICS software, in the form of a code written in MATLAB programming

environment (The MathWorks, Natick, MA), can be obtained by directly contacting Thomas Schmidt or Stefan Semrau (Leiden Institute of Physics, Leiden University) (Semrau and Schmidt, 2007). A multistep analysis was performed for each image sequence acquired, yielding information for five different time lags of 25, 50, 75, 100, and 125 ms. In PICS analysis, individual particles are not tracked, but correlations between the location of molecules in consecutive frames are determined. This way, cumulative probability distributions of the squared displacements were generated for each of the time lags, and fitted to one- or two-population model. The former is described by the equation:

$$P(r^2, t_{lag}) = 1 - exp\left(-\frac{r^2}{r_0^2(t_{lag})}\right) (1),$$

which describes the probability that a particle exhibiting Brownian motion at the arbitrary origin is found within a circle of a radius r at the time lag t_{lag} , and its mean square displacement equals $r_0^2(t_{lag})=4Dt_{lag}$. However, in case that the populations of the molecules can be differentiated into two different populations equation (1) is transformed into:

$$P\left(r^2,t_{lag}\right) = 1 - \left[\alpha \cdot exp\left(-\frac{r^2}{r_1^2\left(t_{lag}\right)}\right) + (1-\alpha) \cdot exp\left(-\frac{r^2}{r_2^2\left(t_{lag}\right)}\right)\right] \ (2),$$

where the mean square displacement of fast-diffusing and slow-diffusing populations are denoted by r_1^2 and r_2^2 , and their relative sizes by α and $1-\alpha$, respectively (Schaaf et al., 2009). Hence, α represents the fraction size of the fast-diffusing H-Ras molecules and is represented as a percentage of the total population.

To examine whether any of these populations confine to a certain area, the values of r_1^2 and r_2^2 were plotted against the time lag. For the larger time lags the variance increases due to the smaller number of statistically independent measurements of r^2 (Kusumi et al., 1993). The positional accuracy dx led to a constant offset in r^2 of $4 \cdot (dx)^2$, which, in our case, equaled 0.0049 μ m². The plots were fitted by a free Brownian diffusion model, with a diffusion coefficient D in the fitted equation $r_i^2(t_{lag}) = 4Dt_{lag}$, or by a confined diffusion model described by the equation:

$$r_i^2(t_{lag}) = \frac{L^2}{3} \cdot \left[1 - exp\left(-\frac{12 \cdot D_0 \cdot t_{lag}}{L^2} \right) \right]$$
 (3),

in which the molecules move freely with an initial diffusion coefficient D_0 , but are confined by impermeable barriers within an area described by a square of a side length L.

Experimental design. In every experiment, three different zebrafish embryos were selected for the TIRF microscopy imaging. In each of the selected embryos, at least three separate areas were imaged. The data shown reflect a minimum of three independent experiments, each performed on three different days. Six independent experiments were done for YFP-C10H-Ras (18 individual embryos), and three for the wild-type YFP-H-Ras, YFP-H-Ras^{N17}, and YFP-H-Ras^{V12} (9 individual embryos per H-Ras construct). For studying the influence of the developmental stage on the YFP-C10H-Ras dynamics, an analogous design was implemented (3 experiments, 3 individual embryos per each experiment), yet the embryos were selected and imaged at 48-, 56-, 72-, and 80-hour post fertilization. For studying the influence of zebrafish treatment with LatB and MBCD on the YFP-C10H-Ras and YFP-H-Ras^{V12} dynamics, an analogous design was implemented (3 experimental days, 3 individual embryos selected per vehicle, LatB treatment and MBCD treatment groups). In the case of transfected HEK293T cells, three independent experiments were performed for both YFP-C10H-Ras and wild-type YFP-H-Ras. In each of those experiments, three different coverslips with growing cells were selected from a 6-well-plate, and at least three different cells were imaged on each of the coverslips.

Statistical Analysis. Values of the fast-diffusing population sizes and squared displacements were averaged per experimental day for each time lag in all individual groups (i.e., YFP-C10H-Ras, YFP-H-Ras, YFP-H-Ras^{N17}, and YFP-H-Ras^{V12}). Statistical analysis of the data (presented in Table 2) was performed for the experimental time lag of 25 ms by comparing: (a) results obtained for HEK293T cells expressing YFP-C10H-Ras and wild-type YFP-H-Ras; (b) results obtained zebrafish embryos expressing YFP-C10H-Ras at 48-, 56-, 72-, and 80-hour post fertilization; (c) results obtained from zebrafish embryos expressing wild-type YFP-H-Ras, YFP-H-Ras^{N17}, and YFP-H-Ras^{V12}; (d) results obtained from zebrafish embryos expressing wild-type YFP-H-Ras and YFP-H-Ras^{V12} after treatment with LatB and MBCD. In addition, a comparison between biological models was

performed, using results obtained for YFP-C10H-Ras and wild-type YFP-H-Ras for both zebrafish embryos and HEK293T cells. Intragroup variability analysis was carried out between all experimental groups belonging to the same biological model and construct expressed. Initial diffusion coefficients and confinement area sizes were obtained through a confined model fit, by pooling and averaging values of mean square displacements for each individual H-Ras construct, biological model, treatment, and time post-fertilization.

In order to check if data were normally distributed, a Shapiro-Wilk statistical test was performed. Significance of the results was performed using a Student's t-test for comparison of means between two, normally distributed, groups. When multiple groups were compared, a one-way ANOVA was implemented with a Tukey range test for post hoc analysis. Ultimately, the source of potential variability of the data was examined by using a hierarchical linear model to account for nested structure of the data (i.e., different areas within an embryo, different embryos within an experimental day). The values of the r^2 were logarithm-transformed and the α logit-transformed to meet the hypotheses of the statistical model.

COMPETING INTERESTS

The authors declare no competing financial interests.

FUNDING

R.J.G. was funded by Marie Sklodowska-Curie ITN project 'ImageInLife' (Grant Agreement No. 721537)

AUTHOR CONTRIBUTIONS

Conceptualization: M.J.M.S.; Methodology: R.J.G., B.J., M.A.R., T.S., M.J.M.S.; Software: R.J.G., B.J., P.H., T.S., J.N.; Validation: R.J.G., M.J.M.S.; Formal analysis: R.J.G., F.S., P.H.; Investigation: R.J.G., M.A.R, F.S., P.H.; Resources: M.J.M.S.; Data curation: R.J.G., M.J.M.S.; Writing - original draft: R.J.G., M.J.M.S.; Writing - review & editing: R.J.G., J.N., T.S., M.J.M.S.; Supervision: M.J.M.S.; Project administration: M.J.M.S.; Funding acquisition: M.J.M.S.

REFERENCES

- Belanis, L., Plowman, S. J., Rotblat, B., Hancock, J. F. and Kloog, Y. (2008). Galectin-1 is a novel structural component and a major regulator of h-ras nanoclusters. *Mol. Biol. Cell* 19, 1404–1414.
- Bello-Perez, M., Pereiro, P., Coll, J., Novoa, B., Perez, L. and Falco, A. (2020). Zebrafish C-reactive protein isoforms inhibit SVCV replication by blocking autophagy through interactions with cell membrane cholesterol. Sci. Rep. 10, 566.
- **Bobroff, N.** (1986). Position measurement with a resolution and noise-limited instrument. *Rev. Sci. Instrum.* **57**, 1152–1157.
- **Brunsveld, L., Waldmann, H. and Huster, D.** (2009). Membrane binding of lipidated Ras peptides and proteins The structural point of view. *Biochim. Biophys. Acta BBA Biomembr.* **1788**, 273–288.
- Canedo, A. and Rocha, T. L. (2021). Zebrafish (Danio rerio) using as model for genotoxicity and DNA repair assessments: Historical review, current status and trends. *Sci. Total Environ.* **762**, 144084.
- Chudakov, D. M., Matz, M. V., Lukyanov, S. and Lukyanov, K. A. (2010). Fluorescent Proteins and Their Applications in Imaging Living Cells and Tissues. *Physiol. Rev.* **90**, 1103–1163.
- **Detrich, H. W., III, H. W. D., Westerfield, M. and Zon, L. I.** (2011). The Zebrafish: Genetics, Genomics and Informatics. Academic Press.
- Eggeling, C., Ringemann, C., Medda, R., Schwarzmann, G., Sandhoff, K., Polyakova, S., Belov, V. N., Hein, B., von Middendorff, C., Schönle, A., et al. (2009). Direct observation of the nanoscale dynamics of membrane lipids in a living cell. *Nature* **457**, 1159–1162.
- Feng, Y., Santoriello, C., Mione, M., Hurlstone, A. and Martin, P. (2010). Live imaging of innate immune cell sensing of transformed cells in zebrafish larvae: parallels between tumor initiation and wound inflammation. *PLoS Biol.* **8**, e1000562.
- Fujiwara, T., Ritchie, K., Murakoshi, H., Jacobson, K. and Kusumi, A. (2002). Phospholipids undergo hop diffusion in compartmentalized cell membrane. *J. Cell Biol.* 157, 1071–1081.
- Garcia, G. R., Noyes, P. D. and Tanguay, R. L. (2016). Advancements in zebrafish applications for 21st century toxicology. *Pharmacol. Ther.* 161, 11–21.
- Garcia-Parajo, M. F., Cambi, A., Torreno-Pina, J. A., Thompson, N. and Jacobson, K. (2014). Nanoclustering as a dominant feature of plasma membrane organization. *J. Cell Sci.* **127**, 4995–5005.

- Gheber, L. A. (2018). The Life of a Membrane Protein. Biophys. J. 114, 2762-2763.
- **Ghosh, S., Strum, J. C., Sciorra, V. A., Daniel, L. and Bell, R. M.** (1996). Raf-1 kinase possesses distinct binding domains for phosphatidylserine and phosphatidic acid. Phosphatidic acid regulates the translocation of Raf-1 in 12-O-tetradecanoylphorbol-13-acetate-stimulated Madin-Darby canine kidney cells. *J. Biol. Chem.* **271**, 8472–8480.
- Gore, A. V., Pillay, L. M., Galanternik, M. V. and Weinstein, B. M. (2018). The zebrafish: A fintastic model for hematopoietic development and disease. *WIREs Dev. Biol.* **7**, e312.
- Groeneweg, F. L., Royen, M. E. van, Fenz, S., Keizer, V. I. P., Geverts, B., Prins, J., Kloet, E. R. de, Houtsmuller, A. B., Schmidt, T. S. and Schaaf, M. J. M. (2014). Quantitation of Glucocorticoid Receptor DNA-Binding Dynamics by Single-Molecule Microscopy and FRAP. *PLOS ONE* **9**, e90532.
- Haffter, P., Granato, M., Brand, M., Mullins, M. C., Hammerschmidt, M., Kane, D. A., Odenthal, J., van Eeden, F. J., Jiang, Y. J., Heisenberg, C. P., et al. (1996). The identification of genes with unique and essential functions in the development of the zebrafish, Danio rerio. *Development* 123, 1–36.
- Hancock, J. F. and Parton, R. G. (2005). Ras plasma membrane signaling platforms. Biochem. J. 389, 1-11.
- Harms, G. S., Sonnleitner, M., Schütz, G. J., Gruber, H. J. and Schmidt, Th. (1999). Single-Molecule Anisotropy Imaging. *Biophys. J.* 77, 2864–2870.
- Harms, G. S., Cognet, L., Lommerse, P. H. M., Blab, G. A. and Schmidt, T. (2001). Autofluorescent Proteins in Single-Molecule Research: Applications to Live Cell Imaging Microscopy. *Biophys. J.* 80, 2396–2408.
- **Herrero, A., Matallanas, D. and Kolch, W.** (2016). The spatiotemporal regulation of RAS signaling. *Biochem. Soc. Trans.* **44**, 1517–1522.
- Hobbs, G. A., Der, C. J. and Rossman, K. L. (2016). RAS isoforms and mutations in cancer at a glance. J. Cell Sci. 129, 1287–1292.
- **Jacobson, K., Liu, P. and Lagerholm, B. C.** (2019). The Lateral Organization and Mobility of Plasma Membrane Components. *Cell* **177**, 806–819.
- Kaufman, C. K., Mosimann, C., Fan, Z. P., Yang, S., Thomas, A. J., Ablain, J., Tan, J. L., Fogley, R. D., Rooijen, E. van, Hagedorn, E. J., et al. (2016). A zebrafish melanoma model reveals emergence of neural crest identity during melanoma initiation. Science 351.

- **Kawakami, A., Fukazawa, T. and Takeda, H.** (2004). Early fin primordia of zebrafish larvae regenerate by a similar growth control mechanism with adult regeneration. *Dev. Dyn.* **231**, 693–699.
- Kugler, E. C., van Lessen, M., Daetwyler, S., Chhabria, K., Savage, A. M., Silva, V., Plant, K., MacDonald, R. B., Huisken, J., Wilkinson, R. N., et al. (2019). Cerebrovascular endothelial cells form transient Notch-dependent cystic structures in zebrafish. EMBO Rep. 20, e47047.
- **Kusumi, A., Sako, Y. and Yamamoto, M.** (1993). Confined lateral diffusion of membrane receptors as studied by single particle tracking (nanovid microscopy). Effects of calcium-induced differentiation in cultured epithelial cells. *Biophys. J.* **65**, 2021–2040.
- Kusumi, A., Shirai, Y. M., Koyama-Honda, I., Suzuki, K. G. N. and Fujiwara, T. K. (2010). Hierarchical organization of the plasma membrane: investigations by single-molecule tracking vs. fluorescence correlation spectroscopy. FEBS Lett. 584, 1814–1823.
- Kusumi, A., Fujiwara, T. K., Chadda, R., Xie, M., Tsunoyama, T. A., Kalay, Z., Kasai, R. S. and Suzuki, K. G. N. (2012). Dynamic Organizing Principles of the Plasma Membrane that Regulate Signal Transduction: Commemorating the Fortieth Anniversary of Singer and Nicolson's Fluid-Mosaic Model. *Annu. Rev. Cell Dev. Biol.* 28, 215–250.
- Kwik, J., Boyle, S., Fooksman, D., Margolis, L., Sheetz, M. P. and Edidin, M. (2003). Membrane cholesterol, lateral mobility, and the phosphatidylinositol 4,5-bisphosphate-dependent organization of cell actin. *Proc. Natl. Acad. Sci. U. S. A.* 100, 13964–13969.
- Langenau, D. M., Keefe, M. D., Storer, N. Y., Guyon, J. R., Kutok, J. L., Le, X., Goessling, W., Neuberg, D. S., Kunkel, L. M. and Zon, L. I. (2007). Effects of RAS on the genesis of embryonal rhabdomyosarcoma. *Genes Dev.* 21, 1382–1395.
- **Li, W., Han, M. and Guan, K. L.** (2000). The leucine-rich repeat protein SUR-8 enhances MAP kinase activation and forms a complex with Ras and Raf. *Genes Dev.* **14**, 895–900.
- **Lieschke, G. J. and Currie, P. D.** (2007). Animal models of human disease: zebrafish swim into view. *Nat. Rev. Genet.* **8**, 353–367.
- **Lingwood, D. and Simons, K.** (2010). Lipid Rafts As a Membrane-Organizing Principle. *Science* **327**, 46–50.
- Lommerse, P. H. M., Blab, G. A., Cognet, L., Harms, G. S., Snaar-Jagalska, B. E., Spaink, H. P. and Schmidt, T. (2004). Single-Molecule Imaging of the H-Ras Membrane-Anchor Reveals Domains in the Cytoplasmic Leaflet of the Cell Membrane. *Biophys. J.* **86**, 609–616.

- **Lommerse, P. H. M., Snaar-Jagalska, B. E., Spaink, H. P. and Schmidt, T.** (2005). Single-molecule diffusion measurements of H-Ras at the plasma membrane of live cells reveal microdomain localization upon activation. *J. Cell Sci.* **118**, 1799–1809.
- Lommerse, P. H. M., Vastenhoud, K., Pirinen, N. J., Magee, A. I., Spaink, H. P. and Schmidt, T. (2006). Single-Molecule Diffusion Reveals Similar Mobility for the Lck, H-Ras, and K-Ras Membrane Anchors. *Biophys. J.* **91**, 1090–1097.
- Malumbres, M. and Barbacid, M. (2003). RAS oncogenes: the first 30 years. Nat. Rev. Cancer 3, 459-465.
- Mayrhofer, M., Gourain, V., Reischl, M., Affaticati, P., Jenett, A., Joly, J.-S., Benelli, M., Demichelis, F., Poliani, P. L., Sieger, D., et al. (2017). A novel brain tumour model in zebrafish reveals the role of YAP activation in MAPK- and PI3K-induced malignant growth. *Dis. Model. Mech.* 10, 15–28.
- Michailidou, C., Jones, M., Walker, P., Kamarashev, J., Kelly, A. and Hurlstone, A. F. L. (2009). Dissecting the roles of Raf- and PI3K-signaling pathways in melanoma formation and progression in a zebrafish model. *Dis. Model. Mech.* **2**, 399–411.
- Murakoshi, H., Iino, R., Kobayashi, T., Fujiwara, T., Ohshima, C., Yoshimura, A. and Kusumi, A. (2004).

 Single-molecule imaging analysis of Ras activation in living cells. *Proc. Natl. Acad. Sci.* **101**, 7317–7322.
- **Nickels, J. D., Smith, J. C. and Cheng, X.** (2015). Lateral organization, bilayer asymmetry, and inter-leaflet coupling of biological membranes. *Chem. Phys. Lipids* **192**, 87–99.
- Plowman, S. J., Muncke, C., Parton, R. G. and Hancock, J. F. (2005). H-ras, K-ras, and inner plasma membrane raft proteins operate in nanoclusters with differential dependence on the actin cytoskeleton. *Proc. Natl. Acad. Sci.* **102**. 15500–15505.
- Prior, I. A., Harding, A., Yan, J., Sluimer, J., Parton, R. G. and Hancock, J. F. (2001). GTP-dependent segregation of H-ras from lipid rafts is required for biological activity. *Nat. Cell Biol.* **3**, 368–375.
- Prior, I. A., Muncke, C., Parton, R. G. and Hancock, J. F. (2003). Direct visualization of Ras proteins in spatially distinct cell surface microdomains. *J. Cell Biol.* **160**, 165–170.
- Reisser, M., Palmer, A., Popp, A. P., Jahn, C., Weidinger, G. and Gebhardt, J. C. M. (2018). Single-molecule imaging correlates decreasing nuclear volume with increasing TF-chromatin associations during zebrafish development. *Nat. Commun.* **9**, 5218.

- Santoriello, C., Gennaro, E., Anelli, V., Distel, M., Kelly, A., Köster, R. W., Hurlstone, A. and Mione, M. (2010). Kita driven expression of oncogenic HRAS leads to early onset and highly penetrant melanoma in zebrafish. *PloS One* **5**, e15170.
- Schaaf, M. J. M., Koopmans, W. J. A., Meckel, T., van Noort, J., Snaar-Jagalska, B. E., Schmidt, T. S. and Spaink, H. P. (2009). Single-Molecule Microscopy Reveals Membrane Microdomain Organization of Cells in a Living Vertebrate. *Biophys. J.* **97**, 1206–1214.
- Schütz, G. J., Schindler, H. and Schmidt, T. (1997). Single-molecule microscopy on model membranes reveals anomalous diffusion. *Biophys. J.* **73**, 1073–1080.
- Seefeldt, B., Kasper, R., Seidel, T., Tinnefeld, P., Dietz, K.-J., Heilemann, M. and Sauer, M. (2008). Fluorescent proteins for single-molecule fluorescence applications. *J. Biophotonics* 1, 74–82.
- **Semrau, S. and Schmidt, T.** (2007). Particle Image Correlation Spectroscopy (PICS): Retrieving Nanometer-Scale Correlations from High-Density Single-Molecule Position Data. *Biophys. J.* **92**, 613–621.
- Shalom-Feuerstein, R., Plowman, S. J., Rotblat, B., Ariotti, N., Tian, T., Hancock, J. F. and Kloog, Y. (2008). K-ras nanoclustering is subverted by overexpression of the scaffold protein galectin-3. *Cancer Res.* **68**, 6608–6616.
- Silva, M. C. G. da, Silva, J. F. da, Santos, T. P., Silva, N. P. C. da, Santos, A. R. D., Andrade, A. L. C. de, Souza, E. H. L. da S., Sales Cadena, M. R., Sá, F. B. de, Silva Junior, V. A. da, et al. (2019). The complexation of steroid hormones into cyclodextrin alters the toxic effects on the biological parameters of zebrafish (Danio rerio). *Chemosphere* 214, 330–340.
- **Singer, S. J. and Nicolson, G. L.** (1972). The Fluid Mosaic Model of the Structure of Cell Membranes. *Science* **175**, 720–731.
- van Rheenen, J., Achame, E. M., Janssen, H., Calafat, J. and Jalink, K. (2005). PIP2 signaling in lipid domains: a critical re-evaluation. *EMBO J.* **24**, 1664–1673.
- Willumsen, B. M., Christensen, A., Hubbert, N. L., Papageorge, A. G. and Lowy, D. R. (1984). The p21 ras C-terminus is required for transformation and membrane association. *Nature* **310**, 583–586.
- **Zhou, Y. and Hancock, J. F.** (2015). Ras nanoclusters: Versatile lipid-based signaling platforms. *Biochim. Biophys. Acta* **1853**, 841–849.
- Zhou, Y., Liang, H., Rodkey, T., Ariotti, N., Parton, R. G. and Hancock, J. F. (2014). Signal Integration by Lipid-Mediated Spatial Cross Talk between Ras Nanoclusters. *Mol. Cell. Biol.* **34**, 862–876.

Zhou, Y., Prakash, P., Gorfe, A. A. and Hancock, J. F. (2018). Ras and the Plasma Membrane: A Complicated Relationship. *Cold Spring Harb. Perspect. Med.* **8**, a031831.

SUPPLEMENTARY FIGURE

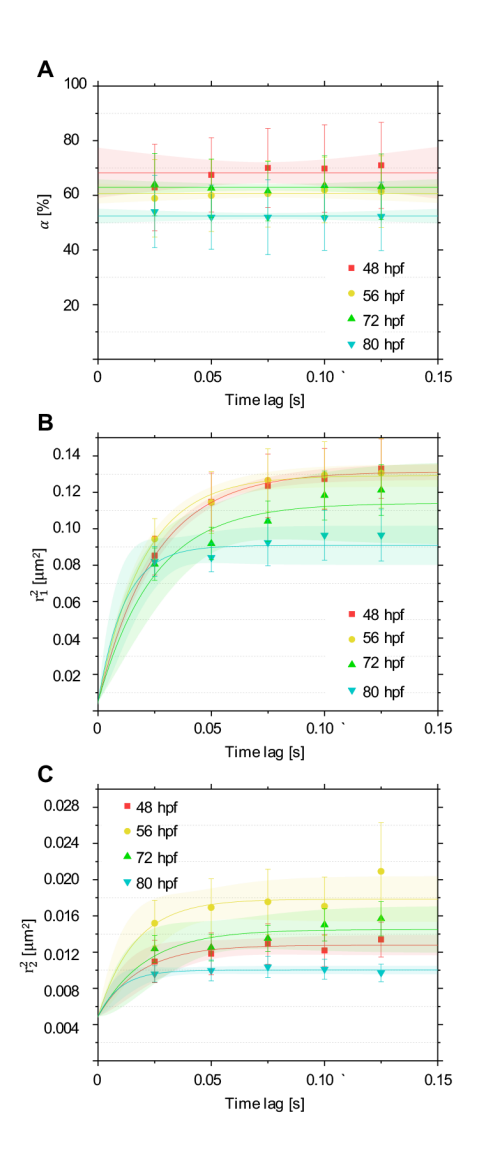


FIGURE S1: Mobility patterns of YFP-C10H-Ras in epidermal cells of the zebrafish embryos at different developmental stages. (A) Fraction size of the fast-diffusing population (α), plotted against the time lag. (B) Mean squared displacements plotted against the time lag for the fast-diffusing fraction (r_1^2) . (C) Mean squared displacements plotted against the time lag for the slow-diffusing fraction (r_2^2) . Results of the fits are summarized in Table 1. To establish the values of dynamic parameters, 3 different embryos were imaged on each of the 3 different experimental days at 48-, 56-, 72-, and 80-hour post fertilization. Each datapoint is presented in the form of a mean ± s.e.m., and the 95% c.i. of the mathematical fit is shown. Shapiro-Wilk statistical test was performed to check for normality of the data set. Statistical analysis was performed using a one-way ANOVA (P-value P(α , r_1^2 , r_2^2) > 0.05 at a t_{lag} of 25 ms) with a Tukey's range post-hoc test.

3. MULTIFOCAL TWO-PHOTON EXCITATION FLUORESCENCE MICROS-COPY REVEALS HOP DIFFUSION OF H-RAS MEMBRANE ANCHORS IN EPIDERMAL CELLS OF ZEBRAFISH EMBRYOS

Radoslaw J. Gora, Redmar C. Vlieg, Sven Jonkers, John van Noort, Marcel J.M. Schaaf

ABSTRACT

Developments in fluorescence microscopy techniques have enabled imaging of individual fluorescently labelled proteins in biological systems, and in the current study a single-molecule microscopy (SMM) technique has been applied in vivo, using the zebrafish embryo model. We have used multifocal two-photon excitation fluorescence microscopy (2PEFM) to study the dynamics of a GFP-fused H-Ras membrane-anchoring domain, GFP-C10H-Ras, in epidermal cells of living embryos. In previous studies, a fast and a slow diffusing population of GFP-C10H-Ras molecules had been found. The application of the multifocal 2PEFM technique enabled us to focus on the slow diffusing population, which appears to occur in clusters that diffuse within microdomains of the epidermal cell membranes. Based on their mobility on a short timescale (≤ 1s) we could distinguish between a subpopulation that was diffusing and one that was virtually immobile. Owing to the multifocal 2PEFM imaging mode, we were able to dramatically reduce photobleaching which enabled us to follow the GFP-C10H-Ras particles over a prolonged time (3 - 15 s) and reconstruct their molecular trajectories of the diffusing subpopulation. These trajectories exhibited that the C10H-Ras particles continuously switch between a diffusing state and brief bursts of increased diffusion. As a result, they display an anomalous mobility pattern that can be referred to as hop diffusion. Taken together, this study demonstrates that multifocal 2PEFM offers a powerful approach to studying individual particles for prolonged periods of time, and that using this approach we were able to uncover the hopping behavior of GFP-C10H-Ras.

Keywords: H-Ras, zebrafish, single-molecule microscopy, two-photon excitation fluorescence microscopy, membrane microdomains, anomalous diffusion, hop diffusion

Manuscript in preparation

3.1 INTRODUCTION

Dissection of complex molecular processes, such as the dynamic behavior of proteins and lipids in the phospholipid membranes of living cells, requires an advanced technological approach that goes beyond traditional ensemble averaging techniques and a static molecular overview (Yokota, 2020). Single-molecule microscopy (SMM) techniques provide such advanced technology, and they have enabled scientists to detect individual molecules and quantitatively analyze their dynamics with unprecedented spatial and temporal resolution (e.g. Harms et al., 2001; Kusumi et al., 1993; Kusumi et al., 2012; Luo et al., 2020; Murakoshi et al., 2004). SMM is predominantly performed using advanced fluorescence microscopy approaches that include, among others, total internal reflection fluorescence (TIRF), highly-inclined and laminated optical sheet (HILO), and light-sheet fluorescence microscopy (LSFM) (e.g. Bernardello et al., 2021; Lommerse et al., 2006; Miller et al., 2018; Schaaf et al., 2009; Shashkova and Leake, 2017). Microscopy setups designed for imaging of individual fluorescent molecules are generally equipped with a laser beam used to excite fluorophores, and with a highly sensitive charged-couple device (CCD) or a complementary metal-oxide-semiconductor (CMOS) camera for efficient recording of the emitted photons (Axelrod, 2001). Numerous possibilities exist for the optimal fluorescent labelling of the molecules of interest, depending on the biological model and the properties of the imaging setup used (Chudakov et al., 2010; Seefeldt et al., 2008). Fluorescent labelling of proteins can, for example, be achieved through genetic fusion with traditional autofluorescent proteins, such as Green or Yellow Fluorescent Proteins (GFP, YFP), or photoactivable variants of these proteins (Li and Vaughan, 2018).

Until now, the majority of SMM studies have been performed in cultured eukaryotic, and often immortalized, cell lines (e.g. Chen et al., 2014; Gebhardt et al., 2013; Groeneweg et al., 2014; Ha et al., 1999; Keizer et al., 2019; Lommerse et al., 2004; Lommerse et al., 2005). These cell lines often show artefacts, have a limited translational value, and do not take into consideration the influence of cell-cell interactions as well as their interplay with the extracellular environment that occurs in an intact organism. Therefore, there is a need for the development of SMM techniques that can be applied to living organisms. For this purpose, we use zebrafish embryos, which are increasingly utilized in biomedical research as a vertebrate animal model, and are well suited for SMM imaging due to

their optical clarity and because they are relatively easy to manipulate (Gore et al., 2018; Lu et al., 2015; Mione and Trede, 2010). The SMM techniques used for these *in vivo* studies should produce a limited background signal, make use of a large field of view (FoV), facilitate maintaining a biological sample alive over a prolonged period, and, preferably, not interfere with the natural biological processes of a sample by reducing, for instance, phototoxic and physicochemical stressors.

Thus far, we have extended SMM studies to living zebrafish embryos by investigating the mobility patterns of a yellow fluorescent protein (YFP) genetically fused to the human H-Ras protein, (YFP-H-Ras^{WT}), its constitutively active and inactive genetic mutants (YFP-H-Ras^{VI2} and YFP-H-Ras^{NI7}, respectively), and its membrane anchor (YFP-C10H-Ras) (Gora et al., 2021; Schaaf et al., 2009). The H-Ras protein is a member of the Ras protein family, which consists of small GTPases that activate intracellular signaling cascades, and thereby regulate crucial biological processes taking place in various cells, such as growth, proliferation, and differentiation (Malumbres and Barbacid, 2003). By use of the TIRFM technique and a dedicated mounting procedure, where the embryo tail tightly adheres to the coverslip, we succeeded in detecting individual, YFP-bound H-Ras proteins anchored to the apical cell membranes of cells in the outer epithelial layer of the epidermis, and in analyzing the dynamics of these molecules (Gora et al., 2021).

Using this approach, we were able to validate the results of previous studies, as we distinguished a fast- and a slow-diffusing fraction of H-Ras molecules, which both exhibited a confined type of diffusion. The fast-diffusing population contained most of the H-Ras proteins and was characterized by an initial diffusion coefficient that was approximately 10 to 15 times higher than the diffusion coefficient of the slow-diffusing H-Ras molecules. In addition, we discovered that a constitutively active H-Ras mutant (H-Ras^{V12}) exhibited a significantly higher diffusion coefficient and a larger confinement area than wild type H-Ras. These increased dynamic parameters of the H-Ras^{V12} fast-diffusing fraction are generally considered to reflect preferential localization to specific membrane microdomains which have been suggested to result from local differences in lipid composition and the structure of the membrane cytoskeleton combined with transmembrane proteins anchored to the actin filaments (Fujiwara et al., 2002; Kusumi et al., 2012; Murakoshi et al., 2004). Therefore, we also studied the effect of zebrafish

treatment with methyl-β-cyclodextrin (MBCD) and latrunculin B (LatB), which are known to disrupt the formation of a specific type of cholesterol-rich membrane microdomain, so-called lipid rafts, by cholesterol depletion or by inhibiting the formation of actin filaments respectively (Kwik et al., 2003). Both compounds significantly increased initial diffusion coefficients of the fast-diffusing fractions for the wild type H-Ras and its constitutively active, oncogenic mutant, H-Ras^{V12}, together with their fraction sizes. The largest effects were observed for the non-activated wild type H-Ras, which is in line with its higher affinity for lipid rafts (Hancock and Parton, 2005; Prior et al., 2001).

Due to the limited penetration depth of the TIRFM technique, the applicability of this approach is restricted to proteins in the apical membrane of the outer epidermal cell layer. In the present study, we have explored the possibilities of a novel in vivo SMM approach using a multifocal two-photon excitation fluorescence microscopy (2PEFM) setup in order to develop a method with wider applicability (van den Broek et al., 2013). The 2PEFM is based on the near-simultaneous excitation of a fluorescent molecule with two photons, each containing approximately half the energy required to excite a molecule. The absorption of the two photons needs to occur within the fluorophore relaxation time of 10⁻⁹s, which means that 2PEFM can only be performed using very high light intensities, which are achieved using pulsed laser sources with high peak intensities (in the range of kW-GW) and relatively low average laser power (2-5 W). This allows for lower laser beam absorption by a specimen being imaged and, therefore, reduced heating and phototoxic damage to the sample (Soeller and Cannell, 1999). Since the excitation light is generally in the near-infrared (NIR) wavelengths, and since biological tissues face less light scattering and absorption at NIR than at visible wavelengths, this makes 2PEFM a powerful technique for deep-tissue imaging. In addition, the background fluorescence is strongly reduced in 2PEFM, because the excitation of molecules is restricted to the confocal volume and the large anti-Stokes spectral difference between the excitation and emission light facilitates their spectral separation. To reduce the bandwidth limitations of the two-photon confocal microscopy, 2PEFM, we have combined it with multifocal scanning microscopy. In our multifocal microscope, a polygonal array of excitation light spots is generated in the image plane by passing the incident beam through a diffractive optical element (DOE). A two-dimensional fluorescence image is then created by scanning the array of spots across the sample plane within the camera exposure time, ensuring that the entire field of view (FoV) to be spanned by such an array of spots is homogenously illuminated.

In the present study, we have used a multifocal 2PEFM setup to analyze the mobility pattern of GFP fused to the human H-Ras membrane-anchoring domain (referred to as GFP-C10H-Ras) in epidermal cells of two-day-old zebrafish embryos. The multifocal 2PEFM technique enabled us to visualize GFP-C10H-Ras molecules of the slow-diffusing fraction. We show that these molecules occur in clusters that move through the plasma membrane, and that this population consists of a diffusing and an immobile fraction. By following the mobility of the diffusing molecules over a long time, in the range of 3 to 15 seconds (i.e., 12-60 frames), we showed that these diffusing GFP-C10H-Ras molecules alternate between a diffusing state and a state with an increased diffusion rate which is referred to as 'hopping'.

3.2 RESULTS

Imaging of GFP-C10H-Ras molecules in epidermal cells of zebrafish embryos using 2PEFM

To analyze the *in vivo* mobility pattern of the H-Ras membrane anchor, the GFP fusion protein of the H-Ras membrane-anchoring domain, GFP-C10H-Ras, was studied in 2 days-post-fertilization (dpf) zebrafish embryos using a 2PEFM setup. We focused our observations on the apical membrane of the outer epidermal cell layer, i.e., the superficial stratum, in the tail fin of the embryos from a *Tg(bactin: GFP-C10H-Ras)*^{vu119} transgenic line (Fig. 1). The embryos from this line stably express the GFP-tagged H-Ras membrane anchor in virtually all cells, including the epidermal cells in their tail fin, which is illustrated by a homogenous GFP-C10HRas localization in pentagonal and hexagonal cells of the outer epidermal cell layer (Fig. 1). The 2 dpf zebrafish embryos were placed on a coverslip and the tail fin region was covered with a 0.75-mm-thick sheet of agarose, which was used to gently press the tail fin towards the surface and, therefore, further reduce the possible movement of the anaesthetized embryo on the coverslip during the imaging. The rest of the zebrafish body was covered with a drop of water. Zebrafish vital functions, including heartbeat and the blood flow in its cardiovascular system, were controlled under a stereofluorescence microscope post-imaging.

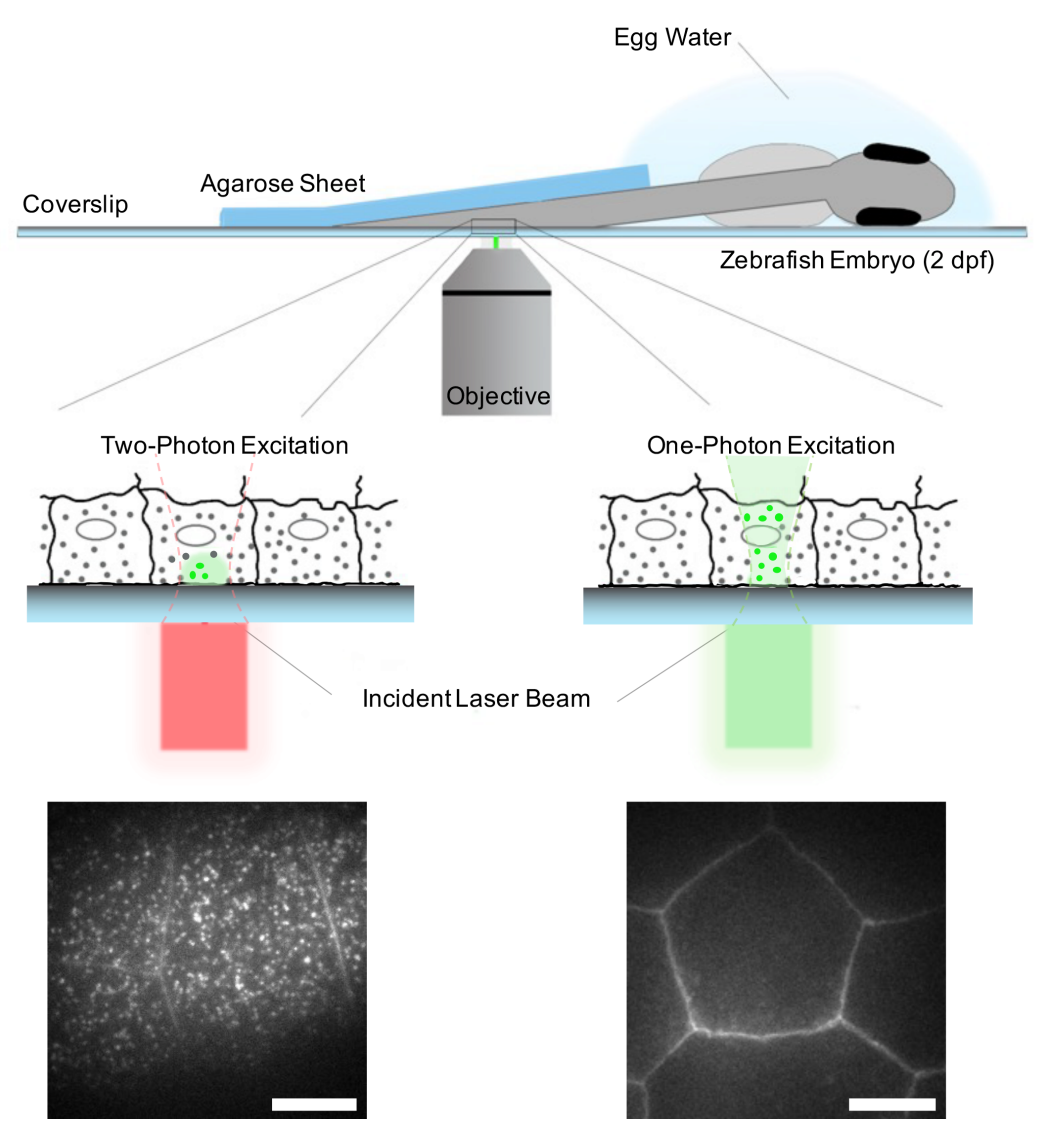


FIGURE 1: Schematic overview of SMM applied to a living zebrafish embryo. A zebrafish embryo from a Tg/bactin: GFP-C10H-Ras)^{vul19} transgenic line stably expressed the GFP-tagged H-Ras anchor in the zebrafish tailfin. At 2 dpf, it was placed on a coverslip coated with poly-L-lysine and coated with a drop of egg water. The tail region of the embryo was covered with a 0.75-mm-thick agarose (2%) sheet. On the lower right part of the figure, a picture of the outer layer of the epidermis is presented, showing the fluorescent signal of GFP-C10H-Ras in the cell membranes. This picture was taken using a one-photon excitation fluorescence microscopy technique. Morphologically, the cells in this layer are homogenous and are characterized by pentagonal and hexagonal shapes. On the lower left part, a 2PEFM image of an area with the same FOV is presented, with clearly visible localizations of the GFP particles within the zebrafish outer epidermal layer. Scale bar: 5 µm.

Image sequences with a time lag of 200 ms were acquired using the 2PEFM setup. As a first step in the analysis, we investigated the characteristics of the fluorescence intensity peaks detected in our images (Fig. 2A). We fitted the intensity peaks to a Gaussian surface, using custom-made software developed previously (Harms et al., 2001; Schütz et al., 1997a). Interestingly, we observed particles with varying maximum intensity counts, as shown in the density plots for these parameters (Fig. 2BCD), indicating that GFP particles of varying molecular compositions occur in our molecular populations which indicates clustering of GFP-C10H-Ras molecules. The extremum of the FWHM density plot equaled 327 nm, whereas the extremum of the density plot for the maximum intensity value equaled 893 counts.

In order to study possible changes in the peak characteristics over time, we generated the density plots for the maximum intensities of the peaks in the first and the last 50 frames of five different image sequences, which all comprised a total of 600 frames. A clear difference in the density plot of the maximum intensity values was observed, as the extremum of the density dropped from 875 counts (median of 943) in the first 50 frames to 567 (median of 582) in the last 50 frames of the time lapses (Fig. 3D). There was a wide distribution in the peak intensity in the first frames of the image sequence as a result of the clustering of molecules, but these intensities converge to a level of around 500-600 counts in the final frames, most likely as a result of photobleaching of molecules within the clusters which near the end of the image sequence mainly contain only a single fluorescent molecule.

In a subsequent, more detailed analysis of clustering and photobleaching events, all GFP peaks were identified using the ImageJ plug-in TrackMate (Tinevez et al., 2017). In the plug-in, a circular selection with a diameter of 5 pixels was drawn around each of the located GFP particles. The located GFP particles were sorted according to their intensity levels, defined by the pixel with the highest intensity value within the circular selection (Fig. 3E). Using this analysis, we studied the alterations in the characteristics of the individual intensity peaks over time (Fig. 2F). The circular selections representing GFP clusters were followed over time, and their maximum intensity counts were averaged.

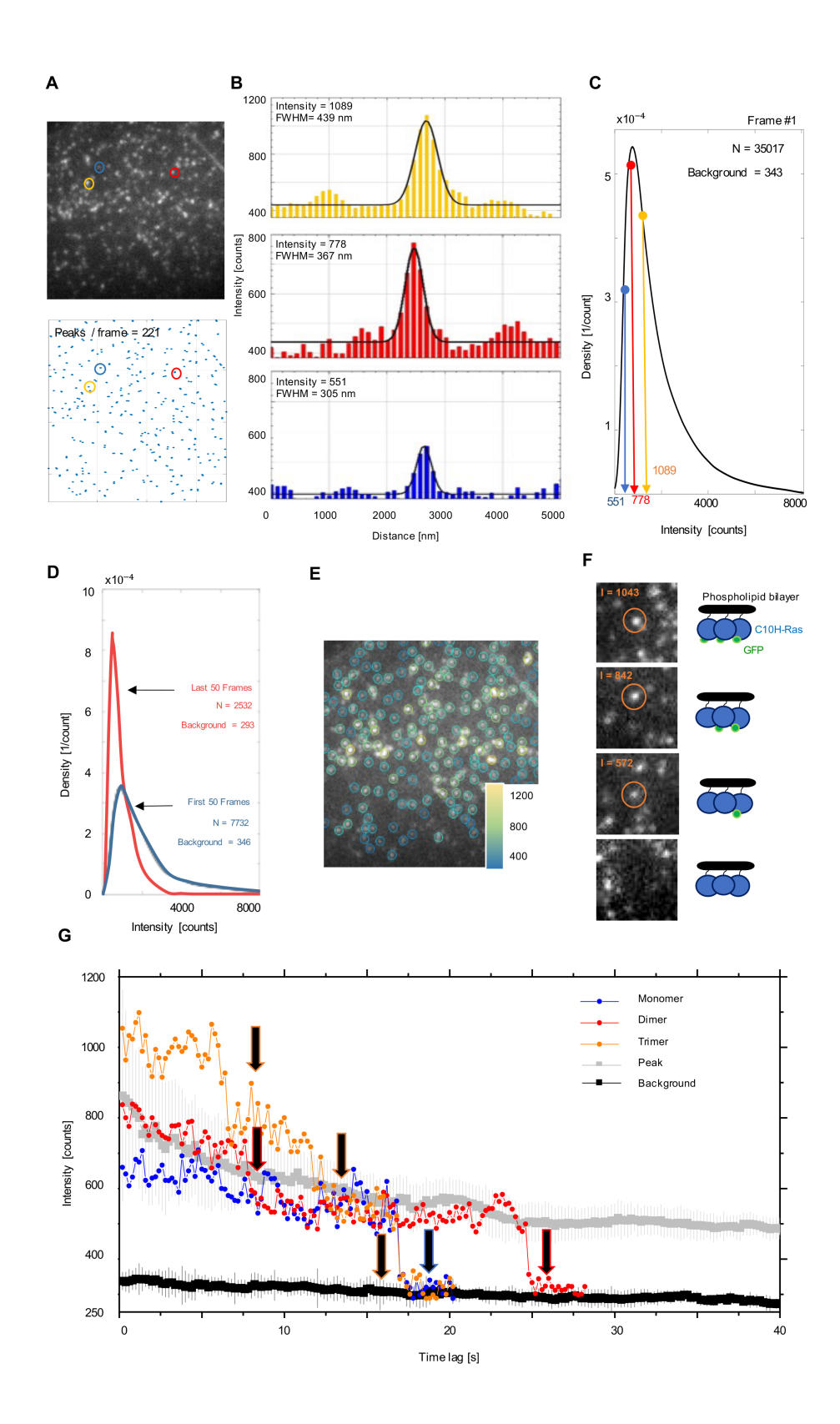


FIGURE 2: Structural analysis of the H-Ras anchor populations observed in the 2PEFM setup. (A) 2PEFM image of the GFP particles with a selection of three particles with differing intensities in circles (upper panel); localization map of the GFP particles in the same image, acquired through a custom-made MATLAB software (lower panel). (B) 2D Gaussian curves fitted onto the three particles selected in (A). The graph in yellow denotes an intensity profile example of a trimeric GFP, the one in red a dimeric GFP, and the one in blue a single GFP molecule. (C) Examples of density plots of the intensity values in the first frame of a time lapse. Values of the three particles selected in (A) are overlayed, indicating the wide spectrum of GFP multiplicities present in our molecular population. (D) Density plots of the intensity counts in the first and the last 50 frames of the time lapse consisting of 600 individual frames. Notable is the switch in the most abundant GFP populations, from polymeric GFPs in the first 50 frames to monomeric GFP molecules. (E) The 2PEFM image from (A) with a GFP particles attributed a circular selection of 5 pixels in diameter, with intensity of each selection determined by the pixel with the highest intensity count within the selection, performed by an ImageJ plug-in, TrackMate (lower panel). (F) Visualization of a photobleaching event, with an example of a GFP trimer. Three distinctive intensity levels are depicted, denoting a step-like decrease of their intensity count. (G) Single-step photobleaching experiment. Intensity values of the GFP circular selections were acquired from five individual 2PEFM time lapses, and are depicted as the means with the corresponding standard error values (in grey). The background intensity is defined as a mean intensity count of all the pixels falling outside the peak selections within each frame, and are depicted as the means with the corresponding standard error values (in black). Molecules selected in (A) are overlayed and followed over time, indicating their step-like intensity drop. I, intensity count; N, number of localized molecules; Background, mean background intensity.

The background intensity of an image was defined as the average intensity count of all pixels that fell outside the circular selections. Then, we followed three peaks with varying initial intensity values over time, and it appeared that all three peaks exhibited stepwise photobleaching. The intensity level prior to the final photobleaching step was in the range of 500-600 intensity counts (Fig. 2G), indicating that this intensity level corresponded to a population of single fluorescent GFP molecules. This finding was further confirmed by the analysis of the average peak intensity count per image, which decreased over time and stabilized during the final stage of the time-lapse around this intensity range (Fig. 3G, grey line). The outcome was in line with the single GFP signals being the most abundant among all detected intensity peaks at this stage, as a result of the photobleaching. Based on these results, we concluded that it is possible to detect single GFP molecules with our 2PEFM setup, and that most of the detected GFP-C10H-Ras molecules formed clusters in the plasma membrane.

Analysis of the mobility pattern of GFP-C10H-Ras molecules in epidermal cells of zebrafish embryos using 2PEFM

Subsequently, the mobility patterns of the GFP-fused H-Ras membrane anchoring domains were analyzed using Particle Image Correlation Spectroscopy (PICS) software (Semrau and Schmidt, 2007). In this analysis, correlations between the locations of molecules in consecutive frame pairs were determined. Based on this analysis, cumulative probability distributions of the displacements were generated for each time lag. These curves were then fitted to a one-, (Eq. 1) a two- (Eq. 2), or a three-population (Eq. 3) model (Fig. 2A; for further reference, see Materials and Methods section). The one-population model fitted the 2PEFM data with a Pearson's correlation coefficient of 0.948, whereas the two-population model much better reflected the mobility patterns of the GFP-C10H-Ras, and the correlation coefficient of the fit equaled 0.999. Since the three-population models yielded a similar correlation coefficient, we used the two-population model for further analysis, which best fitted the experimental data with the least number of populations. Using this model, which suggests the presence of two fractions of molecules with different diffusion rates, the relative size of the fast-diffusing fraction (α) and the mean squared displacements of the fast- and slow-diffusing fractions (r_1^2 and r_2^2 , respectively) were determined. By using a multistep analysis to investigate the GFP-C10H-Ras dynamics, these parameters were determined at five different time lags: 200, 400, 600, 800, and 1000 ms.

Subsequently, the parameters α , r_1^2 , and r_2^2 were plotted against the time lag (Fig. 2BCD). The relative size of the GFP-C10H-Ras fast-diffusing fraction α was stable over all time lags (Fig. 2B, Table 1), and equaled $49.5 \pm 0.4\%$. For both the fast- and the slow-diffusing fraction, the plots presenting the mean squared displacements (r_1^2 and r_2^2) as a function of the time lag reached a plateau (Fig. 2CD). Hence, we fitted these curves to a confined diffusion model (Eq. 4), in which the H-Ras membrane anchors move with an initial diffusion coefficient D_0 and their mobility is confined to a squared area with sides of length L (Bobroff, 1986; Lingwood and Simons, 2010; Schaaf et al., 2009). Based on our analysis, the D_0 of the fast-diffusing fraction equaled $0.066 \pm 0.005 \, \mu m^2 \, s^{-1}$ and the size of its confinement area L equaled 253 ± 3 nm. The slow-diffusing fraction of the GFP-C10H-Ras

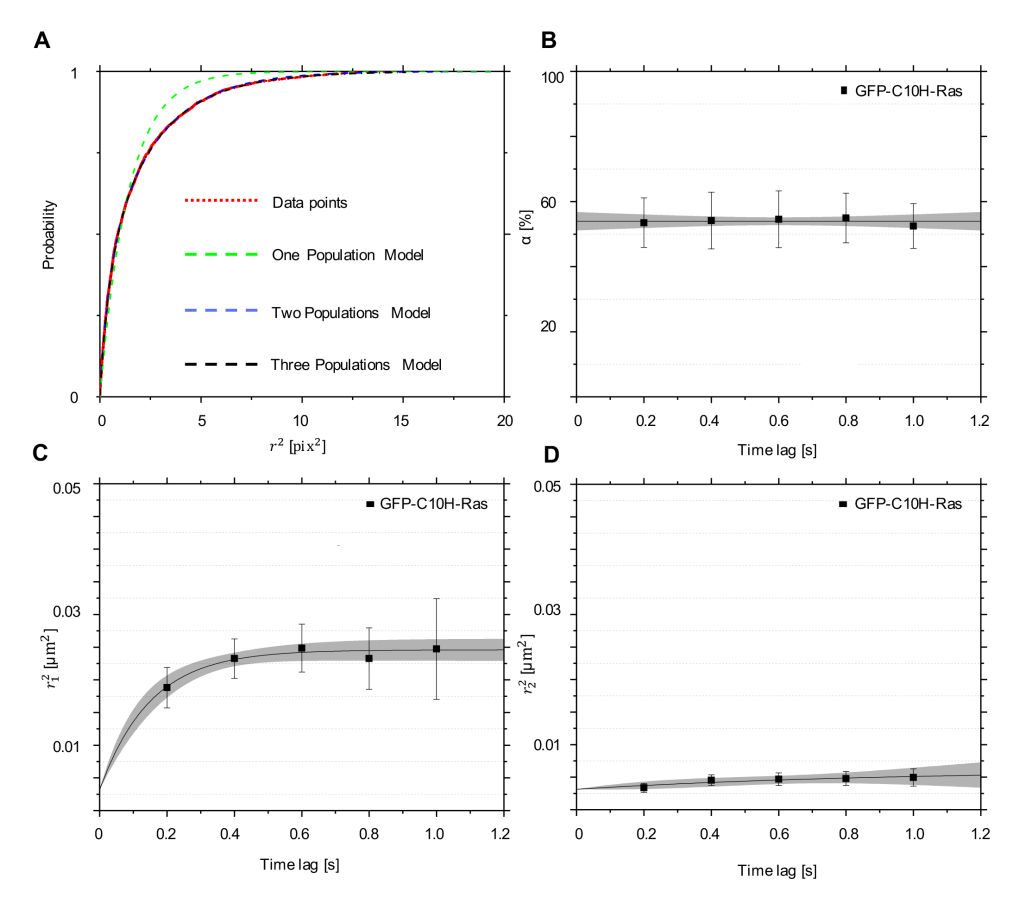


FIGURE 3: Mobility patterns of GFP-C10H-Ras in epidermal cells of the zebrafish embryos. (A) Cumulative probability distribution function of the GFP-C10H-Ras squared displacements calculated for the 2PEFM datasets. Data points are shown in red, and their population fits in dashed green for a one-population model, in dashed blue for a two-population model, and in dashed black for a three-population model. No significant difference was observed between the fitting of the two- and the three-population models, which both best fitted the cumulative probability distribution. Fitting of the data points to the two-population model allowed for calculation of the mean squared displacements of these populations $(r_1^2 \text{ and } r_2^2)$. This procedure was repeated for each of the time lags used. (B, C, D) Plots representing mobility patterns of the GFP-C10H-Ras inside the zebrafish embryos from the Tg/bactin: GFP-C10H-Ras)va119 transgenic line. (B) Fraction size of the fast-diffusing population (α) , plotted against the time lag. (C) Mean squared displacements plotted against the time lag for the fast-diffusing fraction (r_1^2) . (D) Mean squared displacements plotted against the time lag for the slow-diffusing fraction (r_2^2) . To establish the values of dynamic parameters for the GFP-C10H-Ras from the Tg/bactin: GFP-C10H-Ras)^{vuji9} line, 5 different embryos were imaged on each of the 5 different experimental days. Parameters obtained upon curve fitting are presented in Table 1. Each data point is presented in the form of a mean ± s.e.m., and the 95% c.i. of the mathematical fit is shown. Shapiro-Wilk statistical test was performed to check for normality of the data set. Statistical analysis for all treatment groups was performed using a one-way ANOVA (P-value $P(\alpha,$

 (r_1^2, r_2^2) > 0.05 at a t_{lag} of 200 ms) with a Tukey's range posthoc test (for details of the post-hoc test results, see Table 2).

hardly diffused with a D_0 of 0.80 \cdot 10⁻³ \pm 0.10 \cdot 10⁻³ μ m² s⁻¹, and was confined to a smaller area (L of 94 \pm 5 nm). Since the mean squared displacements of this population were similar to the offset value in this plot (0.0031 μ m², based on the positional accuracy of ~28 nm), the molecules in this population may be considered immobile. When the data were analyzed using the one-population model, the D_0 of this single population equaled 0.116 \pm 0.011 μ m² s⁻¹ and the confinement area size L equaled 302 \pm 54 nm (Fig. S1).

Interestingly, the initial diffusion coefficients and confinement area sizes of the two GFP-C10H-Ras subpopulations that were determined in the zebrafish epidermal cells using 2PEFM imaging did not correspond to the findings previously obtained for YFP-C10H-Ras in the same cells using a TIRFM setup (Gora et al., 2021; Schaaf et al., 2009). In particular, the fast-diffusing fraction, as identified in the previous TIRFM experiments, was not detected in the current study. In addition, the slow-diffusing YFP-C10H-Ras population previously identified using TIRFM showed a mobility pattern highly similar to that of the fast-diffusing subpopulation that was discerned using 2PEFM imaging in this study (Gora et al., 2021; Schaaf et al., 2009). This suggests that using the current approach we are not able to detect the fast-diffusing population of GFP-C10H-Ras molecules that we previously observed using TIRFM. Moreover, the slow-diffusing population that was previously identified in our TIRFM experiments was observed in the present study, and this population could be further divided into a slow-diffusing and an immobile subpopulation based on the novel data.

Comparison of the GFP-C10H-Ras dynamics between 2PEFM and TIRFM with different temporal resolutions

In order to determine whether the absence of the fast subpopulation of GFP-C10H-Ras molecules is a result of the temporal resolution of the 2PEFM, we determined dynamic parameters for GFP-C10H-Ras by using the TIRFM setup and imaging the same batches of zebrafish embryos. We imaged embryos with a time lag of 25 ms, which had also been used in previous studies (Gora et al., 2021; Schaaf et al., 2009), and a time lag of 200 ms, which corresponds to the time lag used in the 2PEFM experiments (Fig. 4A). With both time lags, we could distinguish a fast- and a slow-diffusing fraction of molecules

using the analysis based on a two-population model (Fig. 4B), and all fractions showed confined diffusion, but generally, the mobility of GFP-C10H-Ras decreased with increasing time lag (Fig. 4CD). The size of the fast-diffusing fraction decreased significantly $(66.0 \pm 5.3\% \text{ at } 25 \text{ ms, and } 52.5 \pm 1.1\% \text{ at } 200 \text{ ms})$, as did the initial diffusion coefficients D_0 for the fast-diffusing fraction (1.46 \pm 0.16 μ m² s⁻¹ at 25 ms. and 0.22 \pm 0.03 μ m² s⁻¹ at 200 ms). On the other hand, the size of the confinement area L for GFP-C10H-Ras increased $(468 \pm 4 \text{ nm} \text{ at } 25 \text{ ms} \text{ and } 553 \pm 2 \text{ nm} \text{ at } 200 \text{ ms})$. For the slow-diffusing fraction, the initial diffusion coefficients decreased with increasing time lag $(0.152 \pm 0.047 \text{ µm}^2 \text{ s}^{-1} \text{ at})$ 25 ms and $0.312 \cdot 10^{-2} \pm 0.101 \cdot 10^{-2}$ µm² s⁻¹, whereas the size of the confinement area increased (103 ± 5 nm at 25 ms and 128 ± 2 nm at 200 ms). Taken together, these findings demonstrate that the temporal resolution of the microscopy setup affects the dynamic parameters determined for GFP-C10H-Ras. In particular, an increase in the time lag results in lower mobility. It is most likely that due to a longer illumination time, the signal of the fast-diffusing molecules is spread over a larger area, generating a motion blur, and making it impossible to distinguish single fluorescent signal spots above the background signal.

Thus, we demonstrated that the time lag of 200 ms was largely responsible for the decreased mobility that we determined in our 2PEFM study compared to our previous TIRFM studies. When we compared the results from the TIRFM and 2PEFM experiments, both using a 200 ms time lag, we found no significant differences between the population sizes, and the mobility pattern of the slow-diffusing populations (Table 1, 2). However, the fast-diffusing population observed in the 2PEFM experiment still showed a lower diffusion coefficient and a smaller confinement area than its equivalent observed by TIRFM, so the lower mobility observed of this fraction using 2PEFM cannot entirely be explained by the lower time resolution.

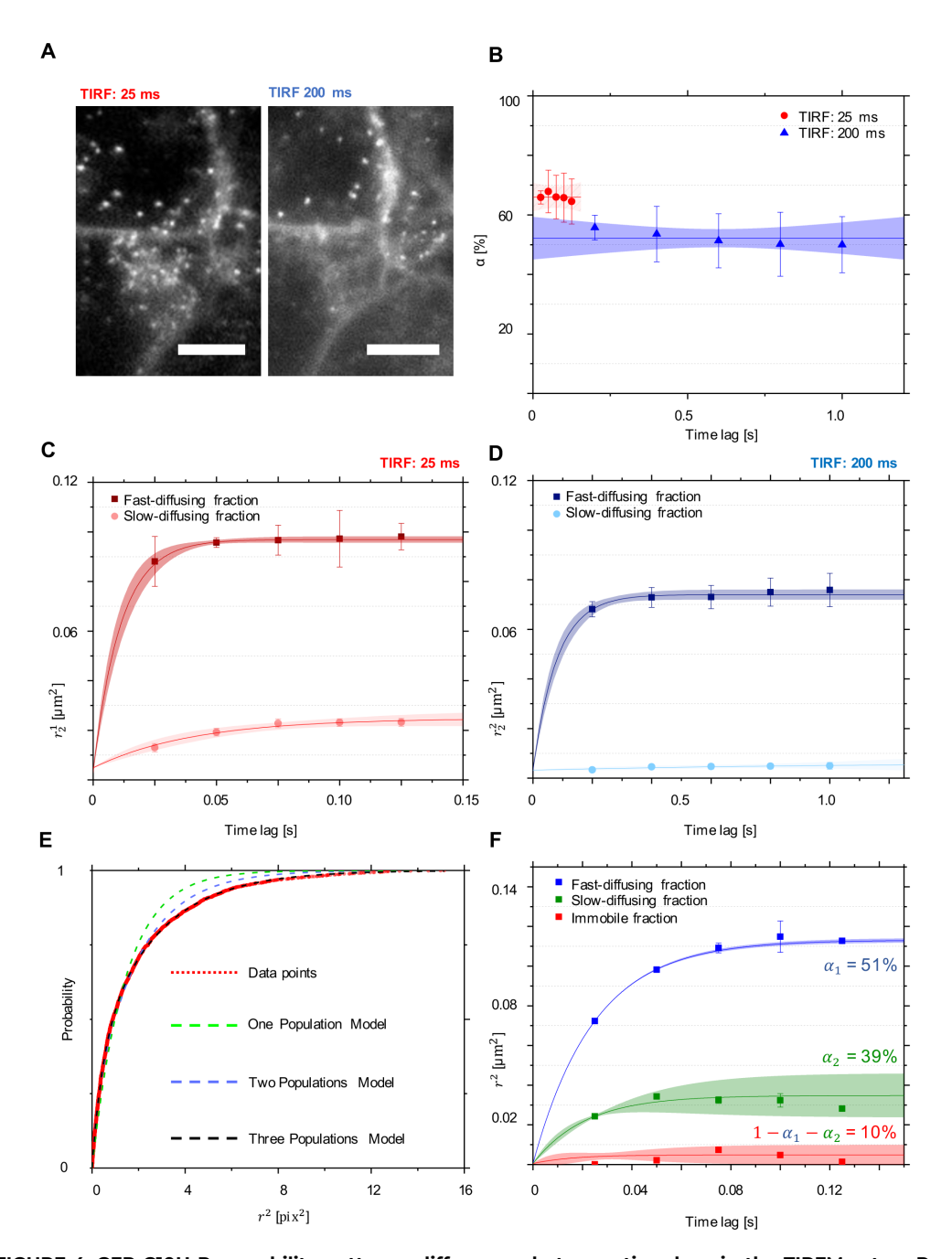


FIGURE 4: GFP-C10H-Ras mobility patterns: differences between time lags in the TIRFM setup. Results of different multi-fractional model fitting to the TIRFM data. (A) Examples of two images, each representing the same FoV, with differing temporal resolutions. (B) Fraction size of the fast-diffusing population (α) , plotted against the time lag. (C) Mean squared displacements plotted against the time lag for a fast- (r_1^2) and a slow-diffusing (r_2^2) fractions for the images acquired in TIRFM with a time lag of 25 ms.

(D) Mean squared displacements plotted against the time lag for a fast- (r_1^2) and a slow-diffusing (r_2^2) fractions for the images acquired in TIRFM with a time lag of 200 ms. Results of the fits are summarized in Table 1. To establish the values of dynamic parameters, 5 different embryos per each TIRFM imaging approach were imaged on each of the 3 different experimental days. Each datapoint is presented in the form of a mean ± s.e.m., and the 95% c.i. of the mathematical fit is shown. Shapiro-Wilk statistical test was performed to check for normality of the data set. Statistical analysis was performed using a one-way ANOVA with a Tukey's range post-hoc test (for details of the statistical test results, see Table 2). (E) Cumulative probability distribution function of the GFP-C10H-Ras squared displacements calculated for the TIRFM datasets. Data points are shown in red, and their population fits in dashed green for a one-population model, in dashed blue for a two-population model, and in dashed black for a three-population model (formulae shown). Fitting of the data points to the three-population model allowed for calculation of a relative size of the subpopulations (α_1 and α_2) and their mean squared displacements (r_1^2, r_2^2 and r_3^2). This procedure was repeated for each of the time lags used. (F) Mean squared displacements plotted against the time lag for a fast-diffusing, a slow-diffusing, and an immobile fraction $(r_1^2, r_2^2, \text{ and } r_3^2)$, using the three-population model fit. Values of the fast-diffusing and the slow-diffusing fraction sizes, α_1 and α_2 , are shown.

To investigate the GFP-C10H-Ras in more detail, we utilized the TIRFM data with a temporal resolution of 25 ms, presented in Fig. 4BC, and we fitted one-population ($R^2 \sim 0.912$, Eq. 1), two-population ($R^2 \sim 0.982$, Eq. 2), and three-population ($R^2 > 0.999$, Eq. 3) models to the data (Fig. 4EF, Table 1). Interestingly, the analysis for the TIRFM data exhibited that it is the three-population model that is most suitable to describe the dynamics of the H-Ras anchors imaged using this microscopy setup (Fig. 4E). Based on the threepopulation model for the TIRFM data, we could differentiate between a fast-diffusing, a slow-diffusing, and an immobile population. The percentage of GFP-tagged H-Ras anchors equaled 51% for the fast-diffusing fraction, and 39% for the anchors in the slowdiffusing population. Immobile molecules constituted 10% of the total GFP-C10H-Ras population (Fig. 4F). The initial diffusion coefficient D_0 for the fast-diffusing population equaled $1.15 \pm 0.03 \,\mu\text{m}^2 \,\text{s}^{-1}$, and $0.306 \pm 0.045 \,\mu\text{m}^2 \,\text{s}^{-1}$ for the slow-diffusing one. The corresponding confinement area size L equaled 581 \pm 8 nm and 286 \pm 16 nm for the fastdiffusing and the slow-diffusing population, respectively. Consequently, fitting the three-population model to the TIRFM data not only showed the occurrence of three populations, but also confirmed that the fastest population of H-Ras anchors is not detected in the 2PEFM setup. The dynamic parameters of the two populations acquired by imaging GFP-C10H-Ras with the 2PEFM setup (Fig. 3CD) mostly corresponded to the slow-diffusing and immobile fraction observed in the TIRFM setup with the time lag of 25 ms (Fig. 4F).

Analysis of the excitation laser power impact on the GFP-C10H-Ras mobility pattern

To study a possible effect of the excitation laser power on the observed mobility patterns, we used the TIRFM setup with a time lag of 25 ms and imaged GFP-C10H-Ras in zebrafish embryos with increasing excitation laser power, i.e., 10%, 30%, and 50% of the setup's maximal power, which measured at the sample plane equaled ~40 mW (with the illumination focal plane area of $1.65 \cdot 10^5$ cm², the laser power density equaled ~2.42 kW cm⁻²). The results of this experiment showed no significant differences as a result of the changed laser power. The size of the fast-diffusing fraction did not differ significantly between the different laser powers applied, and equaled 61.0 \pm 15.7% for 10%, 60.7 \pm 9.8% for 30%, and $54.8 \pm 6.3\%$ for 50% of the total laser power (Fig. 5A). Initial diffusion coefficients D_0 for the fast-diffusing fraction did not differ either, and equaled 0.91 \pm 0.14 μ m² s^{-1} for 50%, 1.22 \pm 0.22 μ m² s^{-1} for 30%, and 0.76 \pm 0.02 μ m² s^{-1} for 10% of the total laser power (Fig. 5C). Similarly, the size of the confinement area L for illumination with 50% (444 \pm 3 nm) was similar to those imaged with 30% and 10% of the total laser power (475 ± 5 nm and 536 \pm 3 nm, respectively). The initial diffusion coefficients and the sizes of the confinement areas for the slow-diffusing fractions were also similar for all of the experimental groups (Fig. 5D).

To investigate whether the different populations display different fluorescence intensities and may represent clusters comprising a different number of molecules, we plotted the intensity of selected particles against their squared displacement. We selected 30 individual GFP molecules per fraction, based on a threshold value of 0.01 \square m², for each excitation power. Interestingly, no significant differences in the intensities were observed between the slow- and the fast-diffusing fraction, indicating that the clusters of these fractions contain a similar number of GFP-C10H-Ras molecules. As expected, the mean intensity for the molecules imaged with 50% of the TIRFM maximal laser power was the highest and equaled 47361 \pm 5645 counts for the fast-diffusing fraction and 43661 \pm 5137 counts for the slow-diffusing one. For the 30% of the maximal laser power, the intensity equaled 16113 \pm 1993 counts for the fast-diffusing fraction and 13847 \pm 1310 counts for the slow-diffusing one, whereas for the 10% of the maximal laser power the intensity equaled 2107 \pm 214 counts for the fast-diffusing fraction and 1984 \pm 119 counts for the slow-diffusing one) (Fig. 5B).

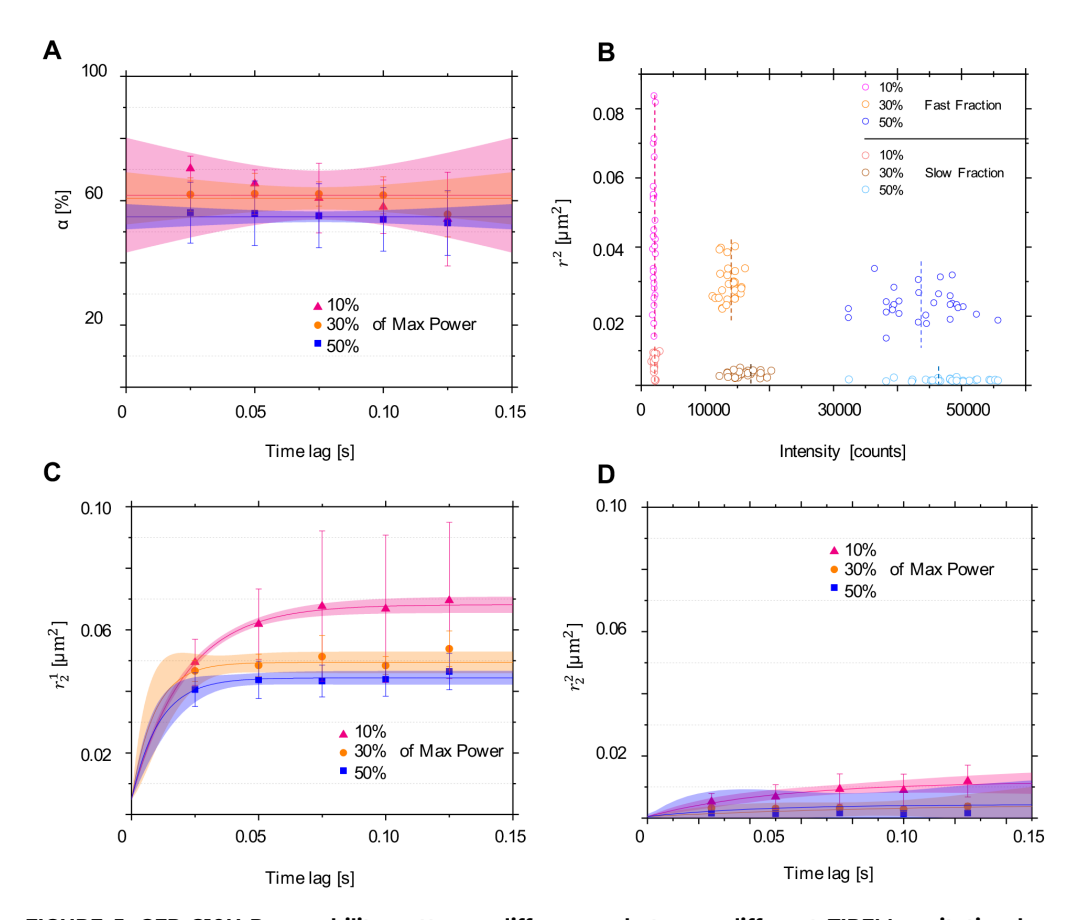


FIGURE 5: GFP-C10H-Ras mobility patterns: differences between different TIRFM excitation laser **powers.** (A) Fraction size of the fast-diffusing population (α), plotted against the time lag of 25 ms. (B) Relationship between intensity counts and squared displacement for 30 molecules selected per their fraction and applied excitation laser power. For 50% of the total laser power, the mean intensity value equaled 47361 ± 5645 for the fast-diffusing fraction and 43661 ± 5137 for the slow-diffusing one, whereas the background intensity equaled 19800 counts. For 30% of the total laser power, the mean intensity value equaled 16113 ± 1993 for the fast-diffusing fraction and 13847 ± 1310 for the slow-diffusing one, whereas the background intensity equaled 6141 \pm 5645 counts. For 10% of the total laser power, the mean intensity value equaled 2107 \pm 214 for the fast-diffusing fraction and 1984 \pm 119 for the slow-diffusing one, whereas the background intensity equaled 534 counts. (C) Mean squared displacements plotted against the time lag for the fast-diffusing fraction (r_1^2) . (D) Mean squared displacements plotted against the time lag for the slow-diffusing fraction (r_2^2) . Results of the fits are summarized in Table 1. To establish the values of dynamic parameters, 5 different embryos per each TIRFM excitation laser power were imaged on each of the 3 different experimental days. Each datapoint is presented in the form of a mean ± s.e.m., and the 95% c.i. of the mathematical fit is shown. Shapiro-Wilk statistical test was performed to check for normality of the data set. Statistical analysis was performed using a one-way ANOVA with a Tukey's range post-hoc test (for details of the statistical test results, see Table 2).

TABLE 1: Summary of the GFP-C10H-Ras mobility patterns acquired using the PICS analytical method.

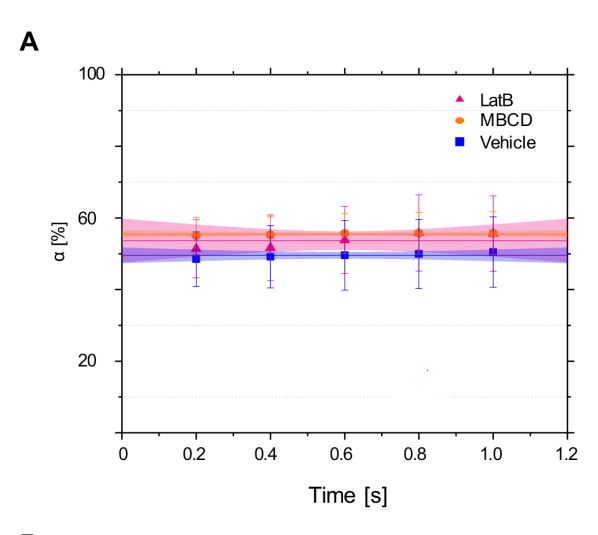
Experiment	D _{0FD} [µm² s ⁻¹]	D _{0SD} [μm² s ⁻¹]	L_{FD} [nm]	L _{SD} [nm]	α [%]		
1.1. Mobility patterns of GFP-C10H-Ras in zebrafish embryos: 2PEFM imaging							
Zebrafish embryo	0.066 ± 0.005	(0.080 ± 0.010) · 10-2	253 ± 3	94 ± 5	49.5 ± 0.4		
1.2. Mobility patterns of GFP-C10H-Ras in zebrafish embryos: comparisons with TIRFM imaging							
Time lag: 25 ms	1.46 ± 0.16	0.152 ± 0.047	468 ± 4	103 ± 5	66.0 ± 5.3		
Time lag: 200 ms	0.22 ± 0.03	(0.312 ± 0.101) · 10 ⁻²	553 ± 2	128 ± 2	52.5 ± 1.1		
Time lag: 25 ms: Three-	0.3 1.15 + 0.03	0.306 ± 0.045 (D _{0SD})	581 ± 8	286 ± 16 (L _{SD})	51.0 ± 3.2 (α ₁)		
population model	1.15 ± 0.05	$0.042 \pm 0.007 (D_{0IM})$		$102 \pm 18 \; (L_{IM})$	$39.2 \pm 2.3 \; (\alpha_2)$		
1.3. Mobility patterns of GFP-C10H-Ras in zebrafish embryos: impact of TIRFM differing excitation power							
50% of the total power	0.91 ± 0.14	0.092 ± 0.010	444 ± 3	108 ± 47	54.8 ± 6.3		
30% of the total power	1.22 ± 0.22	0.089 ± 0.008	475 ± 5	112 ± 27	60.7 ± 9.8		
10% of the total power	0.76 ± 0.02	0.043 ± 0.010	536 ± 3	184 ± 13	61.7 ± 15.7		
1.4. Mobility patterns of GFP-C10H-Ras in zebrafish embryos: effect of vehicle, LatB and MBCD treatments							
GFP-C10H-Ras in vehicle	0.051 ± 0.006	$(0.080 \pm 0.003) \cdot 10^{-2}$	237 ± 3	NA	49.9 ± 0.3		
GFP-C10H-Ras + LatB	0.039 ± 0.007	(0.055 ± 0.006) · 10 ⁻²	213 ± 5	NA	53.7 ± 0.9		
GFP-C10H-Ras + MBCD	0.110 ± 0.020	(0.085 ± 0.005) · 10 ⁻²	277 ± 2	NA	55.5 ± 0.2		

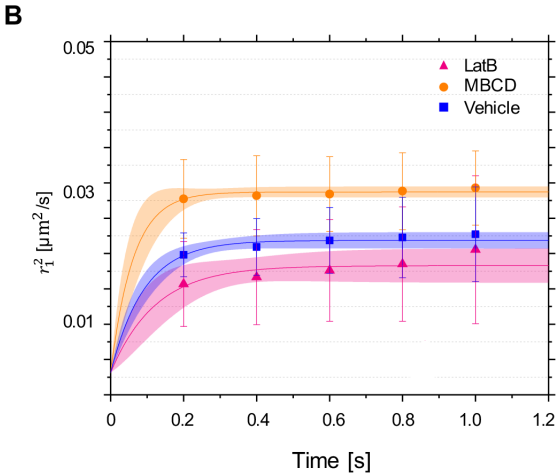
 D_{0FD} , D_{0SD} , D_{0IM} – Initial diffusion coefficients for fast-, slow-diffusing and immobile fractions, respectively; L_{FD} , L_{SD} , L_{IM} – Sizes of the confinement area of fast-, slow-diffusing, and immobile fractions, respectively; α – fast-diffusing fraction size.

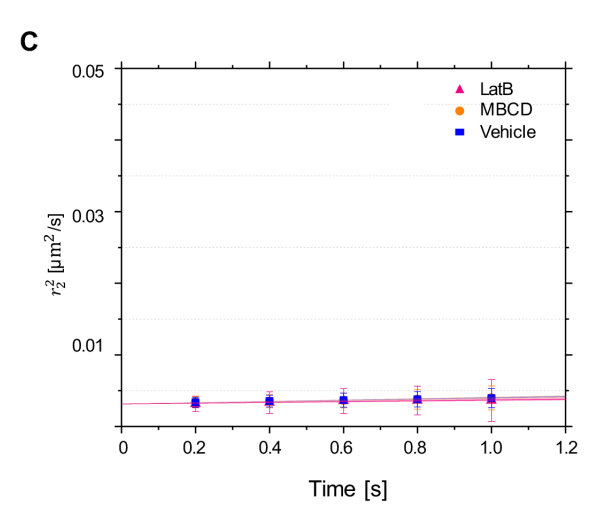
The mobility pattern of GFP-C10H-Ras in epidermal cells of zebrafish embryos after treatment with Latrunculin B and Methyl-β-cyclodextrin

To further evaluate whether the absence of the fast subpopulation of GFP-C10H-Ras molecules is inherent to our 2PEFM-based analysis, we incubated zebrafish embryos with Latrunculin B (LatB) and Methyl- β -cyclodextrin (MBCD). In our previous study employing TIRFM, both LatB and MBCD significantly increased the size of the fast-diffusing fraction of YFP-H-Ras molecules together with its initial diffusion coefficient and confinement area size (Gora et al., 2021). Such changes, however, were not observed in the slow-diffusing fraction, making these treatments a powerful tool to distinguish between the two fractions. Thus, after treating the zebrafish embryos with LatB or MBCD, the 2PEFM was performed and the mobility patterns of GFP-C10H-Ras were analyzed. Again, we observed a slow-diffusing and an immobile fraction of molecules in all experimental groups (Fig. 6C).

FIGURE 6: Mobility patterns of GFP-C10H-Ras in epidermal cells of the zebrafish embryos before and after treatment with Latrunculin B (LatB) and Methyl-β-cyclodextrin (MBCD). (A, B, C) Plots representing mobility patterns of the GFP-C10H-Ras inside the zebrafish embryos from the Talbactin: GFP-C10H-Ras)vu119 transgenic line after the treatments with a vehicle, LatB and MBCD. (A) Fraction size of the fast-diffusing population (α), plotted against the time lag. (B) Mean squared displacements plotted against the time lag for the fast-diffusing fraction (r_1^2) . (C) Mean squared displacements plotted against the time lag for the slow-diffusing fraction (r_2^2) . Parameters obtained upon curve fitting are presented in Table 1. To establish the values of dynamic parameters for the GFP-C10H-Ras from the transgenic line treated with vehicle, LatB and MBCD, 5 different embryos per each treatment group and imaged on each of the 3 different experimental days. Each data point is presented in the form of a mean \pm s.e.m., and the 95% c.i. of the mathematical fit is shown. Shapiro-Wilk statistical test was performed to check for normality of the data set. Statistical analysis for all treatment groups was performed using a one-way ANOVA (P-value P(α , r_1^2 , r_2^2) > 0.05 at a t_{lag} of 200 ms) with a Tukey's range posthoc test (for details of the post-hoc test results, see Table 2).







The size of the slow-diffusing fraction did not significantly change after LatB or MBCD treatment (from $49.9\pm0.3\%$ in the vehicle group to $53.7\pm0.9\%$ and $55.5\pm0.2\%$ after LatB and MBCD treatment, respectively) (Fig. 6A). Additionally, treatment with LatB and MBCD did not significantly alter the initial diffusion coefficient of the slow-diffusing fraction (Fig. 6B). The size of the confinement area of the slow-diffusing fraction was not significantly changed either and equaled 237 ± 3 nm for the vehicle group, 213 ± 5 nm for the LatB treatment group, and 277 ± 2 nm for the MBCD treatment group (Fig. 6B).

These data further confirmed that, in the 2PEFM setup, we did not detect the fast-diffusing GFP-C10H-Ras fraction that was identified in our previous TIRFM experiments, and was largely affected by LatB and MBCD treatment, since the effects induced by these treatments were not observed in the current study. We, therefore, conclude that the fraction detected using the 2PEFM setup that diffused the fastest corresponds to the slow-diffusing subpopulation that we previously identified using TIRFM, which showed a similar mobility pattern and was not affected by LatB and MBCD treatment, either.

TABLE 2: Statistical analysis performed for the values of mean squared displacements and slow-diffusing fraction sizes obtained experimentally for the time lag of 200 ms.

Statistical	Mean squared dis-	Mean squared	Fraction size:	
significance ¹	placement: slow-dif-	displacement:	slow-diffusing fraction	
significance.	fusing fraction (r_1^2)	immobile fraction (r_2^2)	(α)	
GFP-C10H-Ras in				
zebrafish embryos	P = 0.091	P = 0.362	P = 0.324	
treated with LatB and	P = 0.091	P = 0.562	P - 0.324	
MBCD				
	P(2PEFM, TIRFM ²⁵) <	P(2PEFM, TIRFM ²⁵) <	P(2PEFM, TIRFM ²⁵) <	
GFP-C10H-Ras in	0.001	0.001	0.001	
zebrafish embryos im-	P(2PEFM, TIRFM ²⁰⁰) <	P(2PEFM, TIRFM ²⁰⁰) =	P(2PEFM, TIRFM ²⁰⁰) =	
aged with 2PEFM and	0.001	0.619	0.164	
TIRFM setups ²	P(TIRFM ²⁵ , TIRFM ²⁰⁰) <	$P(TIRFM^{25}, TIRFM^{200}) =$	P(TIRFM ²⁵ , TIRFM ²⁰⁰) <	
	0.001	0.005	0.001	
GFP-C10H-Ras in				
zebrafish embryos im-	P > 0.132	P > 0.262	P = 0.294	
aged with TIRFM at dif-	F > 0.132	P > 0.202	P = 0.294	
fering excitation powers				

For comparisons of protein mobility patterns in zebrafish embryos between different chemical treatments, microscopy settings, and TIRFM laser excitation powers, a one-way ANOVA was used. In case the differences between groups were significant in the one-way ANOVA, results of multiple groups comparison are shown, performed by a Tukey's range posthoc test.

²In the case of TIRFM imaging with the time lag of 25 ms, values of α , r_1^2 , and r_2^2 for statistical analysis were obtained experimentally for the time lag of 25 ms.

NS – non-significant (P > 0.05); * - P < 0.05; **** - P < 0.001.

Analysis of the single GFP-C10H-Ras trajectories based on the 2PEFM imaging

In the final part of this study, we wanted to utilize the strongly reduced photobleaching (as demonstrated in Fig. 2) to reconstruct and examine trajectories of GFP-C10H-Ras molecules from the slow-diffusing population. While the time until photobleaching of GFP or YFP molecules in SMM studies is generally in the order of milliseconds (Harms et al., 2001), the 2PEFM imaging allowed us to track the vast majority of GFP-C10H-Ras molecules for at least 15 frames with the 2PEFM integration time of 200 ms, i.e., for more than 3 seconds, which enabled us to study their dynamic behavior over a prolonged time and reconstruct their trajectories.

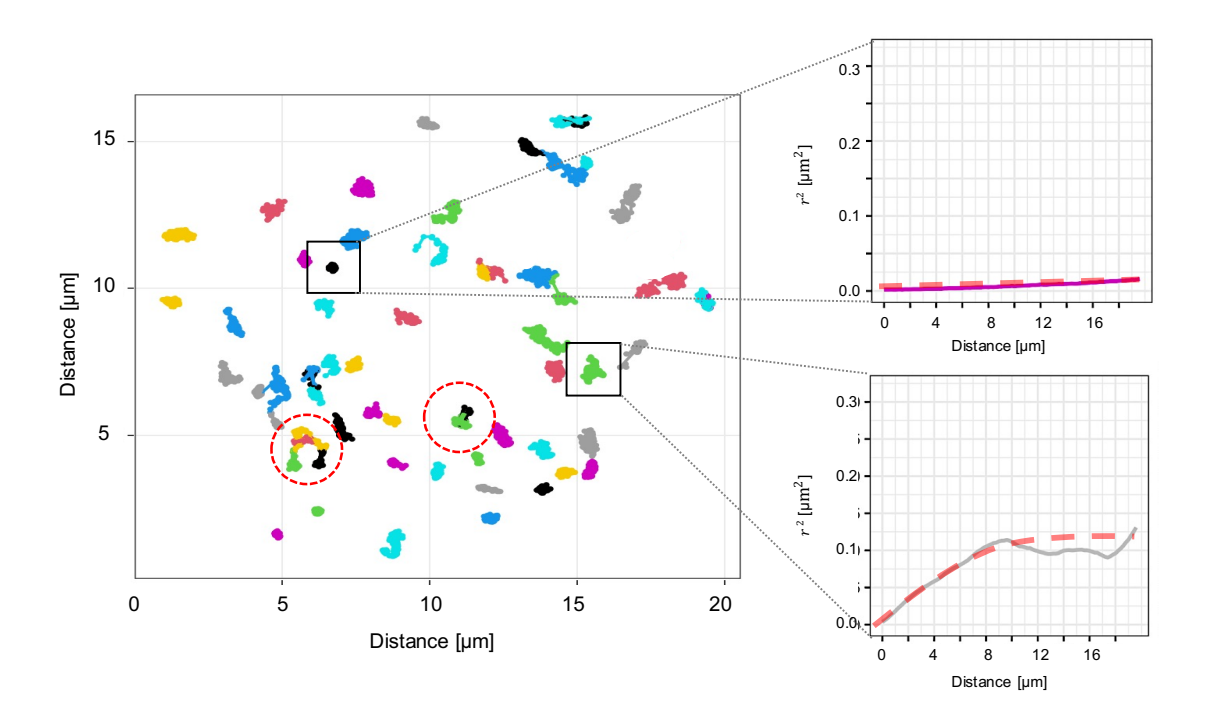


FIGURE 7: Reconstruction of H-Ras anchor molecular trajectories obtained through 2PEFM imaging.

A schematic depicting the process of selection of molecules used for a single GFP-C10H-Ras trajectory analysis. Many particles are distinguished during such an analysis, but not all of those are useful for trajectory reconstruction. Particles inside black square selections denote examples of an immobile molecule and a molecule exhibiting a confined diffusion. Immobile molecules were not used in the further analysis, as they did not diffuse throughout their fluorescence lifetime. Particles inside red circular selections crisscross with each other and, therefore, also cannot be used for further analysis, since it is impossible to reliably assign a single trajectory to particles diffusing in such a proximity.

First, we randomly selected five cells and mapped the trajectories of the GFP-C10H-Ras particles in these cells using the R software (Fig. 7 & 8A). The trajectories were selected based on a low molecular density in their proximity, so that any possibility of crisscrossing and incorrect trace attribution was eliminated. Due to practical lack of movement, the molecules from the immobile group were not included in this analysis. In each of the selected cells, we selected five trajectories, hence 25 in total, to investigate in more detail (Fig. 7).

The squared displacements of all 25 selected molecules were used to generate a plot presenting the mean squared displacement as a function of time, to demonstrate that this selection of molecules is representative of the entire molecular population detected, as shown in Fig. S2. The plotting of the confinement model fit the function of mean squared displacements over time revealed that the initial diffusion coefficient D_0 for this population equaled $0.243 \pm 0.057 \ \mu m^2 \ s^{-1}$, while its confinement area size L equaled $357 \pm 82 \ nm$, values that are similar to those obtained through the one-population model fitting (Fig. S1)

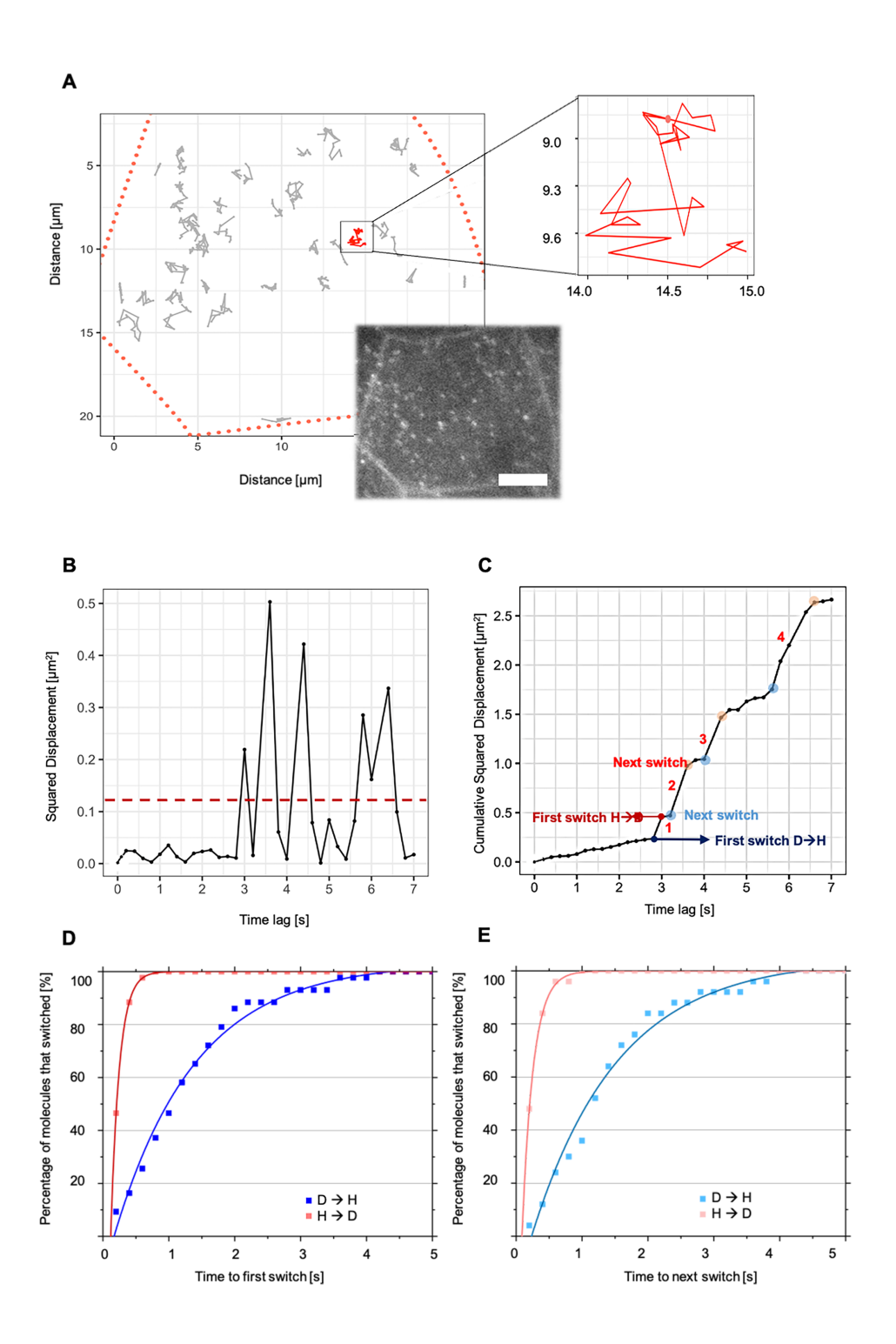


FIGURE 8: Analysis of single GFP-C10H-Ras molecular trajectories and their switches between different diffusion states. (A) Representative image of an epidermal cell selected for reconstruction of the GFP-C10H-Ras molecular trajectories, and its mapped picture designed in the R software. Red dotted line signifies the cell membrane, while isolated trajectories of single molecules are shown in grey. An example of molecular trajectories is highlighted in red. Right side: Enlarged map of a single GFP-C10H-Ras molecules highlighted red in (A). (B) Representative plot of the squared displacement versus time lag for the single GFP-C10H-Ras molecule selected in (A). Periods of short-lived, increased diffusion rates are visible. The threshold for differentiation between the diffusion and hopping states is drawn in dashed red. (C) A plot of the cumulative squared displacements versus time lag for the single GFP-C10H-Ras molecule selected in (A). Identical short-lived periods of increased diffusion rates are visible, each of them is numbered. Molecular switches of the single GFP-C10H-Ras molecule are indicated in blue, for a switch to a hopping state, and in red, for a switch to a diffusing state. The first switch to a hopping state (D \rightarrow H) is marked by blue squares, whereas the first switch to a diffusing state (H \rightarrow D) is marked by red squares. The following switch to a hopping state is marked by light blue squares, whereas the first following switch to a diffusing state is marked by light red squares. (D) Plot of the time needed for a single GFP-C10H-Ras molecule to switch for the first time to a diffusion and a hopping state. The Y-axis represents the percentage of molecules from a population of 25 selected H-Ras anchors that committed to their first switch. (E) Plot of the time needed for a single GFP-C10H-Ras molecule to switch to a diffusion and a hopping state following their first switch. The Y-axis represents the percentage of molecules from a population of 25 selected H-Ras anchors that committed to their switch.

Subsequently, for every one of these molecules, we plotted the squared displacement and the cumulative squared displacement over time (Fig. 8BC). What became apparent from these graphs was the fact that the diffusing GFP-C10H-Ras particles appear to switch between a diffusing state and a state that was characterized by brief bursts of increased diffusion, which may be referred to as hopping. To further analyze the alternating between these two states, we defined the diffusing state by a squared displacement between two consecutive frames smaller than 0.12 μ m² (i.e., $D_0 < 0.15 \mu$ m²/s), and the hopping state by a squared displacement larger than 0.12 μ m² (i.e., $D_0 > 0.15 \mu$ m²/s), based on the squared displacement versus time lag plots, (such as the one shown in Fig. 8, and more examples are presented in Figure S3). This analysis showed that the ratio of time spent in the diffusing versus the hopping state equaled 0.237, indicating that an average molecule spends about four times more time in the diffusing state than in the hopping state. Subsequently, we studied how rapidly a molecule switched between the diffusing and the hopping state, in order to determine the lifetimes of the two diffusion states. To this aim, we analyzed the time required for a molecule to switch from a diffusing to a hopping state and vice versa (Fig. 8D). It appeared that the

diffusing GFP-C10H-Ras molecules remained in this state for relatively long periods, as it took approximately 1.2 s before 50% of the selected molecules had switched to a hopping state. Inversely, it took only around 0.3 s for 50% of the molecules that were hopping to switch back to the diffusing state. On average, GFP-C10H-Ras molecules resided for 2.74 ± 0.32 s in the diffusing state before switching, and only 0.24 ± 0.08 s in the hopping state. Additionally, we also analyzed the time required for the selected group of molecules to switch again to a diffusing or a hopping state after having already switched their diffusion state at least once (Fig. 8E), and no significant differences with the analysis of the first switches were observed, as 50% of the selected diffusing molecules switched again to a hopping state after approximately 1.2 s, and it took around 0.25 s for 50% of the hopping molecules to switch back.

Taken together, in this study we focused on the slow-diffusing fraction of GFP-C10H-Ras molecules in the apical membranes of the epidermal cells in living zebrafish embryos, and show that this population of H-Ras membrane anchors occurs in two different dynamic states. The majority of the time it is found in a diffusing state, which is interrupted by brief periods of hopping. This finding indicates that the mobility pattern of this population of GFP-C10H-Ras molecules can be described as 'hop' diffusion through the plasma membrane.

3.3 DISCUSSION

In the present study, we have applied multifocal 2PEFM to detect individual GFP-C10H-Ras molecules in epidermal cells of living zebrafish embryos. In previous studies using TIRF microscopy, we detected a fast and a slow-diffusing fraction of H-Ras molecules, whereas in this study we exclusively observed the slow-diffusing population of molecules (Gora et al., 2021; Schaaf et al., 2009). This population of GFP-C10H-Ras molecules was found to occur in clusters within the plasma membrane, and to alternate between two diffusion modes, leading to a mobility pattern that can be described as hop diffusion.

In previous SMM studies on the mobility of H-Ras in zebrafish embryos and cultured cells, it was shown that there are two main subpopulations of fluorescently labelled H-Ras or C10H-Ras molecules in the plasma membrane: one that is diffusing at a fast rate

and one that is diffusing at a slow rate (Gora et al., 2021; Lommerse et al., 2004; Schaaf et al., 2009). The fast subpopulation of H-Ras molecules shows confinement to a domain of 400-500 nm and is suggested to form nanoclusters that are located in small (< 15 nm) lipid rafts (Plowman et al., 2005; Prior et al., 2001; Prior et al., 2003). These rafts are considered to be dependent on the presence of cholesterol, since their mobility is altered by LatB or MBCD treatment (Garcia-Parajo et al., 2014; Lingwood and Simons, 2010; Nickels et al., 2015; Zhou and Hancock, 2015). The wild type H-Ras protein shows a similar fastdiffusing subpopulation. However, a constitutively active mutant of H-Ras displays a fast-diffusing subpopulation that is confined to a larger domain (~600 nm) and its mobility is not affected by LatB or MBCD treatment. These data indicate that upon activation of H-Ras its affinity for specific plasma membrane microdomains with different lipid compositions is altered (Hancock and Parton, 2005; Plowman et al., 2005; Prior et al., 2001; Prior et al., 2003; Zhou et al., 2018). In addition, activated GTP-loaded H-Ras molecules have an increased probability to form clusters that are transiently (< 1 s) immobilized (Murakoshi et al., 2004). These clusters are cholesterol-independent, i.e., their mobility is not affected by LatB or MBCD treatment, and are considered to be the sites where I the H-Ras interacts with cytoplasmic proteins such as Galectin-1 and Sur-8, and where active signaling occurs (Belanis et al., 2008; Hancock and Parton, 2005; Herrero et al., 2016; Li et al., 2000; Shalom-Feuerstein et al., 2008; Zhou et al., 2018).

To determine which previously observed H-Ras populations were represented by the molecules observed using the multifocal 2PEFM setup, we compared their dynamic behavior with that of GFP-C10H-Ras molecules found in previous studies. We observed that the mobility of the molecules detected in the 2PEFM data corresponded most closely to the slow-diffusing fraction observed in the previous studies (Gora et al., 2021; Lommerse et al., 2004; Schaaf et al., 2009). We detected the slow-diffusing population of GFP-C10H-Ras proteins, which was previously shown to be not affected by LatB and MBCD treatment (Gora et al., 2021). Indeed, these treatments did not significantly change the mobility pattern of the detected particles. Thus, based on its dynamic behavior and the insensitivity of this behavior to LatB and MBCD treatment, we conclude that the population of GFP-C10H-Ras molecules observed in our 2PEFM study represents the slow-diffusing fraction of molecules that were observed in previous studies. The main reason for the lack of detection of the fast subpopulation of GFP-C10H-Ras molecules was shown to be the relatively large integration time used in the 2PEFM

experiments (200 ms). During this relatively long illumination and detection periods, the signal of the fast-diffusing molecules is spread over the relatively large area in which they move during this integration time, causing a phenomenon called motion blur (Phillips et al., 2020; Travers et al., 2020). Our study, therefore, focuses on the mobility pattern of the slow-diffusing population of GFP-C10H-Ras molecules, which we have been able to investigate in great detail.

Based on the analyzed mobility patterns of GFP-C10H-Ras over short periods (< 1s), the molecules of the slow-diffusing population detected in the present study could, in turn, be subdivided into two fractions: a slow-diffusing population that shows confinement of 253 ± 3 nm, and one that is virtually immobile, with a confinement zone of 94 ± 5 nm. Including the fast-diffusing population of molecules that is undetectable in 2PEFM, this implies that there are three fractions of GFP-C10H-Ras molecules based on their dynamic behavior: a fast- and a slow-diffusing and an immobile population. This was confirmed when we fitted our TIRFM data (obtained with a time lag of 25 ms) to a threepopulation model. However, we also showed that this bulk analysis over such a short time by plotting mean squared displacements over time does not reveal the complexity of the single-molecule mobility patterns. Interestingly, our multifocal 2PEFM approach allowed us to follow the single particles for relatively long periods, which enabled us to analyze molecular trajectories of single GFP-C10H-Ras particles in the slow-diffusing population. Using this analysis, we identified two different dynamic states in which the slow-diffusing molecules occur: a state of diffusion and a state of hopping. The immobile fraction has not been included in the analysis, as the particles in this subpopulation hardly ever diffused, which is reflected by their initial diffusion coefficient of (0.080 ± 0.010) $\cdot 10^{-2} \mu m^2 s^{-1}$.

By examining the switching of the H-Ras anchor between the two different states, we demonstrated that these anchors spend a relatively long time in the diffusion state, since the total time spent in this state was approximately four times longer than the time spent in the hopping state. Based on these findings we concluded that the observed slow-diffusing population of H-Ras anchors exhibit anomalous diffusion patterns, characterized by short-lived bursts of fast-speed diffusion, generally referred to as molecular hopping. It has been reported that many signaling proteins experience two-dimensional hop diffusion on the membrane due to the complex and packed structure

of the plasma membrane (Campagnola et al., 2015; Umemura et al., 2008; Yasui et al., 2014). The plasma membrane is divided into microdomains by the actin-based membrane skeleton, which is closely associated with the cytoplasmic surface of the plasma membrane (Morone et al., 2008). Many transmembrane proteins collide with this membrane skeleton, which induces temporary confinement of the transmembrane proteins in the membrane-skeleton meshwork. Moreover, in the vicinity of immobilized molecules located in the membrane, the movement of any other particles is extremely limited, also because of the hydrodynamic dragging effects of the transmembrane proteins, which further suppress the available membrane space (Murase et al., 2004). In addition, it has been proved that interactions with many cytoplasmic proteins, such as Galectin-1 and Sur-8, are involved in the immobilization of the H-Ras clusters, which are considered to be the sites where active signaling occurs (Belanis et al., 2008; Hancock and Parton, 2005; Herrero et al., 2016; Li et al., 2000; Shalom-Feuerstein et al., 2008; Zhou et al., 2018). With all these obstacles, membrane proteins and lipids often hop from one microdomain to an adjacent one, especially when thermal fluctuations of the membrane and the actin meshwork associated with it create sufficient space between them to enable the passage of integral membrane proteins, or when an actin filament is temporarily severed (Suzuki et al., 2005).

Such a temporary nature of protein-membrane interactions enables a tight temporal regulation of signal transduction processes. It has also been proposed that molecular hopping might be critical in the search for target molecules in eukaryotic cells. A straightforward consequence of membrane hopping is that a molecule remains in its immediate vicinity for a short time and then jumps to a location that is further away than expected from two-dimensional diffusion. In such a way, the search process is allowed to explore larger areas and what allows proteins to bypass diffusion barriers that may be present in the membrane (Lemmon, 2008). As this process seems to be governed predominantly by membrane-protein associations, including electrostatic interactions, it is highly possible that the H-Ras anchor, being the domain that is responsible for attachment of the H-Ras protein to the cell phospholipid membrane, undergoes this type of anomalous diffusion.

The multifocal 2PEFM technology we used in this study induced strongly reduced photobleaching of GFP molecules compared to conventional, one photon excitation-based

SMM technologies, which enabled us to visualize the diffusing proteins for prolonged periods. There may be three reasons for this reduced photobleaching. First, the multifocal 2PEFM setup used, combined with a low-noise sCMOS camera allowed for a low excitation power, being typically of 1.4 mW per focus while maintaining a relatively high signal-to-noise ratio (SNR > 10). This gentle illumination must have contributed to the low bleaching rate of GFP, since this bleaching rate in 2PEFM has been shown to be highly dependent on the laser power, even more than in one-photon excitation. The log-log plot of the excitation power versus the photobleaching rate for one-photon excitation of fluorescein increased with a slope of ~1, whereas this slope was ~3 for twophoton excitation (Graham et al., 2015; Patterson and Piston, 2000). Second, since previous research has indicated that the faster photobleaching processes occur at a fluorophore's higher energetic states, the high fluorophore stability of the GFP molecules that we report may suggest that photobleaching is reduced because fluorophores are excited to their lowest excited energy state (Dittrich and Schwille, 2001; Patterson and Piston, 2000). Third, the high photostability of GFP in our 2PEFM setup might have also been the result of the pulsed excitation mode, due to the use of a pulsed laser combined with multifocal excitation. Many fluorescent molecules end up in a relatively long-lived dark state after excitation, and in this dark state the fluorescent molecules experience a highly increased chance to undergo an irreversible photobleaching reaction. By a rapid and pulsed illumination, the fluorophores residing in their dark (triplet) state have sufficient time between subsequent illuminations to undergo relaxation back to their ground (singlet) state, leading to the overall increase in photostability and fluorescent signal yield (Donnert et al., 2007; Donnert et al., 2009). On top of the fluorophore stability, non-fluorescent absorption is known to cause damage to biological tissues, and the 2PEFM technology with low phototoxicity is, therefore, highly suitable for studies in in vivo systems such as zebrafish embryos (Eggeling et al., 1998; Niesner et al., 2007).

Finally, we studied the nature of the slow-diffusing population of GFP-C10H-Ras particles by determining the intensity of the fluorescence intensity peaks and their photobleaching profile over time. It became apparent that the molecules occur in clusters, since we detected individual fluorescent molecules as well as signals that could be attributed to multiple GFP-C10HRas proteins. It has previously been shown that C10H-Ras, as well as the full-width H-Ras, often reside in small clusters with a radius varying from 40 to 180 nm (Zhou and Hancock, 2021). Moreover, it has been reported that C10H-Ras

localizes to and clusters in cholesterol-rich lipid rafts, however, upon their disruption, disperses over the surface of the plasma membrane, rather than driving associations with other membrane microdomains. These findings are consistent with our data and support a biodynamic model where full-length H-Ras has an affinity for at least two plasma membrane microdomains, lipid rafts and a cholesterol-independent non-raft microdomain, and is in constant equilibrium between them (Murakoshi et al., 2004; Prior et al., 2003).

In conclusion, in the present study, we showed that 2PEFM is a powerful microscopy technique for imaging single molecules *in vivo*. With this technique, we could detect the slow-diffusing population of GFP-C10H-Ras in the membranes of epidermal cells in living zebrafish embryos. We revealed that this population occurs in clusters and displays hop diffusion through the membrane, in which periods of a slow diffusion are interspersed with brief periods of molecular hopping.

3.4 MATERIALS AND METHODS

Zebrafish. Zebrafish larvae (*Danio rerio*) from the transgenic line $Tg(bactin: GFP-C10H-Ras)^{vu119}$ were maintained according to standard protocols (http://ZFIN.org), and exposed to a 14h light and 10h dark diurnal cycle at 28°C. Fertilization was performed by natural spawning at the beginning of the light period. Eggs were collected and raised in egg water (60 µg/ml Instant Ocean Sea salts, Cincinnati, OH, USA) at 28°C. The eggs developed in an incubator at 28°C until 2 days post-fertilization (2 dpf). The viability and development of the eggs were checked daily using fluorescence stereo- or confocal microscopy. All experiments performed on living zebrafish embryos were done in compliance with the directives of the local animal welfare committee of Leiden University.

Fluorescence stereomicroscopy. To screen zebrafish embryos for optimal expression levels of the GFP-C10H-Ras, a Leica M205FA fluorescence stereomicroscope (Leica Microsystems) was used. Images of the zebrafish embryos were taken using a Leica DFC 345FX camera.

Treatment of zebrafish embryos with Latrunculin B (LatB) and Methyl- β -cyclodextrin (MBCD). Inhibition of actin polymerization with LatB was induced using a protocol

described previously (Kugler et al., 2019). LatB (Sigma-Aldrich, St. Louis, MO, USA) was dissolved in 96% ethanol to a 500 μ M stock concentration. At 48 hpf, dechorionated embryos were treated with 100 nM LatB in egg water for 1 hour. A control group was treated with a diluted vehicle (0.02% ethanol in egg water). Treatment with MBCD was based on protocols described before (Bello-Perez et al., 2020; Silva et al., 2019). MBCD (Sigma-Aldrich, St. Louis, MO, USA) was dissolved in PBS (pH 7.4) to a stock concentration of 400 nM. At 48 hpf, dechorionated embryos were treated with MBCD at a final concentration of 40 nM in egg water for 1 hour, A control group was treated with diluted vehicle (10x diluted PBS in egg water). After the LatB or MBCD treatment, zebrafish were immediately transferred and imaged under the 2PEFM setup.

Sample preparation and mounting. Glass coverslips were washed with 99% ethanol (twice), HPLC-grade water (twice), KOH (1M, twice), and acetone (99%, thrice). Each wash was followed by a 30-minute-long sonication period at 50°C. The coverslips were then stored in 99% acetone. Prior to the mounting of the zebrafish embryos, the glass coverslips were coated with 50 µg ml⁻¹ of poly-L-lysine (Sigma-Aldrich, St. Louis, MO, USA) for 5 minutes, followed by a double wash with deionized water and drying with nitrogen gas. Two-day-old zebrafish embryos were equilibrated at room temperature for an hour, anaesthetized with 0.02% aminobenzoic acid ethyl ester (tricaine, Sigma-Aldrich St. Louis, MO, USA), and dechorionated using tweezers. Subsequently, a single zebrafish embryo was placed on a coverslip with a lateral side against the surface, while excess water was aspirated. The tail of the embryo was pressed against the coverslip by a thin agarose sheet (2%, thickness 0.75 mm). A drop of egg water was added to cover the rest of the embryo's body. The coverslip with the embryo was placed into the microscope holder, which was then inserted into the imaging chamber.

Two-Photon Excitation Fluorescence Microscopy (2PEFM). For 2PEFM, a tunable near-IR Ti: Sa laser (Chameleon Ultra; Coherent, Santa Clara, CA, USA) was coupled into a home-built two-photon multifocal microscope. A diffractive optical element (HOLOEYE Photonics AG, Berlin, Germany) diffracted the laser beam into an array of 10 x 10 beam-lets. A fast-scanning mirror (FSM-300-1; Newport, Irvine, CA, USA) scanned the beamlets across the excitation plane. The laser beams were focused using a 60x oil immersion objective (CF160 Apochromat TIRF 60XC, NA 1.49; Nikon, Tokyo, Japan) mounted on a piezo-stage (P-726 PIFOC; Physik Instrumente, Karlsruhe, Germany), illuminating an

area of 40 µm x 40 µm. Two-photon luminescence was collected by the same objective, filtered with a dichroic mirror (700dcxr; Semrock, Rochester, NY, USA) and two shortpass filters (FF01-720-SP and FF01-750-SP; Semrock), and focused on a 2048 x 2048 pixel back-illuminated sCMOS camera (Prime BSI; Teledyne Photometrics, Tucson, AZ, USA). Additional band-pass filters, mounted on a motorized fast-change filter wheel (FW103H/M: Thorlabs, Newton, NJ, USA), were positioned in front of the camera. Using custom-made LabVIEW software (National Instruments, Austin, TX, USA), the scanning mirror, focusing stepper motors and camera were controlled synchronously. For spiral scanning, the fast-scanning mirror (FSM-300-1, Newport) was driven by an Archimedean spiral to rapidly scan the beams producing a homogeneously illuminated wide-field. A single period of the spiral scan took 200 ms and was synchronized with the camera integration time, resulting in the temporal resolution of 200 ms. The excitation laser power at the sample surface equaled 0.1497 mW at the beginning of a time-lapse, and decreased to 0.1425 mW at the end of the recording. Every embryo was imaged for at least 2 minutes, which equaled a minimum of 600 frames in a single time-lapse. All 2PEFM measurements were performed at room temperature.

Total internal reflection fluorescence microscopy (TIRFM). For TIRFM, a custom-made microscope was used with a 100x oil-immersion objective (NA 1.45, Nikon, Tokyo, Japan). Excitation was performed using a 515 nm laser (iChrome MLE, Toptica Photonics, Germany), the field of view was set to a 100 x 100 pixels region with a pixel size of 166 nm, and the laser power equaled 20% of the maximal laser power (40 mW). The incident laser beam was set at the critical angle against the coverslip-water interface, thus being totally reflected and creating the evanescent wave for excitation of fluorophores close to the coverslip-sample interface. Emission light was filtered using a long-pass filter (ET5701p, Chroma Technology, VT, USA), and image sequences were collected using an on-chip multiplication gain CCD camera (model 512B, Cascade, Roper Scientific, Tucson, AZ, USA). Each image sequence contained 1200 frames separated by a 25 or 200 ms time lag, resulting in a total acquisition time of 30 and 240 seconds, respectively. All TIRFM measurements were performed at room temperature.

Analysis of protein diffusion patterns. Fluorescence intensity signals corresponding to GFP molecules were fitted to a two-dimensional Gaussian surface, using a custom-developed software (Groeneweg et al., 2014; Harms et al., 2001; Lommerse et al., 2004;

Lommerse et al., 2005; Schütz et al., 1997a). The software, in the form of a code written in the MATLAB programming environment (The MathWorks, Natick, MA, USA), can be obtained by directly contacting Thomas Schmidt (Leiden Institute of Physics, Leiden University). The location of a particle was defined as the position of the maximum of the Gaussian curve. The Gaussian curve fitting provided information on the intensity and full width at half maximum (FWHM) for the localized GFP peaks, which allowed for plotting the intensity distributions of the GFP peaks for each frame in a time-lapse. The positional accuracy dx of the peak localization equaled approximately 28 nm (Groeneweg et al., 2014; Schütz et al., 1997).

To identify subpopulations of molecules, their diffusion coefficients, and the sizes of their confinement area, the Particle Image Correlation Spectroscopy (PICS) software was used to analyze distributions of squared displacements for individual time lags. The PICS software, a code written in the MATLAB programming environment (The Math-Works, Natick, MA, USA), has previously been described and validated (Semrau and Schmidt, 2007), and can be obtained can by directly contacting Thomas Schmidt or Stefan Semrau (Leiden Institute of Physics, Leiden University). In PICS analysis, individual particles are not tracked, but correlations between the location of molecules in consecutive frames are determined. A multistep analysis was performed for each image sequence acquired, yielding information for five different time lags of 200, 400, 600, 800, and 1000 ms. This way, cumulative probability distributions of the squared displacements were generated for each time lag and fitted to one-, two- or three-population models. The one-population model is described by the equation:

$$P(r^2, t_{lag}) = 1 - exp\left(-\frac{r^2}{r_0^2(t_{lag})}\right)$$
 (1)

which describes the probability that a particle exhibiting Brownian motion at the arbitrary origin is found within a circle of a radius r at the time lag t_{lag} , and its mean square displacement equals $r_0^2(t_{lag}) = 4Dt_{lag}$. However, when a two-population model is used, Equation 1 is transformed into Equation 2:

$$P(r^2, t_{lag}) = 1 - \left[\alpha \cdot exp\left(-\frac{r^2}{r_1^2(t_{lag})}\right) + (1 - \alpha) \cdot exp\left(-\frac{r^2}{r_2^2(t_{lag})}\right)\right]$$
(2)

and, when a three-population model is used, into Equation 3:

$$P(r^{2}, t_{lag}) = 1 - \left[\alpha_{1} \cdot exp\left(\frac{r^{2}}{r_{1}^{2}(t_{lag})}\right) + \alpha_{2} \cdot exp\left(\frac{r^{2}}{r_{2}^{2}(t_{lag})}\right) + (1 - \alpha_{1} - \alpha_{2}) \cdot exp\left(\frac{r^{2}}{r_{3}^{2}(t_{lag})}\right)\right] (3)$$

where the mean squared displacements of the populations are denoted by r_i^2 , and their relative sizes by $\alpha_{(i)}$ (Lommerse et al., 2004; Schaaf et al., 2009). In the two-population model, the fraction size α represents a percentage of the fast-diffusing H-Ras anchor molecules in the total population. The mean squared displacements of the fast- and slow-diffusing fractions in this model are denoted by r_1^2 and r_2^2 , respectively. The three-population model accounts for an additional fraction, denoted as $1-(\alpha_1+\alpha_2)$, and is characterized by the mean squared displacement, r_3^2 .

To examine whether any of these populations confine to specific areas, the values of r_1^2 and r_2^2 , were plotted against the time lag (using OriginLab software, OriginLab Corporation, MA, USA). The positional accuracy dx led to a constant offset in r^2 of $4 \cdot (dx)^2$, which, in our case, equaled 0.0031 μ m². The plots were fitted either to a free Brownian diffusion model, with a diffusion coefficient D determined by the equation

$$r_i^2(t_{lag}) = 4 \cdot D \cdot t_{lag} (4)$$

or to a confined diffusion model described by the equation:

$$r_i^2(t_{lag}) = \frac{L^2}{3} \cdot \left[1 - exp\left(-\frac{12 \cdot D_0 \cdot t_{lag}}{L^2} \right) \right]$$
(5)

in which the molecules move freely with an initial diffusion coefficient D_0 , but are confined to an area with impermeable barriers, described by a square of a side length L.

Analysis of photobleaching. Using an ImageJ plug-in, TrackMate (Tinevez et al., 2017), every fluorescence intensity peak, identified by the Gaussian fitting described above, was followed over time. Throughout this tracing, the threshold on the particle diffusion rate was set to 1.10 $\pm\,0.15~\mu m^2/s$, based on previous data on the H-Ras anchor mobility

rates obtained in living zebrafish embryos (Gora et al., 2021). In every frame, the particle was attributed to a circular area with a radius of 5 pixels. For each particle, the intensity was measured, frame-by-frame, by determining the maximal pixel intensity found within the circular selection. The intensities of molecules with differing initial intensities were plotted against time to study the step-wise decrease in fluorescence intensity as a result of photobleaching. The mean intensity values of all particles identified within a frame and the background intensity were determined as well (based on a sample of five zebrafish cells, each one imaged on a different experimental day). Upon loss of the signal (i.e., when the intensity was similar to the value of the background signal), the area of 3 x 3 μ m that surrounded the last position of a particle was followed for the next 20 frames to determine if this loss was irreversible.

Analysis of GFP-C10H-Ras trajectories. The trajectories of GFP-C10H-Ras particles in the zebrafish epidermal cells were analyzed using the ImageJ plug-in TrackMate and the R Project software (The R Foundation, Vienna, Austria). To eliminate the impact of criss-crossing among particles, traces present in high-density areas were excluded. In addition, immobile particles were excluded. For the included traces, squared displacements and cumulative squared displacements were plotted versus the time lag for each step traversed by a particle until its photobleaching (OriginLab, OriginLab Corporation, MA, USA). Switches between two distinct diffusion states exhibited by the particle were then identified based on a threshold value for the squared displacement between the two consecutive frames. Following that, the lifetime of a particle in either of the two diffusing states was analyzed by generating a distribution plot of the time lengths until the first switch. Additionally, to examine whether the first diffusion switch of a molecule induced a more sustained mobility change, a similar plot was generated for all subsequent switching events as well.

Experimental design. Five independent experiments, performed on five different days, were conducted for the transgenic zebrafish line expressing the GFP-C10H-Ras construct. In every experiment, five different zebrafish embryos were selected for the 2PEFM imaging. In each of the selected embryos, at least six separate areas within the zebrafish tailfin were imaged one time, with each time lapse comprising at least 50 consecutive frames (Fig. 2). To study the influence of zebrafish treatment with LatB and MBCD on the GFP-C10H-Ras dynamics, a similar design was implemented, with five

individual embryos used per vehicle, LatB, and MBCD treatment groups, each imaged on three different experimental days (Fig. 6). Trajectories of isolated particles, localized in the cell areas not affected by crisscrossing were reconstructed in five randomly selected zebrafish cells, each one imaged on a different experimental day. Ultimately, 25 trajectories, five per every zebrafish cell, were selected to examine the switching between different diffusion states (Fig. 8).

To compare 2PEFM with the TIRFM techniques, three independent TIRFM experiments on three individual days were performed, in which five zebrafish embryos per group were used, and six independent areas per embryo were imaged, with a time lag of 25 and 200 ms. Every area was imaged once with each time lapse comprising at least 50 consecutive frames (Fig. 4). Subsequently, to investigate the impact of the excitation laser power on the single-particle dynamics in the TIRFM setup, three independent experiments on three individual days were done, with six independent areas in each of the five zebrafish embryos imaged. The experimental groups were exposed to 50%, 30%, and 10% of the maximal excitation laser power, and a time lag of 200 ms. Following that, 30 particles per fast- and slow-diffusing fractions in all of the experimental groups were selected to test a potential correlation between their intensity count and squared displacement values (Fig. 5). The selection of the particles was performed in TrackMate based on their squared displacement values. The threshold of the mean squared displacement values used for differentiating between the two fractions was set to 0.01 μ m², hence every molecule above this value was assigned to the fast-diffusing subpopulation, whereas every molecule below to the slow-diffusing subpopulation.

Statistical Analysis. Values of the different population sizes and their squared displacements were averaged per experimental day, and their standard errors of the mean (s.e.m.) were calculated. Statistical analysis of these data was performed for the experimental time lag of 200 ms by comparing: (a) results obtained for the transgenic embryos expressing GFP-C10H-Ras, with and without LatB or MBCD treatment; (b) results obtained for transgenic embryos expressing GFP-C10H-Ras imaged using the 2PEFM with the time lag of 200 ms and the TIRFM with the time lags of 25 and 200 ms; (c) results obtained for the transgenic embryos expressing GFP-C10H-Ras, imaged under the TIRFM with 50%, 30%, and 10% of the total excitation laser power. Initial diffusion coefficients and confinement area sizes were obtained by averaging values of mean

square displacements per time lag, plotting them against time and fitting a confined diffusion model yielding these parameters. This was done for each treatment, microscopy technique, and the percentage of the TIRFM total excitation laser power. In each case, a Shapiro-Wilk statistical test was performed to check if data were normally distributed. The significance of the results was analyzed using a Student's t-test for a comparison of means between two, normally distributed, groups. In case multiple groups were compared, a one-way ANOVA was used with a Tukey range test for post hoc analysis.

COMPETING INTERESTS

The authors declare no competing financial interests.

FUNDING

R.J.G. was funded by Marie Sklodowska-Curie ITN project 'ImageInLife' (Grant Agreement No. 721537)

AUTHOR CONTRIBUTIONS

Conceptualization: M.J.M.S.; Methodology: R.J.G., R.V, M.J.M.S.; Software: R.J.G., R.V., J.N.; Validation: R.J.G., R.V., S.J., M.J.M.S.; Formal analysis: R.J.G., R.V., S.J.; Investigation: R.J.G., R.V., S.J.; Resources: J.N., M.J.M.S.; Data curation: R.J.G., S.J., J.N., M.J.M.S.; Writing - original draft: R.J.G., M.J.M.S.; Writing - review & editing: R.J.G., J.N., M.J.M.S.; Supervision: J.N., M.J.M.S.; Project administration: M.J.M.S.; Funding acquisition: M.J.M.S.

REFERENCES

- **Axelrod, D.** (2001). Total internal reflection fluorescence microscopy in cell biology. *Traffic Cph. Den.* **2**, 764–774.
- Belanis, L., Plowman, S. J., Rotblat, B., Hancock, J. F. and Kloog, Y. (2008). Galectin-1 is a novel structural component and a major regulator of h-ras nanoclusters. *Mol. Biol. Cell* 19, 1404–1414.
- Bello-Perez, M., Pereiro, P., Coll, J., Novoa, B., Perez, L. and Falco, A. (2020). Zebrafish C-reactive protein isoforms inhibit SVCV replication by blocking autophagy through interactions with cell membrane cholesterol. *Sci. Rep.* **10**, 566.
- Bernardello, M., Gora, R. J., Van Hage, P., Castro-Olvera, G., Gualda, E. J., Schaaf, M. J. M. and Loza-Alvarez, P. (2021). Analysis of intracellular protein dynamics in living zebrafish embryos using light-sheet fluorescence single-molecule microscopy. *Biomed. Opt. Express* 12, 6205–6227.
- **Bobroff, N.** (1986). Position measurement with a resolution and noise-limited instrument. *Rev. Sci. Instrum.* **57**, 1152–1157.
- Campagnola, G., Nepal, K., Schroder, B. W., Peersen, O. B. and Krapf, D. (2015). Superdiffusive motion of membrane-targeting C2 domains. *Sci. Rep.* **5**, 17721.
- Chen, J., Zhang, Z., Li, L., Chen, B.-C., Revyakin, A., Hajj, B., Legant, W., Dahan, M., Lionnet, T., Betzig, E., et al. (2014). Single-molecule dynamics of enhanceosome assembly in embryonic stem cells. *Cell* 156, 1274–1285.
- Chudakov, D. M., Matz, M. V., Lukyanov, S. and Lukyanov, K. A. (2010). Fluorescent Proteins and Their Applications in Imaging Living Cells and Tissues. *Physiol. Rev.* **90**, 1103–1163.
- **Dittrich, P. S. and Schwille, P.** (2001). Photobleaching and stabilization of. fluorophores used for single-molecule analysis. with one- and two-photon excitation. *Appl. Phys. B* **73**, 829–837.
- **Donnert, G., Eggeling, C. and Hell, S. W.** (2007). Major signal increase in fluorescence microscopy through dark-state relaxation. *Nat. Methods* **4**, 81–86.
- **Donnert, G., Eggeling, C. and Hell, S. W.** (2009). Triplet-relaxation microscopy with bunched pulsed excitation. *Photochem. Photobiol. Sci. Off. J. Eur. Photochem. Assoc. Eur. Soc. Photobiol.* **8**, 481–485

- 3. MULTIFOCAL TWO-PHOTON EXCITATION FLUORESCENCE MICROSCOPY REVEALS HOP DIFFUSION
 OF H-RAS MEMBRANE ANCHORS IN EPIDERMAL CELLS OF ZEBRAFISH EMBRYOS
- Eggeling, C., Widengren, J., Rigler, R. and Seidel, C. A. (1998). Photobleaching of Fluorescent Dyes under Conditions Used for Single-Molecule Detection: Evidence of Two-Step Photolysis. *Anal. Chem.* **70**, 2651–2659.
- Fujiwara, T., Ritchie, K., Murakoshi, H., Jacobson, K. and Kusumi, A. (2002). Phospholipids undergo hop diffusion in compartmentalized cell membrane. *J. Cell Biol.* **157**, 1071–1081.
- Garcia-Parajo, M. F., Cambi, A., Torreno-Pina, J. A., Thompson, N. and Jacobson, K. (2014). Nanoclustering as a dominant feature of plasma membrane organization. *J. Cell Sci.* 127, 4995–5005.
- Gebhardt, J. C. M., Suter, D. M., Roy, R., Zhao, Z. W., Chapman, A. R., Basu, S., Maniatis, T. and Xie, X. S. (2013). Single-molecule imaging of transcription factor binding to DNA in live mammalian cells. Nat. Methods 10, 421–426.
- Gora, R. J., de Jong, B., van Hage, P., Rhiemus, M. A., van Steenis, F., van Noort, J., Schmidt, T. and Schaaf, M. J. M. (2021). Analysis of the H-Ras mobility pattern in vivo shows cellular heterogeneity inside epidermal tissue. *Dis. Model. Mech.* dmm.049099.
- Gore, A. V., Pillay, L. M., Galanternik, M. V. and Weinstein, B. M. (2018). The zebrafish: A fintastic model for hematopoietic development and disease. *WIREs Dev. Biol.* **7**, e312.
- **Graham, D. J. L., Tseng, S.-F., Hsieh, J.-T., Chen, D. J. and Alexandrakis, G.** (2015). Dependence of Two-Photon eGFP Bleaching on Femtosecond Pulse Spectral Amplitude and Phase. *J. Fluoresc.* **25**, 1775–1785.
- Groeneweg, F. L., Royen, M. E. van, Fenz, S., Keizer, V. I. P., Geverts, B., Prins, J., Kloet, E. R. de, Houtsmuller, A. B., Schmidt, T. S. and Schaaf, M. J. M. (2014). Quantitation of Glucocorticoid Receptor DNA-Binding Dynamics by Single-Molecule Microscopy and FRAP. *PLOS ONE* **9**, e90532.
- Ha, T., Ting, A. Y., Liang, J., Caldwell, W. B., Deniz, A. A., Chemla, D. S., Schultz, P. G. and Weiss, S. (1999).
 Single-molecule fluorescence spectroscopy of enzyme conformational dynamics and cleavage mechanism. Proc. Natl. Acad. Sci. U. S. A. 96, 893–898.
- Hancock, J. F. and Parton, R. G. (2005). Ras plasma membrane signaling platforms. Biochem. J. 389, 1-11.
- Harms, G. S., Cognet, L., Lommerse, P. H. M., Blab, G. A. and Schmidt, T. (2001). Autofluorescent Proteins in Single-Molecule Research: Applications to Live Cell Imaging Microscopy. *Biophys. J.* 80, 2396–2408.
- **Herrero, A., Matallanas, D. and Kolch, W.** (2016). The spatiotemporal regulation of RAS signaling. *Biochem. Soc. Trans.* **44**, 1517–1522.

- Keizer, V. I. P., Coppola, S., Houtsmuller, A. B., Geverts, B., van Royen, M. E., Schmidt, T. and Schaaf, M. J. M. (2019). Repetitive switching between DNA-binding modes enables target finding by the glucocorticoid receptor. J. Cell Sci. 132, jcs217455.
- Kugler, E. C., van Lessen, M., Daetwyler, S., Chhabria, K., Savage, A. M., Silva, V., Plant, K., MacDonald, R. B., Huisken, J., Wilkinson, R. N., et al. (2019). Cerebrovascular endothelial cells form transient Notch-dependent cystic structures in zebrafish. EMBO Rep. 20, e47047.
- **Kusumi, A., Sako, Y. and Yamamoto, M.** (1993). Confined lateral diffusion of membrane receptors as studied by single particle tracking (nanovid microscopy). Effects of calcium-induced differentiation in cultured epithelial cells. *Biophys. J.* **65**, 2021–2040.
- Kusumi, A., Fujiwara, T. K., Chadda, R., Xie, M., Tsunoyama, T. A., Kalay, Z., Kasai, R. S. and Suzuki, K. G. N. (2012). Dynamic Organizing Principles of the Plasma Membrane that Regulate Signal Transduction: Commemorating the Fortieth Anniversary of Singer and Nicolson's Fluid-Mosaic Model. *Annu. Rev. Cell Dev. Biol.* 28, 215–250.
- Kwik, J., Boyle, S., Fooksman, D., Margolis, L., Sheetz, M. P. and Edidin, M. (2003). Membrane cholesterol, lateral mobility, and the phosphatidylinositol 4,5-bisphosphate-dependent organization of cell actin. *Proc. Natl. Acad. Sci. U. S. A.* 100, 13964–13969.
- **Lemmon, M. A.** (2008). Membrane recognition by phospholipid-binding domains. *Nat. Rev. Mol. Cell Biol.* **9**, 99–111.
- **Li, H. and Vaughan, J. C.** (2018). Switchable Fluorophores for Single-Molecule Localization Microscopy. *Chem. Rev.* **118**, 9412–9454.
- **Li, W., Han, M. and Guan, K. L.** (2000). The leucine-rich repeat protein SUR-8 enhances MAP kinase activation and forms a complex with Ras and Raf. *Genes Dev.* **14**, 895–900.
- **Lingwood, D. and Simons, K.** (2010). Lipid Rafts As a Membrane-Organizing Principle. *Science* **327**, 46–50.
- Lommerse, P. H. M., Blab, G. A., Cognet, L., Harms, G. S., Snaar-Jagalska, B. E., Spaink, H. P. and Schmidt, T. (2004). Single-Molecule Imaging of the H-Ras Membrane-Anchor Reveals Domains in the Cytoplasmic Leaflet of the Cell Membrane. *Biophys. J.* **86**, 609–616.
- Lommerse, P. H. M., Snaar-Jagalska, B. E., Spaink, H. P. and Schmidt, T. (2005). Single-molecule diffusion measurements of H-Ras at the plasma membrane of live cells reveal microdomain localization upon activation. *J. Cell Sci.* 118, 1799–1809.

- Lommerse, P. H. M., Vastenhoud, K., Pirinen, N. J., Magee, A. I., Spaink, H. P. and Schmidt, T. (2006). Single-Molecule Diffusion Reveals Similar Mobility for the Lck, H-Ras, and K-Ras Membrane Anchors. *Biophys. J.* **91**, 1090–1097.
- Lu, J.-W., Ho, Y.-J., Yang, Y.-J., Liao, H.-A., Ciou, S.-C., Lin, L.-I. and Ou, D.-L. (2015). Zebrafish as a disease model for studying human hepatocellular carcinoma. *World J. Gastroenterol.* 21, 12042–12058.
- Luo, F., Qin, G., Xia, T. and Fang, X. (2020). Single-Molecule Imaging of Protein Interactions and Dynamics. *Annu. Rev. Anal. Chem. Palo Alto Calif* 13, 337–361.
- Malumbres, M. and Barbacid, M. (2003). RAS oncogenes: the first 30 years. Nat. Rev. Cancer 3, 459-465.
- Miller, H., Zhou, Z., Shepherd, J., Wollman, A. J. M. and Leake, M. C. (2018). Single-molecule techniques in biophysics: a review of the progress in methods and applications. *Rep. Prog. Phys. Phys. Soc. G. B.* 81, 024601.
- Mione, M. C. and Trede, N. S. (2010). The zebrafish as a model for cancer. Dis. Model. Mech. 3, 517-523.
- Morone, N., Nakada, C., Umemura, Y., Usukura, J. and Kusumi, A. (2008). Three-dimensional molecular architecture of the plasma-membrane-associated cytoskeleton as reconstructed by freeze-etch electron tomography. *Methods Cell Biol.* 88, 207–236.
- Murakoshi, H., Iino, R., Kobayashi, T., Fujiwara, T., Ohshima, C., Yoshimura, A. and Kusumi, A. (2004).

 Single-molecule imaging analysis of Ras activation in living cells. *Proc. Natl. Acad. Sci.* **101**, 7317–7322.
- Murase, K., Fujiwara, T., Umemura, Y., Suzuki, K., Iino, R., Yamashita, H., Saito, M., Murakoshi, H., Ritchie, K. and Kusumi, A. (2004). Ultrafine membrane compartments for molecular diffusion as revealed by single molecule techniques. *Biophys. J.* **86**, 4075–4093.
- **Nickels, J. D., Smith, J. C. and Cheng, X.** (2015). Lateral organization, bilayer asymmetry, and inter-leaflet coupling of biological membranes. *Chem. Phys. Lipids* **192**, 87–99.
- Niesner, R., Andresen, V., Neumann, J., Spiecker, H. and Gunzer, M. (2007). The power of single and multibeam two-photon microscopy for high-resolution and high-speed deep tissue and intravital imaging. *Biophys. J.* **93**, 2519–2529.
- **Patterson, G. H. and Piston, D. W.** (2000). Photobleaching in two-photon excitation microscopy. *Biophys. J.* **78**, 2159–2162.

- **Phillips, Z. F., Dean, S., Recht, B. and Waller, L.** (2020). High-throughput fluorescence microscopy using multi-frame motion deblurring. *Biomed. Opt. Express* 11, 281–300.
- Plowman, S. J., Muncke, C., Parton, R. G. and Hancock, J. F. (2005). H-ras, K-ras, and inner plasma membrane raft proteins operate in nanoclusters with differential dependence on the actin cytoskeleton. *Proc. Natl. Acad. Sci.* **102**, 15500–15505.
- Prior, I. A., Harding, A., Yan, J., Sluimer, J., Parton, R. G. and Hancock, J. F. (2001). GTP-dependent segregation of H-ras from lipid rafts is required for biological activity. *Nat. Cell Biol.* **3**, 368–375.
- Prior, I. A., Muncke, C., Parton, R. G. and Hancock, J. F. (2003). Direct visualization of Ras proteins in spatially distinct cell surface microdomains. *J. Cell Biol.* **160**, 165–170.
- Schaaf, M. J. M., Koopmans, W. J. A., Meckel, T., van Noort, J., Snaar-Jagalska, B. E., Schmidt, T. S. and Spaink, H. P. (2009). Single-Molecule Microscopy Reveals Membrane Microdomain Organization of Cells in a Living Vertebrate. *Biophys. J.* **97**, 1206–1214.
- Schütz, G. J., Schindler, H. and Schmidt, T. (1997a). Single-molecule microscopy on model membranes reveals anomalous diffusion. *Biophys. J.* **73**, 1073–1080.
- Schütz, G. J., Schindler, H. and Schmidt, T. (1997b). Single-molecule microscopy on model membranes reveals anomalous diffusion. *Biophys. J.* **73**, 1073–1080.
- Seefeldt, B., Kasper, R., Seidel, T., Tinnefeld, P., Dietz, K.-J., Heilemann, M. and Sauer, M. (2008). Fluorescent proteins for single-molecule fluorescence applications. *J. Biophotonics* 1, 74–82.
- **Semrau, S. and Schmidt, T.** (2007). Particle Image Correlation Spectroscopy (PICS): Retrieving Nanometer-Scale Correlations from High-Density Single-Molecule Position Data. *Biophys. J.* **92**, 613–621.
- Shalom-Feuerstein, R., Plowman, S. J., Rotblat, B., Ariotti, N., Tian, T., Hancock, J. F. and Kloog, Y. (2008). K-ras nanoclustering is subverted by overexpression of the scaffold protein galectin-3. *Cancer Res.* **68**. 6608–6616.
- **Shashkova, S. and Leake, M. C.** (2017). Single-molecule fluorescence microscopy review: shedding new light on old problems. *Biosci. Rep.* **37**, BSR20170031.
- Silva, M. C. G. da, Silva, J. F. da, Santos, T. P., Silva, N. P. C. da, Santos, A. R. D., Andrade, A. L. C. de, Souza, E. H. L. da S., Sales Cadena, M. R., Sá, F. B. de, Silva Junior, V. A. da, et al. (2019). The complexation of steroid hormones into cyclodextrin alters the toxic effects on the biological parameters of zebrafish (Danio rerio). *Chemosphere* 214, 330–340.

- **3.** MULTIFOCAL TWO-PHOTON EXCITATION FLUORESCENCE MICROSCOPY REVEALS HOP DIFFUSION

 OF H-RAS MEMBRANE ANCHORS IN EPIDERMAL CELLS OF ZEBRAFISH EMBRYOS
- **Soeller, C. and Cannell, M. B.** (1999). Two-photon microscopy: imaging in scattering samples and three-dimensionally resolved flash photolysis. *Microsc. Res. Tech.* **47**, 182–195.
- **Suzuki, K., Ritchie, K., Kajikawa, E., Fujiwara, T. and Kusumi, A.** (2005). Rapid Hop Diffusion of a G-Protein-Coupled Receptor in the Plasma Membrane as Revealed by Single-Molecule Techniques. *Biophys. J.* **88**, 3659–3680.
- Tinevez, J.-Y., Perry, N., Schindelin, J., Hoopes, G. M., Reynolds, G. D., Laplantine, E., Bednarek, S. Y., Shorte, S. L. and Eliceiri, K. W. (2017). TrackMate: An open and extensible platform for single-particle tracking. *Methods San Diego Calif* 115, 80–90.
- Travers, T., Colin, V. G., Loumaigne, M., Barillé, R. and Gindre, D. (2020). Single-Particle Tracking with Scanning Non-Linear Microscopy. *Nanomater. Basel Switz.* **10**, E1519.
- Umemura, Y. M., Vrljic, M., Nishimura, S. Y., Fujiwara, T. K., Suzuki, K. G. N. and Kusumi, A. (2008). Both MHC class II and its GPI-anchored form undergo hop diffusion as observed by single-molecule tracking. *Biophys. J.* **95**, 435–450.
- van den Broek, B., Ashcroft, B., Oosterkamp, T. H. and van Noort, J. (2013). Parallel nanometric 3D tracking of intracellular gold nanorods using multifocal two-photon microscopy. *Nano Lett.* **13**, 980–986.
- Yasui, M., Matsuoka, S. and Ueda, M. (2014). PTEN Hopping on the Cell Membrane Is Regulated via a Positively-Charged C2 Domain. *PLoS Comput. Biol.* **10**, e1003817.
- **Yokota, H.** (2020). Fluorescence microscopy for visualizing single-molecule protein dynamics. *Biochim. Biophys. Acta Gen. Subj.* **1864**, 129362.
- **Zhou, Y. and Hancock, J. F.** (2015). Ras nanoclusters: Versatile lipid-based signaling platforms. *Biochim. Biophys. Acta* **1853**, 841–849.
- **Zhou, Y. and Hancock, J. F.** (2021). Super-Resolution Imaging and Spatial Analysis of RAS on Intact Plasma Membrane Sheets. *Methods Mol. Biol. Clifton NJ* **2262**, 217–232.
- Zhou, Y., Prakash, P., Gorfe, A. A. and Hancock, J. F. (2018). Ras and the Plasma Membrane: A Complicated Relationship. *Cold Spring Harb. Perspect. Med.* **8**, a031831.

SUPPLEMENTARY FIGURES

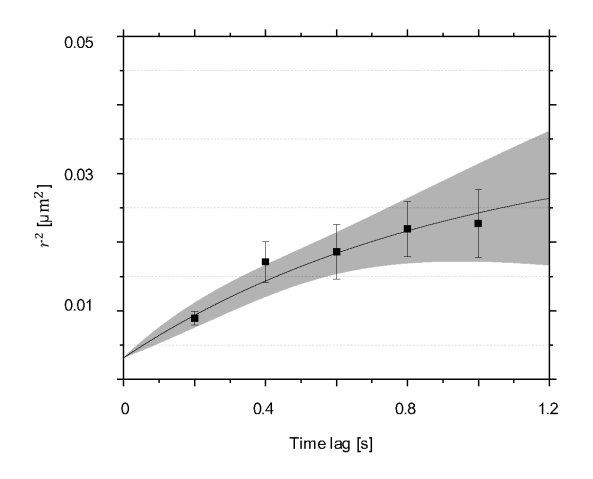


FIGURE S1: GFP-C10H-Ras mobility patterns: results of one-fractional model fitting to 2PEFM data. Fitting of the data points to the one-population model allowed for calculation of the mean squared displacements of this population (r^2). This procedure was repeated for each of the time lags used. Mean squared displacements plotted against the time lag, using the one-population model fit. The initial diffusion coefficient D_0 of this single population equaled 0.116 \pm 0.011 μ m² s⁻¹ and its confinement area size L equaled 302 \pm 54 nm Each data point is presented in the form of a mean \pm s.e.m., and the 95% c.i. of the mathematical fit is shown.

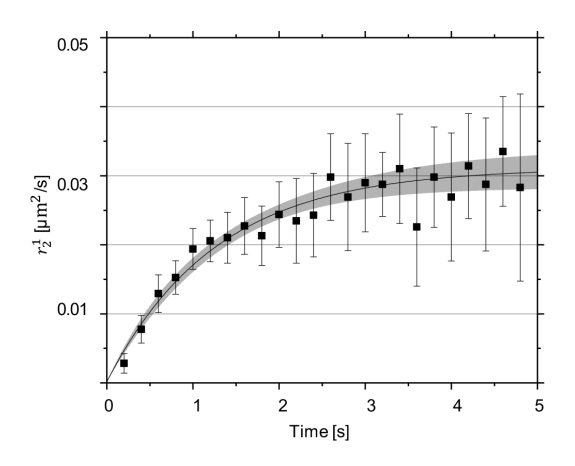


FIGURE S2: GFP-C10H-Ras mobility patterns: mean squared displacement of the molecular trajectories reconstructed for 25 selected particles. The squared displacements of all 25 selected molecules were used to generate a plot presenting the mean squared displacement as a function of time, to demonstrate that this selection of molecules is representative of the entire molecular. The plotting of the confinement model fit the function of mean squared displacements over time revealed that the initial diffusion coefficient D_0 for this population equaled $0.243 \pm 0.057 \, \mu \text{m}^2 \, \text{s}^{-1}$, while its confinement area size L equaled $357 \pm 82 \, \text{nm}$

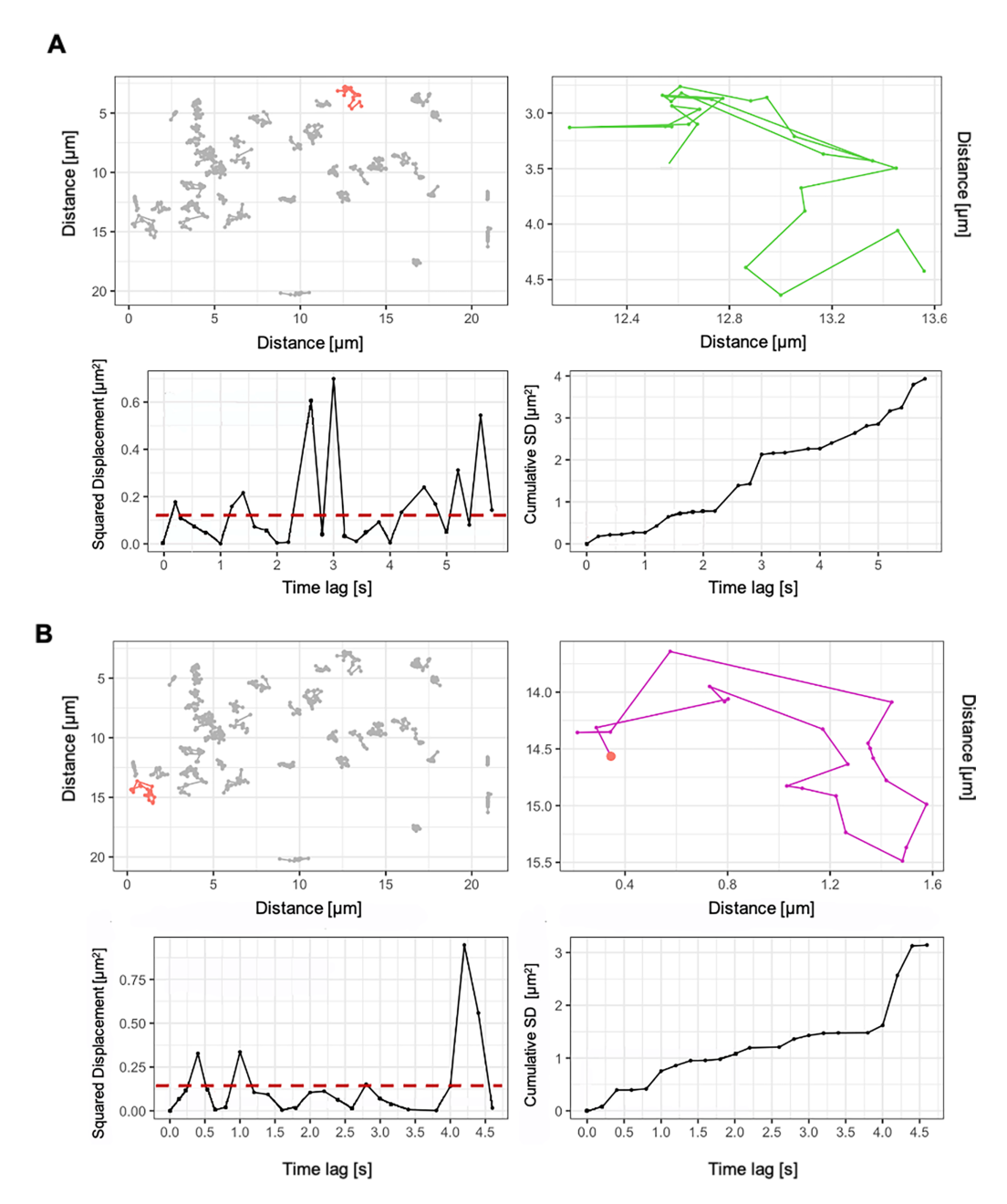


FIGURE 53: Representative images of GFP-C10H-Ras molecular trajectories (AB) Representative images of two molecular trajectories used for the hop diffusion analysis. Upper left in (AB): Inside of the epidermal cell selected for the reconstruction of the GFP-C10H-Ras molecular trajectories. Isolated trajectories of GFP molecules are shown in grey. An enlarged example of molecular trajectories is highlighted in red. Upper right in (AB): Enlarged map of a single GFP-C10H-Ras molecule highlighted red in the upper left panel. Lower left in (AB): A plot of the squared displacement versus time lag for the GFP-C10H-Ras molecule highlighted red in the upper left panel.

C10H-Ras molecule selected in the upper left panel. Periods of short-lived, increased diffusion rates are visible. The threshold for differentiation between the diffusion and hopping states is drawn in dashed red. Lower right in (AB): A plot of the cumulative squared displacements versus time lag for the single GFP-C10H-Ras molecule selected in the upper left panel. Identical short-lived periods of increased diffusion rates are visible.

4. ANALYSIS OF INTRACELLULAR PROTEIN DYNAMICS IN LIVING ZEBRAFISH EMBRYOS USING LIGHT-SHEET FLUORESCENCE SINGLE-

MOLECULE MICROSCOPY

Matteo Bernardello, Radoslaw J. Gora, Patrick van Hage, Gustavo Castro-Olvera, Emilio

J. Gualda, Marcel J.M. Schaaf, Pablo Loza-Alvarez

ABSTRACT

Single-Molecule Microscopy techniques have emerged as useful tools to image individ-

ual molecules and analyze their dynamics inside cells, but their application has mostly

been restricted to cell cultures. Here, a Light-Sheet Fluorescence Microscopy setup is

presented for imaging individual proteins inside living zebrafish embryos. The optical

configuration makes this design accessible to many laboratories and a dedicated sam-

ple-mounting system ensures sample viability and mounting flexibility. Using this

setup, we have analyzed the dynamics of individual glucocorticoid receptors, which

demonstrates that this approach creates multiple possibilities for the analysis of intra-

cellular protein dynamics in intact living organisms.

Keywords: glucocorticoid receptor, zebrafish, single-molecule microscopy, light-sheet

fluorescence microscopy, nucleus, diffusion

doi: 10.1364/BOE.43510

121

4.1 INTRODUCTION

A quantitative imaging-based analysis of the biochemical processes and protein interactions inside cells requires microscopy techniques that go beyond ensemble averaging and a static molecular view (Yokota, 2020). Single-molecule microscopy (SMM) has demonstrated to offer such opportunities and has enabled researchers to detect individual molecules in the variety of their conformations and associations as well as to study their dynamics with unparalleled spatial and temporal resolution. Imaging of individual proteins in living cells is enabled by fluorescent labeling of these proteins, using either genetically encoded fusion to autofluorescent proteins such as green fluorescent protein (GFP) and photoactivatable or switchable variants of these proteins, or linking of nanoparticles or organic dyes to peptide or protein tags (such as Halo-tags), that have been fused to the protein of interest (Harms et al., 2001; lino et al., 2001; Li and Vaughan, 2018; Luo et al., 2020).

SMM has mainly been performed using microscopy techniques such as Widefield Microscopy (WM), Total Internal Reflection Fluorescence (TIRF) microscopy, and Highly-Inclined and Laminated Optical sheet (HILO). In WM, while technically simple, the entire sample is illuminated by the excitation beam, which creates a high background over the weak signal from the single molecules. In TIRF, an evanescent wave of excitation light at the coverslip-sample interface is created, which exponentially decays with the distance to this interface (Axelrod, 2001). As a result, only the fluorophores present in the first 100 to 200 nm are excited, which highly reduces the background intensity, and thereby increases the sensitivity and positional accuracy. However, at the same time, TIRF limits the detection of molecules to the basal membrane of the cells mounted on the coverslip. In HILO microscopy an oblique sheet of light is used to illuminate a section of the specimen, enabling excitation of fluorophores deeper inside cells (Tokunaga et al., 2008). Nevertheless, since the illumination is oblique with respect to the detection focal plane, the size of the lateral Field-of-View (FoV) of the produced images is limited. Moreover, all these approaches are optimized for, and therefore limited to, coverslipbased sample mounting.

Thus far, the vast majority of SMM studies have been performed in cultured eukaryotic cells, often derived from immortalized cell lines. These cells may show artefacts, do not take into consideration the influence of cell-cell interactions, and have a limited translational value compared to studies performed in intact organisms. In addition, studies in cultured cells cannot answer questions concerning differences in protein dynamics in response to different developmental, environmental, and metabolic states that an organism might be presented with in its native habitat. Therefore, there is a need for microscopy techniques that enable in vivo SMM analyses on biologically relevant samples, such as the living zebrafish. These techniques should provide limited background signals and large FoVs, enable maintaining the sample alive for prolonged times, and, ideally, not interfere with natural biological processes by limiting phototoxic effects or other stressors. Previously, we have extended SMM studies to living organisms by analyzing the dynamics of yellow fluorescent protein (YFP) fused to the membrane anchor of the human H-Ras protein in cells inside living zebrafish embryos (Schaaf et al., 2009b). By using TIRF microscopy and a particular sample-mounting procedure to make the zebrafish tail adhere to the coverslip, we managed to detect individual YFP-C10H-Ras molecules in the outer membrane of the outer epithelial cells of the embryonic epidermis, and to study the mobility pattern of these proteins. However, while optimal for studies on membrane protein dynamics, the implementation of the TIRF microscopy is limited by the penetration depth of the evanescent wave and is therefore not suitable for studying molecules located anywhere outside the outer membrane of the outer cell layer of the embryo. In the present study, we have applied Light-Sheet Fluorescence Microscopy (LSFM) as an SMM technique that allows for imaging of individual nonmembrane molecules inside a living organism while not being limited to the cell membrane.

In LSFM, two objectives, positioned orthogonally to each other, are usually employed. A plane of excitation light (light sheet, LS) is sent from the illumination objective through the specimen, exciting only the fluorophores present at the detection focal plane (Olarte et al., 2018). Photons emitted by the fluorophores in the entire illuminated sample section are collected in a widefield configuration by the detection objective. This plane-based configuration permits fast imaging and allows for optical sectioning at low photobleaching and phototoxicity regimes, with low background fluorescent signals.

The use of LSFM in SMM applications has so far been limited, mainly due to mechanical constraints imposed by the geometry of the objectives. Their orthogonality combined with their short working distances restricts the space and displacement possibilities of the sample. This problem has often been circumvented by the use of long-working-distance air objectives for the illumination, and cuvettes containing imaging medium and sample (Ritter et al., 2008; Ritter et al., 2010; Spille et al., 2012; Yu et al., 2016). This solution, however, introduces refractive index mismatches at the air-glass and glass-medium interfaces, leading to spherical aberrations. Consequently, when the cuvette translates in the illumination direction, focal shifts appear and correction strategies need to be implemented (Spille et al., 2012), increasing hardware complexity. To overcome these issues, some LSFM configurations use a modified light path, including prism-based LSFM (PCLSM) (Li et al., 2013), and reflected LSFM (RLSFM) (Gebhardt et al., 2013; Greiss et al., 2016; Reisser et al., 2018). With these LSFM approaches individual, fluorescently labelled molecules have been imaged in aqueous solutions (Ritter et al., 2010; Yu et al., 2016), cell nuclei of salivary glands extracted from C. tentans larvae (Ritter et al., 2010; Spille et al., 2012), and membranes or nuclei of cultured cells (Gebhardt et al., 2013; Li et al., 2013). Interestingly, these technologies also allowed imaging of individual injected Dextran-Alexa647 molecules in Drosophila (Greiss et al., 2016), and transcription factors in zebrafish embryos (Reisser et al., 2018). Custom-made illumination objectives combined with non-Gaussian excitation schemes, such as Bessel plane illumination (Gao et al., 2012) and lattice LSFM (LLSFM) (Chen et al., 2014b), have been used to create a long and thin LS. These techniques have been employed in SMM studies in embryonic stem cells (Chen et al., 2014a; Liu et al., 2014), membrane dynamics in cultured cells and in cells of the zebrafish eye (Aguet et al., 2016), and living Drosophila (Mir et al., 2017; Mir et al., 2018). The Light Sheet Fluorescence Single-Molecule Microscopy (LSFSMM) methods described above offer the possibility to use very high NA (from 1.0 to 1.4) detection objectives, but this is only possible at the expense of a highly increased hardware complexity of the overall system, which will limit the use of LSFSMM.

So far, single-molecule imaging has only been applied to intact living organisms in a few studies (Mir et al., 2018; Reisser et al., 2018; Schaaf et al., 2009b), which could be due to the difficulty for many biological labs in accessing the complex setups that are required. The described hardware complexity also has consequences for the sample mounting systems. In PCLSM (Li et al., 2013), the sample is placed on a glass bottom dish

over an inclined surface. Similarly, RLSFM (Gebhardt et al., 2013; Greiss et al., 2016) and LLSFM have been used for SMM in living zebrafish embryos (Aguet et al., 2016; Reisser et al., 2018), and in these studies the embryos were mounted on a glass bottom dish or glass coverslip and embedded in low melting agarose. In all these methods, the sample's degrees of freedom are constrained by the mounting procedure, as the specimen's movements and orientation possibilities are fixed or limited. Although this might not be a problem for cultured cells, in the case of imaging living organisms it can eventually preclude the performance of certain experiments.

In the present study, we chose an iSPIM (Wu et al., 2011) configuration to perform SMM, to have a simpler setup compared to the previously mentioned LSFM alternatives, without custom-made optical elements such as coatings (Gebhardt et al., 2013; Reisser et al., 2018) or objectives (Chen et al., 2014b), thereby avoiding potential instability issues and maintaining a straightforward optical alignment procedure. Although the collection NA achieved in our system is smaller or equal compared to the NA of PCLSM, RLSFM, or LLSFM setups, our sample mounting approach is superior in terms of sample viability and sample mounting flexibility. We believe that these are crucial factors when extending the application of SMM to intact living organisms. In addition, our design will enable the possibility to perform more complex SMM studies in vivo, e.g., correlating macrobiological events with the intracellular dynamics at the single molecule level. We therefore describe the sample mounting procedure in detail, with attention to the effects of the embedding medium on the microscope's performance.

We have utilized our LSFSMM setup using cultured cells and living zebrafish embryos as biological samples. HEK293 cells were used to perform a characterization study on the detection of single yellow fluorescent protein (YFP) molecules. Subsequently, we chose zebrafish embryos to test our capacity to image in vivo, since it is a relevant vertebrate animal model that is commonly used in research areas, ranging from developmental biology to toxicology and drug screening (Detrich et al., 2011; Stainier et al., 1996). As a protein of interest, we selected the Glucocorticoid Receptor (GR), which is a well-studied steroid receptor. Upon binding of a glucocorticoid ligand (either an endogenous hormone such as cortisol or a synthetic drug such as dexamethasone), the GR translocates to the nucleus and acts as a transcription factor, regulating gene expression by binding to specific DNA sequences and interacting with other proteins. Previous

studies have allowed researchers to study the intranuclear dynamics of individual fluorescently tagged GR molecules in cultured cells and, for instance, establish the duration of the DNA binding time (Garcia et al., 2021; Gebhardt et al., 2013; Groeneweg et al., 2014; Keizer et al., 2019; Paakinaho et al., 2017). Furthermore, it has been exhibited that the zebrafish GR gene shows a high level of similarity with its human counterpart, through the similarity of a C-terminal GR splice variant, resembling the human GR β , and the fact that both zebrafish and human genomes contain only one gene encoding the GR protein (Schaaf et al., 2009a).

By using our custom-made and optimized mounting system in our LSFSMM, we demonstrate that it is possible to successfully image individual molecules in living embryos for a prolonged period of time. To validate the robustness of our LSFSMM, we have analyzed the GR mobility pattern. As expected, dexamethasone administration significantly alters the dynamics of GR. By further characterization of the sources of variation in the in vivo results, we found that most of the variability in the results comes from imaging different areas within an individual zebrafish embryo, and to a lesser extent from imaging individual embryos on different experimental days, discarding the microscope setup as a source of variation. Overall, our data suggest that the relative simplicity of the optical design, constructed with conventional optical elements together with the described sample mounting system and protocols, will further promote in vivo LSFSMM applications in membranes, cytoplasm, and nuclei of cells inside zebrafish and other living organisms.

4.2 RESULTS

An LSFM platform for in vivo SMM imaging (LSFSMM)

In order to achieve *in vivo* SMM on whole live organisms we have designed and built a customized LSFM platform. We took into special consideration the development of sample mounting protocols adapted to the experimental requirements and sample needs. Finally, we have characterized its optical performance and its ability to conduct SMM experiments.

Our LSFSMM implementation is built on a Nikon Eclipse body, on top of which two perpendicular objectives are mounted in iSPIM configuration (Wu et al., 2011). Since the two

objectives are positioned perpendicularly between each other, but at 45° respect to the optical table, we define the coordinate system xyz to be the reference for the optical table and motor stages, while the coordinate system $x\hat{y}\hat{z}$ is defined as the reference for the imaging planes, with $x\hat{y}\hat{z}$ being the clockwise rotation of 45° around the y-axis of xyz. A schematic overview of the illumination and detection light paths is depicted in Fig. 1A. The light sheet plane is generated by a cylindrical lens that focuses the light onto a galvo-mirror. The mirror is positioned plane-conjugate with the back-focal-plane of a water dipping illumination objective by a relay lens system. This arrangement permits to change the position in \hat{z} (i.e., across the sample volume) of the light sheet by electronically controlling the angle of the galvo-mirror. This capability can be used for alignment purposes and to scan different sample areas. With this illumination system, we experimentally measured the LS thickness to be of about 2 µm at its waist (Fig. 2A). The illumination FoV along x_i i.e., the portion of the light sheet that is considered to be of homogeneous thickness, is calculated to be about 13.5 μ m, in good agreement with the measured value of about 14.5 µm (Fig. 2A). The total magnification of the optical system is 44.4X (See Material and Methods section), leading to an image pixel size of 146.4 nm. Considering the size along the ŷ axis of the sCMOS chip of the camera (2048 pixels), this means that the system enables the imaging of an area of about 13.5 µm x 300 µm.

In order to enable imaging in zebrafish embryos, an appropriate sample mounting system is key and should allow both optical quality and sample wellness. In the iSPIM configuration, the two objectives offer a limited volume in which the sample can be inserted. The sample mounting system must allow simple insertion of a zebrafish embryo and provide conditions for the embryo to stay alive during the experiment, with as little stress imposed as possible. At the same time, the sample mounting system needs to avoid the introduction of unwanted optical aberrations. We have implemented and characterized a fully motorized sample mounting stage and efficient sample mounting protocols using tailored FEP tubes and multilayer agarose mounting, as depicted in Fig. 1BCD.

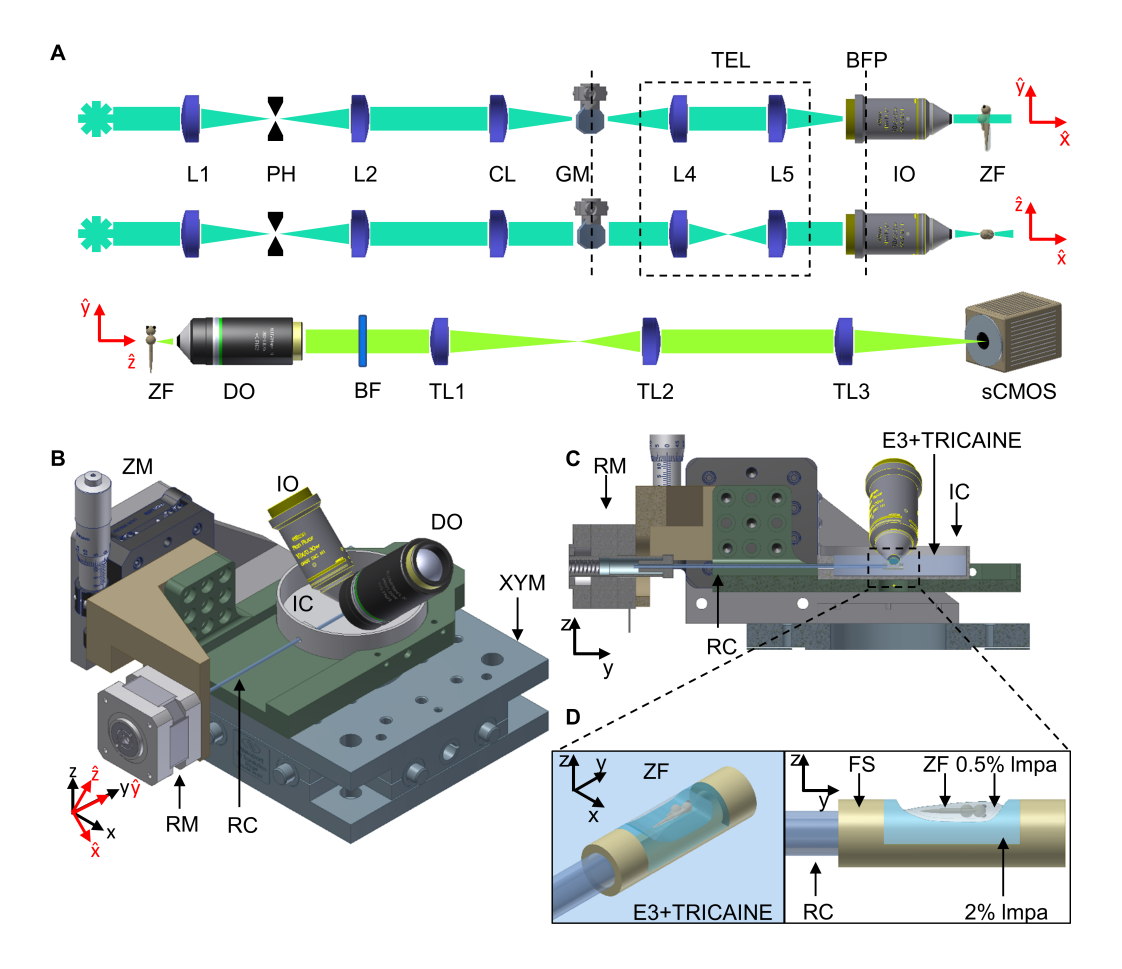


FIGURE 1: Schematic overview of the LSFM platform for in vivo SMM imaging. (A) schematic of the optical illumination (top two) and detection (bottom one) light paths; (B) schematic of the sample mounting system, with (C) its lateral section view, (D) the FEP support for zebrafish mounting. L = lens, PH = pinhole, CL = cylindrical lens, GM = galvo-mirror, BFP = back focal plane, TEL = telescope plane-conjugating GM to BFP, IO = Illumination objective, DO = detection objective, BF = bandpass filter, TL = tube lens, ZF = zebrafish, RC = rotation capillary, FS = FEP support, RM= rotational motor, IC = imaging chamber, ZM = motorized stage in z, XYM = motorized stage in xy, Impa = low melting point agarose.

The developed sample mounting system makes use of a FEP tube which was cut to free the top part. In this way the tube serves as a horizontal support for the relatively big and heavy sample without covering it. Its proximal and distal tips and the basis of the tube are filled with 2% low melting point agarose (Impa). The zebrafish embryo is placed in the remaining space inside a drop of 0.5% Impa with the addition of tricaine for

anesthesia. The FEP tube is suspended inside a petri-dish-like chamber by a 12 cm glass capillary, which is inserted into the proximal end of the FEP tube. The glass capillary is connected to a motorized rotator motor on its other end, and optimal orientation of the zebrafish embryo with respect to the LS can be obtained by rotating the capillary using simple electronic control of the motor. Finally, the incubation chamber, which is on top of an *x-y-z* motorized translational stage is filled with E3 medium (with the addition of tricaine), to completely immerse the zebrafish embryo and the tips of the objectives.

To characterize the effect of the sample mounting protocol on the generated optical aberrations, a FEP tube filled with a 0.5% Impa cylinder, in which sub-diffraction sized fluorescent beads (100 nm in diameter) were embedded, was introduced in the imaging volume. The image of a 100 nm fluorescent bead would present a theoretical FWHM of 334 nm, given by the convolution of the Gaussian PSF generated by a 1.0 NA waterobjective, with the step-size profile of the bead. The images obtained from beads inserted close to the middle axis of the Impa cylinder would instead heavily suffer from distortions, enlarging the total PSF and reducing the actual optical resolution (Fig. 2CD). For beads at this location, we calculated FWHMs of 567.6 ± 59.2 nm and 536.5 ± 65.3 nm (average ± standard deviation, in x and ŷ direction respectively, N=11 beads). In contrast, images from beads closer to the surface of the 0.5% Impa cylinder did not suffer from significant distortions (Fig. 2EF). For beads at this location, we calculated FWHMs of 393.0 \pm 39.9 nm and 371.4 \pm 34.8 nm (average \pm standard deviation, in x and \hat{y} direction respectively, N=11 beads). The position of the point source within the Impa cylinder is therefore critical in assessing the optical resolution, which significantly differs for objects at the two locations (Fig. 2B). The difference between the measured values from the beads close to the surface and the theoretical one is most probably imputable to a residual aberration caused by the remaining agarose layer, and thus depending on the exact position of the single beads. The system and protocol for mounting zebrafish embryos was therefore here developed such that the living specimen was covered by a maximally 100 µm-thick layer of 0.5% Impa, in order to minimize optical aberrations.

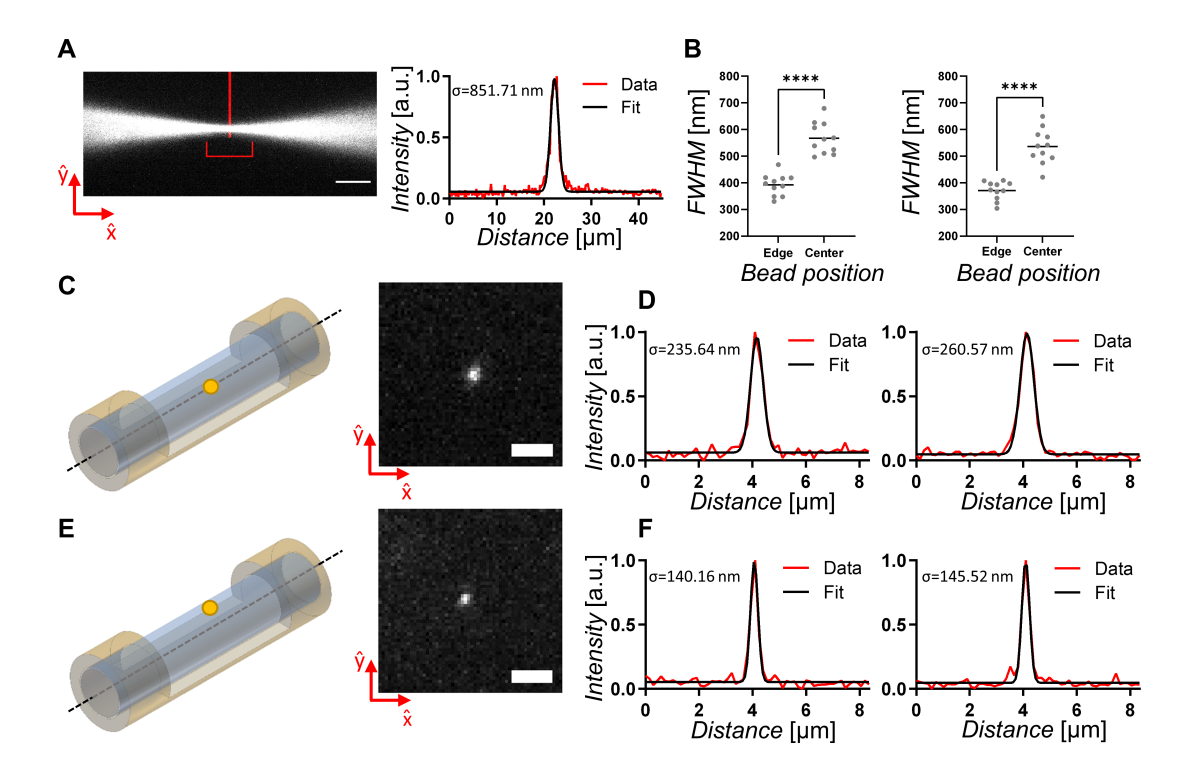


FIGURE 2: LSFSMM system performances. (A) Illumination light beam focused by removal of the cylindrical lens. Measurement of the intensity profile through a Gaussian fit demonstrated a 2 μm diameter (FWHM) at its waist (indicated by vertical red line). The illumination FoV is also indicated (red horizontal bracket). Scale bar 10 μm. **(B)** Distributions and comparison of the measured FWHM of the Gaussian fits of beads close to the surface (N=11) and in the center (N = 11) of the mounting Impa cylinder. Values were measured along x (left panel) and \hat{y} (right panel) direction. Shapiro-Wilk test was performed to check if data is normally distributed. Unpaired t-tests were then conducted to check for statistically significant difference between the two conditions and calculate two-tailed P-values. Horizontal bar represents the mean value, **** means P < 0.0001. **(C)** Schematic of a 100 nm fluorescent bead positioned in the middle of a 0.5% Impa cylinder and **(D)** normalized intensity profile measurement and Gaussian fit in x (left panel) and \hat{y} (right panel) direction of an imaged bead. Scale bar 2 μm. **(E)** Schematic of a 100 nm fluorescent bead positioned close to the surface of a 0.5% Impa cylinder and **(F)** normalized intensity profile measurement and Gaussian fit in x (left panel) and \hat{y} (right panel) direction of an imaged bead. Scale bar 2 μm. For all the Gaussian fits here presented R² > 0.96, and σ represents the standard deviation of the Gaussian curve.

Characterization of detected fluorescence signals from individual YFP-GR molecules

The experiment was performed on HEK293 cells transiently transfected with an expression vector for YFP-GR. The cells were fixed to guarantee immobility of the fluorophores so they would not diffuse out of the FoV. Subsequently, the fixed cells were mounted on the LSFSMM setup for imaging. Characteristics of the YFP molecule fluorescence signal (Fig 3A), was determined by analysis of 1241 fluorescence intensity spots that displayed single-step photobleaching, which indicates the presence of a single fluorescent protein within a diffraction-limited spot. Almost 85% of all the single-molecule traces were 3 frames long or shorter, and the average trace length of a single YFP-GR molecule equaled 2.3 frames (Fig 3B).

To extract the information about the point-spread function (PSF) of the fluorescence from a single YFP molecule, a Gaussian function was plotted over the 2D intensity profile (Fig. 3A). We determined the maximum of the Gaussian function as a measure for the intensity, while its full width at half maximum (FWHM) as a measure for the width of the PSF of a single YFP molecule. The maximum of the Gaussian function of 1241 signals from immobilized YFP-GR molecules in the fixed HEK293 cell equaled 139.8 ± 22.4 counts, which corresponds to 22.3 ± 9.7 photons (Fig. 3C). The mean FWHM value of the Gaussian curves fitted on the single-molecule intensity profiles equaled 357.5 ± 12.6 nm. These characteristics of the fluorescence signals from individual YFP molecules were subsequently used to determine the threshold values for the identification of signals attributed to single YFP-GR molecules in the images acquired from living zebrafish embryos using previously developed, customized software (Harms et al., 2001; Lommerse et al., 2004; Schmidt et al., 1996) (Fig. 3D). The mean number of single YFP-GR molecules identified per image frame equaled 19.6 ± 8.7. The positional accuracy of the measurements was determined by calculating the quotient of the FWHM and square root of the number of photons detected, and equaled 76 nm (Bobroff, 1986), while Signal-to-Noise Ratio (SNR), being defined as the intensity of an individual fluorophore (139.8 ± 22.4 counts) divided by the standard deviation of the background signal (7.2 counts), equaled circa 20 (Fig. 3C).

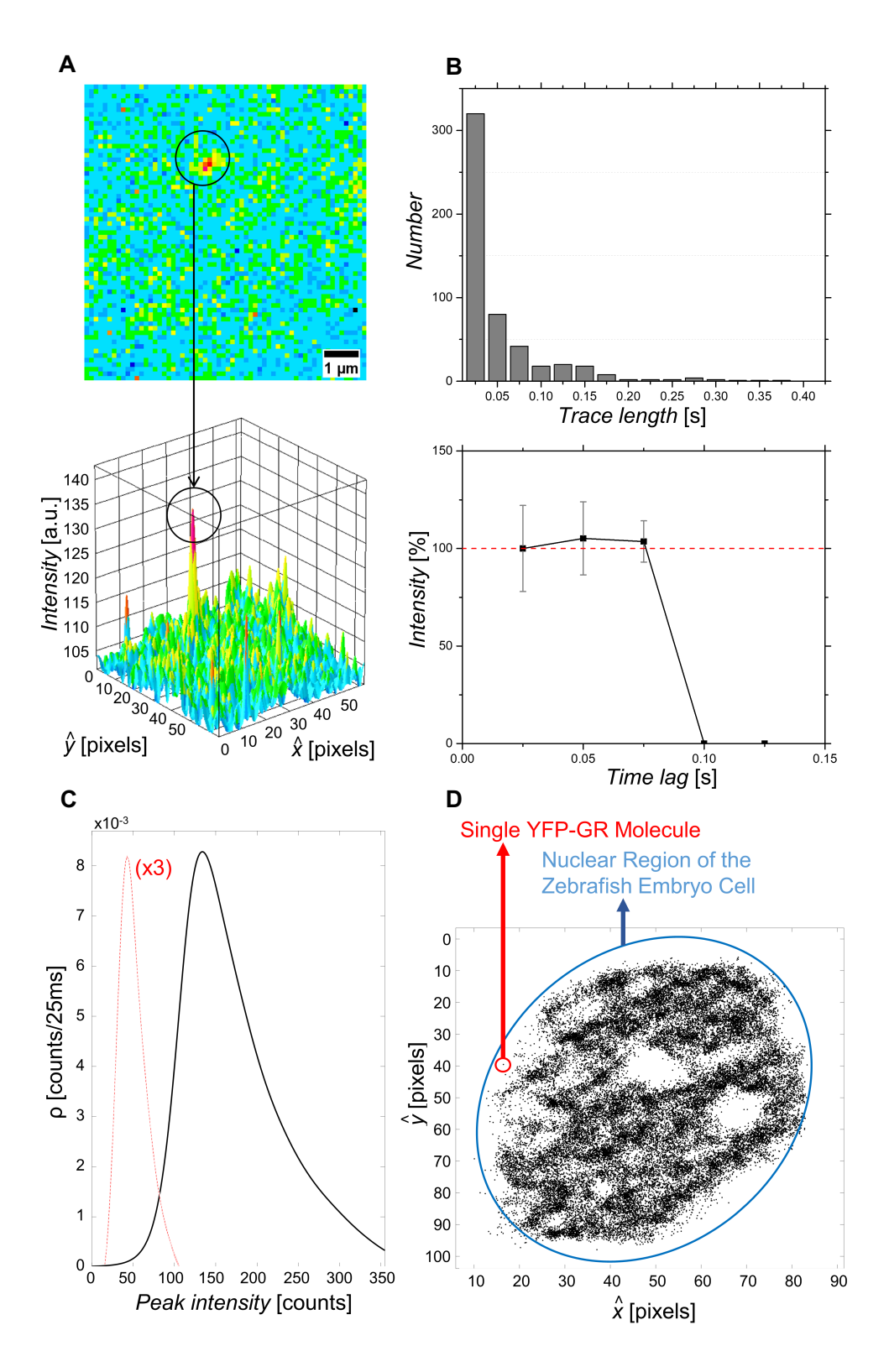


FIGURE 3: Characterization of detected fluorescence signals from individual YFP-GR molecules in fixed HEK293 cells. (A) Localization of a single fluorescent molecule. The circle indicates a fluorescence intensity spot that was attributed to an individual YFP molecule based on single-step photobleaching. (B) *Top*: Bar graph depicting the trace length of 1241 single molecules (521 traces) identified in images of fixed HEK293 cells. The average trace lengths equaled 2.3 frames, and approximately 85% of all traces consisted of 1-3 frames. *Bottom*: Time trace of the relative single-molecule fluorescence signals determined for all YFP-GR molecules showing a trace length of 1-3 frames. All traces show single-step photobleaching indicating that the signals can indeed be attributed to single YFP-GR molecules. (C) Density (ρ) plot representing the distribution of the peak intensity of 1241 fluorescence signals. The curve is nearly Gaussian-shaped with a maximum of 139.8 counts per 25 ms, corresponding to 22.3 photons. The signal intensity of the background is shown for comparison (dashed red line, density values are multiplied by 3 for better visualization). (D) Localization of single YFP-GR molecules in the nucleus of a nucleus in a living zebrafish embryo. The image depicts a representative localization of YFP-GR molecules, with an average of 19.6 ± 8.7 peaks per frame, accumulated from 3000 consecutive frames. Nucleoli are visible (white circular regions inside of the nucleus), in which YFP-GR molecules are not found.

Experiments on live fish and data analysis

In order to confirm the presence of the YFP-GR molecules and their localization within the nuclei of the embryonic cells, embryos of the Ta(actb2:mCherry-H2A) transgenic zebrafish line, which express a fusion protein of mCherry and the nuclear protein histone 2A in all cells, were injected with the YFP-GR expression vector and imaged at 1 dpf (day post-fertilization) using a different custom-made LSFM system setup. This multiview LSFM microscope allowed us to visualize, at 1.3 µm lateral resolution and extended field of view, the development of the whole embryo (Krzic et al., 2012). The resulting images showed the expression of the YFP-GR molecules and their co-localization with the H2A histone signal (Fig. 4ABC) within the nuclei of the cells in the embryonic body. The YFP-GR expression was particularly evident in the external yolk syncytial nuclei (eYSN), which have migrated to cover the yolk sac during gastrulation. They are part of the yolk syncytial layer (YSL), a syncytium containing yolk syncytial nuclei (YSN) that is formed during early embryogenesis as a result of mitotic divisions without cytokinesis. It consists of internal YSN (iYSN, located between the yolk sac and the proper embryo) and eYSN that cover the yolk sac. The YSL plays an important role in meso- and endodermal differentiation, epiboly and cardiac formation, and it plays a nutritive role during embryonic and larval stages (Carvalho and Heisenberg, 2010; Chu et al., 2012; Kimmel and Law, 1985; Kimmel et al., 1995). These giant nuclei are transcriptionally very active and have previously been shown to display high levels of transgene expression, which may be due

to a high transcriptional activity or enhanced transgene replication in these nuclei (Williams et al., 1996). We therefore chose these nuclei as target for our SMM intranuclear analysis, as upon DNA injection their expression levels are significantly higher than those of somatic nuclei.

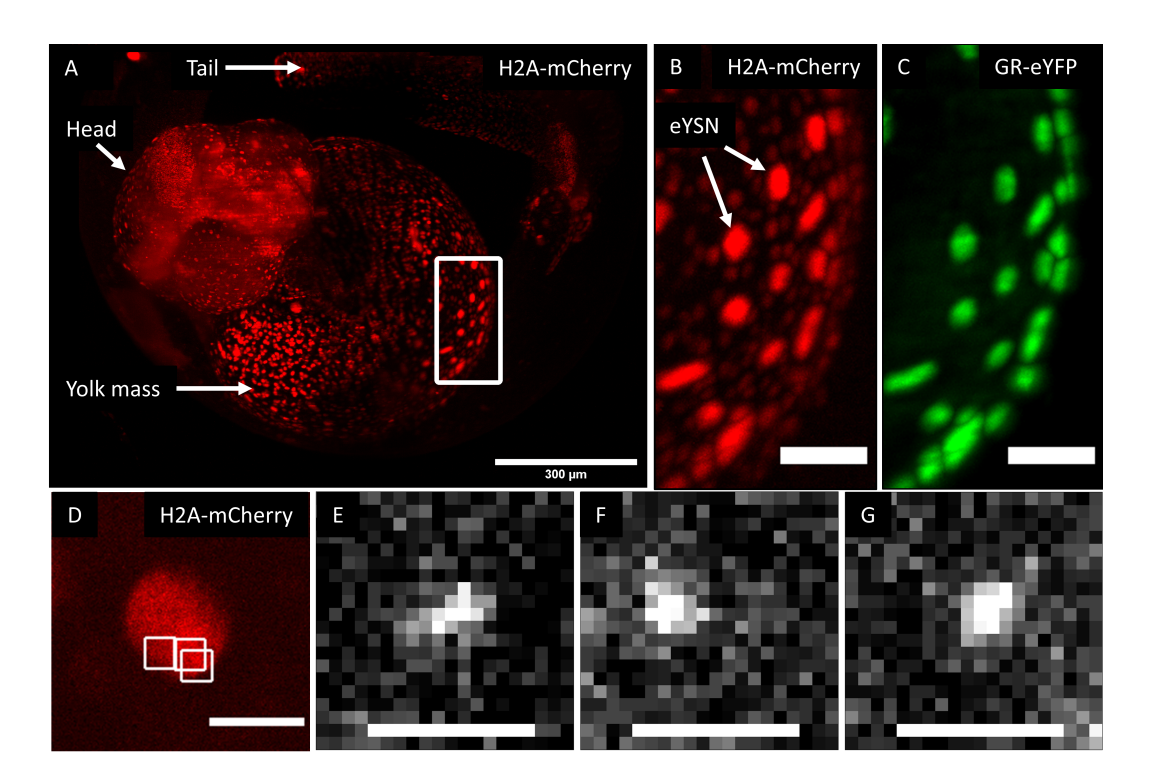


FIGURE 4: Imaging of YFP-GR in a zebrafish embryo. (A) Maximum intensity projection of a z-stack obtained using LSFM imaging of a developing ldpf Tg(actb2:mCherry-H2A) zebrafish embryo injected with a YFP-GR expression vector (only H2A signal shown in A). Scale bar 300 μ m. **(B, C)** Higher magnification image of the highlighted ROI showing the **(B)** mCherry-H2A and **(C)** the YFP-GR signal (maximum intensity projections, scale bars 50 μ m). Imaging performed using a different LSFM setup. The expression of GR is evident, as well as the localization within the eYSN. **(D)** Image of a nuclei in the yolk from a 2dpf live zebrafish embryo obtained using the LSFSMM setup. Only H2A signal shown, scale bar 10 μ m. **(E-G)** Three individual YFP-GR molecules imaged through the LSFSMM setup within the ROIs highlighted in D (white squares), in a 2 dpf zebrafish embryo. Scale bars 2 μ m.

Subsequently, using the LSFSMM system high-resolution image sequences of the YFP-GR in the embryos were acquired with a time lag of 25 ms and a length of 1000-4000 frames (Fig. 4D). To study the effect of GR activation, embryos were imaged in the absence and presence of the synthetic glucocorticoid dexamethasone. One zebrafish

embryo was selected for both vehicle- and dexamethasone-treated groups, and in each of the selected embryos three separate areas were imaged. Images exhibited the presence of fluorescence intensity peaks, which were then attributed to single molecules. A projection of 1000-4000 consecutive frames (as shown in Fig. 3D) showed a different density of fluorescence intensity peaks between the nucleus and the cytoplasm and served as a matrix for selecting the area of studying protein mobility patterns, so only localizations of nuclear GRs were taken into consideration. Resulting average density of GR molecules per image equaled 19.6 \pm 8.7. A representative image depicting nuclear GRs localization is presented in Supplement 1, Fig. S3.

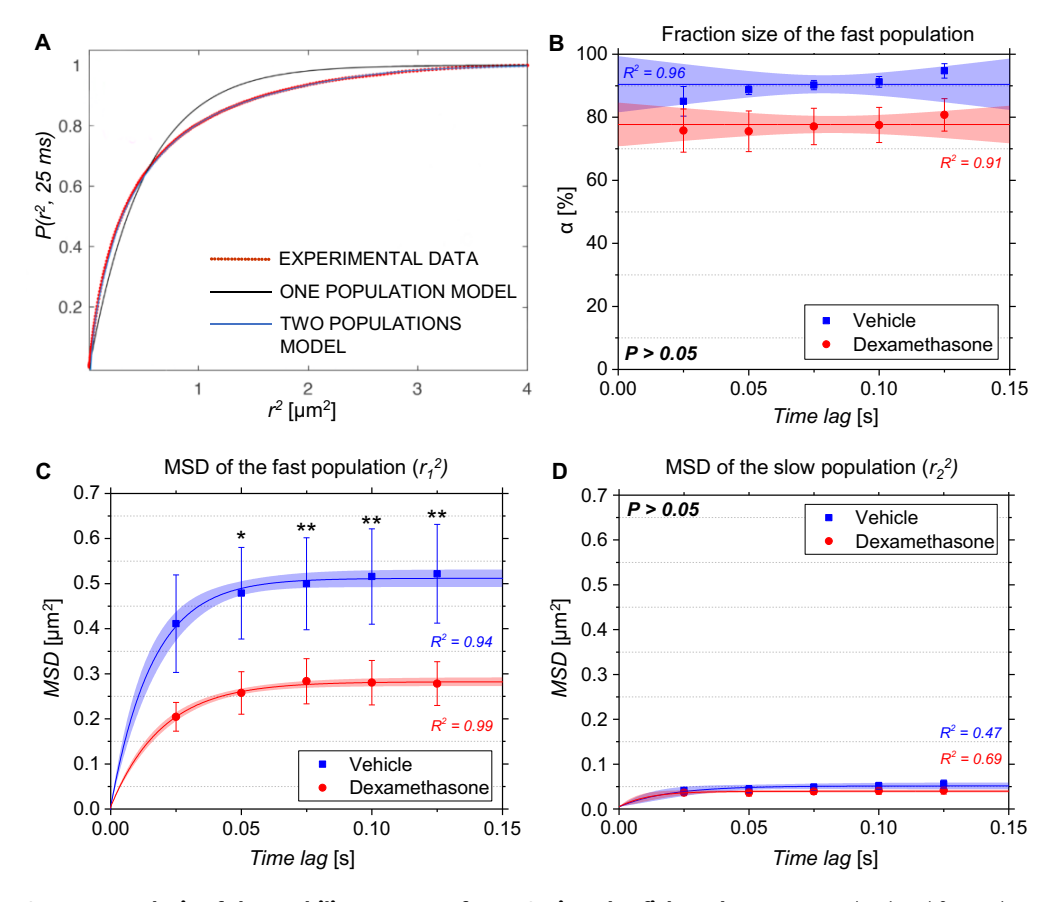


FIGURE 5: Analysis of the mobility pattern of YFP-GR in zebrafish embryos. Data obtained from three embryos from both the vehicle- (red) and dexamethasone-treated (blue) groups were pooled, and their averages with standard deviations are presented. **(A)** Cumulative probability P plot of squared displacement measurements r^2 , obtained experimentally for a time lag of 25 ms. Experimental data are best fitted using a two-population model, yielding the size of the fast subpopulation and the MSD for each time lag. Number of MSD replicates per time lag in each of the group equaled to 30. **(B)** Fast subpopulation fraction

size in the vehicle-and dexamethasone-treated groups, fitted to a linear model with a fixed slope. P(t = 25 ms): 0.72, P(t = 50 ms): 0.49, P(t = 75 ms): 0.69, P(t = 100 ms): 0.92, P(t = 125 ms): 0.81. The 95% confidence interval and the standard deviation are shown. **(C)** MSD values for the fast subpopulation for the vehicle-and dexamethasone-treated groups, fitted using a confined diffusion model. The 95% confidence interval and the standard deviation are shown. P(t = 25 ms): 0.11, P(t = 50 ms): 0.02, P(t = 75 ms): < 0.01, P(t = 100 ms): < 0.01, P(t = 125 ms): < 0.01. **(D)** MSD values for the slow subpopulation for the vehicle- and dexamethasone-treated groups, fitted using a confined diffusion model. P(t = 25 ms): 0.15, P(t = 50 ms): 0.83, P(t = 75 ms): 0.24, P(t = 100 ms): 0.27, P(t = 125 ms): 0.42. The 95% confidence interval and the standard deviation are shown. For **(BCD)**, Shapiro-Wilk test was performed to check if data is normally distributed. Significance of the results was conducted using a mixed-effect model for comparison of means between two normally distributed groups. Significant differences are indicated by an asterisk (Significance levels: P > 0.05, non-significant; P < 0.05, *; P < 0.01, **). Pearson's correlation coefficients R2 of the model fitness are shown.

To determine the mobility pattern of the molecules, the particle image correlation spectroscopy (PICS) analysis was used, which in contrast to other methods that are based on tracking of molecules, requires no a priori knowledge about the dynamical coefficients and works in principle for arbitrarily large molecule densities (Semrau and Schmidt, 2007). In PICS analysis, positions of single YFP-GR molecules between all consecutive image pairs are correlated. After elimination of random correlations, differences in molecular positions between subsequent images resulting from movement of individual molecules (i.e., squared displacements) remained. The latter were plotted in a cumulative distribution plot and fitted to a biexponential probability function, which indicated the presence of two subpopulations: a fast and a slow subpopulation based on their differing mean squared displacements (MSDs) (Fig. 5A). Next, values of subpopulation sizes and MSDs for the fast and slow subpopulations were determined and plotted for each of the selected time lags (i.e., 25, 50, 75, 100, and 125 ms). The resulting plot, depicting the size of the fast population α , showed that this parameter remained stable across time lags (Fig. 5B). Th. The plots depicting MSD function of time for both the fast (Fig. 5C) and the slow (Fig. 5D) subpopulation showed curves that reached a plateau at larger time lags. Therefore, we fitted these MSDs curves using a confined diffusion model, in which the molecules diffuse freely with an initial diffusion coefficient D_0 and are confined to an area described by a square with a side length L. Analogous analysis was performed in the fixed HEK293 cells data for comparison, results of which can be found in the Supplement 1, Fig. S1. This analysis showed the predominant presence of one fraction (94.8 ± 1.3%) with the diffusion coefficient of 0.041 ± 0.038 µm² s⁻¹. Evident

immobility of this fraction obtained for the fixed YFP-GR molecules signifies that the PICS software is a suitable tool for diffusion analyses in both mobile and immobile molecular fractions.

The results of this analysis exhibited that, in the absence of dexamethasone, the size of the fast subpopulation equaled 90.4 \pm 1.0%. Treatment with dexamethasone did not result in a significant change in the size of the fast subpopulation (77.7 \pm 0.9%) (Fig. 5B, Table 1). The initial diffusion coefficient (D_0) of the fast subpopulation was 7.90 \pm 0.53 μ m² s⁻¹ in vehicle-treated embryos. Treatment with dexamethasone significantly lowered this coefficient (3.52 \pm 0.12 μ m² s⁻¹). Similarly, the size of confinement area (L) of the fast subpopulation differed significantly between the vehicle- (1233 \pm 7 nm) and the dexamethasone-treated (912 \pm 5 nm) embryos (Fig. 5C, Table 1).

Corresponding D_0 values in the slow subpopulations were lower when compared to their fast counterpart, and equaled $0.78 \pm 0.18 \, \mu m^2 \, s^{-1}$ for the vehicle- and $0.61 \pm 0.13 \, \mu m^2 \, s^{-1}$ for the dexamethasone-treated group. These values were not affected by dexamethasone treatment. Small sizes of the confinement areas, were observed for the slow subpopulations (322 \pm 4 nm in the vehicle-, and 373 \pm 9 nm in the dexamethasone-treated group). They were three- to four-fold lower than the confinement areas observed in the fast subpopulation (Fig. 5D).

TABLE 1: Results of the analysis of the mobility pattern of YFP-GR in zebrafish embryos.

Parameter	Vehicle-treated	Dexamethasone-treated		
α [%]	90.4 ± 1.0	77.7 ± 0.9		
D_0 fast subpopulation [μ m ² s ⁻¹]	7.90 ± 0.53	3.52 ± 0.12		
D_0 slow subpopulation [μ m ² s ⁻¹]	0.78 ± 0.18	0.61 ± 0.13		
L fast subpopulation [nm]	1233 ± 7	912 ± 5		
L slow subpopulation [nm]	322 ± 4	373 ± 9		

Finally, we characterized the patterns of variability to determine the main sources of variation during the experiments. First, we analyzed the correlations between the number of molecules per image and the parameters describing the mobility pattern (size of the fast subpopulation and MSDs for fast and slow subpopulations, obtained experimentally for the time lag of 25 ms). The results of this analysis showed that there was no correlation between the number of molecules and any of these parameters (correlation

coefficients equaled 0.14, 0.46, and 0.22, respectively), indicating that the measured parameters were independent from the density of detected molecules in the FoV.

Subsequently, we used a linear mixed model approach to estimate the variance components within our data, and to determine the sources of the measurement error. In this analysis, we also included residual variance that displays the extent of variability that cannot be explained by our experimental design (See Table 2).

TABLE 2: The variance values σ^2 per source parameter and their percentage contribution towards the total variance for the given parameter.

	Source of variance					
Subscale	α		MSD fast subpopulation		MSD slow subpopulation	
	σ²	%	σ^2	%	σ²	%
Embryo	0.324	24.9	0.109	21.9	0.016	15.5
Area	0.136	10.5	0.194	39.1	0.006	5.9
Image	0.042	3.2	0.061	12.3	0.015	13.8
Residual ^a	0.800	61.4	0.132	26.7	0.069	64.8

^a Residuals account for variance that cannot be explained by the experimental design.

A quantitative presentation of the variance analysis together with percentage contributions of each source of variation are presented in Table 2. In this table, the contribution is presented of a single embryo (or an experimental day, since one embryo was imaged per day), an area within an embryo, and the consecutive images taken within the same embryo to the overall variability of the size of the fast subpopulation α , and the MSDs of the fast and slow subpopulations. For all of parameters selected in the statistical design of our data, a high percentage of the variability came from the sources that could not be controlled for during the experimental design (residual variance of 61.4% for fast subpopulation fraction size, α , 26.7% for MSD of fast subpopulation, 64.8% for MSD of slow subpopulation; see Table 2). If we exclude the contribution of the unexplained variance towards the total data variability, the linear mixed model analysis demonstrated that most of the variability is observed between imaging different embryos (total variance contribution of 24.9% for fast subpopulation size (α), 21.9% for MSD of fast and 15.5% of slow subpopulations respectively). Interestingly, imaging of different areas within an individual embryo showed a large contribution to the variance of the MSD of fast subpopulation (39.1%), but had little effect on the variation of the fast subpopulation size (10.5%) and the MSD of the slow subpopulation (5.9%). By contrast, imaging of the same cell area within an embryo contributed less to the overall variability of the results (See Table 2, Fig. S2).

4.3 DISCUSSION

LSFSMM setup

Here we have presented our implementation of a custom LSFM platform that permits imaging at SMM sensitivity not only in cultured cells, but also in larger and more physiologically relevant biological samples, such as living zebrafish embryos. In a previous study, we have used TIRF microscopy to perform SMM in zebrafish embryos, which enabled SMM analysis in the apical membrane of the outer epidermal cell layer of the embryo (Schaaf et al., 2009a). Other related techniques, such as HILO microscopy, would have permitted to reach deeper structures inside these cells, e.g., the nuclei, but the FoV of these techniques are inherently limited. Using the LSFSMM setup presented in this study, we are able to visualize individual molecules not only at the membrane of the outer cell layers, but also inside cells, and at a relatively large FoV (13.5 x 300 μ m). The developed sample mounting system allowed us to easily position specimens in the tight volume between the two objectives, permitting 3D translations and rotations in order to image the areas of interests. The FEP support and the multilayer Impa mounting permits to sustain samples of various sizes, ranging from cultured cells to zebrafish embryos, with minimal optical aberrations.

Compared to LSFM techniques commonly used for SMM studies (Chen et al., 2014b; Gao et al., 2012; Gebhardt et al., 2013; Greiss et al., 2016; Li et al., 2013; Reisser et al., 2018), the presented LSFSMM setup features a simpler optical design: in the excitation path, conventional Gaussian beams are employed, which helps also non-expert users in both alignment and experimental procedures. This illumination path also facilitates the sample mounting, as no additional components (such as a prism (Li et al., 2013) or micromirrors (Gebhardt et al., 2013; Greiss et al., 2016; Reisser et al., 2018)) are inserted. Moreover, the iSPIM configuration permits to free the top part of the FEP support, minimizing optical aberrations. Finally, the setup is assembled from commercially available parts. Altogether, this implementation will permit other laboratories to adopt the technique

as well to further expand the application of LSFM to the sub-cellular level within living organisms such as zebrafish embryos.

We demonstrated the capability of our LSFSMM platform to image individual molecules inside an intact living organism using zebrafish embryos. Our custom-designed sample support and sample-mounting procedure enabled the conduction of experiments on the same 2 dpf zebrafish embryos for several hours, while leaving the embryo in a healthy condition. At the same time this procedure helped in minimizing the optical aberrations due to the mounting medium. After the imaging sessions we always confirmed that the samples had survived the procedure stress-free, as we were able to let them further develop without mortality or obvious malformations. Moreover, in two experiments we performed imaging on a 2 dpf zebrafish embryo, kept it overnight in the microscope and continued the experiment the next day. These quality control experiments enabled us to conclude that no phototoxicity or adverse developmental effects were induced in the embryos during the imaging session and ensured the suitability of the developed method.

We therefore believe that our implementation permits innovative SMM studies in which the mobility patterns of the single molecules are analyzed not only at a single time point, but also over prolonged periods of time in the same living individual, which enables investigating the correlation between sub-cellular molecular dynamics and macroevents such as the developmental stage, metabolism, drug induction or cell and tissue differentiation. To perform this kind of experiments, the imaging chamber is also designed to support a temperature control system ensuring ideal environmental conditions for zebrafish development or other living organisms readily mountable using our setup.

The glucocorticoid receptor mobility patterns in zebrafish embryos

In this study, we have used our LSFSMM setup to analyze the dynamics of the GR inside nuclei (in particular the eYSN) in living zebrafish embryos. The results of this analysis show that single YFP-GR molecules can be detected in these nuclei with a positional accuracy of 76 nm and a temporal resolution of 25 ms. The positional accuracy in our study is relatively lower than the values of circa 40 nm, which were reported in previous

studies (Groeneweg et al., 2014; Keizer et al., 2019; Schaaf et al., 2009a). The difference is due to the implemented microscopy setup, which incorporated the detection objective of a lower NA (1.0). Analysis of the mobility pattern of the GR inside these nuclei revealed that these molecules can be divided in a fast and a slow diffusing subpopulation. The occurrence of a fast- and a slow-diffusing subpopulation of GR molecules has been observed previously for GR and other transcription factors (Groeneweg et al., 2014), and has been interpreted as GRs that diffuse freely within the nucleus, and receptors that interact with DNA respectively. In a recent study, it was shown that this fast subpopulation could, in turn, be divided into two fractions with different mobility, of which the fastest one was interpreted as receptors diffusing freely through the nucleus, and the slowest one as GRs interacting non-specifically with the DNA (Keizer et al., 2019). The biological function and implications of such GR-DNA interactions have been widely discussed in previous studies (Chen et al., 2014a; Gebhardt et al., 2013; Groeneweg et al., 2014; van Royen et al., 2007). As a result of the lower spatial and temporal resolution of the imaging, fitting of the data with a three-population model did not yield consistent results, so in the current research, we could only distinguish two GR subpopulations. Our findings show that the vast majority of the GR molecules belonged to the fast subpopulation, which constituted approximately 90% of the total GR population in the vehicle-, and 77% in the dexamethasone-treated group. This percentage is remarkably higher than previously reported sizes of this subpopulation, which were between 45 and 60% in the nuclei of cultured cells upon activation by cortisol or dexamethasone (Gebhardt et al., 2013; Groeneweg et al., 2014; Keizer et al., 2019; Presman et al., 2014). The difference between our control-treated zebrafish embryos and previously reported cortisol-treated cellular models, might be explained by a lack of a properly developed cortisol secretion in 2 dpf embryos (Alsop and Vijayan, 2009), but this does not entirely explain the differences between these models upon dexamethasone treatment. The high percentage of fast-diffusing molecules is better explained by the large size of the eYSN. A larger fraction of freely-diffusing GRs may be expected with more nuclear space available and the same amount of chromatin present.

Interestingly, GR molecules in either of the subpopulations did not move within the entire nuclear environment, but were confined to areas with a size of around 1233 nm for the fast subpopulation and 322 nm for the slow subpopulation (which is so close to the spatial resolution of our setup that this subpopulation might as well be considered

immobile). The confinement of the GRs has not been observed in previous studies on the receptor mobility patterns. In our approach, however, we were able to reconstruct the square displacements of GRs in both fractions over a longer period of time, to determine the occurrence of nuclear areas beyond which the diffusion of the GRs is restricted. Such a confinement of the fast GR subpopulation indicates that the receptors diffuse within areas surrounded by barriers, which in the nucleus could be formed by chromatin.

The (initial) diffusion coefficients of the two subpopulations equaled 7.90 \pm 0.53 μ m² s¹ for the fast subpopulation, and 0.78 \pm 0.18 μ m² s¹ for the slow subpopulation. Previous studies reported on values of the GR fast fraction diffusion coefficients to fall within the range of circa 2.5 and 9 μ m² s¹ (Gebhardt et al., 2013; Groeneweg et al., 2014; Keizer et al., 2019), which was also observed for other transcription factors, such as p53 or STATI (Mazza et al., 2012; Speil et al., 2011). We conclude that the values for the diffusion coefficients that were obtained in our approach fall well within the previously published range. The slow subpopulation was characterized by a tenfold lower diffusion coefficient. Studies performed on cellular models report that these coefficients for the GR slow subpopulation to fall within the range between 0.03 and 0.50 μ m² s¹ (Gebhardt et al., 2013; Groeneweg et al., 2014; Keizer et al., 2019).

The effect of dexamethasone treatment on the mobility patterns of the glucocorticoid receptor subpopulations

In the present study, we found that treating zebrafish embryos with dexamethasone for 3 hours prior to the imaging did not significantly alter the size of the subpopulation of GRs. However, in previous studies it has consistently been shown that dexamethasone, as a high-affinity GR agonist, decreases the size of the fast subpopulation, which is generally believed to reflect a larger fraction of GRs interacting with DNA in order to modulate the transcription of genes (Groeneweg et al., 2014). We may have failed to detect a significant decrease in population size due to a limited resolution of our experimental approach, but alternatively, the lack of a dexamethasone effect on the population size in our study may be due to the specific characteristics of the eYSN.

In addition, we show that treatment with dexamethasone leads to a smaller confinement area (912 nm) for the fast GR subpopulation. The smaller size of the confinement area for the fast GR subpopulation of the dexamethasone-treated group may be explained by the dexamethasone-activated GR molecules constituting a part of larger multi-protein complexes. These complexes, containing multiple receptor molecules and transcriptional coregulatory proteins, are present inside the cell nucleus and participate in transcription of GR target genes. Diffusion of the GR molecules in such bulky multi-protein aggregates might, therefore, be limited, resulting in the smaller confinement areas in the dexamethasone-treated groups.

Treatment with dexamethasone also resulted in a decrease of the diffusion coefficient from 7.90 to 3.52 μ m² s¹ in the fast subpopulation, and from 0.78 to 0.61 μ m² s¹ in the slow one. In a previous study conducted on cultured cells, activation with a high affinity ligand such as dexamethasone resulted in lower diffusion coefficients of the mobile fraction as well, although a smaller effect was observed (Groeneweg et al., 2014). Lower diffusion coefficients of the mobile fraction might also point to a previously described slow-diffusion state, in which GR-ligand molecules bind non-specifically to the DNA in search of their proper binding site (Keizer et al., 2019). Our results, therefore, confirm the findings established in cellular models that the interactions between ligand and receptor determine GR-DNA binding events.

It must be pointed out that the exposure time (t) used in our experiments (0.025 s) is relatively long compared to the diffusion coefficient (D_0) and size of confinement area (L) of the molecules under investigation. Due to motion blur, this may result in incorrect determination of the parameters L and D_0 . However, a set of formulas, $\frac{L^2}{12} \cdot D_0 \ge \frac{2T}{3}$, proposed by Destainville and Salomé (Destainville and Salomé, 2006), can be used to calculate the accurate values from the experimentally determined ones. Using this method, which was recently validated by Mortensen et al. (Mortensen et al., 2021), we determined confinement sizes of 1872 and 1236 nm for the vehicle- and dexamethasone-treated groups, respectively, and diffusion coefficients of 37.9 and 11.1 μ m² s⁻¹. These latter values are surprisingly high, especially compared to previous results obtained in cultured cells (Gebhardt et al., 2013; Groeneweg et al., 2014; Keizer et al., 2019), and in future studies we would like to attempt confirming these remarkably high diffusion rates of GRs in eYSN of zebrafish embryos.

Variability of the glucocorticoid receptor mobility patterns

Finally, we analyzed the sources of variation in these experiments. This analysis revealed that most of the existing variability in *in vivo* protein mobility measurements originated from imaging different embryos as well as imaging different cell areas within an individual embryo. However, while imaging different embryos constituted a major component of the data variability for all parameters measured (from 15.5% of the total variability for slow population MSD till 24.9% for the size of the fast population, see Table 2), imaging different cell areas was a major component only in the case of the fast population MSD (39.1% of the total variability). We suggest that the differences in values of the parameters between individual embryos might stem from an inherent genetic variation between different zebrafish batches. The absence of inbred zebrafish strains and resulting increased genetic variability is a factor that probably contributed to the overall variability of the GR mobility patterns. As imaging different cell areas within an individual embryo leads to an increase in variability of the fast subpopulation MSD only, it is likely that the architecture of the nucleus hinders the displacement of the fast-diffusing GRs in a cell-dependent manner. Specific nuclear chromatin organization might have led to the increase in observed differences in the MSD values of the fast subpopulation between individual nuclei of embryonic cells.

4.4 MATERIALS AND METHODS

Zebrafish. Zebrafish (*Danio rerio*) were grown, maintained and handled in compliance with the directives of the local animal welfare body. They were exposed to a 14h light and 10h dark diurnal cycle at 28°C. Fertilization was performed by natural spawning at the beginning of the light period, and the fertilized eggs were collected and maintained in E3 medium (5 mM NaCl, 0.17 mM KCl, 0.33 mM CaCl₂, 0.33 mM MgSO₄) at 28°C. All experiments were performed using embryos from the *Tg(actb2:mCherry-H2A)* zebrafish line.

Microinjection and treatment of embryos. A cDNA construct encoding eYFP-GR(alpha), hereafter referred to as YFP-GR, was genetically cloned into a PCS2+ zebrafish expression plasmid. The resulting PCS2+-eYFP-GR(alpha) plasmid was microinjected into

zebrafish embryos at the 1-2 cell stage (30 pg per embryo), resulting in a mosaic expression of the eYFP-GR(alpha) protein in the zebrafish embryo. Microinjections were done under a stereomicroscope (Leica S8APO), using a microinjector (Pneumatic Pico Pump PV820, WPI) and a micromanipulator with pulled microcapillary pipettes (model GC100F-15 from Harvard Apparatus, pulled with P-97 Micropipette Puller from Sutter Instrument). Injected eggs were left to develop in an incubator at 28°C. Viability and development of the eggs after microinjections were checked on a daily basis using a fluorescence stereomicroscope (Nikon SMZ1000 C-DSD230). To prevent embryonic pigmentation, embryos were incubated in 0.003% phenylthiourea (PTU) from 10 hpf (hours post-fertilization) onwards, and this solution was refreshed daily. For treatment with the synthetic glucocorticoid dexamethasone, a 10 mM stock solution in DMSO was prepared. The zebrafish embryos were incubated in dexamethasone (final concentration of 25 μ M) in egg water for 3 hours, at 28°C, prior to the microscopy imaging. As a control, a group of zebrafish embryos was incubated in a vehicle solution of 0.01% DMSO.

LSFSMM setup details. In the LSFSMM setup, the light from an ArKr laser (Innova 70C Spectrum, Coherent) is first passed through an acousto-optic tunable filter (AOTFnC-400.650-TN, AAOptoelectronics) to select the needed illumination wavelengths (514.5 nm for the YFP, and 568.2 nm for the mCherry molecules). After the AOTF (see Fig. 1A), the light beam is sent to a telescope (AC254-030-A-ML, AC254-250-A-ML, Thorlabs), going through a spatial filter (with a 30 µm pinhole) to produce a clean Gaussian beam. The collimated beam is then focused by a cylindrical lens (focal length of 75 mm, LJ1703RM-A, Thorlabs). An additional telescope (AC254-100-A-ML, AC254-200-A-ML, Thorlabs) is then used to illuminate the back-focal plane (BFP) aperture of a water immersion illumination objective (10X Nikon CFI Plan Fluorite Objective, 0.30 NA, 3.5 mm working distance (WD)) that will finally project the light sheet at the sample plane. The illumination path also incorporates, in a conjugated plane with the BFP of the illumination objective, a galvanometric mirror (GVS002, Thorlabs) that allows scanning the light sheet across the sample volume. In the detection path, the fluorescent signal is collected by a water-dipping detection objective (20X Olympus XLUMPLFLN Objective, 1.00 NA, 2.0 mm WD). This is passed through a motorized filter wheel (FW103H, Thorlabs) and a 200 mm tube lens (TTL200-A, Thorlabs). A periscope formed by an additional telescope (TTL100-A and TTL200-A, Thorlabs) permits an additional 2x magnification and projects the image onto the chip of a sCMOS camera (OrcaFlash4 v.3, Hamamatsu).

With this configuration (Olympus objective coupled to 200 mm tube lens and 2x periscope), the total magnification is 44.4x.

Determination of imaging parameters. To measure the thickness of the light sheet, the cylindrical lens was removed from the optical path, and the beam that was focused through a fluorescent solution by the illumination objective was imaged. Using FIJI software (Tinevez et al., 2017), the intensity line profile at the beam waist was generated and Gaussian-fitted (Fig. 2A). The standard deviation σ of the Gaussian fit was used to calculate the full width at half maximum (FWHM) of the intensity line profile as $FWHM = 2\sigma$. $\sqrt{(2 \cdot \ln 2)} \approx 2.355\sigma$, which represents the light sheet thickness waist diameter, and equaled 2 µm. The illumination field of view (FoV) was calculated as in Olarte et al. (Olarte et al., 2018), i.e., $FoV = 1.78 \cdot n \cdot \frac{\lambda}{(NA)^2}$, where n is the medium refractive index (water), λ is the illumination wavelength, and NA is the illumination objective's numerical aperture, and equaled 13.5 µm. The illumination FoV, considered as the double of the Rayleigh range, was also measured on the imaged beam profile and found to be 14.5 µm, in good agreement with the theoretical value. To obtain the excitation power density, the optical losses introduced by the illumination path were first determined. These were about 69%, due to the overfilling of the back-focal plane of the objective, to ensure homogeneous illumination. By setting the power at the input port of the microscope at 66 mW, the power at the sample plane resulted in 20.25 mW. Being the illumination focal plane area defined by the thickness (2 µm) and height (1.2 mm) of the light sheet, the resulting power density equaled ~ 0.85 kW cm⁻². To measure the optical resolution of the system, sub-diffraction fluorescent beads (100 nm in diameter) were embedded in 0.5% low melting point agarose (Impa) and placed as sample in the microscope using a Fluorinated Ethylene Propylene (FEP) support. Images were taken for beads close to the middle axis and near the surface of the produced agarose cylinder (Fig. 2C and Fig. 2E, respectively). The intensity profiles in x and ŷ were measured, Gaussian fitted, and their FWHMs calculated. Shapiro-Wilk tests were performed to confirm the normal distribution of the FWHMs values. Unpaired t-tests were then conducted to check for statistically significant difference between the values obtained for beads close to the middle axis (N = 11 beads) and near the surface (N = 11 beads), in both lateral directions (Fig. 2B).

Cultured cells fixation, mounting, and LSFSMM imaging. To determine the characteristics of the detection of a single YFP molecule in the LSFSMM setup, HEK293 cells were transfected with the plasmid PCS2+-eYFP-GR(alpha) for expression of YFP-GR. For transfection, cells were cultured in DMEM (Dulbecco's Modified Eagle Medium, Invitrogen, Waltham, MA, USA) supplemented with penicillin and streptomycin (10 µg ml⁻¹, Invitrogen), Glutamax (10 µg ml⁻¹, Invitrogen) and 10% fetal calf serum (Invitrogen) at 37°C in humidified atmosphere containing 5% of CO2. Before transfection, cells were transferred onto a sterile glass coverslip (diameter 25 mm, Marienfeld, Germany) and placed in a well of a 6-well plate. At a confluence level of 20-30%, cells were transfected with 1 µg of DNA per well, using FuGENE 6 (Roche Molecular Biochemicals, Indianapolis, USA). The transfection efficiency, determined by fluorescence microscopy screening at 48h after transfection, was approximately 20%. Two days post-transfection cells were fixed with 4% PFA. Fixed cells were then immersed in 0.5% Impa, transferred into a cut FEP support tube, and mounted in the LSFSMM system. Movies were taken using continuous illumination and a 25 ms exposure time per frame for 1000-4000 frames.

Determination of the fluorescence signals characteristics derived from individual YFP molecules. To determine the characteristics of the fluorescence signals derived from individual YFP molecules, as detected using our setup, we imaged fixed transfected HEK293 cells (3 days post-transfection). For this purpose, a two-dimensional Gaussian curve was fitted over all the fluorescence intensity spots found in the images of a fixed HEK293 cell. Subsequently, the maximal value and the full width at half maximum (FWHM) of the fitted Gaussian curves were determined in order to establish threshold values for the proper identification of intensity spots reflecting single molecules (Harms et al., 2001). Tracking of the identified intensity spots using custom software (Schmidt et al., 1996) showed single-step photobleaching for all spots, confirming that they could be attributed to individual YFP molecules.

Live zebrafish embryo mounting and LSFSMM imaging. A cut FEP tube was mounted through a glass capillary inside the incubation chamber. Lmpa solutions (2% and 0.5% in E3 medium) were heated up to 70°C, and 2% Impa was applied to the distal and proximal ends of the cut tube as well as at the basis (see Fig. 1) and left to solidify. Naturally hatched zebrafish embryos were transferred to a petri dish containing E3 medium with tricaine (100 mg L-1). Subsequently, an embryo was transferred to a glass bottom petri

dish, the E3 medium was removed, and 0.5% Impa (cooled down, with 100 mg L-1 tricaine) was poured onto the glass petri dish. While still liquid, a drop of 0.5% Impa, together with the zebrafish embryo, was aspired through a glass pipette and carefully transferred into the FEP support, on top of the already present 2% Impa layer. The incubation chamber with the FEP tube containing the zebrafish embryo was mounted into the setup, on top of a platform connected to a xyz motorized stage (8MTF from Standa for xy-translations, 8302 Picomotor Actuator from Newport, connected to LX10/M from Thorlabs, for z-translations). The glass capillary was connected, using a screw, to a stepper motor (L4018S1204-M6, Nanotec) for sample rotation. E3 medium with tricaine (100mg L⁻¹) was poured into the imaging chamber at room temperature, to completely immerse the sample and the tip of the objectives. Using a custom-made software in LabVIEW, the position of the sample in x, y, and z was adjusted to be in the FoV of the detection objective. Rotation around the y-axis of the specimen and the movement in \hat{z} of the light sheet provided additional alignment flexibility and possibilities to change the imaged area. The position of the detection objective was manually adjusted. A region of interest (ROI) was selected based on the mCherry signal (from the nuclear mCherry-H2A protein, illumination wavelength 568.2 nm, emission filter FF01-620/14-25, Semrock) to localize the nuclei. The YFP signal (from the YFP-GR protein, illumination wavelength 514.5 nm, emission filter FF01-535/22-25, Semrock) was chosen to confirm the expression of the fluorescently labeled GR. Once a ROI was selected, a movie of the YFP signal was recorded using continuous illumination and a 25 ms exposure time per frame for 1000-4000 frames. The PTU treatment prevented the pigmentation of the sample, i.e., avoiding light-sheet shadowing effects. In case a shadowing effect would have occurred, the region of interest could have been changed through sample translation/rotation.

Live imaging using the muviSPIM setup. To check the presence and localization of GR in the zebrafish embryos, lower resolution imaging was performed. A PTU-treated, non-dechorionated 1 dpf embryo was embedded in a 1.5% Impa cylinder and immersed in the incubation chamber of a custom-made LSFM setup in the muviSPIM configuration (Krzic et al., 2012). The incubation chamber was filled with E3 medium with tricaine (400 mg L⁻¹) and its temperature maintained at 26.5°C. Z-stack images were acquired of the embryos for both the YFP and mCherry signals every 15 minutes during 22 hours. A sequential illumination scheme was employed to illuminate both sides of the embryo.

Light sheets (at 488 nm for YFP excitation and at 561 nm for mCherry excitation) were generated through the coupling of cylindrical lenses (LJ1703RM-A, Thorlabs, focal length 75mm) and air objectives (4X Nikon Plan Fluorite Imaging Objective, 0.13 NA, 17.2 mm WD). The emitted photons were collected through a 10X Nikon CFI Plan Fluorite Objective (0.30 NA, 3.5 mm WD) and a sCMOS camera (OrcaFlash4 v.2, Hamamatsu).

Data Analysis. To study the mobility of proteins, Particle Image Correlation Spectroscopy (PICS) analysis was used, described in detail previously (Schütz et al., 1997; Semrau and Schmidt, 2007). In PICS analysis, individual molecules are not tracked, but all possible correlations between the locations of molecules in two image frames are determined. This way, a cumulative distribution function of distances is generated, which includes both contributions from diffusing molecules as well as random correlations between unrelated molecules in the two frames. The latter follows a linear relation in the cumulative distribution plot and is subtracted prior to further analysis, yielding cumulative probability distributions of displacements r_i for each of the time lags, which are fitted to a one- or two-fractional model. The former is described by the equation:

$$(r^2, t_{lag}) = 1 - exp\left(-\frac{r^2}{r_0^2(t_{lag})}\right) (1),$$

which assumes the probability of the molecule starting at the arbitrary origin can be found within a circle of a radius r at the time lag t_{lag} . Alternatively, in case the population of molecules could be divided into two subpopulations with different mobility, Equation (1) was transformed into the equation:

$$P\left(r^{2},t_{lag}\right)=1-\left[\alpha\cdot exp\left(-\frac{r^{2}}{r_{1}^{2}\left(t_{lag}\right)}\right)+\left(1-\alpha\right)\cdot exp\left(-\frac{r^{2}}{r_{2}^{2}\left(t_{lag}\right)}\right)\right] \ (2),$$

where the displacements r of two subpopulations are denoted by r_1 and r_2 , and the relative size of these subpopulations by α and $1 - \alpha$.

A multistep analysis was performed for each movie acquired, analyzing correlations over five different time lags (25, 50, 75, 100, and 125 ms). Due to photobleaching the number of displacements r^2 becomes smaller with increasing time lag. Nonetheless, even

for such higher time lags, a minimal number of displacements remains in the order of 10^5 , as the number of images per movie is large (1000-4000 images per movie). To examine the type of diffusion of these subpopulations of molecules, the values of r_1^2 and r_2^2 were plotted against the time lag. The positional accuracy (dx) led to a constant offset in r_i^2 of $4 \cdot (dx)^2$. In case this plot showed a linear relationship, a Brownian diffusion was assumed, and a curve was fitted with the equation:

$$r_i^2(t_{lag}) = 4 \cdot D \cdot t_{lag} \quad (3),$$

in which D is the diffusion coefficient. If the plot reached a plateau at larger time lags, a confined model was fitted with the Equation (4):

$$r_i^2(t_{lag}) = \frac{L^2}{3} \cdot \left[1 - exp\left(-\frac{12 \cdot D_0 \cdot t_{lag}}{L^2} \right) \right]$$
 (4),

in which the molecules diffuse freely with an initial diffusion coefficient D_0 and are confined to an area described by a square with a side length L.

Experimental Design. On three experimental days, one zebrafish embryo was selected for the LSFSMM imaging per experimental (vehicle- and dexamethasone-treated) group, and in each of the selected embryos, three separate areas were imaged, yielding three independent movies of 1000-4000 consecutive frames. All movies were analyzed individually, resulting in a value per movie for α , r_1^2 and r_2^2 for each time lag. In the analysis of the HEK293 cells, one cell was selected for single peak shape analysis and single-step photobleaching. The values of α , r_1^2 and r_2^2 were also determined in fixed HEK293 cell data for comparison (See Supplement 1, Fig. S1, Table S1).

Statistical Analysis. Statistical analysis was performed in R statistical software (R: a language and environment for statistical computing, https://www.R-project.org). Values of α and r_1^2 were compared between the two groups, vehicle- and dexamethasone-treated, pooling all the values from individual images from three experimental days. In order to check if data were normally distributed, a Shapiro-Wilk test was performed. Significance of the results was conducted using a mixed-effect model for comparison of means between two normally distributed groups.

A hierarchical linear model was used to estimate the variance components within a hierarchically nested sampling design, between embryos from each experimental day, different cell nuclei in a single embryo, and different images of the same nucleus in an individual embryo. The model also took into account the residual variability component, which accounts for the variability that cannot be explained by the parameters used in our experimental design. As a single, time lapse, image might contain up to 30 thousand trajectories of single molecules, correlation coefficients were calculated for the relationships between number of such trajectories and fast-diffusing fraction size, α , as well as mean squared displacements of fast- and slow-diffusing fractions, r_1^2 and r_2^2 . Subsequently, sources of potential variability within the experimental design were estimated by using a linear mixed model with square root transformation of r_1^2 , to ensure that the random errors follow a Gaussian distribution. Use of linear mixed models extends the applicability of a simple linear model, since the former incorporate both fixed and random effects. Random effects represent the special case of fixed effects that are nested within the data, and demonstrate a subject- or group-specific variation. Linear mixed models are commonly used to account for the data where measurements are made on clusters of related statistical units (Bates et al., 2015; Luke, 2017).

The fitting of the linear mixed model was performed in R package, *Ime4* (Bates et al., 2015). To evaluate the contribution of each variance component towards the total variability, caterpillar plots were plotted to report the estimated group intercepts and the associated 95% confidence intervals, as a measure of relative deviation from the global mean of the data (See Supplement 1, Fig. S2). For instance, an average value of one experimental day contained measurements of the same parameter obtained in all the areas of an embryo within the same day, while the analogous average for a single area entailed only those measurements that were acquired during repetitive imaging of only one area within the embryo. Those values were then sorted from the ones deviating most negatively from the total average to the ones that deviated most positively. Sorted deviations of the values were ultimately juxtaposed, in order to assess which variance component constitutes the major source of the measurement error. The corresponding values of variance for each of the parameter measured together with residual variance were calculated and presented together with their percentage contribution towards the total data variability.

FUNDING

Ministerio de Economía y Competitividad (RYC-2015-17935, CEX2019-000910-S); Fundación Cellex (Mir-Puig); Laserlab-Europe (871124); Generalitat de Catalunya (CERCA); Fundación Cellex; Horizon 2020 Framework Programme (721537).

ACKNOWLEDGMENTS

We thank Dr. Verena Ruprecht from the Centre for Genomic Regulation (CRG, Barcelona) for the Tg(actb2:mCherry-H2A) embryos, Prof. Dr. Thomas Schmidt (Leiden University) for support with the analysis of the GR mobility pattern, Dr. Maria Marsal and Dr. Jordi Andilla (ICFO, Barcelona) for scientific advice and logistic assistance. MB and RJG are supported from funding from the European Union's Horizon 2020 research and innovation programme under the Marie Sklodowska-Curie grant agreement Imageln-Life (No 721537). We acknowledge financial support from the Spanish Ministry of Economy and Competitiveness through the "Severo Ochoa" program for Centres of Excellence in R&D (CEX2019-000910-S), from Fundació Privada Cellex, Fundació Mir-Puig, Generalitat de Catalunya through the CERCA program and Laserlab-Europe EU-H2020 (871124). EJG acknowledges MINECO/FEDER Ramón y Cajal program (RYC-2015-17935).

DISCLOSURES

The authors declare no conflict of interests.

DATA AVAILABILITY

Data underlying the results presented in this paper are not publicly available at this time but may be obtained from the authors upon reasonable request.

AUTHORS CONTRIBUTIONS

MB, RJG, and MJMS designed the experiments. MB and RJG conducted the experiments. MB, GCO, and EJG built the microscopes and implemented the acquisition software. MB developed the sample mounting system, RJG conducted the single molecule analysis, PvH conducted the data statistical analysis. MB and RJG wrote the manuscript, all authors reviewed and edited the manuscript. EJG, MJMS and PLA supervised the work.

REFERENCES

- Aguet, F., Upadhyayula, S., Gaudin, R., Chou, Y.-Y., Cocucci, E., He, K., Chen, B.-C., Mosaliganti, K., Pasham, M., Skillern, W., et al. (2016). Membrane dynamics of dividing cells imaged by lattice light-sheet microscopy. *Mol. Biol. Cell* **27**, 3418–3435.
- **Alsop, D. and Vijayan, M. M.** (2009). Molecular programming of the corticosteroid stress axis during zebrafish development. *Comp. Biochem. Physiol. A. Mol. Integr. Physiol.* **153**, 49–54.
- **Axelrod, D.** (2001). Total internal reflection fluorescence microscopy in cell biology. *Traffic Cph. Den.* **2**, 764–774.
- Bates, D., Mächler, M., Bolker, B. and Walker, S. (2015). Fitting Linear Mixed-Effects Models Using Ime4.

 J. Stat. Softw. Vol 1 Issue 1 2015.
- **Bobroff, N.** (1986). Position measurement with a resolution and noise-limited instrument. *Rev. Sci. Instrum.* **57**, 1152–1157.
- Carvalho, L. and Heisenberg, C.-P. (2010). The yolk syncytial layer in early zebrafish development. *Trends Cell Biol.* **20**, 586–592.
- Chen, J., Zhang, Z., Li, L., Chen, B.-C., Revyakin, A., Hajj, B., Legant, W., Dahan, M., Lionnet, T., Betzig, E., et al. (2014a). Single-molecule dynamics of enhanceosome assembly in embryonic stem cells. *Cell* 156. 1274–1285.
- Chen, B.-C., Legant, W. R., Wang, K., Shao, L., Milkie, D. E., Davidson, M. W., Janetopoulos, C., Wu, X. S., Hammer, J. A. 3rd, Liu, Z., et al. (2014b). Lattice light-sheet microscopy: imaging molecules to embryos at high spatiotemporal resolution. *Science* **346**, 1257998–1257998.
- Chu, L.-T., Fong, S. H., Kondrychyn, I., Loh, S. L., Ye, Z. and Korzh, V. (2012). Yolk syncytial layer formation is a failure of cytokinesis mediated by Rock1 function in the early zebrafish embryo. *Biol. Open* 1, 747–753.
- **Destainville, N. and Salomé, L.** (2006). Quantification and correction of systematic errors due to detector time-averaging in single-molecule tracking experiments. *Biophys. J.* **90**, L17-9.
- Detrich, H. W., III, H. W. D., Westerfield, M. and Zon, L. I. (2011). The Zebrafish: Genetics, Genomics and Informatics. Academic Press.

- Gao, L., Shao, L., Higgins, C. D., Poulton, J. S., Peifer, M., Davidson, M. W., Wu, X., Goldstein, B. and Betzig, E. (2012). Noninvasive imaging beyond the diffraction limit of 3D dynamics in thickly fluorescent specimens. *Cell* 151, 1370–1385.
- Garcia, D. A., Fettweis, G., Presman, D. M., Paakinaho, V., Jarzynski, C., Upadhyaya, A. and Hager, G. L. (2021). Power-law behavior of transcription factor dynamics at the single-molecule level implies a continuum affinity model. *Nucleic Acids Res.*
- Gebhardt, J. C. M., Suter, D. M., Roy, R., Zhao, Z. W., Chapman, A. R., Basu, S., Maniatis, T. and Xie, X. S. (2013). Single-molecule imaging of transcription factor binding to DNA in live mammalian cells. Nat. Methods 10, 421–426.
- **Greiss, F., Deligiannaki, M., Jung, C., Gaul, U. and Braun, D.** (2016). Single-Molecule Imaging in Living Drosophila Embryos with Reflected Light-Sheet Microscopy. *Biophys. J.* **110**, 939–946.
- Groeneweg, F. L., Royen, M. E. van, Fenz, S., Keizer, V. I. P., Geverts, B., Prins, J., Kloet, E. R. de, Houtsmuller, A. B., Schmidt, T. S. and Schaaf, M. J. M. (2014). Quantitation of Glucocorticoid Receptor DNA-Binding Dynamics by Single-Molecule Microscopy and FRAP. *PLOS ONE* **9**, e90532.
- Harms, G. S., Cognet, L., Lommerse, P. H., Blab, G. A. and Schmidt, T. (2001). Autofluorescent proteins in single-molecule research: applications to live cell imaging microscopy. *Biophys. J.* 80, 2396– 2408.
- **lino, R., Koyama, I. and Kusumi, A.** (2001). Single molecule imaging of green fluorescent proteins in living cells: E-cadherin forms oligomers on the free cell surface. *Biophys. J.* **80**, 2667–2677.
- Keizer, V. I. P., Coppola, S., Houtsmuller, A. B., Geverts, B., van Royen, M. E., Schmidt, T. and Schaaf, M. J. M. (2019). Repetitive switching between DNA-binding modes enables target finding by the glucocorticoid receptor. J. Cell Sci. 132, jcs217455.
- **Kimmel, C. B. and Law, R. D**. (1985). Cell lineage of zebrafish blastomeres. II. Formation of the yolk syncytial layer. *Dev. Biol.* **108**, 86–93.
- Kimmel, C. B., Ballard, W. W., Kimmel, S. R., Ullmann, B. and Schilling, T. F. (1995). Stages of embryonic development of the zebrafish. *Dev. Dyn. Off. Publ. Am. Assoc. Anat.* **203**, 253–310.
- Krzic, U., Gunther, S., Saunders, T. E., Streichan, S. J. and Hufnagel, L. (2012). Multiview light-sheet microscope for rapid in toto imaging. *Nat. Methods* **9**, 730–733.
- **Li, H. and Vaughan, J. C.** (2018). Switchable Fluorophores for Single-Molecule Localization Microscopy. *Chem. Rev.* **118**, 9412–9454.

- **Li, Y., Hu, Y. and Cang, H.** (2013). Light sheet microscopy for tracking single molecules on the apical surface of living cells. *J. Phys. Chem. B* **117**, 15503–15511.
- Liu, Z., Legant, W. R., Chen, B.-C., Li, L., Grimm, J. B., Lavis, L. D., Betzig, E. and Tjian, R. (2014). 3D imaging of Sox2 enhancer clusters in embryonic stem cells. *eLife* **3**, e04236–e04236.
- Lommerse, P. H. M., Blab, G. A., Cognet, L., Harms, G. S., Snaar-Jagalska, B. E., Spaink, H. P. and Schmidt, T. (2004). Single-Molecule Imaging of the H-Ras Membrane-Anchor Reveals Domains in the Cytoplasmic Leaflet of the Cell Membrane. *Biophys. J.* **86**, 609–616.
- **Luke, S. G.** (2017). Evaluating significance in linear mixed-effects models in R. *Behav. Res. Methods* **49**, 1494–1502.
- Luo, F., Qin, G., Xia, T. and Fang, X. (2020). Single-Molecule Imaging of Protein Interactions and Dynamics. *Annu. Rev. Anal. Chem. Palo Alto Calif* 13, 337–361.
- Mazza, D., Abernathy, A., Golob, N., Morisaki, T. and McNally, J. G. (2012). A benchmark for chromatin binding measurements in live cells. *Nucleic Acids Res.* **40**, e119–e119.
- Mir, M., Reimer, A., Haines, J. E., Li, X.-Y., Stadler, M., Garcia, H., Eisen, M. B. and Darzacq, X. (2017).

 Dense Bicoid hubs accentuate binding along the morphogen gradient. *Genes Dev.* **31**, 1784–1794.
- Mir, M., Reimer, A., Stadler, M., Tangara, A., Hansen, A. S., Hockemeyer, D., Eisen, M. B., Garcia, H. and Darzacq, X. (2018). Single Molecule Imaging in Live Embryos Using Lattice Light-Sheet Microscopy. *Methods Mol. Biol. Clifton NJ* **1814**, 541–559.
- Mortensen, K. I., Flyvbjerg, H. and Pedersen, J. N. (2021). Confined Brownian Motion Tracked With Motion Blur: Estimating Diffusion Coefficient and Size of Confining Space. *Front. Phys.* **8**, 601–601.
- Olarte, O. E., Andilla, J., Gualda, E. J. and Loza-Alvarez, P. (2018). Light-sheet microscopy: a tutorial. *Adv. Opt. Photonics* 10, 111–179.
- Paakinaho, V., Presman, D. M., Ball, D. A., Johnson, T. A., Schiltz, R. L., Levitt, P., Mazza, D., Morisaki, T., Karpova, T. S. and Hager, G. L. (2017). Single-molecule analysis of steroid receptor and cofactor action in living cells. *Nat. Commun.* 8, 15896–15896.
- Presman, D. M., Ogara, M. F., Stortz, M., Alvarez, L. D., Pooley, J. R., Schiltz, R. L., Grøntved, L., Johnson, T. A., Mittelstadt, P. R., Ashwell, J. D., et al. (2014). Live cell imaging unveils multiple domain

- requirements for in vivo dimerization of the glucocorticoid receptor. *PLoS Biol.* **12**, e1001813–e1001813.
- Reisser, M., Palmer, A., Popp, A. P., Jahn, C., Weidinger, G. and Gebhardt, J. C. M. (2018). Single-molecule imaging correlates decreasing nuclear volume with increasing TF-chromatin associations during zebrafish development. *Nat. Commun.* **9**, 5218.
- Ritter, J. G., Veith, R., Siebrasse, J.-P. and Kubitscheck, U. (2008). High-contrast single-particle tracking by selective focal plane illumination microscopy. *Opt. Express* **16**, 7142–7152.
- Ritter, J. G., Veith, R., Veenendaal, A., Siebrasse, J. P. and Kubitscheck, U. (2010). Light sheet microscopy for single molecule tracking in living tissue. *PloS One* **5**, e11639.
- Schaaf, M. J. M., Chatzopoulou, A. and Spaink, H. P. (2009a). The zebrafish as a model system for gluco-corticoid receptor research. *Comp. Biochem. Physiol. A. Mol. Integr. Physiol.* 153, 75–82.
- Schaaf, M. J. M., Koopmans, W. J. A., Meckel, T., van Noort, J., Snaar-Jagalska, B. E., Schmidt, T. S. and Spaink, H. P. (2009b). Single-molecule microscopy reveals membrane microdomain organization of cells in a living vertebrate. *Biophys. J.* **97**, 1206–1214.
- Schmidt, T., Schütz, G. J., Baumgartner, W., Gruber, H. J. and Schindler, H. (1996). Imaging of single molecule diffusion. *Proc. Natl. Acad. Sci. U. S. A.* **93**, 2926–2929.
- Schütz, G. J., Schindler, H. and Schmidt, T. (1997). Single-molecule microscopy on model membranes reveals anomalous diffusion. *Biophys. J.* **73**, 1073–1080.
- **Semrau, S. and Schmidt, T.** (2007). Particle Image Correlation Spectroscopy (PICS): Retrieving Nanometer-Scale Correlations from High-Density Single-Molecule Position Data. *Biophys. J.* **92**, 613–621.
- Speil, J., Baumgart, E., Siebrasse, J.-P., Veith, R., Vinkemeier, U. and Kubitscheck, U. (2011). Activated STATI transcription factors conduct distinct saltatory movements in the cell nucleus. *Biophys. J.* 101, 2592–2600.
- **Spille, J.-H., Kaminski, T., Königshoven, H.-P. and Kubitscheck, U.** (2012). Dynamic three-dimensional tracking of single fluorescent nanoparticles deep inside living tissue. *Opt. Express* **20**, 19697–19707.
- Stainier, D. Y., Fouquet, B., Chen, J. N., Warren, K. S., Weinstein, B. M., Meiler, S. E., Mohideen, M. A., Neuhauss, S. C., Solnica-Krezel, L., Schier, A. F., et al. (1996). Mutations affecting the formation and function of the cardiovascular system in the zebrafish embryo. *Dev. Camb. Engl.* 123, 285–292.

- Tinevez, J.-Y., Perry, N., Schindelin, J., Hoopes, G. M., Reynolds, G. D., Laplantine, E., Bednarek, S. Y., Shorte, S. L. and Eliceiri, K. W. (2017). TrackMate: An open and extensible platform for single-particle tracking. *Methods San Diego Calif* 115, 80–90.
- **Tokunaga, M., Imamoto, N. and Sakata-Sogawa, K.** (2008). Highly inclined thin illumination enables clear single-molecule imaging in cells. *Nat. Methods* **5**, 159–161.
- van Royen, M. E., Cunha, S. M., Brink, M. C., Mattern, K. A., Nigg, A. L., Dubbink, H. J., Verschure, P. J., Trapman, J. and Houtsmuller, A. B. (2007). Compartmentalization of androgen receptor protein-protein interactions in living cells. *J. Cell Biol.* 177, 63–72.
- Williams, D. W., Müller, F., Lavender, F. L., Orbán, L. and Maclean, N. (1996). High transgene activity in the yolk syncytial layer affects quantitative transient expression assays in zebrafish Danio rerio) embryos. *Transgenic Res.* **5**, 433–442.
- Wu, Y., Ghitani, A., Christensen, R., Santella, A., Du, Z., Rondeau, G., Bao, Z., Colón-Ramos, D. and Shroff, H. (2011). Inverted selective plane illumination microscopy (iSPIM) enables coupled cell identity lineaging and neurodevelopmental imaging in Caenorhabditis elegans. Proc. Natl. Acad. Sci. U. S. A. 108, 17708–17713.
- **Yokota, H.** (2020). Fluorescence microscopy for visualizing single-molecule protein dynamics. *Biochim. Biophys. Acta Gen. Subj.* **1864**, 129362–129362.
- Yu, B., Yu, J., Li, W., Cao, B., Li, H., Chen, D. and Niu, H. (2016). Nanoscale three-dimensional single particle tracking by light-sheet-based double-helix point spread function microscopy. *Appl. Opt.* **55**, 449–453.

SUPPLEMENTARY FIGURES

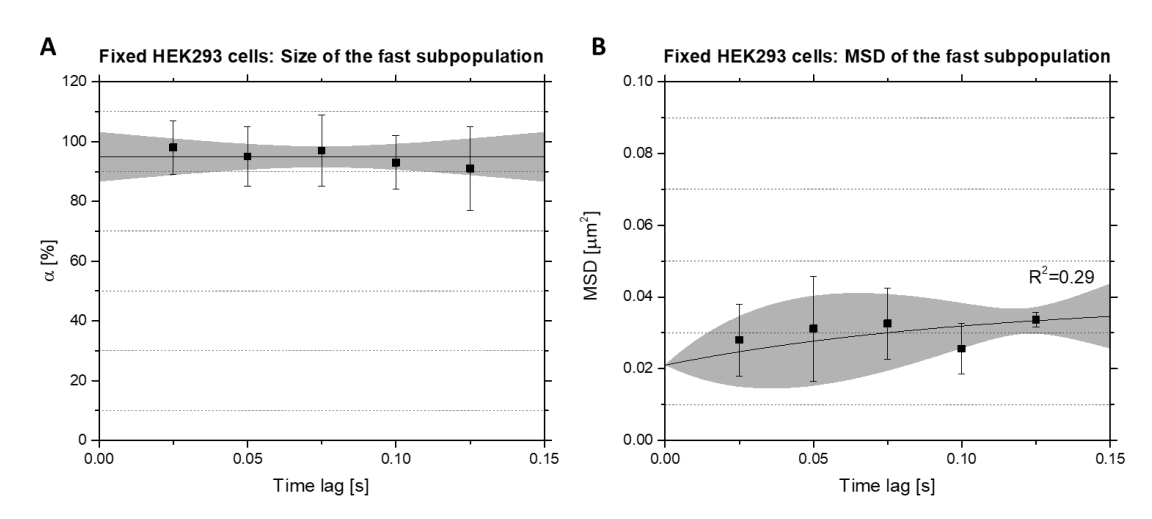


FIGURE S1: Analysis of the mobility pattern of YFP-GR in fixed HEK293 cells. (A) Fast subpopulation fraction size fitted to a linear model with a fixed slope. Since $94.8 \pm 1.3\%$ of all the YFP-GR belong to one, fast-diffusing population, impact of the slow-diffusing fraction can in this case be neglected. (B) MSD values for the fast subpopulation, fitted using a confined diffusion model. The offset value of the measurement is $0.023 \ \mu m \ s^{-1}$, and equals to $4 \cdot (dx)^2$, with the (dx) equaling 76 nm. The MSDs of this population are so close to the offset that the molecules can be considered immobile. In both graphs, the 95% confidence interval, standard deviation, and Pearson's correlation coefficients R^2 of the model fitness are shown.

TABLE S1: Results of the analysis of the mobility pattern of YFP-GR in fixed HEK293 cells.

Parameter	Fixed HEK293 cells
α [%]	94.8 ± 1.3
$m{D_0}$ fast subpopulation [$\mu m^2 s^{-1}$]	0.041 ± 0.038
L fast subpopulation [nm]	233 ± 151

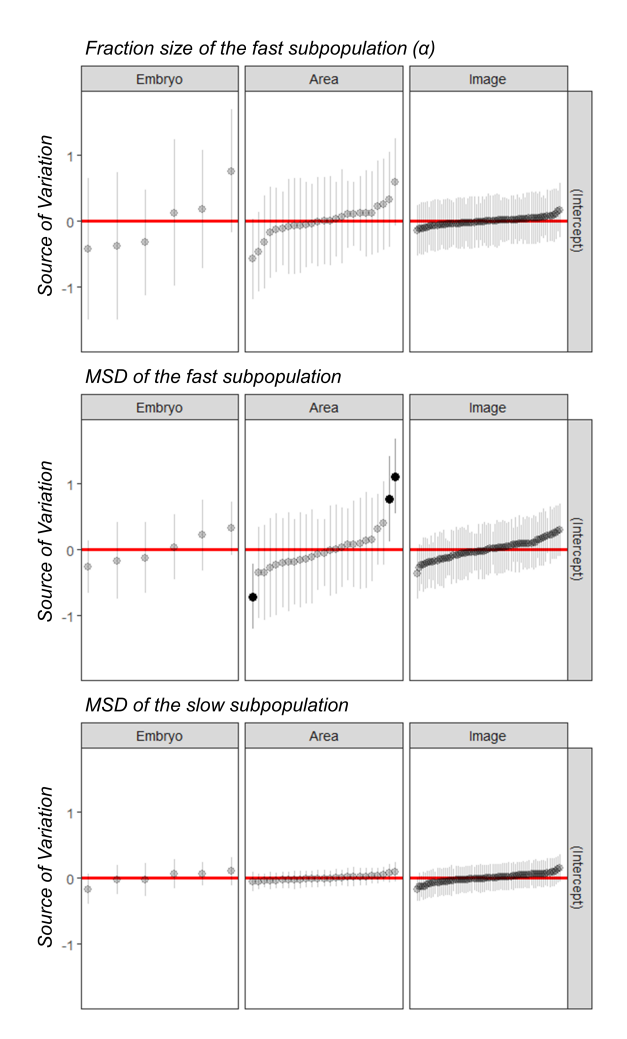


FIGURE S2: Results of the mixed linear model analysis reveal potential sources of the data variability. To establish effect ranges, data were logit-transformed and presented on a logit scale. Caterpillar plots present the effect from random components as the deviation of the group intercepts from the global mean of the data. The effect range represents the deviation between different embryos, different areas within an embryo, and different images of the same area within an embryo, that are parts of the total measurement error in the mobile fraction size, α (A), MSD of the mobile fraction (B), and MSD of the immobile fraction (C). Red lines indicate the global mean of the data, while black dots signify significant deviations from the global mean among embryos, areas, and images. The data points are sorted from the ones most negatively deviating from the global average to the ones that deviate most positively.

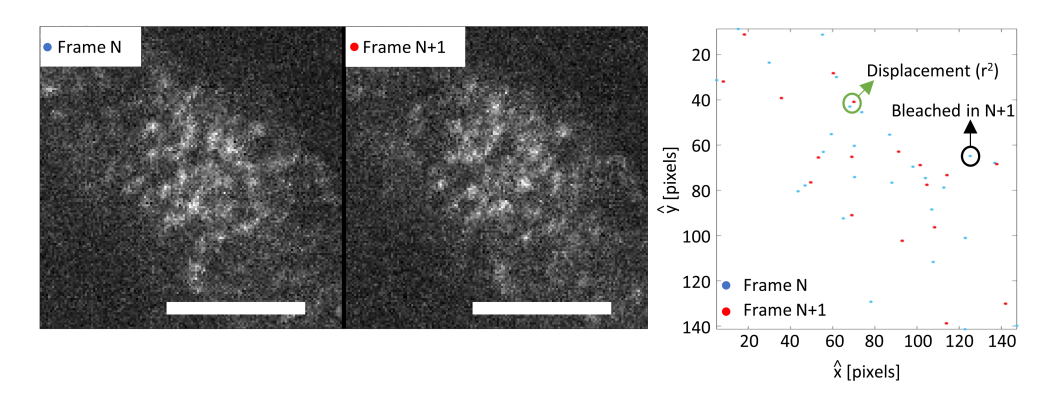


FIGURE S3: Representative image of a displacement analysis based on a single image pair (Frames N and N+1). Not every molecule is positionally correlated due to the photobleaching. The average number of peaks per image here equals 23.0. This image pair is a part of a 3000-image movie. For the entire movie, the total number of displacements found in the 2999 image pairs equals to 35467.

5. SUMMARY AND DISCUSSION

5.1 SUMMARY OF THE THESIS

Single-molecule microscopy (SMM) techniques constitute potent tools that facilitate the imaging of individual particles over time. With help of these techniques, it is possible to analyze the dynamics of single molecules in a variety of biological systems and to study the impact of structural and biochemical components on their mobility patterns. In this thesis, we have optimized three advanced fluorescence microscopy techniques and applied them to perform SMM in the zebrafish embryo model. We have used two proteins to investigate the consistency and reproducibility of the results obtained using our *in vivo* SMM approaches: H-Ras as a model membrane protein and the glucocorticoid receptor (GR) as a model nuclear protein.

In Chapter 2 of this thesis, we have investigated the mobility patterns of the full-length functional H-Ras protein in the epidermal apical membranes of living two-day-old zebrafish embryos using TIRF microscopy. We found that in these cells H-Ras is present in two distinctive fractions, one that is fast-diffusing and another that is slow-diffusing. Interestingly, we discovered that both H-Ras fractions do not diffuse freely throughout the entire surface of the plasma membrane, but that they show confinement to specific membrane microdomains. By studying a constitutively active mutant H-Ras protein, we demonstrated that the activation status of the H-Ras protein plays a role in defining its dynamics. In particular, the diffusion coefficient and the confinement area of the fastdiffusing fraction were increased compared to the wild type H-Ras protein. Subsequently, to determine the nature of the membrane microdomains that form the confinement zones, we tested whether these zones represented so-called lipid rafts, which are dependent on the presence of cholesterol and the actin filaments attached to the plasma membrane. We found that cholesterol depletion and disruption of the actin cytoskeleton had a similar effect on the H-Ras mobility, also increasing the diffusion coefficient and the confinement area of the fast-diffusing fraction, suggesting that the fastdiffusing fraction of the inactive form of H-Ras resides in lipid rafts, whereas for the active form this fraction is predominantly located in larger, cholesterol- and actin-independent domains. Furthermore, by analyzing the sources variability of the data, we demonstrated that the differences between individual cells within a tissue, rather than differences between embryos, were the main contributors to the variation in our results.

Following the TIRFM studies performed on H-Ras in vivo, in Chapter 3 we employed multifocal 2PEF microscopy, which significantly reduces out-of-focus phototoxicity to the biological samples along with the photobleaching of the fluorophores. By the use of this technology, we succeeded in visualizing H-Ras anchor molecules over longer periods, which enabled us to reconstruct their trajectories. This way, we departed from the population-based description of the single-molecule dynamics and focused on analyzing molecular trajectories of individual H-Ras anchor molecules. We used this approach to analyze the mobility pattern of the H-Ras membrane anchor fused to GFP in the membranes of epidermal cells of zebrafish embryos. This imaging approach enabled us to solely detect the slow-diffusing population of molecules and perform a detailed analysis of their dynamic behavior. The analysis of the trajectories revealed that the GFPtagged H-Ras anchors of the slow-diffusing subpopulation continuously switch between a diffusing and a hopping mode. Strikingly, we found that the time they spend in the hopping state is relatively short compared to the time spent in the diffusing state, implying that the anchors exhibit an anomalous mode of diffusion, which could be referred to as molecular hopping.

Finally, in **Chapter 4** of this thesis, we aimed to test whether it is also possible to perform SMM beyond the membranes of the zebrafish epidermal cells. To this end, we employed LSF microscopy that creates a plane of light, called a light sheet, which only excites the fluorophores present in the illuminated plane. For long-term imaging of the zebrafish embryos using this microscopy technique, we designed a custom-made imaging chamber. With the customized LSF microscopy setup in place, we visualized single glucocorticoid receptors (GRs) inside the yolk syncytial nuclei (YSN) of one-day-old embryos, and analyzed their mobility patterns. As previously found in cultured cells, we identified a fast- and a slow-diffusing population of GRs in our *in vivo* system. By treating the embryos with the GR agonist, dexamethasone, we decreased the diffusion of the GRs, confirming results previously found in cultured cells and thereby validating the *in vivo* measurements. Similarly to the H-Ras data, most of the variability in the results came from imaging different cells within an individual zebrafish embryo.

5.2 THE MOBILITY PATTERNS OF H-RAS AND C10H-RAS IN EPIDERMAL CELLS OF LIVING ZEBRAFISH EMBRYOS (Chapters 2 and 3)

To analyze the mobility patterns of H-Ras, H-Ras mutants and C10H-Ras molecules in the membranes of epidermal cells in zebrafish embryos in detail, we utilized two different SMM techniques. By using TIRF microscopy, we were able to image individual proteins with a temporal resolution of 25 ms, which enabled us to determine the existence of two H-Ras subpopulations with different diffusion coefficients and the size of their confinement area. As the photobleaching in the TIRF illumination significantly affects the lifespan of the fluorescent molecules, it is impractical to reconstruct the tracks of molecules over more than a few image frames for the vast majority of molecules. Hence, to bypass this issue, we employed a 2PEF microscopy technique that, due to its two-photon excitation mode, allowed us to limit photobleaching and increase the lifetime of the fluorophores genetically fused to the H-Ras anchors and, consequently, properly reconstruct their trajectories.

Throughout the first investigations of the H-Ras mobility patterns in which we used TIRF microscopy, we observed that the H-Ras proteins are present in two distinctive subpopulations, a fast- and a slow-diffusing one, which both showed confined diffusion. The presence of the two subpopulations was consistent and reproducible between different experimental approaches that we employed, i.e., between experiments performed in HEK293T cells and the ones performed in epidermal cells of zebrafish embryos, between different developmental stages of the zebrafish embryos, and between the full-length, functional H-Ras protein and its membrane anchor, C10H-Ras, as well as its constitutively active (H-Ras^{V12}) and inactive (H-Ras^{N17}) mutants. The existence of different dynamic subpopulations validated our *in vivo* experimental approach, as the fast- and slow-diffusing fractions had already been observed in several single-molecule studies conducted in cultured cells on full-width H-Ras (Lommerse et al., 2005; Lommerse et al., 2006) and on its anchoring domain C10H-Ras, which had also been studied in zebrafish embryos (Lommerse et al., 2004; Schaaf et al., 2009).

During our investigations, we noticed that the full-length H-Ras protein traversed plasma membranes of zebrafish epidermal cells with a lower diffusion coefficient than

it did in the membranes of the HEK293T cells. This phenomenon held for both fractions of the functional H-Ras protein, however, we did not observe similar behavior in the case of C10H-Ras which showed slower diffusion in both systems. This suggested that interactions between the functional full-width H-Ras protein and cell-specific components inside the plasma membrane or cytoplasm are also involved in determining its mobility patterns. This hypothesis was strengthened by the fact that fast-diffusing fractions of H-Ras and its anchor were all confined to specific areas of the plasma membrane, which has not been reported in all previous studies (Lommerse et al., 2006; Schaaf et al., 2009). We speculate that the lack of confinement of the fast-diffusing subpopulation in earlier studies stems from the combined effects of short time ranges used (< 50 ms) and larger variability due to smaller sample sizes.

In the next set of experiments, we evaluated the role of H-Ras activation on its mobility patterns by using constitutively active and inactive H-Ras mutants, H-Ras^{V12} and H-Ras^{N17}, respectively. We compared the dynamic parameters determined for the wild-type H-Ras protein and its C10H-Ras to the parameters obtained for H-Ras^{V12} and H-Ras^{N17}. We found that the constitutively active mutant H-Ras^{V12} displayed a significantly larger diffusion coefficient and size of its confinement area for the fast-diffusing sub-population in comparison to the same population of wild-type H-Ras, C10H-Ras, and H-Ras^{N17} proteins. As the other three H-Ras constructs (H-Ras, C10H-Ras, and H-Ras^{N17}) exhibited similar mobility patterns, distinct from the H-Ras^{V12} pattern, we concluded that the vast majority of the wild-type H-Ras proteins diffusing in the epidermal cells of zebrafish embryos are in an inactive state. Because it had also been shown that H-Ras^{V12} can induce oncogenic changes in a variety of zebrafish cell types upon overexpression, we conclude that the altered mobility is associated with the active signaling of this protein in the zebrafish cells (Feng et al., 2010; Michailidou et al., 2009; Santoriello et al., 2010).

The increased mobility of the active mutant H-Ras^{V12} probably originated from an altered affinity of H-Ras proteins for specific plasma membrane microdomains upon activation, which has been demonstrated before (Hancock and Parton, 2005; Plowman et al., 2005; Prior et al., 2001; Prior et al., 2003; Zhou et al., 2018). A myriad of scientific reports has revealed that the H-Ras and its anchor alone both can form nanoclusters that are located in small lipid rafts (Fig. 1) (Plowman et al., 2005; Prior et al., 2001; Prior et al., 2003). These lipid rafts are domains of 10-100 nm in size that are dependent on the presence

of cholesterol (Garcia-Parajo et al., 2014; Lingwood and Simons, 2010; Nickels et al., 2015; Zhou and Hancock, 2015). Interestingly, a similar dependence on cholesterol was observed for nanoclusters of activated, GTP-loaded, N-Ras, but not for K-Ras nanoclusters or active forms of H-Ras, indicating the formation of alternative nanoclusters in distinct membrane domains that appear to be slightly smaller and cholesterol-independent (Plowman et al., 2005; Prior et al., 2001; Prior et al., 2003). Such a preferential dependence on lipids suggests that each type of Ras nanoclusters has a unique lipid composition and, therefore, reflects varying lipid-binding properties between different Ras proteins and between their active and inactive forms (Zhou et al., 2018). For example, phosphatidylserine (PtdSer) and phosphatidylinositol 4-phosphate are found in clusters of both GDP- and GTP-bound H-Ras, but only K-Ras localization and clustering on the plasma membrane are sensitive to varying PtdSer concentrations, enabling PtdSer contentsensitive sorting of H- and K-Ras into spatially distinctive lipid assemblies (Zhou et al., 2014). These results show that Ras nanoclusters assemble a distinctive set of plasma membrane phospholipids, which corresponds to their specific effector activation profiles (Zhou and Hancock, 2015; Zhou et al., 2018).

Increased diffusion coefficients and confinement zone of the fast-diffusing fraction observed for H-Ras^{V12} in our study most likely reflect the different diffusion properties of the domains to which the activated H-Ras localizes. The lower affinity for lipid rafts is associated with an increased diffusion rate and confinement zone size. These confinement zones in the plasma membrane have been suggested to underline the concept of membrane compartmentalization resulting from the structure of the membrane cytoskeleton, a filamentous actin meshwork associated with the cytoplasmic surface of the plasma membrane, and various transmembrane proteins anchored to these actin filaments (Fujiwara et al., 2002; Kusumi et al., 2010). We argue that the diffusion of nonactive H-Ras clusters is even more hindered by these cytoskeleton-based boundaries than the clusters of activated H-Ras molecules, due to the size of the lipid rafts they are localized in (Fig. 1).

Subsequently, we presented that methyl- β -cyclodextrin (MBCD) administration also increased the initial diffusion coefficients and size of confinement areas for wild-type H-Ras and H-Ras^{V12}. In the presence of this compound, the differences between the mobility patterns of the non-activated and activated form of H-Ras were no longer

observed. MBCD leads to cholesterol depletion in the cells and, therefore, the disruption of lipid raft formation, which is in line with the largest effect of this compound on the non-active H-Ras that has a higher affinity for lipid rafts. It has been shown that LatB also disrupts the clustering of non-active H-Ras forms and, therefore, that an intact cytoskeleton is required for lipid raft formation (Plowman et al., 2005). Since it has also been shown that cholesterol depletion disrupts the actin cytoskeleton, the interaction between lipid rafts and the cytoskeleton seems to be bidirectional (Kwik et al., 2003).

In addition, previous evidence showed that GTP-loading increased the probability of H-Ras clusters being transiently (< 1 s) immobilized (Murakoshi et al., 2004), and that interactions with many cytoplasmic proteins, such as Galectin-1 and Sur-8, appear to be involved in the formation of these immobile H-Ras clusters, which are considered to be the sites where active signaling occurs (Belanis et al., 2008; Hancock and Parton, 2005; Herrero et al., 2016; Li et al., 2000; Shalom-Feuerstein et al., 2008; Zhou et al., 2018). The slow-diffusing fraction observed in our study had a diffusion rate similar to this previously identified immobile population (Murakoshi et al., 2004), and we suggest that the slow-diffusing population contains the actively signaling H-Ras molecules. In addition, after fitting the three-population model, it has been possible to further subdivide the slow-diffusing fraction by distinguishing an immobile population. Contrary to the previous experiments performed in cultured cells (Lommerse et al., 2005; Murakoshi et al., 2004), the size of the slow-diffusing fraction in the current study was not increased for the active form of H-Ras. Ultimately, the size of the slow-diffusing H-Ras fraction decreased significantly for both wild-type H-Ras and H-Ras^{V12} upon treatment with LatB and MBCD, which underlines the importance of the structure and composition of the plasma membrane in the process of H-Ras clusters immobilization.

Using multifocal 2PEF microscopy, we focused our attention on the mobility patterns of the slow-diffusing population of C10H-Ras molecules. First, we optimized the 2PEFM technique to image single molecules in living zebrafish embryos. However, with a time lag of 200 ms, it was not possible to image fluorescent molecules that belonged to the fast-diffusing fraction that we had previously identified in our TIRF microscopy studies. Nevertheless, owing to the imaging mode, the photobleaching of the fluorescent molecules was greatly reduced, which enabled us to visualize the slow-diffusing C10H-Ras molecules for a time ranging from 3 to 15 seconds and, consequently, reconstruct their

trajectories. Throughout the single-step photobleaching analysis, we were able to distinguish individual photobleaching steps, which signified that H-Ras anchor molecules in the slow-diffusing population form clusters consisting of varying numbers of molecules. Following that, we uncovered that single H-Ras membrane anchor mobility patterns are more suitably presented by the analysis of their trajectories rather than by the population-based examination of the mean squared displacements. The C10H-Ras molecules appeared to switch between two different states, a diffusing and a hopping one (Fig. 1). For most of the time, these molecules resided in a diffusing state and this diffusion was interrupted by brief periods of hopping. The total time spent in this hopping state was approximately four to five times shorter than the C10H-Ras molecules spend in the diffusing state, and the ratio between the time spent in the hopping state and the diffusion state equaled 0.237. Taken together, our findings revealed that the H-Ras membrane anchors exhibit an anomalous mobility pattern, which can be referred to as molecular hopping.

The events of molecular hopping for the H-Ras membrane anchor or the full-length H-Ras protein had not been observed before. However, it has been reported that many signaling proteins experience two-dimensional hop diffusion on the membrane in search of their target and because of the packed structure of the plasma membrane itself (Campagnola et al., 2015; Umemura et al., 2008; Yasui et al., 2014). The plasma membrane is made of hundreds of microdomains, caused by the actin-based membrane skeleton, which is closely associated with the cytoplasmic surface of the plasma membrane. Consequently, many transmembrane proteins collide with the membrane skeleton, which induces temporary confinement of the transmembrane proteins in the membrane-skeleton meshwork. Thus, in the vicinity of immobilized molecules located in the membrane, the movement of any other particles is extremely limited. With all these obstacles, membrane proteins often hop from one microdomain to another one, especially when thermal fluctuations of the membrane and the actin meshwork associated with it create sufficient space between them to enable the passage of integral membrane proteins, or when an actin filament is temporarily severed (Suzuki et al., 2005)

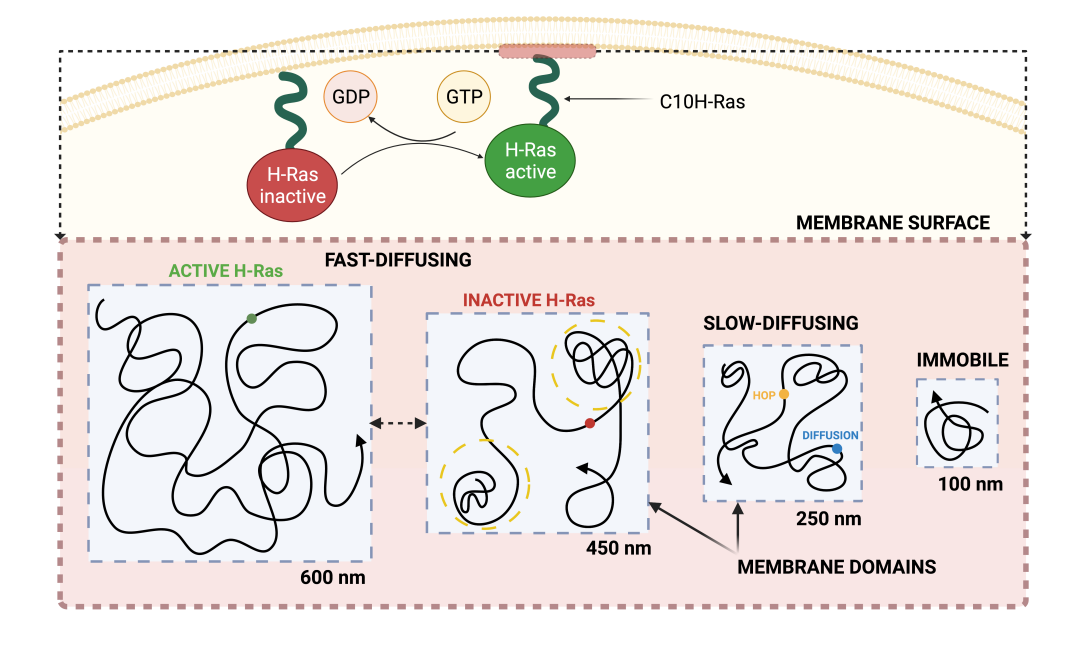


FIGURE 1: Summary of the H-Ras anchor mobility patterns in the membranes of epidermal cells in the living zebrafish embryos. Analysis of the TIRFM data revealed the presence of two dynamic subpopulations of Ras proteins, a fast- and a slow-diffusing one. The data from 2PEFM allowed for further addition of an immobile subpopulation, in which particles barely diffused. In the fast-diffusing fraction, inactive, GDP-loaded H-Ras mostly resides in lipid rafts which limits its mobility, confining it to an area that is smaller than the cholesterol-independent area in which the active, GTP-loaded H-Ras, is predominantly diffusing. This confinement most likely results from transmembrane proteins, lipids, and the actin meshwork attached to the plasma membrane. In the slow-diffusing fraction, it has been possible, using the 2PEFM results, to distinguish two different states in which the H-Ras molecules can occur: a diffusing and a hopping state. This hopping state is relatively sporadic and brief, occurring approximately four times less frequent than the diffusing state.

Such a temporary nature of protein-membrane interactions enables a tight temporal regulation of signal transduction processes. It has also been suggested that molecular hopping might be critical in the search for target molecules in eukaryotic cells. A straightforward consequence of membrane hopping is that a molecule remains in its immediate vicinity for a short time and then jumps to a location that is further away than expected from two-dimensional diffusion. In such a way, the search process is allowed to explore larger areas, which allows proteins to bypass diffusion barriers that may be present in the membrane (Lemmon, 2008). Since the H-Ras membrane anchor experiences this type of diffusion, we suggest that this process is governed

predominantly by electrostatic, membrane-protein associations, and not by interaction with other proteins and does not involve active protein signaling.

5.3 THE MOBILITY PATTERN OF THE GLUCOCORTICOID RECEPTOR IN LIVING ZEBRAFISH EMBRYOS (Chapter 4)

We used LSF microscopy to enable the analysis of the dynamics of intracellular proteins in living zebrafish embryos, and we used this approach to study the mobility patterns of GR inside the yolk syncytial nuclei (YSN). This analysis revealed that the GRs in the YSN are divided into a fast- and a slow-diffusing subpopulation. The existence of two fractions had been observed before for GR and other transcription factors. The fast and the slow fraction are generally considered to reflect GRs that diffuse freely within the nucleus, and receptors that interact with DNA, respectively. In a recent study, it was shown that the fast subpopulation could, in turn, be divided into two fractions with different mobility, of which the fastest one was interpreted as receptors diffusing freely through the nucleus, and the slowest one as GRs interacting non-specifically with the DNA (Keizer et al., 2019).

Our findings show that the vast majority of the GR molecules in the YSN belonged to the fast subpopulation, which constituted around 90% of the total GR population in the vehicle-, and 77% in the dexamethasone-treated group. This percentage is significantly higher than previously observed in cultured cells, where this fraction was estimated to constitute between 45 and 60% of the total number of molecules diffusing in the nuclei upon activation by either cortisol or dexamethasone (Alsop and Vijayan, 2009; Groeneweg et al., 2014; Keizer et al., 2019). The difference between our control-treated zebrafish embryos and previously reported cortisol-treated cellular models can be explained by a lack of a properly developed cortisol secretion in two-day-old embryos (Alsop and Vijayan, 2009), but this does not account for the differences between these models upon dexamethasone treatment. The high percentage of fast-diffusing molecules is better explained by the large size of the YSN, between 8 and 12 µm. A larger fraction of freely-diffusing GRs may be expected with more space available in the YSN and the same amount of chromatin present. GR molecules in either of the subpopulations did not move within the entire nuclear environment, but were confined to areas with a size of around 1233 nm for the fast subpopulation and 322 nm for the slow subpopulation. The confinement of the GRs has not been observed in previous studies on the receptor mobility patterns. In our approach, however, we were able to reconstruct the squared displacements of GRs in both fractions over a longer time, which enabled us to determine the occurrence of nuclear areas in which the diffusion of the GRs is restricted. Such confinement of the fast GR subpopulation indicates that the receptors diffuse within areas surrounded by barriers, which in the nucleus could be formed by chromatin. In addition to that, previous studies reported values for the diffusion coefficients of the GR fast fraction to be within the range of circa 2.5 and 9 µm² s⁻¹ (Gebhardt et al., 2013; Groeneweg et al., 2014; Keizer et al., 2019), and similar values have been observed for other transcription factors, such as p53 or STATI (Mazza et al., 2012; Speil et al., 2011). The values for the diffusion coefficient of the fast subpopulation that were obtained in our approach, i.e., 7.90 ± 0.53 µm² s⁻¹, fall well within the previously published range. The slow subpopulation was characterized by a tenfold lower diffusion coefficient (0.78 ± 0.18 µm² s⁻¹), which agreed with the values reported previously, estimated to range between 0.03 and 0.50 µm² s⁻¹ (Gebhardt et al., 2013; Groeneweg et al., 2014; Keizer et al., 2019).

In the next step of this study, we found that treating zebrafish embryos with dexamethasone did not significantly alter the size of the fast-diffusing fraction of GRs. In previous studies, it had consistently been shown that administration of a GR agonist decreased the size of the fast subpopulation, believed to reflect a larger fraction of GRs that interact with the DNA to modulate the transcription of genes (Groeneweg et al., 2014). The lack of a dexamethasone effect on the population size in our study might, therefore, be specific to the zebrafish GR, or the specific cell type studied. Despite the lack of effect on the size of the fast subpopulation, incubation of the embryos with dexamethasone did result in a significant decrease of the diffusion coefficients both for the fast- and the slow-diffusing fraction. Lower diffusion coefficients of the fast-diffusing GRs most likely reflect non-specific binding events to DNA in search of their proper binding site, which slow down their diffusion rate (Keizer et al., 2019). Additionally, treatment with dexamethasone reduced the size of the confinement area for the fast-diffusing subpopulation of GRs. This can be explained by the dexamethasone-activated GR molecules constituting a part of larger multi-protein complexes. These complexes, made of receptor molecules and transcriptional coregulatory proteins, are present inside the cell nuclei and take part in the transcription of GR target genes. Diffusion of the GR molecules in these bulky multi-protein aggregates might, thus, be hindered, resulting in the smaller confinement areas in the dexamethasone-treated groups. Our results, therefore, are in accordance with previous findings that indicated that the interactions between ligand and receptor determine the binding events between the GR and the DNA inside the nucleus.

5.4 THE SOURCES OF VARIABILITY OF THE SMM MEASUREMENTS IN THE ZEBRAFISH EMBRYO MODEL (Chapters 2 and 4)

In addition to analyzing the mobility patterns of H-Ras and GR, we have assessed and characterized the variability of the dynamic parameters that we had determined in our zebrafish embryo model. For this purpose, we specified the factors that contributed the most to the variability present in the mobility data obtained during our investigations. Surprisingly, differences between individual embryos had only a modest effect on the overall variation in the results of the H-Ras studies. However, different areas of the embryonic epidermis and different experimental days both appeared to be factors that have largely contributed to the variation in the data. This indicates that the differences between cells within the epidermal tissue of one individual embryo are larger than the differences observed between embryos, and suggests that the cellular context is the main determinant of H-Ras mobility.

In the GR study, the existing variability mostly originated from imaging different cell areas within an individual embryo, too, and this variability was most prominent in the measured mobility patterns exhibited by the fast subpopulation of GRs. We, therefore, suggest that it is the architecture of the nucleus, in particular a specific organization of the nuclear chromatin, that likely affected the diffusion behavior of the fast-diffusing GRs. Additionally, variability was observed between the dynamic parameters displayed by individual zebrafish embryos, and this variability might have originated from genetic variation between different zebrafish batches. The absence of inbred zebrafish strains causes this inherent genetic variability and could have been a factor that contributed to the overall variability of the parameters describing the GR mobility patterns. This source of variation might in the future be avoided by utilizing embryos from one selected couple of adult zebrafish per experiment.

5.5 FUTURE PERSPECTIVES

Taken together, this thesis extends the applications of the SMM techniques to study the mobility patterns of single membrane and nuclear proteins in vivo. Whereas the thesis provides the foundations for imaging the living vertebrate organisms using a variety of SMM techniques, there are several aspects that, if properly implemented, will most certainly improve the quality of the obtained single-molecule data. These aspects include better protein labelling technology, the development of three-dimensional single-molecule imaging methods, and the improvement of the temporal resolution of the SMM setups. In Chapter 2 we present that, while being a useful starting point for imaging single molecules in vivo, traditional autofluorescent proteins suffer from photobleaching and are not optimal for long-term measurement protocols. It is inherent to the TIRF microscopy technique that it is limited to visualization of structures localized in the vicinity of the coverglass-sample interface, making it impossible to image molecules located deeper in the epidermis of the zebrafish embryo model. The use of organic dyes, commonly applied to Halo- and SNAP-tags has thus far been optimized only for in vitro SMM studies. Extension of their application to more complex, biological models would enable the use of superior fluorophores with a higher photostability and quantum yield, which are excitable by a different wavelength of light, enabling the use of wavelengths that cause significantly reduced autofluorescence of these biological samples, and thereby improve the SNR of the acquired images. Following that, in Chapter 3, we show that reduced out-of-focus photobleaching enables following single molecules over longer times than in experiments in which TIRFM and LSFM techniques are used. Yet, we point to the fact that insufficient temporal resolution of the microscopy setup leads to blurring effects that result in missing the fastest molecules in the population. An improvement of the quantum yield of the microscopy setup detector (Mondal, 2014) and, therefore, an increase in the temporal resolution of the setup, is critical for a better imaging output. Lastly, in Chapter 4, we provide the evidence that many molecules do not move along the membranes, but rather inside entire organelles, i.e., in three dimensions. The possibilities of the SMM techniques being performed in three dimensions in vivo are limited and often compromise other imaging parameters, such as temporal or spatial resolution. Currently, the lack of information about mobility in the third dimension is often compensated by computational simulations and stochastic models,

including the Markov chain model. Nonetheless, a few successful studies on *in vitro* 3D imaging of single molecules, such as the transcription factor Sox2, have already been performed (Chen et al., 2014; Liu et al., 2014). Hence, SMM imaging *in vivo* in three dimensions together with other, previously mentioned aspects, all indicate some of the most urgent directions that the future development of SMM imaging *in vivo* should follow.

REFERENCES

- **Alsop, D. and Vijayan, M. M.** (2009). Molecular programming of the corticosteroid stress axis during zebrafish development. *Comp. Biochem. Physiol. A. Mol. Integr. Physiol.* **153**, 49–54.
- Belanis, L., Plowman, S. J., Rotblat, B., Hancock, J. F. and Kloog, Y. (2008). Galectin-1 is a novel structural component and a major regulator of h-ras nanoclusters. *Mol. Biol. Cell* 19, 1404–1414.
- Campagnola, G., Nepal, K., Schroder, B. W., Peersen, O. B. and Krapf, D. (2015). Superdiffusive motion of membrane-targeting C2 domains. *Sci. Rep.* **5**, 17721.
- Chen, J., Zhang, Z., Li, L., Chen, B.-C., Revyakin, A., Hajj, B., Legant, W., Dahan, M., Lionnet, T., Betzig, E., et al. (2014). Single-molecule dynamics of enhanceosome assembly in embryonic stem cells. *Cell* 156, 1274–1285.
- Feng, Y., Santoriello, C., Mione, M., Hurlstone, A. and Martin, P. (2010). Live imaging of innate immune cell sensing of transformed cells in zebrafish larvae: parallels between tumor initiation and wound inflammation. *PLoS Biol.* **8**, e1000562.
- Fujiwara, T., Ritchie, K., Murakoshi, H., Jacobson, K. and Kusumi, A. (2002). Phospholipids undergo hop diffusion in compartmentalized cell membrane. *J. Cell Biol.* **157**, 1071–1081.
- Garcia-Parajo, M. F., Cambi, A., Torreno-Pina, J. A., Thompson, N. and Jacobson, K. (2014). Nanoclustering as a dominant feature of plasma membrane organization. *J. Cell Sci.* **127**, 4995–5005.
- Gebhardt, J. C. M., Suter, D. M., Roy, R., Zhao, Z. W., Chapman, A. R., Basu, S., Maniatis, T. and Xie, X. S. (2013). Single-molecule imaging of transcription factor binding to DNA in live mammalian cells. Nat. Methods 10, 421–426.
- Groeneweg, F. L., Royen, M. E. van, Fenz, S., Keizer, V. I. P., Geverts, B., Prins, J., Kloet, E. R. de, Houtsmuller, A. B., Schmidt, T. S. and Schaaf, M. J. M. (2014). Quantitation of Glucocorticoid Receptor DNA-Binding Dynamics by Single-Molecule Microscopy and FRAP. *PLOS ONE* **9**, e90532.
- Hancock, J. F. and Parton, R. G. (2005). Ras plasma membrane signaling platforms. Biochem. J. 389, 1-11.
- **Herrero, A., Matallanas, D. and Kolch, W.** (2016). The spatiotemporal regulation of RAS signaling. *Biochem. Soc. Trans.* **44**, 1517–1522.
- Keizer, V. I. P., Coppola, S., Houtsmuller, A. B., Geverts, B., van Royen, M. E., Schmidt, T. and Schaaf, M. J. M. (2019). Repetitive switching between DNA-binding modes enables target finding by the glucocorticoid receptor. J. Cell Sci. 132, jcs217455.

- Kusumi, A., Shirai, Y. M., Koyama-Honda, I., Suzuki, K. G. N. and Fujiwara, T. K. (2010). Hierarchical organization of the plasma membrane: investigations by single-molecule tracking vs. fluorescence correlation spectroscopy. *FEBS Lett.* **584**, 1814–1823.
- Kwik, J., Boyle, S., Fooksman, D., Margolis, L., Sheetz, M. P. and Edidin, M. (2003). Membrane cholesterol, lateral mobility, and the phosphatidylinositol 4,5-bisphosphate-dependent organization of cell actin. *Proc. Natl. Acad. Sci. U. S. A.* 100, 13964–13969.
- **Lemmon, M. A.** (2008). Membrane recognition by phospholipid-binding domains. *Nat. Rev. Mol. Cell Biol.* **9**, 99–111.
- **Li, W., Han, M. and Guan, K. L.** (2000). The leucine-rich repeat protein SUR-8 enhances MAP kinase activation and forms a complex with Ras and Raf. *Genes Dev.* **14**, 895–900.
- **Lingwood, D. and Simons, K.** (2010). Lipid Rafts As a Membrane-Organizing Principle. *Science* **327**, 46–50.
- Liu, Z., Legant, W. R., Chen, B.-C., Li, L., Grimm, J. B., Lavis, L. D., Betzig, E. and Tjian, R. (2014). 3D imaging of Sox2 enhancer clusters in embryonic stem cells. *eLife* **3**, e04236–e04236.
- Lommerse, P. H. M., Blab, G. A., Cognet, L., Harms, G. S., Snaar-Jagalska, B. E., Spaink, H. P. and Schmidt, T. (2004). Single-Molecule Imaging of the H-Ras Membrane-Anchor Reveals Domains in the Cytoplasmic Leaflet of the Cell Membrane. *Biophys. J.* **86**, 609–616.
- **Lommerse, P. H. M., Snaar-Jagalska, B. E., Spaink, H. P. and Schmidt, T.** (2005). Single-molecule diffusion measurements of H-Ras at the plasma membrane of live cells reveal microdomain localization upon activation. *J. Cell Sci.* **118**. 1799–1809.
- Lommerse, P. H. M., Vastenhoud, K., Pirinen, N. J., Magee, A. I., Spaink, H. P. and Schmidt, T. (2006).

 Single-Molecule Diffusion Reveals Similar Mobility for the Lck, H-Ras, and K-Ras Membrane Anchors. *Biophys. J.* **91**, 1090–1097.
- Mazza, D., Abernathy, A., Golob, N., Morisaki, T. and McNally, J. G. (2012). A benchmark for chromatin binding measurements in live cells. *Nucleic Acids Res.* 40, e119–e119.
- Michailidou, C., Jones, M., Walker, P., Kamarashev, J., Kelly, A. and Hurlstone, A. F. L. (2009). Dissecting the roles of Raf- and PI3K-signaling pathways in melanoma formation and progression in a zebrafish model. *Dis. Model. Mech.* **2**, 399–411.
- Mondal, P. P. (2014). Temporal resolution in fluorescence imaging. Front. Mol. Biosci. 1, 11.

- Murakoshi, H., Iino, R., Kobayashi, T., Fujiwara, T., Ohshima, C., Yoshimura, A. and Kusumi, A. (2004). Single-molecule imaging analysis of Ras activation in living cells. *Proc. Natl. Acad. Sci.* **101**, 7317–7322.
- **Nickels, J. D., Smith, J. C. and Cheng, X.** (2015). Lateral organization, bilayer asymmetry, and inter-leaflet coupling of biological membranes. *Chem. Phys. Lipids* **192**. 87–99.
- **Plowman, S. J., Muncke, C., Parton, R. G. and Hancock, J. F.** (2005). H-ras, K-ras, and inner plasma membrane raft proteins operate in nanoclusters with differential dependence on the actin cytoskeleton. *Proc. Natl. Acad. Sci.* **102**, 15500–15505.
- Prior, I. A., Harding, A., Yan, J., Sluimer, J., Parton, R. G. and Hancock, J. F. (2001). GTP-dependent segregation of H-ras from lipid rafts is required for biological activity. *Nat. Cell Biol.* **3**, 368–375.
- **Prior, I. A., Muncke, C., Parton, R. G. and Hancock, J. F.** (2003). Direct visualization of Ras proteins in spatially distinct cell surface microdomains. *J. Cell Biol.* **160**, 165–170.
- Santoriello, C., Gennaro, E., Anelli, V., Distel, M., Kelly, A., Köster, R. W., Hurlstone, A. and Mione, M. (2010). Kita driven expression of oncogenic HRAS leads to early onset and highly penetrant melanoma in zebrafish. *PloS One* **5**, e15170.
- Schaaf, M. J. M., Koopmans, W. J. A., Meckel, T., van Noort, J., Snaar-Jagalska, B. E., Schmidt, T. S. and Spaink, H. P. (2009). Single-Molecule Microscopy Reveals Membrane Microdomain Organization of Cells in a Living Vertebrate. *Biophys. J.* **97**, 1206–1214.
- Shalom-Feuerstein, R., Plowman, S. J., Rotblat, B., Ariotti, N., Tian, T., Hancock, J. F. and Kloog, Y. (2008). K-ras nanoclustering is subverted by overexpression of the scaffold protein galectin-3. *Cancer Res.* **68**. 6608–6616.
- Speil, J., Baumgart, E., Siebrasse, J.-P., Veith, R., Vinkemeier, U. and Kubitscheck, U. (2011). Activated STATI transcription factors conduct distinct saltatory movements in the cell nucleus. *Biophys. J.* 101, 2592–2600.
- **Suzuki, K., Ritchie, K., Kajikawa, E., Fujiwara, T. and Kusumi, A.** (2005). Rapid Hop Diffusion of a G-Protein-Coupled Receptor in the Plasma Membrane as Revealed by Single-Molecule Techniques. *Biophys. J.* **88**, 3659–3680.
- Umemura, Y. M., Vrljic, M., Nishimura, S. Y., Fujiwara, T. K., Suzuki, K. G. N. and Kusumi, A. (2008). Both MHC class II and its GPI-anchored form undergo hop diffusion as observed by single-molecule tracking. *Biophys. J.* 95, 435–450.

- Yasui, M., Matsuoka, S. and Ueda, M. (2014). PTEN Hopping on the Cell Membrane Is Regulated via a Positively-Charged C2 Domain. *PLoS Comput. Biol.* **10**, e1003817.
- **Zhou, Y. and Hancock, J. F.** (2015). Ras nanoclusters: Versatile lipid-based signaling platforms. *Biochim. Biophys. Acta* **1853**, 841–849.
- **Zhou, Y., Liang, H., Rodkey, T., Ariotti, N., Parton, R. G. and Hancock, J. F.** (2014). Signal Integration by Lipid-Mediated Spatial Cross Talk between Ras Nanoclusters. *Mol. Cell. Biol.* **34**, 862–876.
- **Zhou, Y., Prakash, P., Gorfe, A. A. and Hancock, J. F.** (2018). Ras and the Plasma Membrane: A Complicated Relationship. *Cold Spring Harb. Perspect. Med.* **8**, a031831.

NEDERLANDSE SAMENVATTING

Single-molecule microscopy (SMM)-technieken zijn effectieve en succesvolle experimentele methodes die het mogelijk maken om individuele moleculen af te beelden en deze in de tijd te volgen. Met behulp van deze technologie is het mogelijk om het dynamisch gedrag van individuele moleculen in verschillende biologische systemen te analyseren, en om het effect van structurele en biochemische componenten van zo'n systeem op de mobiliteit van de moleculen te bestuderen. In het onderzoek dat in dit proefschrift is beschreven hebben we drie geavanceerde fluorescentie-microscopische technieken geoptimaliseerd om SMM toe te passen op het zebravis embryo-model. We hebben twee eiwitten gebruikt om de robuustheid en reproduceerbaarheid te bestuderen van de resultaten die we verkregen met onze *in vivo* SMM aanpak: H-Ras als model voor een eiwit dat in de plasma-membraan zit en de glucocorticoïd receptor (GR) als model voor een eiwit dat zich in de kern bevindt.

In Hoofdstuk 2 van dit proefschrift hebben we het mobiliteitspatroon van het H-Ras eiwit bestudeerd in de buitenste membraan van de buitenste cellaag van de epidermis van twee dagen oude zebravisembryo's met behulp van total internal reflection fluorescence (TIRF)-microscopie. We vonden dat H-Ras in deze cellen aanwezig is in twee verschillende fracties: één die snel diffundeert en één die langzaam diffundeert door de membraan. Interessant was dat we ontdekten dat beide H-Ras fracties niet vrij door het oppervlak van de plasma-membraan konden bewegen, maar dat hun diffusie begrensd was binnen bepaalde micro-domeinen in de membraan. Door een mutant van het H-Ras eiwit te gebruiken die zich permanent in een geactiveerde toestand bevindt, hebben we laten zien dat activatie van H-Ras het dynamische gedrag van dit eiwit sterk beïnvloedt. In het bijzonder zagen we een verhoogde diffusiecoëfficiënt voor de snel diffunderende fractie, en het microdomein waarin de begrensde diffusie van deze fractie plaatsvindt was groter voor de actieve mutant in vergelijking met wild type H-Ras. Vervolgens hebben we, om een idee te krijgen over de aard van de waargenomen microdomeinen die de diffusie van H-Ras begrenzen, getest of deze gebiedjes wellicht zogenaamde 'lipid rafts' zijn, waarvan bekend is dat hun vorming afhankelijk is van de aanwezigheid van cholesterol en actine-vezels van het cytoskelet. We zagen dat cholesterol-depletie en verstoring van de vorming van het cytoskelet ongeveer dezelfde uitwerking hadden op de mobiliteit van H-Ras als activering van het eiwit (leidend tot verhoging van de diffusiecoëfficiënt en een vergroting van het microdomein voor de snel diffunderende fractie). Dit suggereert dat de snel-diffunderende fractie van de nietgeactiveerde vorm van H-Ras zich in de lipid rafts bevindt, terwijl deze fractie zich wanneer H-Ras geactiveerd is voornamelijk in grotere domeinen bevindt die onafhankelijk zijn van cholesterol en de actine-vezels van het cytoskelet. Verder hebben we de variatie in de resultaten gedetailleerd bestudeerd. Daarmee hebben we laten zien dat de verschillen tussen individuele cellen binnen een weefsel (in dit geval de epidermis) de belangrijkste bijdrage leveren aan de variatie in de data, en niet de verschillen tussen individuele embryo's.

Na deze TIRF-microscopie studies hebben we in **Hoofdstuk 3** multifocale two-photon excitation fluorescence (2PEF)-microscopie gebruikt. Deze methode wordt gebruikt om de schade die 'out-of-focus' excitatielicht te verminderen, maar 2PEF-microscopie blijkt ook de photobleaching van de fluorescente moleculen enorm te kunnen reduceren. Door deze techniek te gebruiken, slaagden we erin om enkele H-Ras moleculen voor een langere periode te volgen, wat het mogelijk maakte om het exacte traject dat ze in die periode hebben afgelegd te reconstrueren. Hierdoor hoefden we het dynamische gedrag van de moleculen niet meer in termen van verschillende fracties te beschrijven, maar konden we ons richten op het analyseren van de trajecten van individuele moleculen. We gebruikten deze aanpak om de mobiliteit van het membraan-anker van H-Ras (C10H-Ras), dat fluorescent was gelabeld door het te fuseren met green fluorescent protein (GFP), te bestuderen in de membranen van epidermale cellen van zebravisembryo's. Deze methode maakte het mogelijk om uitsluitend de langzaam diffunderende fractie moleculen te detecteren en een gedetailleerde analyse te maken van hun bewegingen. Deze analyse liet zien dat deze langzame fractie van met GFP gefuseerde H-Ras ankers continu wisselen tussen een diffunderende ('diffusing') en een springende ('hopping') toestand. Wat hierbij opviel was dat de tijd die de moleculen doorbrachten in de 'hopping' toestand relatief kort was ten opzichte van de tijd die ze in de 'diffusing' toestand waren. Dit impliceert dat deze eiwitten een zogenaamd 'anomalous' diffusiepatroon vertonen, wat vaak wordt beschreven als 'molecular hopping'.

Tenslotte hebben we in **Hoofdstuk 4** van dit proefschrift getest of het ook mogelijk is om met SMM in zebravisembryo's eiwitten te bestuderen die zich niet in de celmembraan bevinden, maar elders in de cel. Hiervoor hebben we light sheet fluorescence

(LSF)-microscopie gebruikt, waarbij een vlak van licht wordt gecreëerd, de zogenaamde 'light sheet'. Hierdoor worden alleen fluorescente moleculen in dit vlak geëxciteerd. Om met deze techniek embryo's voor langere tijd te kunnen bestuderen, hebben we een speciale 'imaging chamber' ontworpen. Met deze speciaal ontworpen LSF-microscopieopstelling hebben we in embryo's van één dag oud individuele GRs zichtbaar gemaakt in de kernen van de 'yolk syncitial layer', een laag over de dooierzak van het embryo die een groot aantal kernen bevat. Vervolgens hebben we de mobiliteit van deze GRs in deze kernen geanalyseerd, en de resultaten van deze analyse lieten een snel diffunderende en een langzaam diffunderende fractie zien, zoals al eerder was vastgesteld in vergelijkbare studies aan GR in gekweekte cellen. Behandeling van de embryo's met de GR agonist dexamethason verlaagde de diffusie van de receptoren, en ook dit was in lijn met eerdere resultaten in gekweekte cellen en valideerde daarmee de in vivo metingen. Net zoals we bij de analyse van de beweging van H-Ras in zebravisembryo's zagen, kwam ook in deze studie de meeste variatie in de resultaten doordat we verschillende cellen binnen een embryo bestudeerden, en niet doordat we verschillende embryo's gebruikten.

In conclusie, met behulp van een drietal technieken, TIRF-, 2PEF- en LSF-microscopie, hebben we de mogelijkheden van *in vivo* SMM uitgebreid. Met TIRF-microscopie hebben we individuele membraaneiwitten in de buitenste membraan van de epidermis van zebravisembryo's zichtbaar kunnen maken en hun beweging kunnen analyseren. Door 2PEF-microscopie konden we deze eiwitten voor een langere periode volgen, wat het mogelijk maakte om het afgelegde traject van individuele eiwitten te reconstrueren. Dit was overigens alleen mogelijk voor een langzaam diffunderende populatie van moleculen. Verder maakt LSF-microscopie het mogelijk om ook eiwitten te bestuderen die zich niet in de membraan bevinden. Met deze technieken hebben we het mogelijk gemaakt om in een intact organisme de dynamiek van H-Ras en de GR te bestuderen en factoren te identificeren die deze dynamiek beïnvloeden. Verdere ontwikkeling van deze technologie zal zich moeten richten op het verbeteren van de fluorescente labels die worden gebruikt, de ontwikkeling van driedimensionale analyse-methodes, en het verbeteren van de temporele resolutie van de gebruikte SMM-opstellingen.

CURRICULUM VITAE

Radosław Jakub Góra was born on the 25th of July, 1991 in Wrocław, Poland. There, in 2014, he completed his bachelor's studies at the Wrocław University of Science and Technology and majored in biotechnology and molecular biology. During his bachelor's studies, he interned in the Hirszfeld Institute of Immunology and Experimental Therapy of the Polish Academy of Sciences, where he investigated the role of Toll-like receptors in metabolic pathways engaged in the immune response. In 2014, Radosław moved to Stockholm, Sweden, to obtain his master's degree in biomedicine and toxicology at the Karolinska Institute. Throughout his studies, he served as the Institute's global digital ambassador for prospective students and as an associate editor of the student magazine Medicor. The pinnacle of his degree studies was to participate in the iGEM competition in synthetic biology, in which he worked as a part of the Stockholm team to find a reproducible, specific and transferable biomarker that would help detect breast cancer at the early stage of the disease development. After graduating in 2016, Radosław remained at the Karolinska Institute and worked as a research assistant in the Department of Microbiology, Tumor, and Cell Biology. There, he participated in studies on phenotypic plasticity and interchangeable modes of cell invasion and growth in cancer metastasis and drug resistance. In 2017, he moved to the European Commission Joint Research Centre, located in Ispra, Italy, to start his internship in the EU Reference Laboratory for Alternatives to Animal Testing. During that time, he contributed to the development and validation of in vitro models for toxicological profiling of several chemicals and drug candidates. Following this internship, in September 2017 Radosław began his PhD studies in the group of Dr. Schaaf at Leiden University. His work focused on developing tools that utilize single-molecule microscopy techniques to image individual proteins inside cells of living zebrafish embryos. In the course of his studies, Radosław completed a six-month-long secondment at the Institute of Photonic Sciences (Castelldefels, Spain) where he collaborated with the group of Dr. Loza-Alvarez to develop novel applications of the light-sheet fluorescence microscopy to image single glucocorticoid receptors diffusing in nuclei inside zebrafish embryos. Currently, Radosław works as a post-doctoral research scholar in the group of Prof. Shan at the California Institute of Technology. He is involved in single-molecule microscopy studies intended to improve our understanding of co-translational mechanisms of sorting and delivery of nascent proteins to their functional targets on cell membranes..

LIST OF PUBLICATIONS

Gora RJ, Vlieg RC, Jonkers S, van Noort J, Schaaf MJM. Multifocal two-photon excitation

fluorescence microscopy reveals hop diffusion of H-Ras membrane anchors in epider-

mal cells of zebrafish embryos.

Manuscript in preparation

Gora RJ, de Jong B, van Hage P, Rhiemus MA, van Steenis F, van Noort J, Schmidt T,

Schaaf MJM. (2022) Analysis of the H-Ras mobility pattern in vivo shows cellular hetero-

geneity inside epidermal tissue. Dis Model Mech. 15(2): dmm049099

doi: 10.1242/dmm.049099

Bernardello M, Gora RJ, Van Hage P, Castro-Olvera G, Gualda EJ, Schaaf MJM, Loza-Al-

varez P. (2021) Analysis of intracellular protein dynamics in living zebrafish embryos us-

ing light-sheet fluorescence single-molecule microscopy. Biomed Opt Express. 12(10):

6205-6227

doi: 10.1364/BOE.435103

185